



Climate Change Research Centre
Faculty of Science
The University of New South Wales
Sydney, Australia

El Niño and El Niño Modoki impacts on
South American rainfall

Alejandro Silva Brito

Supervisors: Matthew England and Andréa Taschetto

A thesis submitted in fulfilment of the requirements for the
degree of Master in Science by research

2011

ORIGINALITY STATEMENT

'I hereby declare that this submission is my own work and to the best of my knowledge it contains no materials previously published or written by another person, or substantial proportions of material which have been accepted for the award of any other degree or diploma at UNSW or any other educational institution, except where due acknowledgement is made in the thesis. Any contribution made to the research by others, with whom I have worked at UNSW or elsewhere, is explicitly acknowledged in the thesis. I also declare that the intellectual content of this thesis is the product of my own work, except to the extent that assistance from others in the project's design and conception or in style, presentation and linguistic expression is acknowledged.'

Signed

Date

Abstract

The impacts of El Niño and El Niño Modoki events on interannual rainfall variability over South America are investigated. The emphasis is on the South American rainy season which is comprised of austral summer and autumn periods. We use Singular Value Decomposition analysis to identify the modes of covariability between Sea Surface Temperature (SST) and rainfall patterns associated with inter El Niño variations.

During austral summer the first (second) mode of covariability represents El Niño (El Niño Modoki). South America shows negative rainfall anomalies over the tropics associated with the anomalous descending branch of the Walker circulation during El Niño. However during El Niño Modoki, the tropical regions experience above average rainfall generated by enhanced convection activity in the South Atlantic Convergence Zone region. The subtropics feature positive (negative) rainfall anomalies associated with an anomalously strong (weak and redirected) South American Low Level Jet (SALLJ) during El Niño (El Niño Modoki).

During autumn season tropical (subtropical) South America features positive (negative) rainfall anomalies during El Niño Modoki, contrasting with El Niño conditions. In the tropics, this is a direct consequence of the shift in the descending branch of the anomalous Walker circulation toward the eastern Pacific, which allows the seasonal migration of Atlantic Intertropical Convergence Zone. This mechanism is found to be reinforced by the tropical Atlantic SST conditions further increasing the associated convection activity over the tropical band. Over the subtropics, wave-like propagations from the central Pacific lead to a barotropic anticyclonic anomaly. It modulates the low level circulation over the continent by redirecting and weakening the SALLJ and thus reinforcing the positive (negative) rainfall anomalies over the tropics (subtropics).

During the late spring period, El Niño Modoki events are associated with enhanced rainfall south of Southeastern South America (SESA). This signal seems to be driven by an anomalous barotropic anticyclone triggered by upper level wave-like propagations emanating from the anomalous heating source in the central equatorial Pacific. During El Niño conditions the anomalous SALLJ favours the occurrence of positive rainfall anomalies over north of SESA instead.

Our results are supported by Atmospheric General Circulation Model (AGCM) perturbation experiments.

Acknowledgments

First, I would like to thank my supervisors Prof. Matthew England and Dr. Andréa Taschetto for their invaluable supervision, comments and suggestions throughout my candidature bringing substantial enhancements to the development and design of this project. I cannot leave without mentioning Andréa's infinite and tireless patience with my countless queries especially during the last stage. It was a nice team.!

The help and comments of Dr. Steven Phipps particularly during the modelling stage made my life surprisingly easier and funnier than expected. I really enjoyed exploring the climate modelling world. This experience has, without doubt, enormously contributed to my formation.

The comments of Dr. Alex Sen Gupta on early stage of research were also very helpful and important to delimit the shape of this project.

To CCRC and UNSW administrative and technical staff for allowing me to easily sort out my student requirements during the whole period of my candidature.

The constant support and eternal love from my dearest family over the years, especially from my two little sisters Roxana and Paula, have been all that I need to accomplish every goal in my life. Thanks for everything, I know you are proud of this achievement.

To the amazing people that I met during my stay in Sydney. Sarah, Vance, Tim, Peng, Kookhee, Yin Er Lee, Mauricio, Jose and Aldo. Your friendship, help and the funny experiences we shared are much appreciated and will not be forgotten.

I also want to thank my previous supervisors in Chile, Dr. Luis Soto, Sergio Salinas and Dr. Jaime Letelier. Your previous support, tools and shared-experiences have been very helpful to me and of course they will over time.

My deepest thank (and also very important!) to CONICYT-CHILE scholarship program and to CCRC for providing partial funding to undertake this Master program.

All of you have contributed to complete one part of this story that began long time ago, when I discovered the existence of a fantastic and challenging journey of the Physical Oceanography and climate sciences...

Table of Content

Originality Statement	i
Abstract	ii
Acknowledgements	iii
List of Figures	vii
List of Tables	xvii
List of Acronyms	xviii
CHAPTER 1	1
EL NIÑO AND EL NIÑO MODOKI AS TWO DIFFERENT CLIMATE MODES	1
1.1 BACKGROUND.....	1
1.1.1 Main features	1
1.1.2 Impacts on regional climate	5
1.1.2 The role of the Atlantic variability	10
1.2 THESIS MOTIVATION AND OBJECTIVES.....	12
1.2.1 Main objectives	12
1.3 SCOPE	13
1.4 THESIS STRUCTURE	13
CHAPTER 2	15
MODEL, DATASET DESCRIPTION AND MODEL EVALUATION.....	15
2.1 GENERAL MODEL DESCRIPTION	15
2.2 ATMOSPHERE GENERAL CIRCULATION MODEL	15
2.3 LIMITATIONS	17
2.4 DATASET DESCRIPTION.....	18
2.5 MODEL EVALUATION	19
2.5.1 Rainfall.....	19
2.5.2 Specific Humidity	24
2.5.3 Outgoing longwave radiation (OLR)	25
2.5.4 Temperature	26
2.5.5 Low level wind and sea level pressure	28
CHAPTER 3	31
METHODOLOGY AND EXPERIMENTAL DESIGN	31
3.1 COMPOSITE ANALYSIS	31
3.1.1 Supporting composites for DJF	33
3.2 SINGULAR VALUE DECOMPOSITION (SVD) ANALYSIS: AN OVERVIEW	37
3.3 AGCM PERTURBATION EXPERIMENTS	37
3.4 ESTIMATION OF THE SIGNIFICANCE LEVELS	41
3.4.1 Composites.....	41
3.4.2 Correlations	41

CHAPTER 4	43
EL NIÑO AND EL NIÑO MODOKI IMPACTS DURING THE AUSTRAL SUMMER PERIOD	43
4.1 SEA SURFACE TEMPERATURE	43
4.2 RAINFALL COMPOSITES	45
4.2.1 Large scale features.....	45
4.2.2 South American rainfall anomalies	46
4.3 ASSESSING COUPLED MODES OF SST AND RAINFALL VARIABILITY	49
4.4 LOW-LEVEL CIRCULATION.....	54
4.4.1 Observed conditions during El Niño and El Niño Modoki.....	54
4.4.2 AGCM perturbation experiments	57
4.5 UPPER LEVEL CIRCULATION.....	60
4.5.1 Observed conditions during El Niño and El Niño Modoki.....	60
4.5.2 AGCM perturbation experiments	66
4.6 VERTICAL CIRCULATION	69
4.6.1 Observed conditions during El Niño and El Niño Modoki.....	69
4.6.2. AGCM perturbation experiments	70
4.7 TROPICAL ATLANTIC CONDITIONS AND ITS RELATIONSHIP WITH EL NIÑO AND EL NIÑO MODOKI.....	74
4.8 SOUTH AMERICAN RAINFALL VARIABILITY AND ITS REMOTE CONNECTIONS WITH SST ANOMALIES	78
4.9 SUMMARY AND DISCUSSION	80
CHAPTER 5	87
CHANGES IN THE WALKER CIRCULATION CELL BETWEEN EL NIÑO AND EL NIÑO MODOKI EVENTS AND IMPLICATIONS FOR SOUTH AMERICAN RAINFALL DURING AUTUMN	87
5.1 ANOMALOUS SST CONDITIONS.....	87
5.2 RAINFALL COMPOSITES	89
5.2.1 Large scale features.....	89
5.2.2 South American rainfall anomalies	91
5.3 ASSESSING COUPLED MODES OF SST AND RAINFALL VARIABILITY	94
5.4 LOW-LEVEL CIRCULATION.....	98
5.4.1 Observed conditions during El Niño and El Niño Modoki.....	98
5.4.2 AGCM perturbation experiments	102
5.5 UPPER LEVEL CIRCULATION.....	103
5.5.1 OBSERVED CONDITIONS DURING EL NIÑO AND EL NIÑO MODOKI	103
5.5.2 AGCM perturbation experiments	107
5.6 VERTICAL CIRCULATION	109
5.6.1 Observed changes in the Walker circulation between El Niño and El Niño Modoki events.....	109
5.6.2 AGCM perturbation experiments	110
5.7 A RAINFALL INDEX AS A PROXY OF THE SEASONAL MIGRATION OF THE ATLANTIC ITCZ	113
5.8 OBSERVED AND MODELLED OLR CONDITIONS	115
5.9 SUMMARY AND DISCUSSION	118

CHAPTER 6	124
ANOMALOUS CONDITIONS OF EL NIÑO AND EL NIÑO MODOKI EVENTS AND THEIR IMPACTS DURING THE WINTER AND SPRING SEASONS	124
6.1 THE WINTER SEASON.....	124
6.1.1 Assessing coupled modes of SST and rainfall variability	124
6.1.2 AGCM perturbation experiments: Anomalous Rainfall	128
6.1.3 Vertical circulation.....	130
6.2 THE SPRING SEASON	133
6.2.1 Assessing coupled modes of SST and rainfall variability	133
6.2.2 AGCM perturbation experiments: Anomalous Rainfall	137
6.2.3 Lower level circulation.....	139
6.2.4 Upper level circulation.....	141
6.3 SUMMARY AND DISCUSSION	145
CHAPTER 7	150
CONCLUDING REMARKS	150
REFERENCES	153

List of Figures

- Figure 1.1: First two leading modes of tropical monthly SST anomalies from 1979 through 2004, multiplied by its respective standard deviations of the principal components. a) First mode accounts for 44% of the SST variability representing El Niño. b) Second mode accounts for 12% of the SST variability representing El Niño Modoki. The SST data is from Hadley Centre (HadISST1) as described by Rayner et al. (2003). Boxes represent areas used to average the SST anomalies for their corresponding indices. They all are specified in the text.....2
- Figure 1.2: Normalized time series of PC1 (red), and PC2 (blue).....4
- Figure 1.3: South American topography (m) from National Geophysical Data Center (2006) ETOPO2V2, highlighting some of the key areas mentioned in the text such as Southeastern South America (SESA) in black, Southeastern Brazil (SEB) in red and central eastern Brazil (CEB) in black.....7
- Figure 2.1: Seasonally averaged (a) observed rainfall (CMAP), (b) modelled rainfall Mk3L and (c) the difference between Mk3L and CMAP. The CMAP dataset was interpolated onto the Mk3L atmosphere model grid. The CMAP climatology analysed period is from January 1979 through July 2008. Seasons are indicated in the upper right corner of each panel.....22
- Figure 2.2: Zonally averaged (30°N-60°S) rainfall for the Mk3L stand alone atmosphere model (red), and CMAP (black). The CMAP climatology analysed period is from January 1979 through July 2008.....23
- Figure 2.3: Upper panel as in Fig. 2.1a, but focused on South America during the (left) summer and (right) autumn seasons. The lower panel displays the observed (black) and modelled (red) annual cycle for net South American continental rainfall. The CMAP climatology analysed period is from January 1979 through July 2008.....23
- Figure 2.4: Time longitude plot of 850-hPa specific humidity from (a) NCEP/ NCAR Reanalysis I products (b) and from Mk3L. The average was taken over the full domain between 30°N - 60°S excepting the Indian Ocean basin (40°E - 101°E). Observations were interpolated onto the Mk3L atmosphere model grid. Data correspond to the 850-hPa level. The NCEP/NCAR climatology analysed period is from January 1979 through July 2008.....25
- Figure 2.5: Hovmöller plot of zonally averaged observed NOAA interpolated OLR dataset (a) and (b) simulated OLR over the whole globe excepting the Indian Ocean basin (40°E - 101°E). For symmetry purposes the zonal domain was extended to 60°N - 60°S. Observations were interpolated onto the Mk3L atmosphere model grid. The OLR climatology analysed period is from January 1979 through July 2008.....26
- Figure 2.6: Hovmöller plot of zonally averaged temperature from NCEP/NCAR reanalysis I products (a) and (b) temperature difference Hovmöller plot between the model and observations. The averaged area corresponds to the whole globe excepting the Indian Ocean basin (40°E-101°E). For symmetry purposes the zonal domain was extended to 60°N-60°S. Observations were interpolated onto the Mk3L atmosphere model grid. Data corresponds to 850-hPa level. The NCEP/CNAR climatology analysed period is from January 1979 through July 200827

Figure 2.7: Observed (black) and modelled (red) air temperature annual cycles for South America. The NCEP/NCAR climatology analysed period is from January 1979 through July 2008. Data corresponds to 850-hPa level.....27

Figure 2.8: Seasonally averaged (a) SLP (shading) and 850hPa horizontal winds (vectors) from the NCEP/NCAR reanalysis I, (b) and modelled SLP and 850hpa horizontal wind. (c) Seasonal difference between the observed and modelled SLP (shading), 850hPa horizontal zonal winds (contours). Negative (positive) or solid (dashed) contours mean weaker (stronger) zonal winds than observation in Mk3L. Observations were interpolated onto the Mk3L atmosphere model grid. The NCEP/NCAR climatology analysed period is from January 1979 through July 2008. Seasons are indicated in the upper right corner of each panel.....29

Figure 2.9: Zonally averaged (30°N-60°S) 850hPa horizontal winds for the Mk3L stand alone atmosphere model (red), and NCEP/ NCAR reanalysis I (black). Observations were interpolated onto the Mk3L atmosphere model grid. The NCEP/NCAR reanalysis climatology analysed period is from January 1979 through July 2008.....30

Figure 3.1: NINO3 time series and the 0.7 standard deviation threshold applied (black line) used to composite the observations. The 1.0 standard deviation (red line) threshold used to prepare perturbation experiments (See Section 3.3).....32

Figure 3.2: As in Fig. 3.1 but for EMI time series.....32

Figure 3.3: Extended time series of the NINO3 index highlighting the new 5 summer periods (S1, S2, ... ,S5) used to create the supporting composites for the DJF period, and the corresponding 0.7 standard deviation threshold used (black line).....33

Figure 3.4: (a) Composite of SST anomalies for the summer periods of 1982/83, 1997/98, black line indicates zero SST anomaly contours. (b) Composite for the extended NINO3 index going back to 1950, black line indicates statistically significant SST anomalies regions at the 90% confidence level according to a two-tailed Student t-test. Note different intensities in (a) and (b)34

Figure 3.5: (a) Composite of 850-hPa wind anomalies and sea level pressure (shading) for the summer periods of 1982/83, 1997/98. Black line indicates zero SLP anomaly contours. (b) Composite for the extended NINO3 index going back to 1950. Black contours (vectors) indicate statistically significant regions (pixels) at the 90% confidence level according to a two-tailed Student t-test.....35

Figure 3.6: (a) Composite of rainfall anomalies for the summer periods of 1982/83, 1997/98 using CMAP and (b) Global Precipitation Climatology Centre (GPCC) datasets. (c) Composite of the extended NINO3 index going back to 1950, black contour indicates statistically significant regions at the 90% confidence level according to a two-tailed Student t-test.....36

Figure 3.7: Interpolated SST anomalies (HadISST1) during the monthly evolution of El Niño onto the Mk3L atmosphere model grid. The composites are derived according to a 1.0 standard deviation threshold of the NINO3 index (See Fig. 3.1). The dashed green line denotes the forcing region (specified in the text). Elsewhere the SST forcing is taken to be the climatological monthly mean.....39

Figure 3.8: As in Fig. 3.7 but for El Niño Modoki.....40

Figure 4.1: Composites of SST anomalies during the austral summer for (a) El Niño and (b) El Niño Modoki conditions (See Table 3.1). The SST data is from HadISST1 dataset as described by Rayner et al. (2003). The SST anomalies are a departure of the monthly climatology based on the period from January 1979 through July 2008. Black contours represent statistically significant regions at the 90% confidence level according to a two-tailed Student t-test. Note different intensities in (a) and (b).....44

Figure 4.2: As in Fig.4.1, but for the Atlantic Ocean only. (a) El Niño, and (b) El Niño Modoki conditions. Black contours represent statistically significant regions at the 90% confidence level according to a two-tailed Student t-test. Note different intensities in (a) and (b).....44

Figure 4.3: Composites of the observed rainfall anomalies (CMAP) during (a) El Niño, and (b) El Niño Modoki conditions (See Table 3.1), (c) modelled rainfall anomalies for El Niño (EN-P), and (d) El Niño Modoki (ENM-P) perturbation experiments. The forcing was applied over the Pacific Ocean only. Black contours represent statistically significant regions at the 90% confidence level according to a two-tailed Student t-test.....48

Figure 4.4: Observed rainfall anomalies for (a) El Niño, (b) El Niño Modoki. Modelled rainfall anomalies for (c) El Niño (EN-P), (d) El Niño Modoki (ENM-P), and including the perturbation experiments forced with SST anomalies over the Atlantic Oceans according to (e) EN-PA, (f) ENM-PA, and including the difference between (g) EN-PA minus EN-P, (h) ENM-PA minus ENM-P, (i) ENM-P minus EN-P and (j) ENM-PA minus EN-PA perturbation experiments. Black contours represent statistically significant regions at the 90% confidence level according to a two-tailed Student t-test.....49

Figure 4.5: The first mode of an SVD analysis between the SST (left) and rainfall anomalies (right) during the austral summer period. It accounts for $33.0 \pm (8.5)$ % of the square covariance fraction (SCF). Black contours indicate statistical significant regions at the 90% confidence level according to a two-tailed Student t-test. Time series of the SVD expansion coefficient (below). Red (black) line is associated with the SST (rainfall) mode. The coupling strength (r) between these fields is 0.75. The thin blue line represents the NINO3 index. The correlation coefficient between the SST mode (red) and the NINO3 index (blue) is 0.98. The correlations are statistically significant at the 95% confidence level.....50

Figure 4.6: The second mode of an SVD analysis between the SST (left) and rainfall anomalies (right) during the austral summer period. It accounts for $9.3 \pm (2.4)$ % of the square covariance fraction (SCF). Black contours indicate statistical significant regions at the 90% confidence level according to a two-tailed Student t-test. Time series of the SVD expansion coefficient (below). Red (black) line is associated with the SST (rainfall) mode. The coupling strength (r) between these fields is 0.4. The thin blue line represents the EMI index. The correlation coefficient between the SST mode (red) and EMI index (blue) is 0.89. The correlations are statistically significant at the 95% confidence level.....51

Figure 4.7: The second mode of an SVD analysis between the SST (left) and rainfall anomalies (right) conditions during the austral summer period including the tropical Atlantic SST anomalies. It accounts for $10.5 \pm (2.5)$ % of the square covariance fraction (SCF). Black contours indicate statistical significant regions at the 90% confidence level according to a two-tailed Student t-test. Time series of the SVD expansion coefficient (below). Red (black) line is associated with the SST (rainfall) mode. The coupling strength (r) between these fields is 0.51. The thin blue line represents the EMI index, the correlation coefficient between the SST mode (red) and EMI index (blue) is

0.69. The correlations are statistically significant at the 95% confidence level.....52

Figure 4.8: The first mode of an SVD analysis between the SST (left) and rainfall anomalies (right) during the austral summer period including the tropical Atlantic SST anomalies. It accounts for $28.5 \pm (7.0)$ % of the square covariance fraction (SCF). Black contours indicate statistical significant regions at the 90% confidence level according to a two-tailed Student t-test. Time series of the SVD expansion coefficient (below). Red (black) line is associated with the SST (rainfall) mode. The coupling strength (r) between these fields is 0.75. The thin blue line represents the NINO3 index, the correlation coefficient between the SST mode (red) and NINO3 index (blue) is 0.98. The correlations are statistically significant at the 95% confidence level.....53

Figure 4.9: Regression of the observed DJF 850-hPa wind (vector) and SLP (shading) anomalies onto (a) SST PC1 (El Niño-related) and (b) PC2 (El Niño Modoki-related). Simulated 850-hPa wind and SLP anomalies for (c) EN-P, (d) ENM-P, (e) EN-PA, and (f) ENM-PA experiments. Difference between (g) EN-PA minus EN-P, and (h) ENM-PA minus ENM-P. Black contours (vectors) represent statistically significant regions (pixels) at the 90% confidence level according to a two-tailed Student t-test.....55

Figure 4.10: As in Fig. 4.9 but focused on South America. Difference between perturbation experiments not included. Black contours (vectors) encompass statistically significant regions (pixels) at the 90% confidence level according to a two-tailed Student t-test.....56

Figure 4.11: Regression of the observed DJF 200-hPa wind (vector) and geopotential height anomalies (shading) anomalies onto (a) SST PC1 (El Niño-related) and (b) PC2 (El Niño Modoki-related). Simulated 200-hPa wind and geopotential height anomalies for (c) EN-P, (d) ENM-P, (e) EN-PA, and (f) ENM-PA experiments. Difference between (g) EN-PA minus EN-P, and (h) ENM-PA minus ENM-P. Black contours (vectors) represent statistically significant regions (pixels) at the 90% confidence level according to a two-tailed Student t-test.....62

Figure 4.12: Regression of the observed DJF 200-hPa asymmetric streamfunction anomalies onto (a) SST PC1 (El Niño-related) and (b) PC2 (El Niño Modoki-related). Simulated anomalous 200-hPa asymmetric streamfunction for (c) EN-P, (d) ENM-P, (e) EN-PA, and (f) ENM-PA experiments. Difference between (g) EN-PA minus EN-P and (h) ENM-PA minus ENM-P, units are m^2/s . Black contours represent statistically significant regions at the 90% confidence level according to a two-tailed Student t-test.....63

Figure 4.13: Composites of the observed anomalous 200-hPa divergent winds (vectors) and velocity potential (shading) during the summer period of (a) El Niño, and (b) El Niño Modoki (See Table 3.1). The blue (red) shading regions indicate anomalous upper level divergence (convergence) centres. Composites of simulated anomalous 200-hPa divergent winds and velocity potential for (c) EN-P, (d) ENM-P, (e) EN-PA, and (f) ENM-PA perturbation experiments, and the velocity potential anomaly difference between (g) EN-PA minus EN-P and (h) ENM-PA minus ENM-P. The units of divergent wind (velocity potential) are m/s (m^2/s). Black contours represent statistically significant regions at the 90% confidence level according to a two-tailed Student t-test.....64

Figure 4.14: Composites of the observed vertical velocity anomalies during (a) El Niño and (b) El Niño Modoki events (See Table 3.1). The simulated vertical velocity anomaly for (c) EN-P, (d) ENM-P, (e) EN-PA, (f) ENM-PA, and the vertical velocity anomaly difference between (g) EN-PA minus EN-P, and (h) ENM-PA minus ENM-P perturbation experiments. The vertical velocity was averaged over the 10°N-10°S latitudinal band. Blue (red) shading is associated with upward (downward) motion. The associated SST anomalies (°C) are shown below. Black contours represent statistically significant regions at the 90% confidence level according to a two-tailed Student t-test.....72

Figure 4.15: Composite of the observed anomalous 500-hPa vertical velocity during the summer period of El Niño Modoki according to a 0.7 standard deviation threshold of the EMI index (See Table 3.1). Negative (positive) values indicate ascending (descending) motion. Dashed black boxes indicate the regions, i.e. Eastern equatorial Pacific (5°N-5°S, 138°W-88°W) and Eastern equatorial South America (5°N-5°S, 63°W-38°W), used to estimate the Walker Index during El Niño conditions. Solid Black boxes indicate the regions, i.e. Central equatorial Pacific (5°N-5°S, 188°W-163°W) and Western equatorial South America (5°N-5°S, 75°W-63°W), used to estimate a suitable Walker Index during El Niño Modoki conditions, i.e. the Modoki-Walker Index.....73

Figure 4.16: (upper) The NINO3 and Walker indices and its corresponding correlation coefficient in the upper right corner (-0.77 at zero lag). (Middle) The EMI and Walker indices and its corresponding correlation coefficient in the upper right corner (0.28, when the EMI leads the Walker Index by 6 months). (Lower) The EMI and the Modoki-Walker indices and its corresponding correlation coefficient in the upper right corner (-0.51 at zero lag). The correlations are statistically significant at the 95% confidence level.....73

Figure 4.17: Time series of (a) the NINO3 and tNA, (b) NINO3 and tSA, (c) EMI and tNA, and (d) EMI and tSA indices. The NINO3 and EMI (tNA and tSA) indices are represented in black (red) lines. The maximum correlation coefficient (r) of the corresponding lagged cross correlations is indicated in the upper right corner of each panel. In: (a) the tNA lags the NINO3 index by 5 months, (b) the tSA leads the NINO3 index by 8 months, (c) the tNA leads the EMI index by 4 months,(d) the tSA lags the EMI index by 3 months. Only the correlations undertaken for the NINO3 index are statistically significant at the 95% confidence level.....76

Figure 4.18: (a) Cross correlation between the EMI and tNA (black) and the NINO3 and tNA indices (red). (b) Cross correlation between the EMI and tSA (black) and the NINO3 and tSA indices (red). The analysis is undertaken during El Niño and El Niño Modoki years only according to the Table 3.1.....77

Figure 4.19: Composite of the monthly evolution of the Atlantic SST anomalies during (left panels) El Niño and (right panels) El Niño Modoki. Months are indicated in the upper right corner of each box. The monthly evolution is determined according to the Table 3.1. Solid green rectangles (left panel of January) indicate the tNA (5°N-25°N, 60°W-30°W) and tSA (25°S-5°S, 30°W-0°E) regions respectively as described by Giannini et al. (2004). Black line represents zero contour SST anomalies.....77

Figure 4.20: Correlation between the expansion coefficient time series of the first (upper panel) and second (lower panel) rainfall modes of variability, PC1 and PC2 respectively, with the monthly SST anomalies during the austral summer period. The black contours encompass areas where the correlations are statistically significant at the 90% confidence level.....79

Figure 5.1: Composite of the SST anomalies during the austral autumn for (a) El Niño and (b) El Niño Modoki conditions (See Table 3.1). The SST data is from the HadISST1 dataset as described by Rayner et al. (2003). The SST anomalies are a departure of the monthly climatology based on the period from January 1979 through July 2008. Black contours represent statistically significant regions at the 90% confidence level according to a two-tailed Student t-test.....88

Figure 5.2: As in Fig. 5.1, but for the Atlantic Ocean only. (a) El Niño, and (b) El Niño Modoki conditions. Black contours represent statistically significant regions at the 90% confidence level according to a two-tailed Student t-test.....89

Figure 5.3: Composites of the observed rainfall anomalies (CMAP) during (a) El Niño, and (b) El Niño Modoki conditions (See Table 3.1), (c) modelled rainfall anomalies for El Niño (EN-P), and (d) El Niño Modoki (ENM-P) perturbation experiments. The forcing was applied over the Pacific Ocean only. Black contours represent statistically significant regions at the 90% confidence level according to a two-tailed Student t-test.....91

Figure 5.4: Observed rainfall anomalies for (a) El Niño, (b) El Niño Modoki. Modelled rainfall anomalies for (c) El Niño (EN-P), (d) El Niño Modoki (ENM-P), and including the perturbation experiments forced with SST anomalies over the Atlantic Oceans according to (e) EN-PA, (f) ENM-PA, and including the difference between (g) EN-PA minus EN-P, (h) ENM-PA minus ENM-P, (i) ENM-P minus EN-P and (j) ENM-PA minus EN-PA perturbation experiments. Black contours represent statistically significant regions at the 90% confidence level according to a two-tailed Student t-test.....94

Figure 5.5: The first mode of an SVD analysis between the SST (left) and rainfall anomalies (right) during the austral autumn period. It accounts for $31 \pm (8)$ % of the square covariance fraction (SCF). Black contours indicate statistical significant regions at the 90% confidence level according to a two-tailed Student t-test. Time series of the SVD expansion coefficient (below). Red (black) line is associated with the SST (rainfall) mode. The coupling strength (r) between these fields is 0.7. The thin blue line represents the NINO3 index. The correlation coefficient between the SST mode (red) and the NINO3 index (blue) is 0.98. The correlations are statistically significant at the 95% confidence level.....95

Figure 5.6: The second mode of an SVD analysis between the SST (left) and rainfall anomalies (right) associated with El Niño Modoki conditions during the austral autumn period. It accounts for $9.7 \pm (2.6)$ % of the square covariance fraction (SCF). Black contours indicate statistical significant regions at the 90% confidence level according to a two-tailed Student t-test. Time series of the SVD expansion coefficient (below). Red (black) line is associated with the SST (rainfall) mode. The coupling strength (r) between these fields is 0.6. The thin blue line represents the EMI index. The correlation coefficient between the SST mode (red) and the EMI index (blue) is 0.95. The correlations are statistically significant at the 95% confidence level.....96

Figure 5.7: Correlation coefficient map between the expansion coefficient time series of the first (upper panel) and second (lower panel) rainfall modes of variability, PC1 and PC2 respectively, with the monthly SST anomalies during the austral autumn period. The black contours encompass areas where the correlations are statistically significant at the 90% confidence level.....98

Figure 5.8: Regression of the observed MAM 850-hPa wind (vector) and SLP (shading) anomalies onto (a) SST PC1 (El Niño-related) and (b) PC2 (El Niño Modoki-related). Simulated 850-hPa wind and SLP anomalies for (c) EN-P, (d) ENM-P, (e) EN-PA, and (f) ENM-PA experiments. Difference between (g) EN-PA minus EN-P, and (h) ENM-PA minus ENM-P. Black contours (vectors) represent statistically significant regions (pixels) at the 90% confidence level according to a two-tailed Student t-test.....100

Figure 5.9: As in Fig. 5.8 but focused on South America. Difference between perturbation experiments not included. Black contours (vectors) encompass statistically significant regions (pixels) at the 90% confidence level according to a two-tailed Student t-test.....101

Figure 5.10: Regression of the observed MAM 200-hPa asymmetric streamfunction anomalies onto (a) SST PC1 (El Niño-related) and (b) PC2 (El Niño Modoki-related). Simulated anomalous 200-hPa asymmetric streamfunction for (c) EN-P, (d) ENM-P, (e) EN-PA, and (f) ENM-PA experiments. Difference between (g) EN-PA minus EN-P and (h) ENM-PA minus ENM-P, units are m^2/s . Black contours represent statistically significant regions at the 90% confidence level according to a two-tailed Student t-test.....105

Figure 5.11: Composites of the observed anomalous 200-hPa divergent winds (vectors) and velocity potential (shading) during the autumn period of (a) El Niño, and (b) El Niño Modoki conditions (See Table 3.1). The blue (red) shading regions indicate anomalous upper level divergence (convergence) centres. Composites of simulated anomalous 200-hPa divergent winds and velocity potential for (c) EN-P, (d) ENM-P, (e) EN-PA, and (f) ENM-PA perturbation experiments, and the velocity potential anomaly difference between (g) EN-PA minus EN-P and (h) ENM-PA minus ENM-P. The units of divergent wind (velocity potential) are m/s (m^2/s). Black contours represent statistically significant regions at the 90% confidence level according to a two-tailed Student t-test.....106

Figure 5.12: Composites of the observed vertical velocity anomalies during (a) El Niño and (b) El Niño Modoki events (See Table 3.1). The simulated vertical velocity anomaly for (c) EN-P, (d) ENM-P, (e) EN-PA, (f) ENM-PA, and the vertical velocity anomaly difference between (g) EN-PA minus EN-P, and (h) ENM-PA minus ENM-P perturbation experiments. The vertical velocity was averaged over the $10^{\circ}N$ - $10^{\circ}S$ latitudinal band. Blue (red) shading is associated with upward (downward) motion. The associated SST anomalies ($^{\circ}C$) are shown below. Black contours represent statistically significant regions at the 90% confidence level according to a two-tailed Student t-test.....112

Figure 5.13: Composites of the rainfall climatology of (left panel) the austral summer and (right panel) autumn seasons. The white circle in the right panel displays the approximate locations of the Fortaleza ($3.7^{\circ}S$, $38.5^{\circ}W$) and Quixeramobim ($5.3^{\circ}S$, $39.3^{\circ}W$) rainfall stations used to estimate the Northeast Brazil rainfall Index (FQI). The rainfall climatology analysed period is from January 1979 through July 2008 based on CMAP dataset as described by Xie and Arkin (1996).....114

Figure 5.14: Time series of (upper panel) PC1 (blue) and the NINO3 (black), FQI (red) indices. The lagged cross correlation (r_1) between the NINO and FQI indices is -0.52 at zero lag. The time series of (lower panel) PC2 (blue) and the EMI (black), FQI (red) indices. The lagged cross correlation (r_2) between the EMI and FQI indices is 0.22 at zero lag. Just the correlation of the upper panel is statistically significant at the 90% confidence level.....115

Figure 5.15: Regression of the observed MAM OLR (Wm^{-2}) anomalies onto (a) SST PC1 (El Niño-related) and (b) PC2 (El Niño Modoki-related). Simulated anomalous OLR for (c) EN-P, (d) ENM-P, (e) EN-PA, and (f) ENM-PA experiments. Difference between (g) EN-PA minus EN-P and (h) ENM-PA minus ENM-P. Black contours represent statistically significant regions at the 90% confidence level according to a two-tailed Student t-test.....117

Figure 5.16: Schematic of the impacts of (upper) El Niño and (lower) El Niño Modoki on South American rainfall during autumn and its associated mechanisms. During El Niño the anomalous ascending branch of the Walker circulation over the eastern equatorial Pacific is compensated with anomalous subsidence over the tropical regions of the continent inhibiting the associated convection activity of the Atlantic ITCZ, leading to negative rainfall anomalies over the tropics. Additionally an anomalously strong SALLJ (green) brings moisture toward SESA favouring anomalous rainfall. The shift in the anomalous warming location during El Niño Modoki leads to anomalous subsidence over the eastern Pacific. Consequently, this favours the normal seasonal migration of the Atlantic ITCZ allowing the Atlantic SST to reinforce the associated convection favouring positive rainfall anomalies. An anomalous offshore barotropic anticyclone (black) is triggered over the subtropics as a consequence of wave-like propagation emanating from the central Pacific. It interacts with the anomalous low level cyclonic pattern (green) leading to anomalous divergence and negative rainfall anomalies over SESA and also to a weakening of the climatological SALLJ further increasing the positive rainfall anomalies over the tropics. Over the continent red (blue) shading indicates positive (negative) rainfall anomalies.....120

Figure 6.1: The first mode of an SVD analysis between the SST (left) and rainfall anomalies (right) during the austral winter period. It accounts for $29.0 \pm (7.5)$ % of the square covariance fraction (SCF). Black contours indicate statistical significant regions at the 90% confidence level according to a two-tailed Student t-test. Time series of the SVD expansion coefficient (below). Red (black) line is associated with the SST (rainfall) mode. The coupling strength (r) between these fields is 0.63. The thin blue line represents the NINO3 index. The correlation coefficient between the SST mode (red) and the NINO3 index (blue) is 0.96. The correlations are statistically significant at the 95% confidence level.....125

Figure 6.2: The second mode of an SVD analysis between the SST (left) and rainfall anomalies (right) during the austral winter period. It accounts for $10.4 \pm (2.6)$ % of the square covariance fraction (SCF). Black contours indicate statistical significant regions at the 90% confidence level according to a two-tailed Student t-test. Time series of the SVD expansion coefficient (below). Red (black) line is associated with the SST (rainfall) mode. The coupling strength (r) between these fields is 0.58. The thin blue line represents the EMI index. The correlation coefficient between the SST mode (red) and the EMI index (blue) is 0.82. The correlations are statistically significant at the 95% confidence level.....126

Figure 6.3: Correlation between the expansion coefficient time series of the first (upper panel) and second (lower panel) rainfall modes of variability, PC1 and PC2 respectively, with the monthly SST anomalies during the austral winter period. The black contours encompass areas where the correlations are statistically significant at the 90% confidence level.....128

Figure 6.4: Observed rainfall anomalies for (a) El Niño, (b) El Niño Modoki. Modelled rainfall anomalies for (c) El Niño (EN-P), (d) El Niño Modoki (ENM-P), and including the perturbation experiments forced with SST anomalies over the Atlantic Oceans according to (e) EN-PA, (f) ENM-PA, and including the difference between (g) EN-PA minus EN-P, (h) ENM-PA minus ENM-P, (i) ENM-P minus EN-P and (j) ENM-PA minus EN-PA perturbation experiments. Black contours represent statistically significant regions at the 90% confidence level according to a two-tailed Student t-test..... 130

Figure 6.5: Composites of the observed vertical velocity anomalies during (a) El Niño and (b) El Niño Modoki events (See Table 3.1). The simulated vertical velocity anomaly for (c) EN-P, (d) ENM-P, (e) EN-PA, (f) ENM-PA, and the vertical velocity anomaly difference between (g) EN-PA minus EN-P, and (h) ENM-PA minus ENM-P perturbation experiments. The vertical velocity was averaged over the 10°N-10°S latitudinal band. Blue (red) shading is associated with upward (downward) motion. The associated SST anomalies (°C) are shown below. Black contours represent statistically significant regions at the 90% confidence level according to a two-tailed Student t-test..... 132

Figure 6.6: The first mode of an SVD analysis between the SST (left) and rainfall anomalies (right) associated with El Niño conditions during the austral spring period. It accounts for $31.5 \pm (8.4)$ % of the square covariance fraction (SCF). Black contours indicate statistical significant regions at the 90% confidence level according to a two-tailed Student t-test. Time series of the SVD expansion coefficient (below). Red (black) line represents the SST (rainfall) mode. The coupling strength (r) between these fields is 0.61. The thin blue line represents the NINO3 index. The correlation coefficient between the SST mode (red) and the NINO3 index (blue) is 0.99. The correlations are statistically significant at the 95% confidence level..... 134

Figure 6.7: The second mode of an SVD analysis between the SST (left) and rainfall anomalies (right) associated with El Niño Modoki conditions during the austral spring period. It accounts for $9.6 \pm (2.5)$ % of the square covariance fraction (SCF). Black contours indicate statistical significant regions at the 90% confidence level according to a two-tailed Student t-test. Time series of the SVD expansion coefficient (below). Red (black) line is associated with the SST (rainfall) mode. The coupling strength (r) between these fields is 0.59. The thin blue line represents the EMI index. The correlation coefficient between the SST mode (red) and the EMI index (blue) is 0.95. The correlations are statistically significant at the 95% confidence level..... 135

Figure 6.8: Correlation between the expansion coefficient time series of the first (upper panel) and second (lower panel) rainfall modes of variability, PC1 and PC2 respectively, with the monthly SST anomalies during the austral spring period. The black contours encompass areas where the correlations are statistically significant at the 90% confidence level..... 137

Figure 6.9: Observed rainfall anomalies for (a) El Niño, (b) El Niño Modoki. Modelled rainfall anomalies for (c) El Niño (EN-P), (d) El Niño Modoki (ENM-P), and including the perturbation experiments forced with SST anomalies over the Atlantic Oceans according to (e) EN-PA, (f) ENM-PA, and including the difference between (g) EN-PA minus EN-P, (h) ENM-PA minus ENM-P. Black contours represent statistically significant regions at the 90% confidence level according to a two-tailed Student t-test..... 139

Figure 6.10: Regression of the observed anomalous 850-hPa winds (vectors) and SLP (shading) for the spring period during (a) El Niño, and (b) El Niño Modoki onto the SST PC1, PC2 time series respectively. The simulated anomalous 850-hPa winds and SLP composites of (c) EN-P, (d) ENM-P, (e) EN-PA, and (f) ENM-PA perturbation experiments. Black contours (vectors) represent statistically significant regions (pixels) at the 90% confidence level according to a two-tailed Student t-test.....140

Figure 6.11: (Left panels) Lagged composites of the observed 200-hPa geopotential height and horizontal winds anomalies from the spring throughout the summer season (from top to bottom) during El Niño conditions. (Right panels) As in the left panel but for El Niño Modoki conditions. For the composite years see Table 3.1. Black contours (vectors) represent statistically significant regions at the 90% confidence level according to a two-tailed Student t-test. The composited period is indicated in the upper right corner of each plot.....142

Figure 6.12: Composites of the observed SON 200-hPa wind (vector) and geopotential height anomalies (shading) anomalies during (a) El Niño and (b) El Niño Modoki conditions (See Table 3.1). Simulated 200-hPa wind and geopotential height anomalies for (c) EN-P, (d) ENM-P, (e) EN-PA, and (f) ENM-PA experiments. Difference between (g) EN-PA minus EN-P, and (h) ENM-PA minus ENM-P. Black contours (vectors) represent statistically significant regions at the 90% confidence level according to a two-tailed Student t-test.....144

List of Tables

Table 2.1: The hybrid vertical levels used within the Mk3L atmosphere model (k), the value of the η -coordinate, the approximate height (m), and the pressure level (hPa) on which some model variables are saved.....	16
Table 3.1: Selected years used to obtain composites above a 0.7 standard deviation threshold of the NINO3 and EMI indices.....	32
Table 3.2: Summary of the different perturbation experiments carried out for this project.....	38
Table 3.3: The factors used to multiply the interpolated monthly anomalous fields to carry out the AGCM perturbation experiments. Note that the same factor is used to multiply the monthly SST anomalies of the perturbation experiments of El Niño.....	38
Table 4.1: Square covariance fraction of El Niño (Mode 1) and El Niño Modoki (Mode 2) for the tropical Pacific Ocean only and for both the tropical Pacific and Atlantic oceans SVD analyses. The coupling strength is estimated by the correlation coefficient of the SVD time series between the SST and rainfall mode. The correlation coefficients are statistically significant at the 95% confidence level.....	53

List of Acronyms

AMIP	Atmospheric Model Intercomparison Project
AGCM	Atmospheric General Circulation Model
CEB	Central eastern Brazil
CMAP	Merged Analysis of Precipitation
CPC	Climate Prediction Center
CSIRO	Commonwealth Scientific and Industrial Research Organization
DJF	December, January, February
ENSO	El Niño Southern Oscillation
EN	El Niño
ENM	El Niño Modoki
EN-P	AGCM perturbation experiment for El Niño conditions undertaken with Pacific SST anomalies
EN-PA	AGCM perturbation experiment for El Niño conditions undertaken with Pacific and Atlantic SST anomalies
ENM-P	AGCM perturbation experiment for El Niño Modoki conditions undertaken with Pacific SST anomalies
ENM-PA	AGCM perturbation experiment for El Niño Modoki conditions undertaken with Pacific and Atlantic SST anomalies
EOF	Empirical Orthogonal Function
GCM	General Circulation model
GPCC	Global Precipitation Climatology Center
HadISST1	Hadley Ice and Sea Surface Temperature
IPCC	Intergovernmental Panel on Climate Change
ITCZ	Intertropical Convergence Zone
JJA	June, July, August
MAM	March, April, May
Mk1,2,3	Versions 1,2,3 of the CSIRO climate system model
NOAA	National Oceanic and Atmospheric Administration
NCEP-NCAR	The National Centers for Environmental Prediction-National Centers Atmospheric Research

OLR	Outgoing Longwave Radiation
PDZ	Pacific Dry Zone
PDO	Pacific Decadal Oscillation
PNA	Pacific North American
PSA	Pacific South American
SACZ	South Atlantic Convergence Zone
SALLJ	South American Low Level Jet
SEB	Southeastern Brazil
SESA	Southeastern South America
SJ	Subtropical Jet
SON	September, October, November
SLP	Sea Level Pressure
SPCZ	South Pacific Convergence Zone
SSCP	Subtropical South Central Pacific
SST	Sea Surface Temperature
SSTa	Sea Surface Temperature anomalies
SVD	Singular Value Decomposition
tNA	tropical North Atlantic
tSA	tropical South Atlantic
WHWP	Western Hemisphere warm pool

Chapter 1

El Niño and El Niño Modoki as two different climate modes

This chapter provides an overview about El Niño Modoki and how it differs from the classical El Niño events. It compares the worldwide effects on climate with emphasis on South American rainfall. Motivation and objectives are also outlined in this chapter.

1.1 Background

1.1.1 Main features

During the last few decades El Niño-Southern Oscillation (ENSO) has been regarded as the dominant climate mode in the equatorial Pacific with worldwide linked-effects on climate (Ropelewski and Halpert, 1987; Kiladis and Diaz, 1989). One of its most important effects are those related with changes in precipitation patterns. Severe floods and droughts associated with ENSO occur in different parts of the world negatively affecting important economic activities of many countries such as, agriculture, hydrology, and tourism.

Ongoing research provides enough supporting evidence that ENSO has changed over time (Trenberth and Stephaniak, 2001; Larkin and Harrison, 2005a; Ashok et al., 2007; Kao and Yu, 2009; Kug et al., 2009), and thus associated impacts. Since 2007, the existence of a new type of ENSO, i.e. ENSO Modoki, had been revealed and several observational studies reported contrasting effects on climate patterns worldwide (Wang and Hendon, 2007; Weng et al., 2007; Ashok et al., 2009b; Ashok et al., 2009a; Weng et al., 2009; Taschetto et al., 2010). Furthermore, these studies converged on a new approach by assessing both phenomena independently to enable a better understanding of their impacts. Since their combined effects have been documented during the last few years, it increases the level of complexity to properly describe its frequency, magnitude and its global effects. Up to now, not enough detailed emphasis has made on the climate impacts to inter-El Niño events over South America. This region is directly affected during El Niño events by important changes in atmospheric circulation producing extreme rainfall and droughts in different areas (Grimm et al., 2000; Drumond, 2001; Ambrizzi et al., 2005; Grimm and Ambrizzi, 2009; Grimm and

Tedeschi, 2009; Silva et al., 2009). However, those described effects have generally not been separated from ENSO Modoki impacts. This is the main goal of the present study.

El Niño Modoki features an anomalous warming in the central Pacific (165°E - 140°W) flanked by anomalous cooling at the western and eastern boundaries of the basin, thus creating an anomalous zonal sea surface temperature (SST) gradient along the equator. In contrast, the “typical” El Niño events are characterized by an anomalous warming extending from the central to the eastern Pacific, reaching the South American coast (Figs. 1.1a,b). Different nomenclature have been used to refer to this new El Niño such as, Trans El Niño (Trenberth and Stephaniak, 2001), central-Pacific El Niño (Kao and Yu, 2009; Yeh et al., 2009), warm pool El Niño (Kug et al., 2009), dateline El Niño (Larkin and Harrison, 2005b), and the one we adopted in this project, “El Niño Modoki” or pseudo El Niño (Ashok et al., 2007).

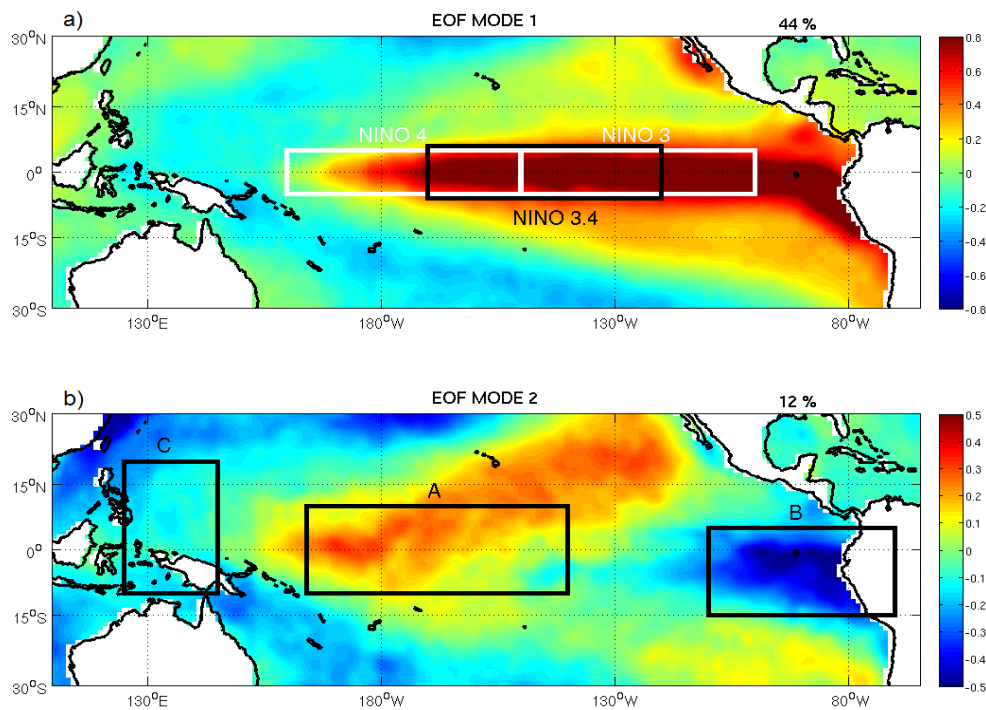


Figure 1.1: First two leading modes of tropical monthly SST anomalies from 1979 through 2004, multiplied by its respective standard deviations of the principal components. a) First mode accounts for 44% of the SST variability representing El Niño. b) Second mode accounts for 12% of the SST variability representing El Niño Modoki. The SST data is from Hadley Centre (HadISST1) as described by Rayner et al. (2003). Boxes represent areas used to average the SST anomalies for their corresponding indices. They all are specified in the text.

Another important difference between both types of El Niño, i.e. besides the anomalous SST zonal gradient, is the teleconnection pattern. During El Niño Modoki, the Walker circulation is featured by a double convective-cell, with an ascending branch over the

central Pacific, and low level (high level) wind convergence (divergence). The descending branches are found at the western (100°E - 130°E), and eastern Pacific (120°W - 85°W) associated with both a rainfall suppression, and low level wind divergence. This differs from the single convective-cell pattern typically found during traditional El Niño events, where most of the tropical Pacific is covered by an ascending branch, and low level westerly wind anomalies (150°E - 85°W) (Ashok et al., 2007; Weng et al., 2007).

Multi-level temperature data also shows rather different spatial characteristics on the atmosphere between both phenomena, especially during the austral summer. At low levels (1000 - 850 hPa), the warming is mainly located at the equatorial eastern Pacific during El Niño, surrounded by anomalous cooler regions that roughly diverge from the dateline towards both hemispheres. Whereas during the different “flavour” of El Niño, this tropospheric warming is also found but with a much broader meridional extent, i.e. from Alaska to Patagonia, and more focused toward the central Pacific. Higher level observations reveal even more differences in term of this tropospheric warming; at both 500 and 200-hPa levels a strong along-equator warming signal is revealed during El Niño, whereas during El Niño Modoki off-equatorial warm and cool centres highlight, hence creating a quadrupole Rossby wave pattern, with temperatures below the average in the western Pacific and Indian Oceans, and above the average toward the central Pacific (Trenberth and Smith, 2009).

The spatial and temporal features of El Niño Modoki are further revealed by the second mode of an Empirical Orthogonal Function (EOF) analysis of the monthly SST anomalies. This mode explains 12% of the total variance for the period 1979 - 2004 in the tropical Pacific, whereas the first mode represents the canonical El Niño pattern with about 45% of the tropical SST variability (Fig. 1.1). Based on this analysis, Ashok et al. (2007) proposed the El Niño Modoki index (EMI). It is defined as $EMI = [SSTA]_A - 1/2 * ([SSTA]_B + [SSTA]_C)$, where the brackets represent the average of SST anomalies over the spanning regions A (165°E - 140°W, 10°S - 10°N), B (110°W - 70°W, 15°S - 5°N), and C (125°E - 145°E, 10°S - 20°N) respectively (Fig. 1.1b). Thus this index has been tuned to obtain the zonal SST gradient along the equator, emphasizing the warming located at the central Pacific. For comparison purposes, the correlation between NINO3 index (averaged area of SST anomalies bounded by 5°N - 5°S, 150°W - 90°W) and the time series of normalized principal component for the first mode (PC1) accounts for 0.98, whereas the correlation between EMI index and the time series of the second EOF (PC2) is 0.91 both statistically significant at the 99% level. Thus,

NINO3 and EMI indices can be used to represent and quantify El Niño and El Niño Modoki respectively (Ashok et al., 2007). The time scales for both events are also different, a wavelet power spectrum analysis of NINO3 shows up an interannual signal with 4 years of periodicity (interannual variability), whereas of EMI reveals a signal with 12 years of periodicity (decadal variability) (Ashok et al., 2007; Weng et al., 2007), a feature that can be seen in Figure 1.2.

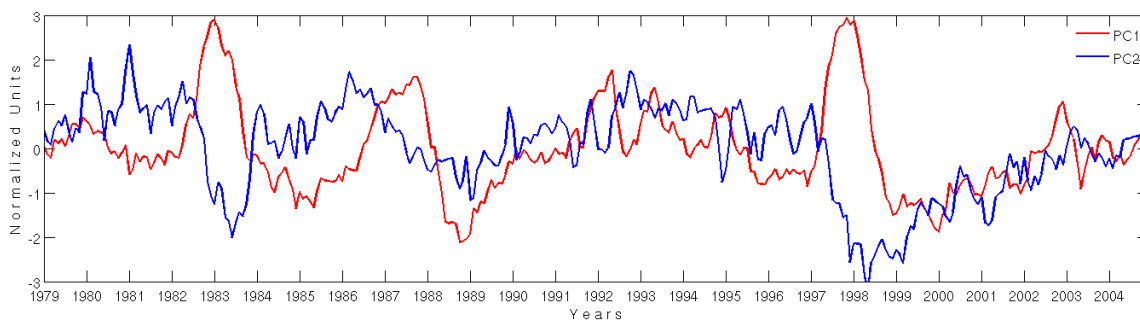


Figure 1.2: Normalized time series of PC1 (red), and PC2 (blue).

The existence of a new index for describing El Niño Modoki offers us a new approach in order to get a better understanding of the tropical variability by treating both events independently. Because El Niño (La Niña) events have been typically quantified by indices based on SST by averaging specific regions onto the equatorial Pacific, the magnitudes of these indices strongly rely on the location of the anomalous warming (cooling). As a consequence, some indices may mix up both types of El Niño. This is exactly what happens when using either NINO3.4 (SST averaged on 5°N – 5°S and 170°W - 120°W) or NINO4 (SST averaged on 5°N – 5°S and 160°E - 150°W) indices to quantify El Niño, as they span the areas in the equatorial Pacific where positive SST anomalies are typically found during both traditional El Niño and El Niño Modoki (Fig. 1.1). Moreover, they do not consider the SST variability on the western and eastern Pacific boundaries, key areas that make El Niño Modoki unique (Fig. 1.1b) (Ashok et al., 2007). A supporting example of contamination of NINO3.4 index is fully described by Weng et al. (2007).

During El Niño Modoki onset, westerly wind anomalies in the western Pacific may play an important role by advecting warm water from the off-equatorial region to the equator, thus driving downwelling Kelvin equatorial waves able to further deepen the thermocline at the central Pacific. In addition, easterly wind anomalies in the eastern Pacific also develop, producing a low level convergence zone that contributes to the deepening of the thermocline (Ashok et al., 2007). However, the understanding about the dynamical processes during El Niño Modoki are still quite controversial as there are

previous studies supporting that equatorial thermocline variations are not important in El Niño Modoki evolution (Kug et al., 2009; Yu and Kim, 2010). In particular, Yu and Kim (2010) obtained depth anomalies of the 20°C isotherm at the equator to suggest that El Niño Modoki develops in different background thermocline conditions, i.e. deeper/shallower than normal or neutral, although this remains uncertain as not enough observations were available to properly assess the thermocline depth during the analysed record.

A coupled GCM study carried out by Kug et al. (2010) shows that during canonical El Niño events, there is a very strong equatorial heat discharge poleward and thus the observed dynamical feedback is consistent with a quick transition to a cold event according to the recharge oscillator paradigm (Jin, 1997a; b). In contrast, during El Niño Modoki, the discharge process is found to be much weaker than a canonical El Niño, and the SST anomaly during El Niño Modoki is thermally damped via evaporative cooling instead, and as a consequence La Niña event does not occur. Moreover, because El Niño Modoki is not followed by a cold event, as the canonical El Niño generally is, it is suggested that its occurrence is contributing to a warming of the mean state of the tropical Pacific according to the tendency found in model results. Using multi-model ensemble simulations, Yeh et al. (2009) suggested that under a global warming scenario the occurrence ratio of El Niño Modoki is increased in contrast to the occurrence ratio for canonical El Niño event.

1.1.2 Impacts on regional climate

Observational studies reveal quite different worldwide impacts on weather and climate patterns between both phenomena. For example, contrasting differences in air temperature during the boreal summer period had been reported. The regions from California to Alaska, Japan, western North America and north of China are anomalously warm during El Niño Modoki whereas they are cool or near normal during El Niño. Further, cool and mostly normal conditions are found over South America during El Niño Modoki, whereas extremely warm conditions are found over much of the continent during typical El Niño events (Weng et al., 2007). A detailed description of the boreal winter period is given by Weng et al. (2009). However during El Niño Modoki, the most relevant difference is the anomalous rainfall spatial distribution. During the boreal summer period, positive rainfall anomalies are mostly located at the west of the international dateline leaving most of the eastern equatorial Pacific with negative rainfall anomalies. In contrast during El Niño, positive rainfall anomalies are typically found from the central Pacific to the eastern side of the basin (Ashok et al., 2007).

Furthermore, during El Niño Modoki the positive rainfall anomalies seem to extend from the central Pacific toward the northeast and southeast with a northward shift of the Inter Tropical Convergence Zone (ITCZ) and a southward expansion of the South Pacific Convergence Zone (SPCZ). This distribution is mainly a response to the zonal 850-hPa wind anomalies as they diverge into three branches by 160°E toward both hemispheres. This pattern is referred as a boomerang distribution, and it roughly matches the SST anomaly distribution during El Niño Modoki (Weng et al., 2007; Weng et al., 2009). In contrast during traditional El Niño, there are well-defined westerly wind anomalies along the equator, and thus the ITCZ and SPCZ tend to partially merge into a single anomalous rainfall band able to reach the coast of South America, bringing anomalous rainfall especially during the boreal summer (Weng et al., 2007; Vincent et al., 2009). In particular during El Niño Modoki, several studies report severe droughts in the western Pacific regions including Indonesia, Malaysia, Singapore, south of Japan, and much of Australia except for January and February when the Australian Monsoon is enhanced (Taschetto et al., 2009). In contrast, over the eastern Pacific negative rainfall anomalies are found during the austral summer season, spanning the whole equatorial and tropical regions of South America. The likely responsible mechanism for the observed deficit of rainfall during El Niño Modoki is the anomalous descending branch of the Walker circulation located at the western and eastern tropical Pacific, producing enhanced subsidence over these areas. This is further confirmed by atmospheric general circulation model (AGCM) ensemble experiments during the boreal summer of the event of 2004 by Ashok et al. (2009b). In addition, over subtropical latitudes (40°S) a branch of positive rainfall anomalies extending southeastward from the central equatorial Pacific toward the South American coast has also been reported.

It is noteworthy to emphasize that all the previous anomalous rainfall patterns are not found during El Niño as the positive SST anomalies tend to be located mostly over the central-to-eastern tropical Pacific. Therefore, wet conditions are mostly found near the coast of north-western America, and over important parts of South America, especially the west coast from the equator to 40°S and also on the southeastern portion of the continent (SESA) (Fig 1.3). In contrast, a reduction of rainfall can be found over the western Pacific, northern and also northeastern-equatorial South America (Ashok et al., 2007; Weng et al., 2007).

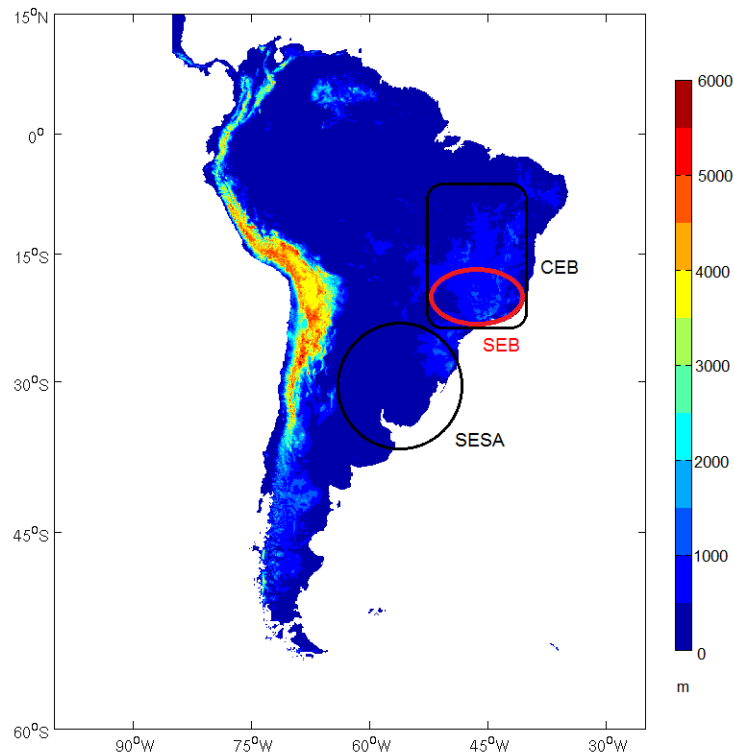


Figure 1.3: South American topography (m) from National Geophysical Data Center (2006) ETOPO2V2, highlighting some of the key areas mentioned in the text such as Southeastern South America (SESA) in black, Southeastern Brazil (SEB) in red and central eastern Brazil (CEB) in black.

Furthermore, the strongest signal, during the negative phase of the Southern Oscillation for the South American monsoon period (DJF), is referred in the literature as a dipole-like pattern, on which negative rainfall anomalies on the northern and northeastern areas of the continent are found, contrasting with the positive rainfall anomalies over the SESA region (Ambrizzi et al., 2005; Grimm and Ambrizzi, 2009). Nevertheless, some early studies had shown some discrepancies between the spatial patterns of this interannual mode. This dipole mode is usually represented by the first EOF mode and it is strongly correlated with the ENSO SST anomalies, although some differences are seen over North-Western South America and central eastern Brazil (CEB) (Zhou and Lau, 2001; Paegle and Mo, 2002). A recent analysis of the interannual rainfall variability for the summer monsoon and spring seasons during the period 1961-2000 by Grimm and Zilli (2009) shows a reversal of this anomalous dipole mode from spring to summer. In particular, they found that the first spring EOF mode explains about 18.5% of the variance and is strongly linked to ENSO. In contrast the first summer EOF mode, which features an opposite spatial pattern explaining 22% of the variability, is not. However, the second summer EOF is linked to ENSO, explaining around 10 % of variance, but this spatial mode tends to show positive anomalies over

both the SESA and CEB regions, and negative anomalies tend to be focused further north of the continent. A shift between remote and local forcing during spring-to-summer transition period seems to be responsible for this dipole inversion. During the austral spring season, when upper level circulation anomalies seem to be remotely forced, low level anticyclonic rotational anomalies are responsible for enhancing (decreasing) moisture fluxes to southeastern (central eastern) South America, increasing (decreasing) anomalous rainfall on that area. In contrast during the summer months, when the local processes overcome the remote forcing, this anticyclonic anomaly evolves into a cyclonic pattern that enhances (decreases) moisture fluxes into central eastern (southeastern) South America leading to enhanced (weakened) anomalous rainfall there. This cyclonic anomaly features a baroclinic vertical structure hypothesized to mainly be a local response to surface-atmosphere feedback, contrasting with the anomalous barotropic circulation found there during the spring season.

Drumond and Ambrizzi (2006) suggest that a shift of the centre of convection at the equatorial Pacific during strong and weak ENSO events may modulate the interannual seesaw rainfall pattern over southeastern and central eastern South America for the spanning period 1950-2001 during the austral summer period. In particular, they report positive rainfall anomalies over the SEB and negative anomalies over the SESA regions, when strong convection activity is located over the central Pacific. In contrast, during strong El Niño events the anomalous convection centre is found throughout the central and eastern Pacific, reversing the rainfall dipole, namely positive (negative) rainfall anomalies over the SESA (SEB) region. However, their classification of events is focused on the anomaly sign over the South Atlantic convergence zone (SACZ) region without consideration of the anomalous warming at the central Pacific versus the central-eastern Pacific. Therefore during the analysis, the authors omitted some typical Modoki events, such as those that typically occurred during the 1990s.

Changes in low level atmospheric circulation have also been reported for South America, in response to a different anomalous warming location in the tropical Pacific. Observational evidence suggests changes in the location of the South American Low-Level Jet east of the Andes (SALLJ) during the austral summer season, where during the El Niño event of 1997-1998 an enhanced moisture transport occurred via the strengthened SALLJ toward the La Plata Basin (30°S), i.e. SESA. During the El Niño of 2002-2003, a Modoki-type event, the SALLJ was displaced northward, hence decreasing the moisture transport to this area (Silva and Ambrizzi, 2006). This

mechanism was further supported by AGCM ensemble experiments by Hill et al. (2009), however, these studies only focused on two particular interannual events. In addition, observations suggest that ENSO variability modulates the SALLJ. Silva et al. (2009) show that during El Niño (La Niña) years, the SALLJ events increase (decrease) in frequency and the Subtropical Jet (SJ) enhances (weakens). It is worth mentioning that, as the authors defined El Niño years based on the NINO3.4 index, they mistakenly classified El Niño Modoki years such as 1991-92, 2002-03 as normal El Niño events or even as neutral events such as 1993-1994, 2003-2004. These years all actually represent typical Modoki-type events according to the definition of Ashok et al. (2007). On the basis that NINO3.4 strongly mixes both phenomena as already stated above, it is likely that these findings may be contaminated by an El Niño Modoki signal.

Reported changes in upper level circulation during El Niño Modoki events feature a shift in the storm track activity during the austral winter in central Argentina in response to the strengthening of the Subtropical Jet (SJ) as shown by the upper level westerlies in Ashok et al. (2009a).

Besides the tropics-to-tropics teleconnection impacts during El Niño and El Niño Modoki years, i.e via the anomalous Walker circulation, tropics-to-extratropic teleconnections are also found over South America, and several inter-event differences have been observed. The typical upper level atmospheric response during El Niño is a wave-train-like pattern propagating from the central-to-western Pacific into the extratropics and then turning northeastward toward South America. This is known as The Pacific South American (PSA) mode (Mo, 2000). This mode is particularly strong over the Pacific region. It has a wavenumber 3 structure at midlatitudes. During the austral summer it exhibits a much more zonally symmetric structure and a weaker magnitude than during the spring season. In particular, during this season the atmospheric mean state is weaker than in summer, allowing the PSA mode to produce a much more important role on teleconnection related effects (Cazes Boezio et al., 2003; Grimm and Ambrizzi, 2009; Grimm and Zilli, 2009). In particular, Vera et al. (2004) explored the upper level Southern Hemisphere response by considering warming/cooling conditions in the Subtropical South Central Pacific (SSCP) and convection linked at the South Pacific Convergence Zone (SPCZ) during the spring season for El Niño events. They provided evidence that during several El Niño years, when cooling (warming) conditions are found at SSCP in conjunction with enhanced (inhibited) convection activity over the SPCZ a strong (weak) PSA mode is found to be linked with a strong (weak) meridional propagation of wave activity flux from the

extratropics toward southeastern South America. As a result during the spring season, upper level cyclonic anomalies develop at the southern tip of South America whereas anticyclonic anomalies occur over the southeastern portion of the continent. This pattern has an equivalent barotropic structure that strengthens the subtropical jet over this region in association with warm and moist air from the north tending to favour precipitation over that region (Grimm et al., 2000; Grimm, 2003a).

1.1.3 The role of the Atlantic variability

During ENSO events South American rainfall may also be modulated by Atlantic SST anomalies, specifically over the Amazon and Northeast Brazil regions (Pulwarty, 1994; Nobre and Shukla, 1996; Souza et al., 2000). During the rainy seasons, i.e. DJF and MAM, an anomalous cross-equatorial SST gradient may develop in the tropical Atlantic Ocean. When anomalous warming (cooling) is found over the tropical North Atlantic (tNA) and anomalous cooling (warming) over the tropical South Atlantic (tSA), i.e. a positive (negative) gradient (Servain, 1991), there is a rainfall deficit (enhancement) over the Brazilian Amazon and specially over the northeast region (Giannini et al., 2004). Furthermore, the sign of this cross-equatorial SST gradient modulates the latitudinal position of the ITCZ (Nobre and Shukla, 1996; Souza and Nobre, 1998; Giannini et al., 2004). Thus during the MAM period the Atlantic ITCZ is controlled by SST, trade winds, and sea level pressure changes over the tropical Atlantic (Chiang et al., 2002). As a consequence, strong variations during the rainy season in the northern and northeastern areas of South America are mainly associated with the southward excursion of the ITCZ. Numerical studies support this, during El Niño combined with a positive (negative) dipole over the tropical Atlantic, below (above) average precipitation prevails over northeast Brazil (Pezzi and Cavalcanti, 2001; Giannini et al., 2004). Further Ambrizzi et al. (2005) provides observational evidence about the different impacts on interannual rainfall between inter ENSO variations. They suggest that the Atlantic dipole configuration may produce a different regional atmospheric circulation during weak El Niño and La Niña events compared to the canonical circulation patterns. In addition by focusing on the differences between the Walker and Hadley circulation cells, they report anomalous subsidence at around 20°S, namely northward from the SESA region (Fig. 1.3), during the DJF period for El Niño in conjunction with positive Atlantic gradient conditions. In contrast, during weak El Niño events combined with a negative Atlantic dipole, this subsidence is shifted southward to 30°S just over the SESA region leading to negative rainfall anomalies there and thus producing contrasting rainfall effects compared to typical El Niño events. Ambrizzi et al. (2005) suggest that when Pacific SST anomalies are weak, they produce the necessary

conditions for the Atlantic anomalies to control the circulation pattern and therefore the anomalous rainfall distribution.

Many studies have presented observational evidence that the ENSO phenomenon influences the atmospheric circulation and the SST anomalies over the northern tropical Atlantic through atmospheric teleconnection patterns to the higher latitudes of the Northern Hemisphere, namely via the Pacific North American pattern (PNA) (Horel and Wallace, 1981; Wallace and Gutzler, 1981; Nobre and Shukla, 1996). In particular Horel and Wallace (1981) found that in conjunction with a Pacific equatorial warming, alternating poleward positive and negative geopotential height anomalies emanate from the equatorial Pacific, deflecting eastward and then equatorward. Thus, the PNA induces SLP variations that weaken the North Atlantic Subtropical high cell. As a result it therefore produces variations in the northeast trade winds that tend to favour the occurrence of positive SST anomalies over the tNA.

Another dynamical process for ENSO to influence atmospheric and SST anomalies in the northern tropical Atlantic is via the so-called atmospheric bridge (Alexander et al., 2002; Wang, 2005). During the mature phase of ENSO the Atlantic Hadley cell weakens. i.e. Its climatological descending branch is located over northern South America as well as its ascending branch over the subtropical north Atlantic high pressure system reverse or weakens, leading to an overall weakening of the anticyclonic system likewise the PNA propagation and therefore the associated northeast trade winds over the tNA region. This condition leads to a reduction of evaporation and entrainment processes favouring the positive SST anomalies over tNA region that further enhances the warming produced by the peak of the tropical Western Hemisphere warm pool (WHWP).

1.2 Thesis motivation and objectives

Most of the interannual rainfall studies do not focus on the effects of anomalous warming location in the Pacific Ocean and virtually no updated modelling studies are available in this regard for South America. This motivates us to assess the effects of El Niño Modoki on interannual rainfall variability over this land mass with emphasis in the South American rainy season which comprises the austral summer and autumn periods. In addition, most of the related studies tend not to assess each of this climate modes isolated, we focus on the separate effects of El Niño and El Niño Modoki. Therefore, in this context this project provides a new chance to use an unexplored criterion for the South American continent in order to estimate the impact of El Niño Modoki for this region and to compare them to those typically found during El Niño events.

It is well known the preconditioning role of the Atlantic Ocean during El Niño in modulating its impact over the continent by either increasing or reducing the magnitude of the anomalies for some properties, further modulating the climate signals over South America. As a complement we explore the role of the Atlantic Ocean conditions during El Niño and El Niño Modoki events, the last remains largely unexplored.

The main objectives for this project are then to evaluate and compare the effects in the South American rainy seasons, i.e. austral summer and autumn period, during both El Niño and El Niño Modoki events.

1.2.1 Main objectives

The main objectives can be summarized as follows:

- To describe the most significant features of ocean surface temperature for the Pacific and Atlantic basin during El Niño and El Niño Modoki years.
- To explore the existence of any new evidence about the role of Atlantic SST anomalies during El Niño Modoki on South American rainfall and to compare them to those typically reported for traditional El Niño events.
- To characterize their corresponding lower and upper level circulation patterns.
- To explore the most important mechanisms able to explain the observed variability in response to a different warming locations over the Pacific Ocean using a general circulation model (GCM) of the atmosphere forced by underlying SST.

1.3 Scope

A complete description of the external atmospheric variability, which is driven by SST, provides critical information in order to better understand the complex ocean-atmosphere interactions in the coupled system. AGCM experiments are aimed to accomplish this. As the main objective of this thesis is to obtain the rainfall response due to anomalous warming conditions over the equatorial Pacific Ocean, our results are based solely on AGCM perturbation experiments, although a detailed model evaluation comparing to observations is also undertaken.

It is important to state that the corresponding AGCM perturbation experiments were also run for La Niña and La Niña Modoki. However, we restrict the thesis content to focus on El Niño and El Niño Modoki events. La Niña and La Niña Modoki impacts on South American rainfall variability are postponed for future research studies.

We remark again that the focus will be on the South American rainy season, which spans the austral summer (DJF) and autumn (MAM) periods. However, we also provide a combined chapter with some relevant results of the winter and spring season.

Finally, some coupled control run were also analyzed. Because the large scale circulation simulated by the AGCM experiments were much more realistic compared to the coupled control run, we decided to retain a focus on the AGCM experiments.

1.4 Thesis Structure

Chapter 1 provides a review of El Niño Modoki as a new climate mode, comparing its worldwide effects on climate, and how it can be quantified from a new perspective, i.e. by using the EMI index. The most important effects of El Niño over South America are described.

Chapter 2 focuses on providing a model description and a regional model evaluation with particular emphasis over South America. A dataset description is also given in this chapter.

Chapter 3 describes the methodology used to undertake this research. The experimental design section provides further details on how the perturbation experiments were undertaken.

Chapters 4 to 6 describe the results obtained. The analyses are stratified by seasons. The observed conditions for December, January and February (DJF) period during El Niño and El Niño Modoki events are described in Chapter 4.

Chapter 5 as in Chapter 4 but for the March, April, May (MAM) period.

Chapter 6 as in Chapter 4 but for the June, July, August (JJA) and September, October, November (SON) periods.

Chapter 7 Concluding remarks.

Chapter 2

Model, dataset description and model evaluation

A brief overview about the climate model used in this project is given. In order to complement this, a model evaluation is also performed for identifying relevant biases found over the study area. This chapter also describes the different datasets used in this project.

2.1 General model description

The model used is the Commonwealth Scientific and Industrial Research Organization (CSIRO) Mk3L climate system model version 1.2. It is a fully coupled atmosphere-sea ice-ocean general circulation model (GCM). The atmospheric component of Mk3L is a low resolution version of CSIRO Mk3, used by the Intergovernmental Panel on Climate Change (IPCC) (Gordon et al., 2002; Phipps, 2006b). The oceanic general circulation model is an upgraded version of the oceanic component of the CSIRO Mk2 coupled model (Gordon and O'Farrell, 1997). The sea-ice model includes both ice dynamics and ice thermodynamics according to O'Farrell (1998). The land surface model is an enhanced version of the soil-canopy scheme of Kowalczyk et al. (1994), with a new parameterization of soil moisture and temperature, a greater number of soil and vegetation types, and a new multi-layer snow cover scheme.

The following section will outline the most relevant features of the atmosphere model, as is the model used to carry out our AGCM perturbation experiments. For further details, the CSIRO Mk3L is fully described by Phipps (2006b; 2010).

2.2 Atmosphere general circulation model

While Mk3 uses a spectral resolution of T63, Mk3L spectral resolution was set up to R21. This is still supported for research purpose (Santoso et al., 2011). Thus the zonal and meridional resolutions are approximately 5.625° and 3.18° respectively.

The atmosphere model uses a hybrid vertical coordinate system with 18 vertical levels. The Earth surface forms the first coordinate surface, as in the σ -system, then gradually reverting to isobaric levels with increasing altitude (Table 2.1). Some variables such as

winds, geopotential height, temperature, specific and relative humidity are interpolated onto pressure levels.

Level (k)	η	Approximate Height (m)	Pressure (hPa)
18	0.0045	36355	5
17	0.0216	27360	10
16	0.0542	20600	20
15	0.1001	16550	30
14	0.1574	13650	50
13	0.2239	11360	70
12	0.2977	9440	100
11	0.3765	7780	150
10	0.4585	6335	200
9	0.5415	5070	250
8	0.6235	3970	300
7	0.7023	3025	400
6	0.7761	2215	500
5	0.8426	1535	600
4	0.8999	990	700
3	0.9458	575	850
2	0.9784	300	925
1	0.9955	165	1000

Table 2.1: The hybrid vertical levels used within the Mk3L atmosphere model (k), the value of the η -coordinate, the approximate height (m), and the pressure level (hPa) on which some model variables are saved.

The topography is obtained by interpolating the worldwide terrain height Scripps dataset on to the model grid. It originally has a $1^\circ \times 1^\circ$ resolution (Gates and Nelson, 1975). Moisture advection is via Semi-Lagrangian transport (McGregor, 1993), and gravity wave drag is parameterised according to Chouinard et al. (1986). The atmospheric model resolves diurnal and seasonal cycles. Cloud radiative forcing is determined by using Method II of Cess and Potter (1987) as clear sky radiation calculations are also performed at each radiation timestep. The shortwave radiation scheme is based on Lacis and Hansen (1974), whereas the longwave radiation scheme uses the parameterization developed by Fels and Schwarzkopf (1975; 1981), and Schwarzkopf and Fels (1985; 1991). Ozone concentrations are taken from the Atmospheric Model Intercomparison Project (AMIP) II dataset (Wang et al., 1995; Wang et al., 2009).

The cumulus convection scheme is based on the U.K. Meteorological Office scheme (Gregory and Rowntree, 1990), which is coupled to the prognostic cloud scheme of Rotstajn (1997; 1998; 2000) to calculate the amount of stratiform cloud by using three

prognostic variables of water vapour mixing ratio, cloud liquid water mixing ratio and cloud ice mixing ratio.

2.3 Limitations

The coarse resolution used in this project implies that many key local processes like orographic precipitation, for instance, and important topographic features like mountains may not be properly taken into account, and hence decreasing the accuracy of the model results. It may also prevent us to obtain a detailed structure of the regional atmospheric circulation when trying to identify a responsible mechanism for the observed variability. Thus, a focus on the large scale circulation features will be taken throughout this thesis.

The study area represents a real challenge for climate models. Firstly, the South American continent features prominent topographic barriers such as The Andes Mountain, representing a narrow chain bordering the western coast of the continent and typically reaching 6000 m at subtropical latitudes. On the other hand the existence of the Brazilian plateau over the tropical eastern South America, although lower in altitude than The Andes Mountain, also adds further complexity. Together these topographic systems create a unique climate signal over the continent. Secondly, the presence of the Amazon basin represents an important strong convective and moisture recycling area implying that in order to get the correct amount of seasonal rainfall, climate models must correctly simulate a number of processes such as evapotranspiration, condensation, and transport among others. The state of the art of climate modelling, unfortunately, is not yet able to fully achieve this. Thus, it is not surprising that most of the climate models tend to present systematic biases over the Amazon region, and it is not any exception for the model used in this study. The next section of this chapter is devoted to a regional model evaluation in this regard.

Finally, it is worth mentioning that El Niño and El Niño Modoki are regarded as a positive or warm phase of a linear oscillation, i.e ENSO and ENSO-Modoki respectively, which comprises of La Niña and La Niña Modoki as their corresponding negative or cold phases. This linear approach is usually done to add simplicity to the complex dynamics involved, and it may potentially not include all the processes involved. Likewise, most of the analyses used here are also mostly based on linear methodologies such as EOF, and regression analyses, further preventing us to properly account for non-linear variability in the system.

2.4 Dataset description

The SST fields used in this study are from The Hadley Centre Global Sea Ice and Sea Surface Temperature (HadISST1) dataset (Rayner et al., 2003). HadISST1 has a spatial resolution of 1° latitude x 1° longitude. The Climate Prediction Center Merged Analysis of Precipitation (CMAP) rainfall dataset (Xie and Arkin, 1996), NOAA interpolated OLR (Liebmann and Smith, 1996), and atmospheric fields provided by NCEP-NCAR reanalysis I (Kalnay et al., 1996) such as sea level pressure, geopotential height, multi-level winds, vertical velocity (ω), velocity potential and streamfunction were also used in this study. Unlike HadISST1, all the others mentioned datasets are available over a $2.5^\circ \times 2.5^\circ$ grid. They all correspond to global monthly observations from January 1979 through July 2008. The anomalies represent a departure from their corresponding monthly climatology considering the spanning period above.

It is important to clarify that, although temperature and specific humidity datasets will be used in the next section for model evaluation, they are not used at further stages of this project.

Three main reasons are important to mention at this stage to support the selected time period of analysis. Firstly, this period of time covers the same Pacific Decadal Oscillation phase, thus in this way we avoid adding unnecessary complexity to the results allowing us to properly contrast the effects between both phenomena. Secondly, the frequency and magnitude of El Niño Modoki has increased after 1978, hence we select strong enough events to properly evaluate their impacts. Lastly this period spans the most reliable period with added quality from satellite products, ensuring high-quality dataset and trustworthy results, further supporting our selected period of analysis.

The following seasons, defined for the Southern Hemisphere, are used to obtain the composites and to perform different analyses such as regression, singular value decomposition: summer (DJF), autumn (MAM), winter (JJA), and spring (SON). They are used in the next section for model evaluation purposes also in further stages in this thesis.

2.5 Model evaluation

As the primary purpose of this project is to estimate the contrasting atmospheric response according to an anomalous warming at both the central and central-eastern Pacific and to evaluate the impacts on rainfall variability over South America, this section is aimed at evaluating the Mk3L atmospheric stand alone model with a focus on regional scale. To accomplish this, we evaluate a vast area from the tropics in the Northern Hemisphere to the extratropical latitudes in the Southern Hemisphere (30°N - 60°S) spanning the whole globe but excluding the Indian Ocean basin (40°E - 101°E). This region represents a suitable area to properly study the inter-El-Niño-related variability and its associated remote teleconnection patterns in conjunction with the influence of the Atlantic Ocean SST variability, which are able to modify the South American climate. A corresponding global coupled model evaluation is described by Phipps (2006a).

2.5.1 Rainfall

To evaluate precipitation, the CMAP dataset (Xie and Arkin, 1996) is used. The observed rainfall climatology (Fig. 2.1a) reveals the main large scale rainfall features such as, the SPCZ peaking during DJF and tending to weaken by MAM, JJA, and then enhancing again during the spring season. The South American monsoon, associated with strong convection activity in the SACZ region, begins during late SON and peaks during the DJF season. This strong convection area has a northwest-to-southeast orientation, with an oceanic portion magnitude weaker than its magnitude over the continent. The retreat of the SACZ begins during MAM toward the northwest, whilst the Atlantic ITCZ presents its southernmost position over the continent. The dynamic associated with both the SACZ and Atlantic ITCZ represent the major component of the rainfall annual cycle over the continent (Zhou and Lau, 2001; Ambrizzi et al., 2005; Cook, 2009). The Pacific Dry Zone (PDZ) located at the western coast of South America presents a major extent during SON and DJF, becoming weak during MAM. The enhanced rainfall region over the western Pacific presents a strong seasonal variability between the Southern Hemisphere during DJF and the Northern Hemisphere during JJA periods.

Although the model is successful at simulating the main large scale rainfall patterns described above, there are still some noteworthy features to highlight such as an excess of rainfall at the western tropical Pacific. The spatial pattern and magnitude of

this bias is found to be much larger during JJA in the Northern Hemisphere than the other seasons, it is also slightly shifted northward in comparison with observations during that period (Figs. 2.1b, c). Opposite biases, i.e. rainfall underestimation, are found over the eastern tropical Pacific and Atlantic Oceans with a similar seasonal behaviour, namely peaking during JJA. These biases represent a common feature in most of the climate models (Randall et al., 2007). As a consequence, the modelled ITCZ tends to have too much rainfall over the western-to-central Pacific, contrasting with the deficient rainfall over the eastern Pacific (Figs. 2.1b, 2.1c). Further, during its seasonal evolution, the ITCZ becomes weak in the model during the JJA and SON seasons around 120°W (Figs. 2.1b, 2.2). A slightly northward shift of the ITCZ during these seasons can also be seen (Fig. 2.2), whereas during the DJF and MAM periods the ITCZ location shows better agreement with observed rainfall. Tropical South African rainfall is found to be excessive in the model throughout the seasons except for JJA.

The intensity of rainfall over the SPCZ is overestimated on its easternmost section throughout the seasons (Figs. 2.1b, 2.1c), whereas over its westernmost portion the simulated rainfall is underestimated. The simulated SPCZ also depicts a larger zonal extent particularly during the DJF and MAM seasons when it becomes stronger around 120°W (Fig. 2.1b). This zonal-like bias represents a common feature also found in multi-model rainfall means (Randall et al., 2007).

The major differences of the modelled PDZ in the eastern Pacific compared to observations are seen during the DJF period. The PDZ tends to reach the international dateline during its development along the equator (Fig. 2.1b, 2.1c). It becomes weak during MAM, and then it strengthens again during JJA and SON in agreement with observations. However, weak negative biases are still found over the western coast of South America throughout the seasons.

Over the South America, simulated rainfall is clearly excessive in the SACZ during the South American Monsoon season (DJF), and also in the Atlantic portion of the ITCZ over the continent during MAM (Fig. 2.1b, 2.1c). A bias in the simulated position of SACZ is also seen during the monsoon period. Further, during MAM there is a southward shift of modelled position of the Atlantic ITCZ compared to observations, this represents a common bias in many AGCMs (Biasutti et al., 2006). Over the equatorial western South America, rainfall is also overestimated throughout the seasons excluding the SON period, when rainfall is overestimated over the northern region instead. The areas of highest topography on the eastern flank of the continent, i.e. the

Bolivian Altiplano which represents a high level (~3800 m) plateau region of the central Andes (15°S), also present slight rainfall overestimation, in particular during the SON and DJF and then weakened by the MAM and JJA seasons. Simulated rainfall is too weak over the subtropics, especially over the SESA region, throughout the seasons (Figs. 2.1b,c). It is worth mentioning that the overwhelming majority of climate models exhibit this negative bias over this region (Christensen et al., 2007). The model also tends to simulate an excess of rainfall over the southern tip of the continent through all seasons.

Since most of the area of the continent is located over the tropics, it is expected that the annual cycle of net continental rainfall is strongly associated with the South American rainy season. As already stated, this period comprises of the austral summer (the South American Monsoon), and the autumn seasons. It is evident from the Figure 2.3 that the contribution to the rainfall annual cycle is mostly due to peak of the SACZ and the southward shift of the Atlantic ITCZ during the austral summer and autumn seasons respectively. The model roughly reproduces this tendency, peaking during the DJF and MAM and consequently presenting a minimum during the JJA season. The magnitude of the rainfall annual cycle is slightly underestimated in the model. In particular, the major differences compared to observations are seen during the rainy season, but also during the JJA period when the simulated rainfall is slightly deficient having the minimum rainfall magnitude occurring during July and August, and thus contrasting with the observed minimum during August.

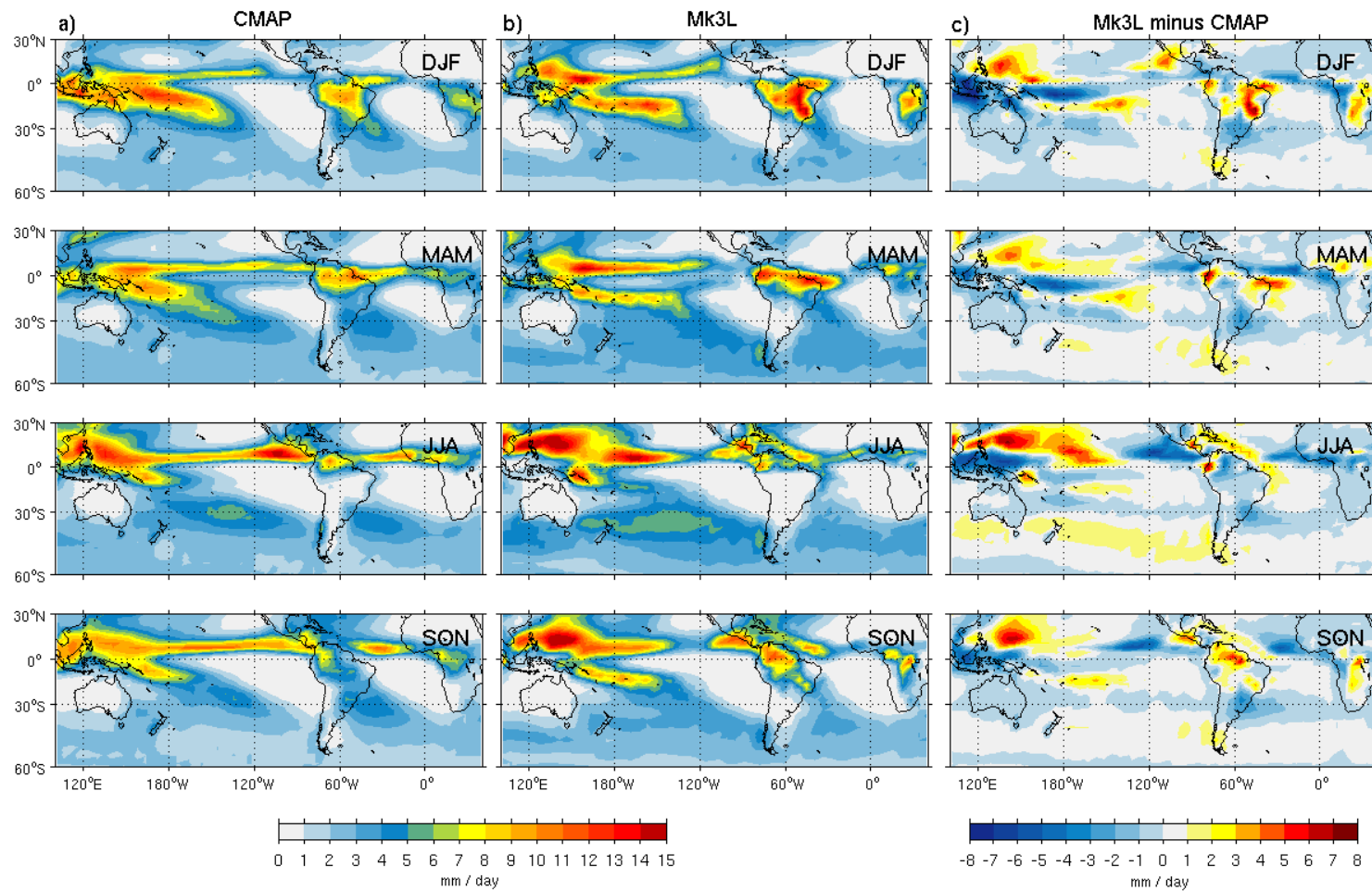


Figure 2.1: Seasonally averaged (a) observed rainfall (CMAP), (b) modelled rainfall Mk3L and (c) the difference between Mk3L and CMAP. The CMAP dataset was interpolated onto the Mk3L atmosphere model grid. The CMAP climatology analysed period is from January 1979 through July 2008. Seasons are indicated in the upper right corner of each panel.

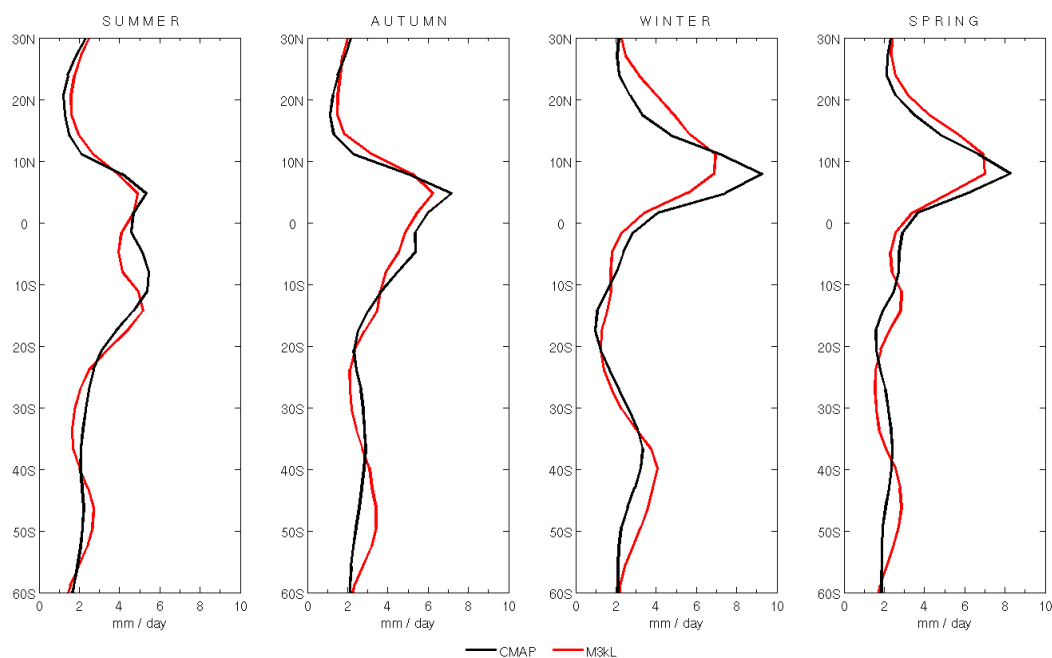


Figure 2.2: Zonally averaged (30°N-60°S) rainfall for the Mk3L stand alone atmosphere model (red), and CMAP (black). The CMAP climatology analysed period is from January 1979 through July 2008.

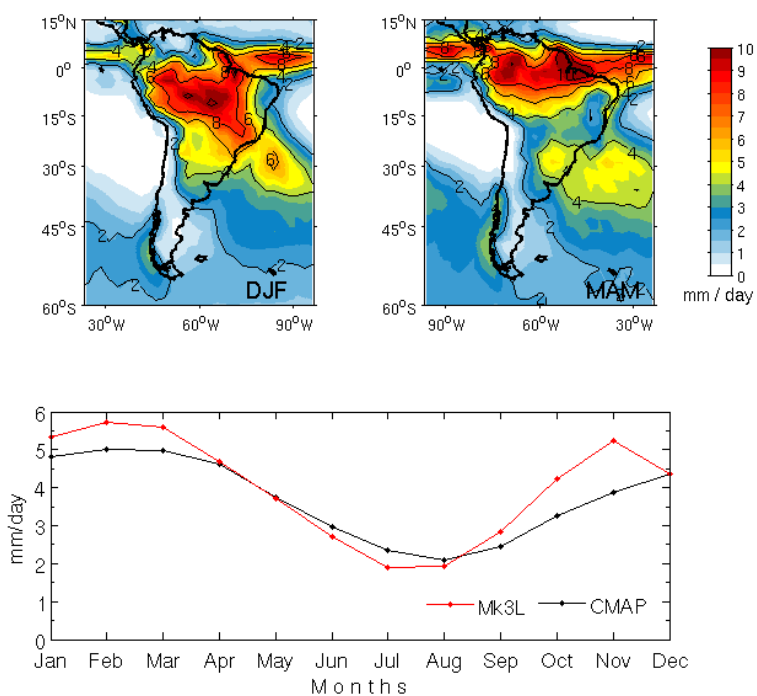


Figure 2.3: Upper panel as in Fig. 2.1a, but focused on South America during the (left) summer and (right) autumn seasons. The lower panel displays the observed (black) and modelled (red) annual cycle for net South American continental rainfall. The CMAP climatology analysed period is from January 1979 through July 2008.

2.5.2 Specific Humidity

For the purpose of supporting the reported rainfall biases, a brief evaluation of specific humidity is undertaken in this section using The National Centers for Environmental Prediction-National Center for Atmospheric Research (NCEP/NCAR) Reanalysis I dataset (Kalnay et al., 1996). Observed specific humidity shows the most expected signals. Firstly, there is a signal peaking over the western Pacific from late MAM to JJA. Secondly, a signal is seen linked to the ITZC over the eastern Pacific peaking during the same period. Finally there is also a signal mostly linked to the SACZ over South America ($35^{\circ}\text{W} - 85^{\circ}\text{W}$) that tends to peak during late SON to DJF (Fig. 2.4a).

It is found that modelled specific humidity fully represents the main temporal and spatial variations (Fig. 2.4b), however, it is slightly overestimated throughout the seasons and specifically peaks during early winter over the tropical western Pacific, in agreement with the observed biases for rainfall (Fig. 2.1b, 2.1c and 2.4b). Over the $135^{\circ}\text{W}-135^{\circ}\text{E}$ region modelled specific humidity is clearly overestimated. It is likely to be a consequence of rainfall overestimation by the model mostly linked to the ITCZ and SPCZ throughout the seasons. This agrees with the rainfall biases reported on section 2.5.1.

Over South America specific humidity linked to the SACZ (around 45°W) is also slightly excessive supporting the positive rainfall biases found during the DJF and MAM seasons (Fig. 2.1c). However from JJA (July) throughout SON (October), modelled specific humidity is in agreement with observations.

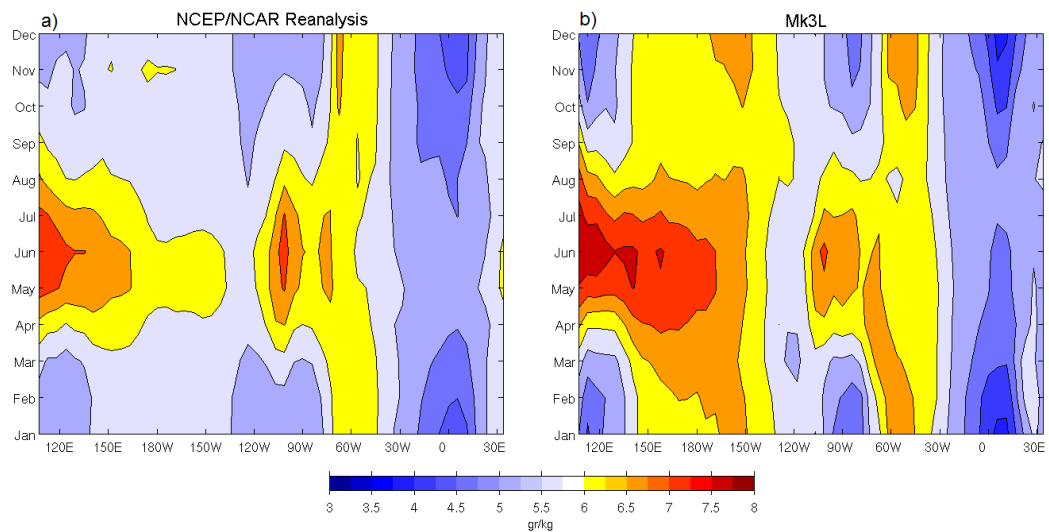


Figure 2.4: Time longitude plot of 850-hPa specific humidity from (a) NCEP/ NCAR Reanalysis I products (b) and from Mk3L. The average was taken over the full domain between 30°N - 60°S excepting the Indian Ocean basin (40°E - 101°E). Observations were interpolated onto the Mk3L atmosphere model grid. Data correspond to the 850-hPa level. The NCEP/NCAR climatology analysed period is from January 1979 through July 2008.

2.5.3 Outgoing longwave radiation (OLR)

The National Oceanic and Atmospheric Administration (NOAA) interpolated OLR dataset (Liebmann and Smith, 1996) (Fig. 2.5a) reveals two OLR maxima of about 260-270 Wm^{-2} over the tropical latitudes in both hemispheres, and an equatorial minimum with seasonal variability linked to the ITCZ. During the JJA (DJF) period, the ITCZ tends to relocate northwards (southwards) in the Northern (Southern) Hemisphere as a response to the differential heating over the ocean/land surface.

Modelled OLR (Fig. 2.5b) represents reasonably well the main temporal and spatial features compared to observations, however, simulated OLR is slightly overestimated over the subtropical latitudes. It mostly occurs during the MAM and JJA periods in the Southern Hemisphere and during the MAM, SON and DJF periods in the Northern Hemisphere. The difference of magnitude of this bias compared to observations is approximately 10 Wm^{-2} . This fact may also explain some difficulties at simulating low clouds in coastal areas over the tropical eastern oceans. It represents a common feature in climate models (Randall et al., 2007). The equatorial OLR minimum associated with the ITCZ shows the expected temporal and spatial evolutions in agreement with observations. Finally modelled OLR overestimation is found over extratropical latitudes in the Southern Hemisphere mainly during the austral summer periods.

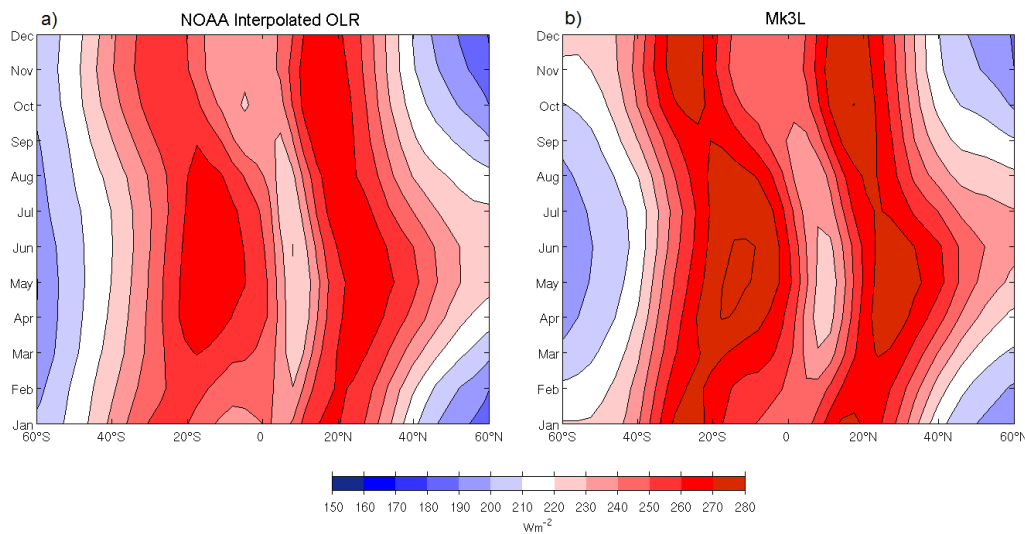


Figure 2.5: Hovmöller plot of zonally averaged observed NOAA interpolated OLR dataset (a) and (b) simulated OLR over the whole globe excepting the Indian Ocean basin (40°E - 101°E). For symmetry purposes the zonal domain was extended to 60°N - 60°S. Observations were interpolated onto the Mk3L atmosphere model grid. The OLR climatology analysed period is from January 1979 through July 2008.

2.5.4 Temperature

The temperature dataset from NCEP/NCAR reanalysis I dataset reveals the well known meridional gradient in response to the incoming solar forcing. The observed maximum is found over the tropics, and then it decreases toward the higher latitudes in both hemispheres. A strong seasonal signal is also evident in response to the boreal summer (JJA) solar radiation influx.

The biases in temperature range from -2° over the subtropics and extratropics of both hemispheres to less than $0.5^{\circ}C$ over the equatorial and tropical regions (Fig. 2.6b). From February to early austral winter, warm biases span from the equator to the tropics in the Southern Hemisphere, whereas in the Northern Hemisphere warm biases occurs from February to April. However, these warm biases do not exceed $1^{\circ}C$. The quality of the temperature estimation decreases over the extratropics, this represents a common feature in climate models (Randall et al., 2007). Furthermore, it is worth mentioning that especially the Southern Oceans feature of sparse observations. This may account for the observed biases over that area.

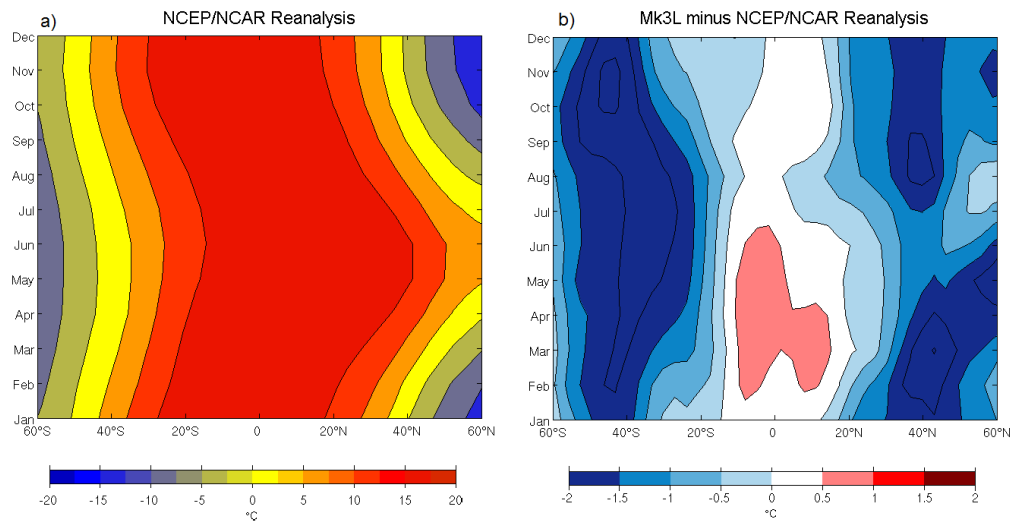


Figure 2.6: Hovmöller plot of zonally averaged temperature from NCEP/NCAR reanalysis I products (a) and (b) temperature difference Hovmöller plot between the model and observations. The averaged area corresponds to the whole globe excepting the Indian Ocean basin (40°E - 101°E). For symmetry purposes the zonal domain was extended to 60°N - 60°S. Observations were interpolated onto the Mk3L atmosphere model grid. Data corresponds to 850-hPa level. The NCEP/CNAR climatology analysed period is from January 1979 through July 2008.

The model successfully reproduces the temperature annual cycle over the South American continent (Fig. 2.7). The differences between the observed and modelled temperature do not exceed 1°C (during May). There is a delayed minimum between the model and observations, i.e. the modelled minimum occurs during June, whereas the observed minimum is seen in July.

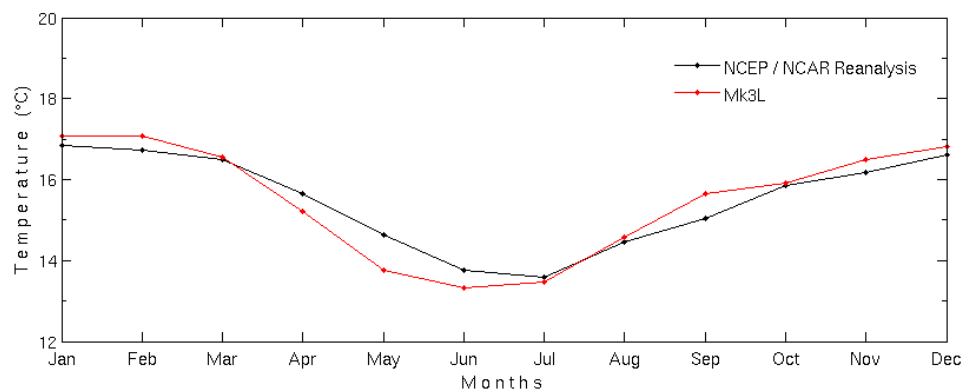


Figure 2.7: Observed (black) and modelled (red) air temperature annual cycles for South America. The NCEP/NCAR climatology analysed period is from January 1979 through July 2008. Data corresponds to 850-hPa level.

2.5.5 Low level wind and sea level pressure

Figure 2.8a depicts the seasonal sea level pressure (SLP) and the 850hPa horizontal zonal wind averages from the NCEP/NCAR reanalysis I products. The most important large scale features to highlight are: The Pacific subtropical high. It tends to peak by the SON period, then it slowly decreases its strength during the austral summer to finally weaken by the autumn. The seasonal evolution of the Atlantic subtropical high evolves similarly, but it is stronger than the Pacific subtropical high system during the JJA period. Both subtropical high systems are fully developed by the spring season. The climatology also shows the typical low level equatorial easterly winds prevailing throughout the seasons and usually peaking (decreasing) by the summer (autumn) period. The westerlies winds are typically found over 30°N - 60°N latitudinal band represent a distinct pattern of the large scale system. They peak during winter and weaken by the summer periods.

When comparing with the model it is found that, SLP is mostly underestimated throughout the seasons over the Pacific Ocean (Fig. 2.8c) especially over the extratropics. Opposite SLP biases are found over the Atlantic Ocean lasting all the seasons excepting over the subtropics during the DJF period. As a consequence of this bias, during JJA the modelled Atlantic subtropical high is stronger than the Pacific subtropical high system. Over the equatorial Pacific region, zonal winds show the best agreement with reanalysis excepting JJA and DJF periods when the modelled winds are slightly stronger than observations (Fig. 2.8). Further, seasonal low level winds are slightly overestimated over the subtropical latitudes in both hemispheres (Figs. 2.8b,c (dashed), 2.9). Whereas over the extratropics zonal modelled winds are much weaker than reanalysis data throughout the seasons (Fig. 2.9). Again this region features sparse observations, potentially accounting for these observed biases. These reported biases are the most evident at regional scale. Figure 2.9 also reveals a northward shift of the modelled westerlies during austral winter. The minor displacements do not exceed 5° of latitude during the DJF and MAM seasons. Finally, the modelled winds minimum during the winter and spring seasons in the Northern Hemisphere are consistent with the modelled rainfall maxima linked to the northward displacement of the ITCZ (Figs. 2.9 and 2.2).

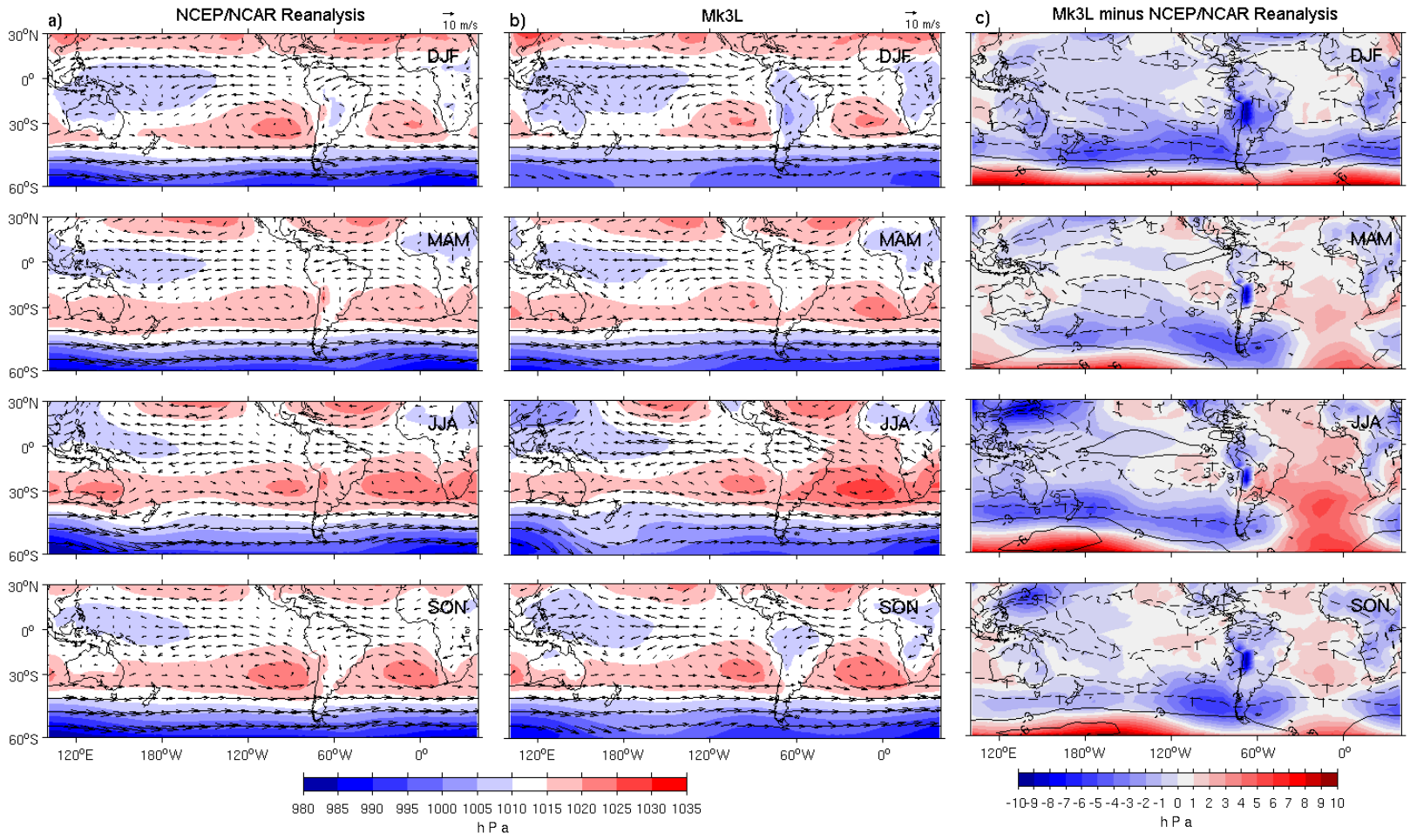


Figure 2.8: Seasonally averaged (a) SLP (shading) and 850hPa horizontal winds (vectors) from the NCEP/NCAR reanalysis I, (b) and modelled SLP and 850hpa horizontal wind. (c) Seasonal difference between the observed and modelled SLP (shading), 850hPa horizontal zonal winds (contours). Negative (positive) or solid (dashed) contours mean weaker (stronger) zonal winds than observation in Mk3L. Observations were interpolated onto the Mk3L atmosphere model grid. The NCEP/NCAR climatology analysed period is from January 1979 through July 2008. Seasons are indicated in the upper right corner of each panel.

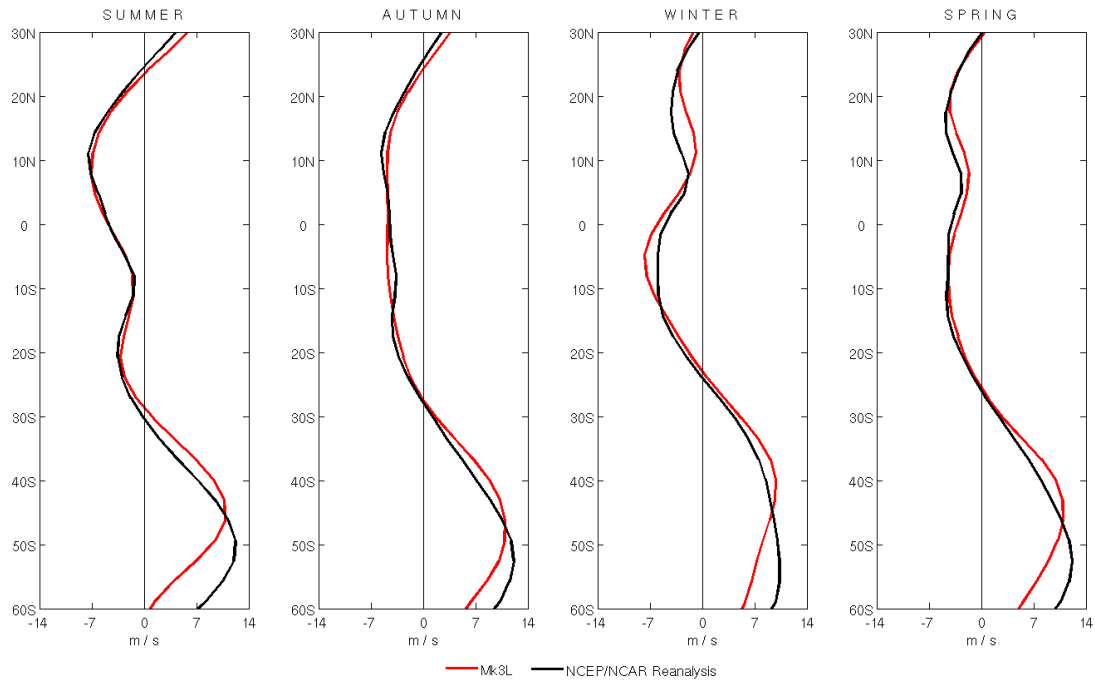


Figure 2.9: Zonally averaged (30°N-60°S) 850hPa horizontal winds for the Mk3L stand alone atmosphere model (red), and NCEP/ NCAR reanalysis I (black). Observations were interpolated onto the Mk3L atmosphere model grid. The NCEP/NCAR reanalysis climatology analysed period is from January 1979 through July 2008.

Chapter 3

Methodology and experimental design

We rely on linear methodologies such as composite average, regressions and Singular Value Decomposition (SVD) analyses. Composites were calculated in order to obtain SST anomalous fields used to perform the AGCM perturbation experiments, and also to obtain the corresponding anomalous patterns of the different variables used in this project. Further support to these patterns is provided by SVD analyses. A brief overview about the SVD analysis is given in this chapter.

3.1 Composite analysis

The ENSO index, i.e. NINO3, is used to quantify the anomalous warming over the central-eastern Pacific region. As stated in the introduction, this index represents the area averaged of monthly SST anomalies over the region encompassed by 5°N - 5°S, 150°W - 90°W. Likewise, but following Ashok et al. (2007), the EMI index is used to quantify the anomalous warming over the central Pacific. It spans over the following three key regions, central (165°E - 140°W, 10°S - 10°N), eastern (110°W - 70°W, 15°S - 5°N), and western Pacific (125°E - 145°E, 10°S - 20°N). Figure 1.1 depicts the geographical location of these two indices. The corresponding time series of EMI is built according to:

$$EMI=[SSTA]_A - \frac{1}{2} ([SSTA]_B + [SSTA]_C) \quad (3.1)$$

El Niño and El Niño Modoki years are then defined by applying a threshold of 0.7 standard deviation over its corresponding standardized time series (Figs. 3.1, 3.2), and seasonal composites are elaborated where only a complete three-month season is found. Thus for El Niño Modoki 7 summers, 7 autumns, 5 winters and 8 spring seasons are obtained, whereas for El Niño 2 summers, 7 autumns, 5 winters and 8 spring periods are found. They all are summarized in the Table 3.1.

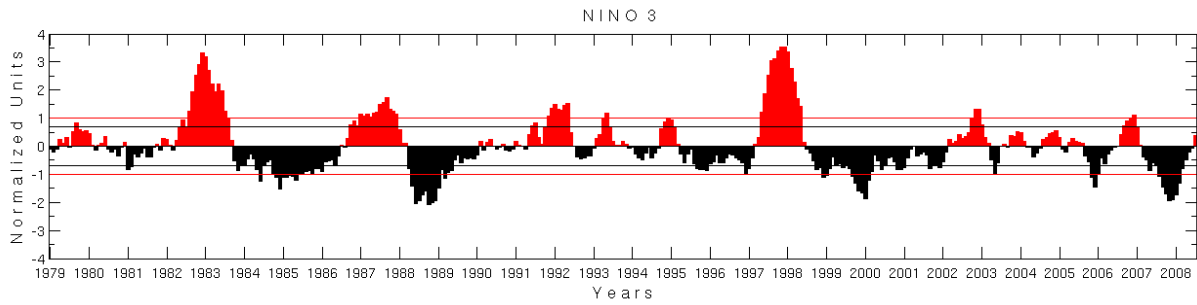


Figure 3.1: NINO3 time series and the 0.7 standard deviation threshold applied (black line) used to composite the observations. The 1.0 standard deviation (red line) threshold used to prepare perturbation experiments (See Section 3.3).

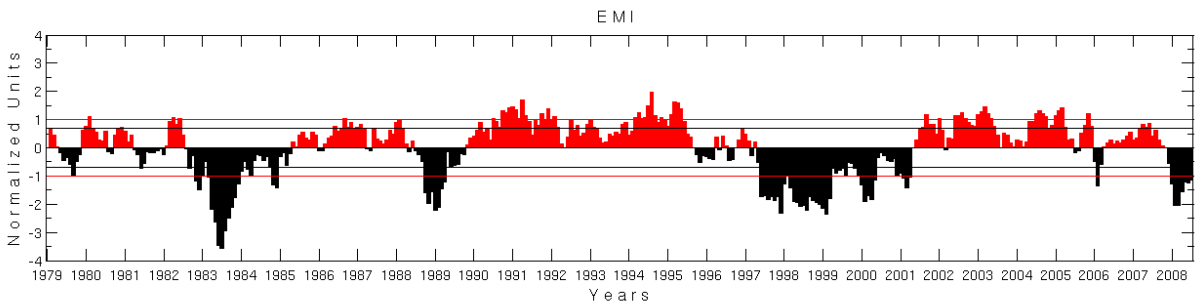


Figure 3.2: As in Fig. 3.1 but for EMI time series.

	El Niño	El Niño Modoki
Summer	1982/1983 1997/1998	1979/1980 1986/1987 1990/1991 1991/1992 1992/1993 1994/1995 2002/2003 2004/2005
Autumn	1983 1987 1998	1982 1991 1994 1995 2003 2005 2007
Winter	1982 1983 1987 1997	1990 1991 1994 2002 2004
Spring	1982 1987 1997 2006	1986 1990 1991 1994 2001 2002 2004 2005

Table 3.1: Selected years used to obtain composites above a 0.7 standard deviation threshold of the NINO3 and EMI indices.

As only two summer periods were found to match the selected central-eastern warming criterion to define canonical El Niño events, the NINO3 index was extended back further in time up to 1950 capturing more DJF seasons in order to obtain enough statistical support for the two-summer composite. The following section (3.1.1) provides further details in this regard.

3.1.1 Supporting composites for DJF

When extending the NINO3 index back further in time it is found that, five summer periods exceed the 0.7 standard deviation threshold as a criterion to define canonical El Niño events. Thus the new summer periods of 1951/1952, 1957/1958, 1965/1966, 1969/1970, 1972/1973 in conjunction with those of 1982/83 and 1997/98 were all used to create supporting anomaly composites of SST, SLP, 850hPa winds, and precipitation. Figure 3.3 shows up the extended NINO3 index, highlighting the new summer periods found with S1, S2, S3, S4 and S5 respectively.

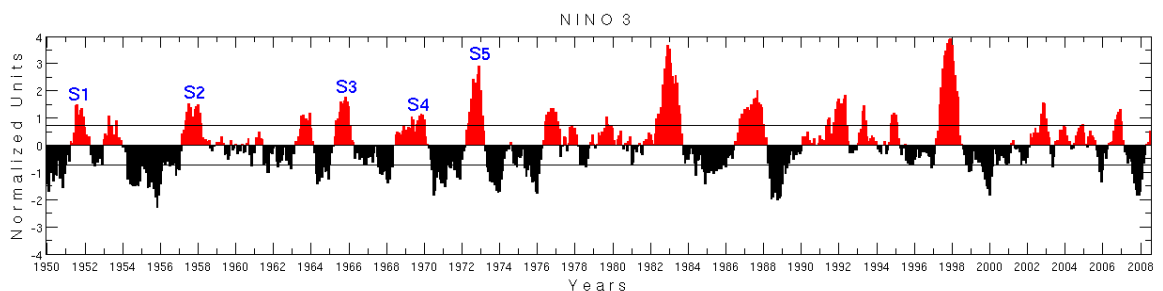


Figure 3.3: Extended time series of the NINO3 index highlighting the new 5 summer periods (S1, S2, ... ,S5) used to create the supporting composites for the DJF period, and the corresponding 0.7 standard deviation threshold used (black line).

The two-summer only composite of SST anomalies (Fig. 3.4a) reveals quite similar patterns compared to the statistically significant features when extending NINO3 index (Fig. 3.4b), excepting the magnitude of the anomalous warming that clearly doubles the magnitude of the composite of the extended NINO3, as this composite represents the two strongest El Niño ever recorded, i.e. 1982/83 and 1997/98. The significant cooling over both the western Pacific and subtropical latitudes in both hemispheres (Fig. 3.4b) reveals similar magnitudes when compared to the two-summer only composite giving further support. The SST anomalies over the Atlantic Ocean are quite similar too, but no statistically significant regions are found.

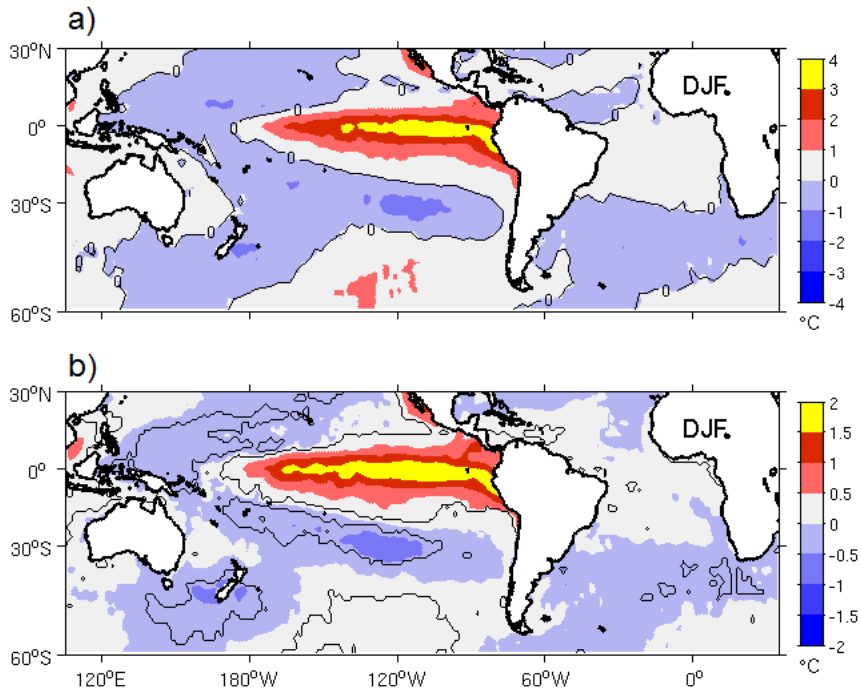


Figure 3.4: (a) Composite of SST anomalies for the summer periods of 1982/83, 1997/98, black line indicates zero SST anomaly contours. (b) Composite for the extended NINO3 index going back to 1950, black line indicates statistically significant SST anomalies regions at the 90% confidence level according to a two-tailed Student t-test. Note different intensities in (a) and (b).

As for the SST composites, the main features of sea level pressure and low level circulation are well represented by using the two-summer only composite (Fig. 3.5a). When extending the NINO3 index, it reveals the same statistically significant features. The sea level pressure gradient found over the Pacific Ocean during the mature phase of El Niño, i.e. DJF, closely resembles to the two-summer only composite, significant positive sea level pressure anomalies are also found over most of the Atlantic Ocean. Finally, the anomalous low level equatorial westerly winds are also quite well represented in both composites.

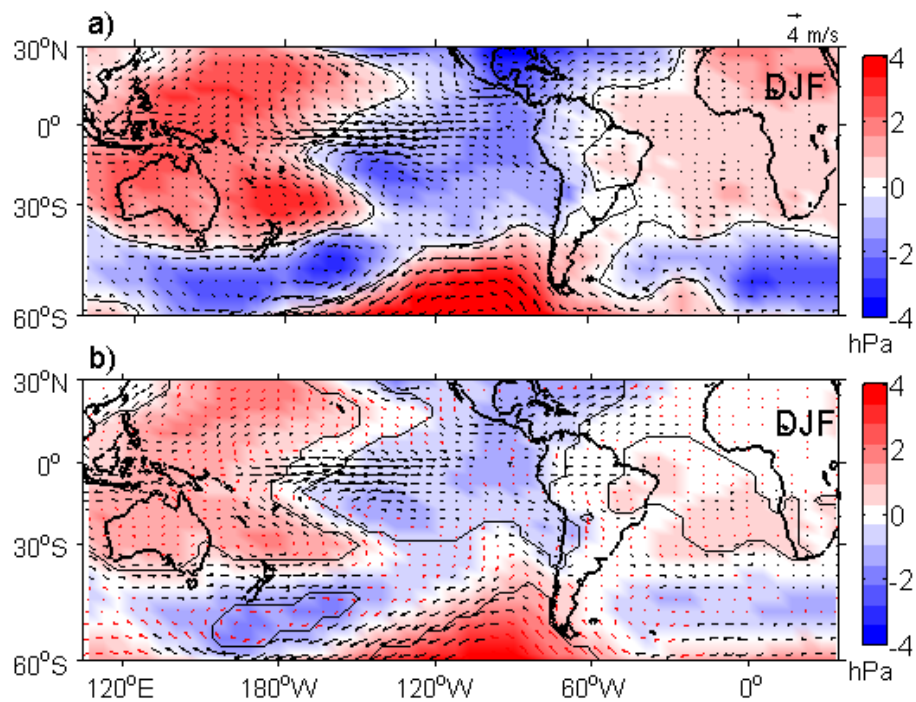


Figure 3.5: (a) Composite of 850-hPa wind anomalies and sea level pressure (shading) for the summer periods of 1982/83, 1997/98. Black line indicates zero SLP anomaly contours. (b) Composite for the extended NINO3 index going back to 1950. Black contours (vectors) indicate statistically significant regions (pixels) at the 90% confidence level according to a two-tailed Student t-test.

As the main anomalous warming and the low level circulation characteristics are well represented by the two-summer only composites, their related effects are not the exception for the South American continent. It is found that the two-summer only rainfall composites using two different datasets reveal quite similar and significant results when extending the NINO3 index. During the DJF period the main anomalous rainfall response to El Niño features a dipole-like pattern, on which positive rainfall anomalies are found over the southeastern South America (around 30°S) and negative anomalies over the northern region of the continent. Additionally, positive rainfall anomalies are also found over the western equatorial South America (Fig. 3.6). As the extended NINO3 rainfall composite (Fig. 3.6c) statistically supports these features, we assume that the two-summer only composite statistically represents the impacts of El Niño events over South America during the DJF period after the 1978.

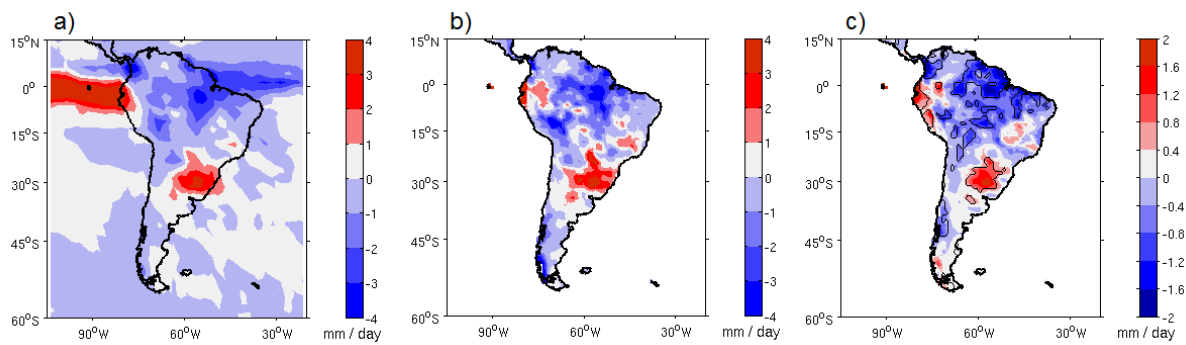


Figure 3.6: (a) Composite of rainfall anomalies for the summer periods of 1982/83, 1997/98 using CMAP and (b) Global Precipitation Climatology Centre (GPCC) datasets. (c) Composite of the extended NINO3 index going back to 1950, black contour indicates statistically significant regions at the 90% confidence level according to a two-tailed Student t-test.

As the CMAP rainfall dataset does not span the period before the 1978, GPCC dataset (Beck et al., 2005; Rudolf and Schneider, 2005), is then used to obtain the supporting composites (Figs. 3.6b,c). In this case the GPCC rainfall anomalies correspond to a departure considering the spanning period from January 1951 through July 2008.

Finally, after verifying that the selected two-summer only composites of SST, SLP, low level circulation and rainfall anomalies fully and statistically represent the main significant features of El Niño during the DJF period, this composite will be then used to contrast with the related features and impacts of El Niño Modoki for the same DJF period in this thesis.

3.2 Singular Value Decomposition (SVD) Analysis: An overview

The SVD analysis is a general decomposition, which decomposes any $n \times m$ matrix F into the form:

$$F = U\Gamma V^t \quad (3.2)$$

Where U is an $n \times n$ orthonormal matrix, V is an $m \times m$ orthonormal matrix and Γ is a diagonal $n \times m$ matrix with p elements down the diagonal. Meaning that for climate applications, U and V can be used with different grids, but they must be measured simultaneously. The columns of the matrices U, V contain the singular vectors of F . The latter represents the temporal cross-covariance matrix between two space and time dependent data fields, namely U and V . The temporal means for each variable are removed from the time series at all grid points.

This method identifies pairs of statistically coupled spatial patterns, with each pair explaining a fraction of the square covariance between the two fields. The first pair of patterns describes the largest fraction of the square covariance and each succeeding pair describes a maximum fraction of the square covariance that is not explained by the previous pairs. The square covariance fraction of a selected pair of singular vectors is proportional to the square of the selected singular value. The expansion coefficient for each variable is computed by projecting the singular vectors onto the corresponding original data field. The correlation coefficient of the corresponding time series quantifies the coupling strength between the coupled modes. Further details about the SVD analysis applications in climate research can be found in Björnsson and Venegas (1997), and Navarra and Somoncini (2010).

3.3 AGCM perturbation experiments

The primary purpose of this thesis is to evaluate the response of South American rainfall variability to variable SST forcing over the Pacific Ocean. However, South American rainfall may also be influenced by the Atlantic SST variability. Thus, SST anomalies over the Atlantic Ocean were also used to prepare complementary perturbation experiments, allowing us to carry out up to 4 different AGCM experiments as follows: one experiment for El Niño conditions forced with monthly varying SST anomalies over the Pacific Ocean only (EN-P). A second experiment as in EN-P but forced with monthly varying SST anomalies over both the Pacific and Atlantic Oceans (EN-PA). Likewise for El Niño Modoki conditions, one perturbation experiment was

forced with monthly varying SST anomalies over the Pacific Ocean only (ENM-P) and the last experiment as in ENM-P, but forced with monthly varying SST anomalies over both the Pacific and Atlantic Oceans (ENM-PA), they all are summarized in Table 3.2 below.

Experiment	Pacific ocean forcing	Atlantic ocean forcing
El Niño (EN-P)	√	–
El Niño (EN-PA)	√	√
El Niño Modoki (ENM-P)	√	–
El Niño Modoki (ENM-PA)	√	√

Table 3.2: Summary of the different perturbation experiments carried out for this project.

A continuous 100 years integration forced by 12 months SST climatology was used as a control experiment (CNTRL). To carry out the different perturbation experiments the threshold to select El Niño and El Niño Modoki episodes is increased up to one standard deviation (Figs. 3.1, 3.2). In that way, the strongest El Niño and El Niño Modoki events are selected. Consequently, their corresponding monthly evolutions are interpolated onto the Mk3L atmosphere grid over both the Pacific (30.5°N - 30.5°S), and the Atlantic oceans (29.5°N - 59.5°S) (Figs. 3.7,3.8, dashed line).The SST anomalies are increased to ensure that the forcing matches with realistic SST anomalies maxima, the factors, summarized below, were applied to the interpolated monthly anomalous field.

	Dec/Jan/Feb	Other months
El Niño	2.5	2.5
El Niño Modoki	5.5	4.0

Table 3.3: The factors used to multiply the interpolated monthly anomalous fields to carry out the AGCM perturbation experiments. Note that the same factor is used to multiply the monthly SST anomalies of the perturbation experiments of El Niño.

In order to avoid unrealistic atmospheric circulation triggered by strong SST gradients on the border of the forcing area, a linear filter was applied to linearly damp the perturbation to zero over the latitudinal band depicted in dashed green lines in Figures 3.7 and 3.8. These anomalies were then superimposed onto the monthly varying SST annual cycle, elsewhere the SST forcing is taken to be the climatological monthly mean. The later was implemented from NOAA OI SST analysis v2 (Reynolds et al., 2002) for the 1982-2001 period. Like the CNTRL case, each perturbation experiment is an integration of 100 years with a repeating 12 month forcing.

The simulations were performed under the default model configuration for pre-industrial conditions on The Australian Partnership for Advanced Computing (APAC) National Facility.

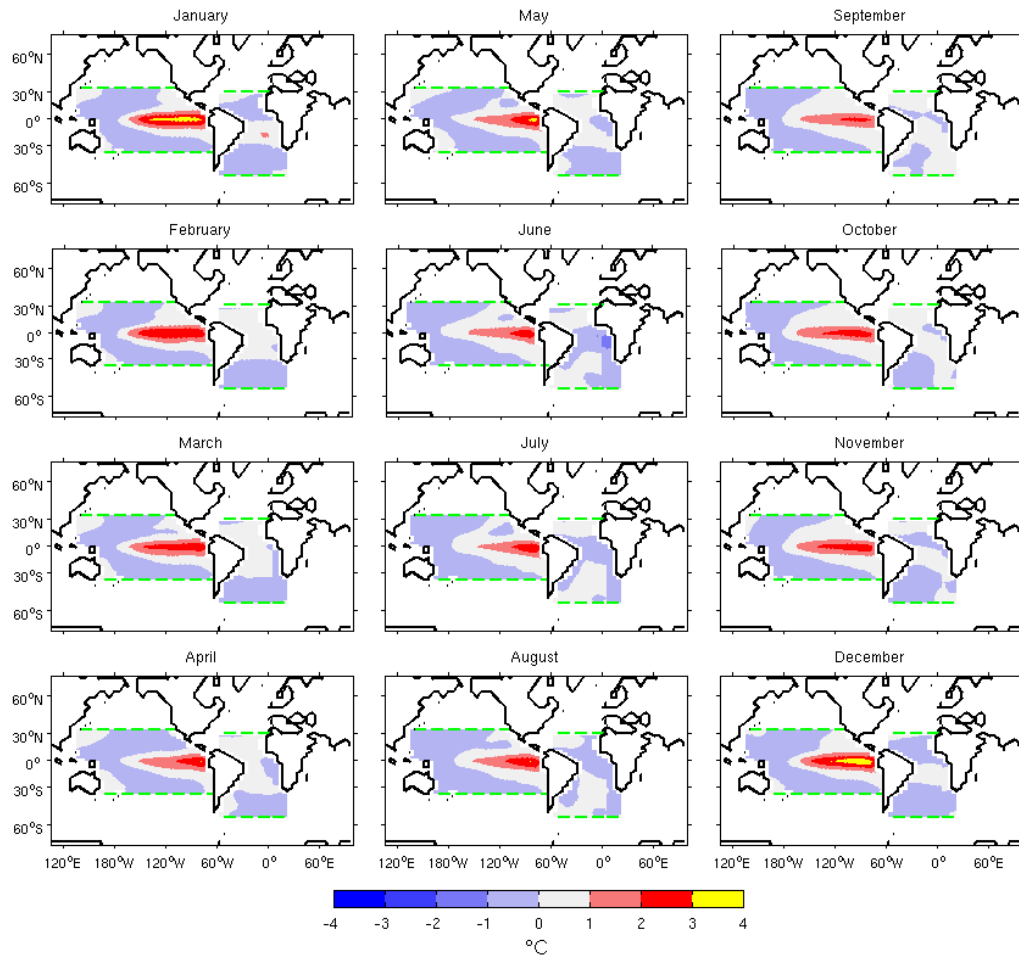


Figure 3.7: Interpolated SST anomalies (HadISST1) during the monthly evolution of El Niño onto the Mk3L atmosphere model grid. The composites are derived according to a 1.0 standard deviation threshold of the NINO3 index (See Fig. 3.1). The dashed green line denotes the forcing region (specified in the text). Elsewhere the SST forcing is taken to be the climatological monthly mean.

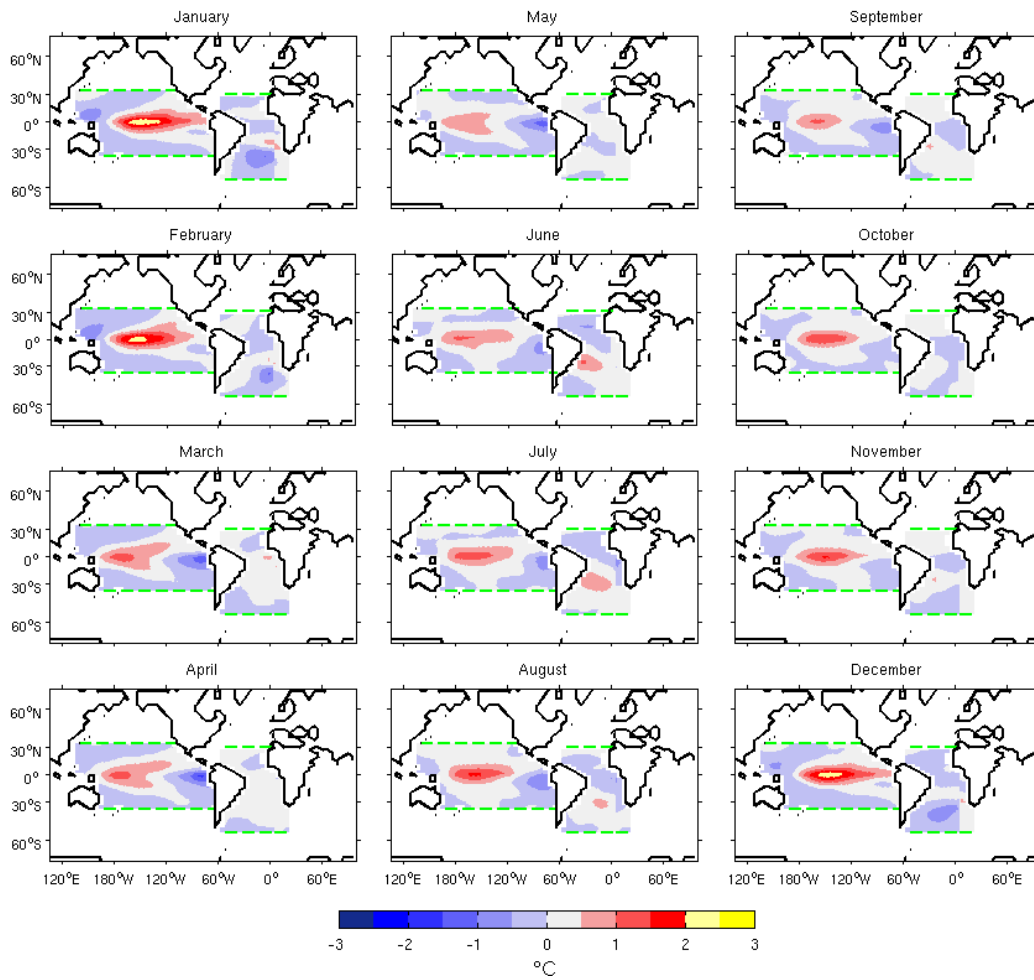


Figure 3.8: As in Fig. 3.7 but for El Niño Modoki.

3.4 Estimation of the significance levels

3.4.1 Composites

All anomalies of variables analysed in this study are assumed to follow a Gaussian distribution. Thus a two-tailed Student t-test for the difference in means between two independent samples is used. Assuming that each season represents one degree of freedom, we test the null hypothesis that the mean between these two independent samples are the same. If the variances of the two independent samples are equal the appropriate test statistic is given by:

$$\hat{t} = \frac{|\bar{a} - \bar{b}|}{\sqrt{\left(\frac{n_a + n_b}{n_a n_b}\right) \left(\frac{(n_a - 1)S_a^2 + (n_b - 1)S_b^2}{n_a + n_b - 2}\right)}} \quad (3.3)$$

where n_a and n_b are the sample sizes, S_a^2 and S_b^2 are the variance of the samples a and b . The null hypothesis is rejected if the measured \hat{t} -value in (3.3) is lower than the critical t -value, which depends on the degrees of freedom $n_a + n_b - 2$ and the significance level α .

Further details about statistical analyses applied to earth science can be easily found in the literature, for example in Trauth (2010), von Storch and Zwiers (2003) and Wilks (2006).

3.4.2 Correlations

The method suggested by Sciremammano (1979) is used to assess the significance levels in the correlation analyses. As the time series used in earth science present some degree of dependency between consecutive values, the effective degrees of freedom are usually lesser than the number of samples taken. This represents the main difference with the classic statistic, which considers for each random variable a magnitude statistically independent in the time series.

The method aims at normalizing the correlation by estimating the large-leg standard error (σ). Its magnitude represents the combined effects of the dominant time scale variation of the analysed process and the available record length. It prevents overestimation of the correlation coefficient when low-frequency variations relative to the time series length are present in the record.

Thus for calculations with at least 10 degrees of freedom, the confidence levels are as follows,

$$C_{99} = 2.6\sigma \quad (3.4)$$

$$C_{95} = 2.0\sigma \quad (3.5)$$

$$C_{90} = 1.7\sigma \quad (3.6)$$

where large-leg standard error for lagged correlations is given by,

$$\sigma^2 = \frac{1}{N - k} \sum_{i=-\infty}^{+\infty} C_{xx}(i\Delta t)C_{yy}(i\Delta t) \quad (3.7)$$

The C_{xx} , C_{yy} are the discrete autocorrelation functions of the two time series $X(t)$, and $Y(t)$ respectively, k is the lag time in units of Δt , and N represents the record length.

Chapter 4

El Niño and El Niño Modoki impacts during the austral summer period

This chapter aims at describing and evaluating the different impacts of El Niño and El Niño Modoki on rainfall variability during the austral summer period over South America. The analysis is focused on obtaining the statistical modes of co-variability between anomalous SST and South American rainfall associated with El Niño and El Niño Modoki, in order to relate them with the different prevailing atmospheric conditions. AGCM perturbation experiments forced by El Niño and El Niño Modoki conditions were used to support the results.

4.1 Sea Surface Temperature

Figure 4.1 depicts the composites of SST anomalies for El Niño and El Niño Modoki conditions. El Niño features a remarkable zonal warming from the central to the eastern Pacific basin clearly reaching the equatorial coast of South America (Trenberth and Caron, 2000; Latif and Keenlyside, 2009). It shows maximum positive SST anomalies of approximately 4°C (Fig. 4.1a). The western Pacific conditions are cooler than normal, with negative SST anomalies around -1°C. This anomalous cooling spreads into the subtropical regions of both hemispheres. A much cooler region located around 30°S with magnitude of about -2°C is also registered. Southward of this anomalous cooling, an anomalous warming of approximately 2°C is found. Over the Atlantic basin, SST anomalies are masked by the magnitude of the anomalous warming in the Pacific Ocean. Thus Figure 4.2a provides a closer view to overcome this. The Atlantic SST anomalies during the peak of El Niño depict an anomalous meridional gradient in the subtropics (Δ anomaly \approx 1°C), in which a subtropic-to-extratropic (30°S-45°S) cooling is found, whereas an anomalous warming is located over the tropical South Atlantic. This gradient pattern resembles the first and second mode of South Atlantic SST anomalies shown by Barreiro et al. (2004) and Venegas et al. (1997) respectively.

During El Niño Modoki conditions, the most important signal is the significant anomalous warming located over the central Pacific nearby the international dateline (Fig. 4.1b). This warming is approximately 1°C. Further, the signal tends to show a northeastward expansion into the Northern Hemisphere. The western Pacific is

significantly cooler than normal, and likewise during El Niño this cooling signal spreads into both hemispheres. In addition, an anomalous cooling signal is also detected over the eastern equatorial coast of South America. It, therefore, produces the reported anomalous SST gradient along the equator during the so-called Modoki pattern, i.e. an anomalous warming in the central Pacific encompassed by an anomalous cooling at both sides of this ocean basin (Ashok et al., 2007). At extratropical latitudes, a significant anomalous warming (around 0.5°C) is found nearly at the same location of El Niño composite. In the Atlantic Ocean (Fig. 4.2b) the dominant signal during the austral summer period corresponds to a significant cooling located in the subtropics between approximately 30°S and 50°S. Cooler conditions are also seen in the equatorial and tropical North Atlantic Ocean. Additionally, anomalous warming is observed along 30°S from the southern tip of Africa to the western coast of tropical South America and in the Brazil-Malvinas confluence region. The latter resembles the SST anomalies linked to the “Benguela Niño” (Florenchie et al., 2004).

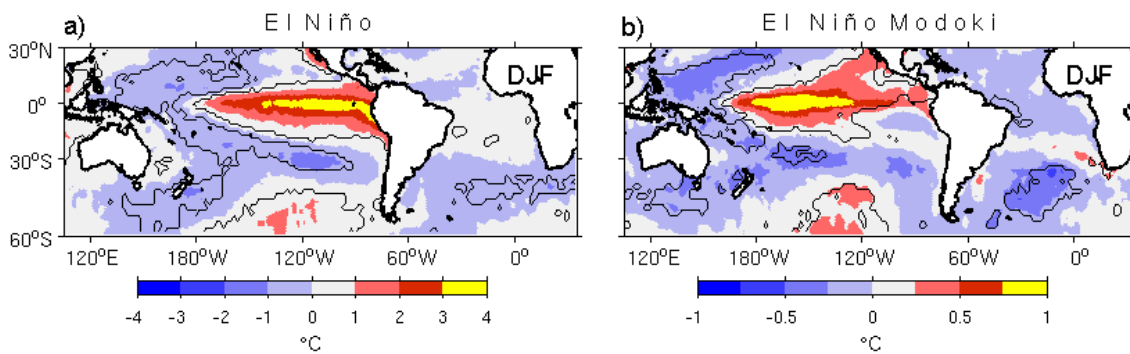


Figure 4.1: Composites of SST anomalies during the austral summer for (a) El Niño and (b) El Niño Modoki conditions (See Table 3.1). The SST data is from HadISST1 dataset as described by Rayner et al. (2003). The SST anomalies are a departure of the monthly climatology based on the period from January 1979 through July 2008. Black contours represent statistically significant regions at the 90% confidence level according to a two-tailed Student t-test. Note different intensities in (a) and (b).

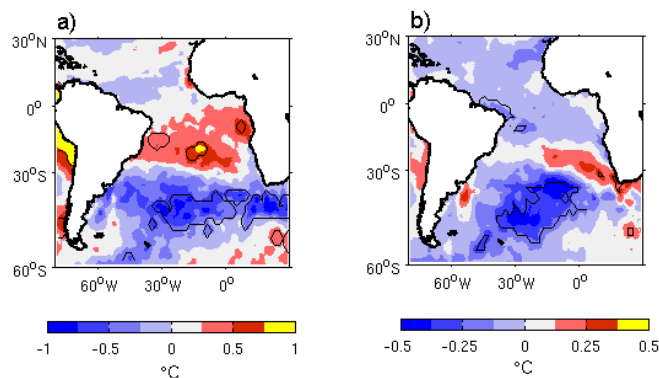


Figure 4.2: As in Fig.4.1, but for the Atlantic Ocean only. (a) El Niño, and (b) El Niño Modoki conditions. Black contours represent statistically significant regions at the 90% confidence level according to a two-tailed Student t-test. Note different intensities in (a) and (b).

The following section examines the observed atmospheric conditions during El Niño and El Niño Modoki events and the simulated response to the Pacific and Atlantic SST pattern during these episodes.

4.2 Rainfall composites

4.2.1 Large scale features

Figure 4.3 shows the observed and simulated rainfall anomalies during El Niño and El Niño Modoki conditions. In particular, during El Niño events the observed and modelled large scale rainfall features are in close agreement with each other (Figs. 4.3a, c). Significant positive rainfall anomalies prevail along the central and eastern equatorial Pacific Ocean. Although both observed and modelled anomalous rainfall signal are found over the eastern equatorial Pacific, the modelled signal on the east is weaker than the observed. The negative anomalies over the western Pacific span into both hemispheres and partially encompass the positive anomalous rainfall band, generating a “horse-shoe” pattern in anomalous rainfall (Figs. 4.3a, c). The observed and modelled anomalous rainfall patterns during El Niño conditions are coherent with the SST anomalies distribution in both observations and the EN-P perturbation experiment (Figs. 3.7, 4.1a, 4.3a,c). These large scale rainfall features had been well documented in the literature, and represent the most common features during El Niño events (Ropelewski and Halpert, 1987; Kayano et al., 1988; Kiladis and Diaz, 1989; Ropelewski and Halpert, 1989; Giannini et al., 2001).

El Niño Modoki conditions exhibit two remarkable and contrasting anomalous large scale rainfall features compared to El Niño (Figs. 4.3 a, b). Firstly, as the SST anomalies distribution is mostly located over the central Pacific (Fig.4.1b), significant and positive rainfall anomalies are roughly found around the dateline and do not reach the equatorial South American coast. This pattern is zonally encompassed by negative anomalies not only in the western, but also in the eastern Pacific. Secondly, the main difference between both events is the occurrence of a weak but positive anomalous rainfall band that diagonally extends from the central Pacific into the Southern Hemisphere, mainly associated with an enhanced convection activity in the SPCZ (Ashok et al., 2007; Weng et al., 2009). The ENM-P perturbation experiment successfully represents the main observed large scale rainfall features of El Niño Modoki (Fig. 4.3d). A detailed description of the anomalous rainfall conditions over the continent and tropical Atlantic region is provided in the next section.

4.2.2 South American rainfall anomalies

The typical anomalous rainfall signal during El Niño is usually referred as a dipole-like pattern in which negative anomalies are located over the northeastern portion of the continent and positive anomalies over SESA (Aceituno, 1988; Kousky and Ropelesky, 1989; Rao and Hada, 1990; Souza et al., 2000; Zhou and Lau, 2001; Paegle and Mo, 2002; Grimm, 2010). This feature is seen in Figure 4.4a with strong negative anomalies over the Amazon basin extending toward the equatorial Atlantic over the ITCZ region, and positive anomalies over South of Brazil and a small area over Ecuador. The perturbation experiments carried out for El Niño conditions, i.e. EN-P and EN-PA, capture the main observed rainfall features over the Northern portion of the continent and the equatorial Atlantic. Positive modelled rainfall anomalies are over SESA, however they are much weaker compared to observations (Figs. 4.4 a, c, e). Furthermore, the EN-P and EN-PA experiments show positive anomalous rainfall at the tropical eastern South America contrasting with observations (around 15°S). This is likely to be a consequence of the positive rainfall bias found during the monsoon season over this region as previously reported on Section 2.5.1.

If we assume that the atmospheric response to tropical Pacific and Atlantic SST anomalies is additive, the difference between the EN-PA minus EN-P perturbation experiments removes the remote forcing from the Pacific Ocean, and thus retains the local response to the Atlantic forcing. Figure 4.4g reveals negative anomalous rainfall difference over most of the continent, including the SESA and northeastern regions. It suggests a stronger subsidence over North of Brazil and ITCZ region as consequence of the Atlantic SST anomalies. Furthermore, the difference also reveals a stronger anomalous rainfall gradient over the South Atlantic Ocean as a response to the anomalous subtropical SST dipole observed during El Niño conditions (Fig. 4.2a). This means that the EN-PA has more (less) rainfall over the tropical (subtropical) South Atlantic compared to EN-P. The positive rainfall anomalies over the tropics are associated with the oceanic portion of the SACZ (Marengo et al., 2001). The fact that the continental portion of the SACZ does not show an evident increase in anomalous rainfall reflects that this area is governed by others processes of that the oceanic SACZ portion as pointed by other studies (Barriero et al., 2002).

During El Niño Modoki conditions, South America reveals a rainfall pattern similar to that of El Niño, however with a weaker intensity. Negative rainfall anomalies span across northern South America and equatorial Atlantic Ocean. Contrasting with El Niño

events, virtually no positive anomalies at the western boundary of the continent are detected (Figs. 4.4 a, b). However, the most remarkable differences are found around the SESA and the SACZ regions, where negative and positive rainfall anomalies are found respectively (Zhou and Lau, 2001; Paegle and Mo, 2002; Grimm and Zilli, 2009; Grimm, 2010). Over extratropical latitudes, there are positive and weak rainfall anomalies over the continent contrasting with El Niño conditions. The corresponding perturbation experiments of El Niño Modoki, i.e ENM-P and ENM-PA, successfully simulate the observed negative rainfall anomalies spanning across northern South America and the equatorial Atlantic Ocean (Figs. 4.4d,f). Over the SESA region, the simulated anomalous rainfall is mostly negative as in observations, especially in the ENM-P experiment. Therefore the model correctly captures the sign of the anomalous precipitation over SESA in the ENM perturbation experiments. Negative rainfall anomalies are found at the southern tip of the continent for both ENM-P and ENM-PA experiments, contrasting with the observed anomalies during El Niño Modoki conditions (Figs. 4.4b,d,f).

Figure 4.4h shows the difference between the ENM-PA and ENM-P experiments. It reveals positive anomalies over equatorial South America in the ENM-PA compared to the ENM-P experiment. This indicates enhanced negative rainfall anomalies over the equatorial South America in the ENM-P compared to ENM-PA experiment, therefore suggesting a stronger downward motion associated with the anomalous descending branch of the Walker circulation due to the Pacific only forcing. The negative difference associated with the SACZ implies less rainfall in ENM-PA compared to ENM-P (Fig. 4.4h). Thus AGCM perturbation experiments suggest that the overall effect of the Atlantic SST anomalies during El Niño Modoki conditions is to weaken the magnitude of the anomalous rainfall over the continent. The difference between the ENM-P and EN-P experiments over the SACZ region (Fig. 4.4i) shows an increase of anomalous rainfall over the region associated with SACZ during El Niño Modoki conditions, and thus some degree of sensitivity to inter El Niño variations. It is worth mentioning that there is a bias in the climatological position of the SACZ (See section 2.5.1, Fig. 2.1a,b), it may account for the difference in the simulated position of the SACZ in the perturbation experiments. Furthermore, the coarse resolution in conjunction with the lack of ocean-land-atmosphere coupling in the simulations may also contribute to this bias. However, as this is an intrinsic bias in the model, a comparison between experiments would still be valuable. The difference between these simulations, i.e ENM-P minus EN-P, also supports the main anomalous observed differences between El Niño and El Niño Modoki events, i.e. the simulated positive rainfall anomalies over

the SESA and Northwestern equatorial South America regions during El Niño. Likewise the negative rainfall anomalies in the northeastern portion of the continent associated with strong subsidence during El Niño conditions are also well simulated (Figs. 4.4i, j).

As a summary, when AGCM perturbation experiment are undertaken with El Niño Modoki (El Niño) conditions, there are positive or increased (negative or decreased) rainfall anomalies over the SACZ and negative (positive) over Pacific coast of equatorial South America and SESA regions. This represents the main differences compared to observed anomalous rainfall over the continent (Figs. 4.4a,b,i). In the tropical areas, the role of the Atlantic SST mainly consists of modulating the strength of the descending branches over the continent and thus the strength of the associated negative rainfall anomalies. In particular during El Niño (El Niño Modoki) the Atlantic conditions tend to increase (decrease) the negative rainfall anomalies over equatorial South America. Over the SESA region, the Atlantic conditions tend to reduce the magnitude of the rainfall anomalies during El Niño and El Niño Modoki events.

In order to provide further support to our selected composites of anomalous SST and rainfall, the goal of next section is to statistically estimate the coupled modes of co-variability between the anomalous SST and rainfall fields.

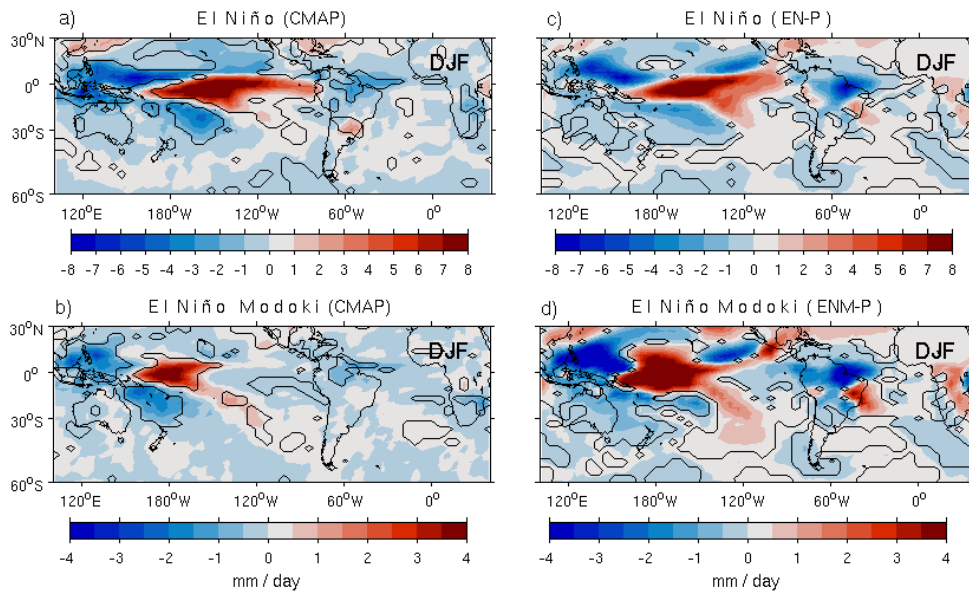


Figure 4.3: Composites of the observed rainfall anomalies (CMAP) during (a) El Niño, and (b) El Niño Modoki conditions (See Table 3.1), (c) modelled rainfall anomalies for El Niño (EN-P), and (d) El Niño Modoki (ENM-P) perturbation experiments. The forcing was applied over the Pacific Ocean only. Black contours represent statistically significant regions at the 90% confidence level according to a two-tailed Student t-test.

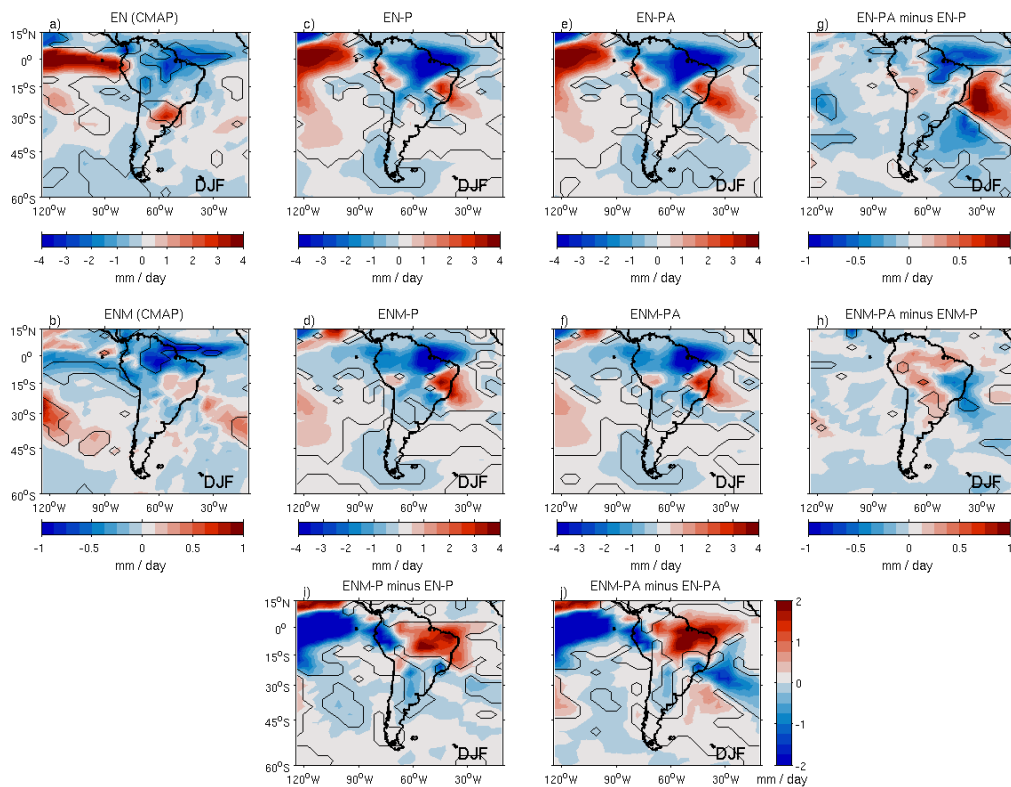


Figure 4.4: Observed rainfall anomalies for (a) El Niño, (b) El Niño Modoki. Modelled rainfall anomalies for (c) El Niño (EN-P), (d) El Niño Modoki (ENM-P), and including the perturbation experiments forced with SST anomalies over the Atlantic Oceans according to (e) EN-PA, (f) ENM-PA, and including the difference between (g) EN-PA minus EN-P, (h) ENM-PA minus ENM-P, (i) ENM-P minus EN-P and (j) ENM-PA minus EN-PA perturbation experiments. Black contours represent statistically significant regions at the 90% confidence level according to a two-tailed Student t-test.

4.3 Assessing coupled modes of SST and rainfall variability

The SVD analysis is used here to identify coupled modes of variability between the austral summer Pacific SST and South American rainfall anomalies. Figure 4.5 depicts the first mode of the coupled variability associated with El Niño conditions, the correlation between the expansion coefficient of the SST time series and NINO3 index is 0.98. Although the spatial modes of SST and rainfall anomalies fully support the main features previously reported in Figures 4.1 and 4.4, some slight and insignificant loading associated with positive rainfall anomalies are detected northeastward (15°S) from the SESA region compared to its corresponding composited pattern (Fig. 4.4a), where a weaker anomalous rainfall is instead observed. The first mode between the SST anomalies associated with El Niño and South American rainfall is strongly coupled, with a correlation coefficient of 0.75. The leading mode is responsible for the 33% of the observed co-variability. Most of the spatial features of this rainfall mode has

been well documented in early studies (Ropelewski and Halpert, 1987; Aceituno, 1988). Other more recent examples include the EOF analysis of Paegle and Mo (2002), in which the first mode explains approximately 12% of the rainfall variance from 1950 to 1999. For a different analysed period and dataset, similar features were found by Zhou and Lau (2001), explaining approximately 27% of total rainfall variance. Finally, this rainfall mode has been also reported as the second mode of rainfall variability (Grimm and Zilli, 2009; Grimm, 2010) for the period spanning 1961-2000, accounting for approximately 10% of the rainfall variability.

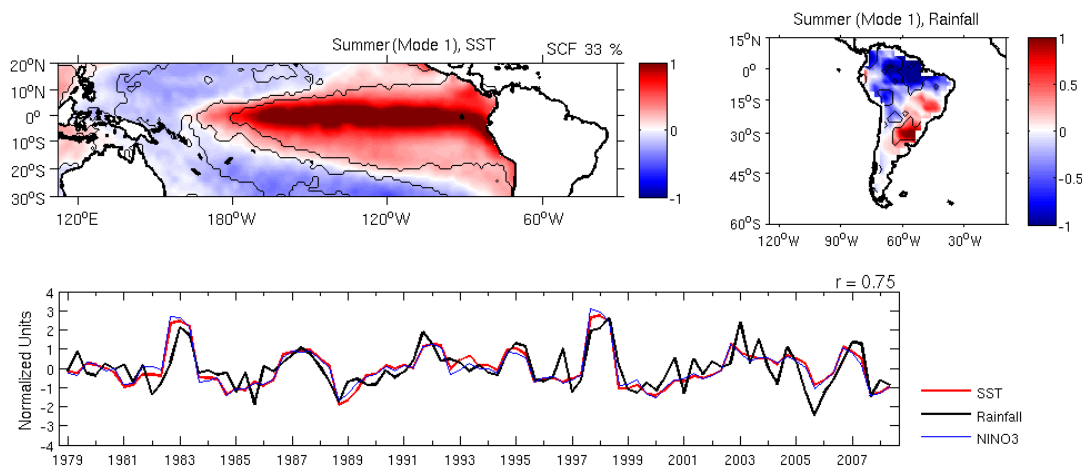


Figure 4.5: The first mode of an SVD analysis between the SST (left) and rainfall anomalies (right) during the austral summer period. It accounts for $33.0 \pm (8.5)$ % of the square covariance fraction (SCF). Black contours indicate statistical significant regions at the 90% confidence level according to a two-tailed Student t-test. Time series of the SVD expansion coefficient (below). Red (black) line is associated with the SST (rainfall) mode. The coupling strength (r) between these fields is 0.75. The thin blue line represents the NINO3 index. The correlation coefficient between the SST mode (red) and the NINO3 index (blue) is 0.98. The correlations are statistically significant at the 95% confidence level.

The second mode of variability is shown in Figure 4.6. The spatial pattern of co-variability linked to the SST anomalies resembles the anomalous equatorial SST gradient associated with El Niño Modoki conditions (See Fig. 4.1b). The corresponding pattern of anomalous rainfall further supports the observed rainfall composite in Figure 4.4b. It shows strong positive loading around northeastern South America involving the northeast Brazil and even part of the eastern Andes, and negative loading over the SESA and equatorial South America regions.

The second mode accounts for 9.3% of the square covariance fraction. It is a moderately coupled mode as the correlation coefficient is only 0.4, but it is still significant at the 95% confidence level. The correlation between the expansion coefficient of the SST time series and the EMI index is 0.89, also significant at the 95% confidence level.

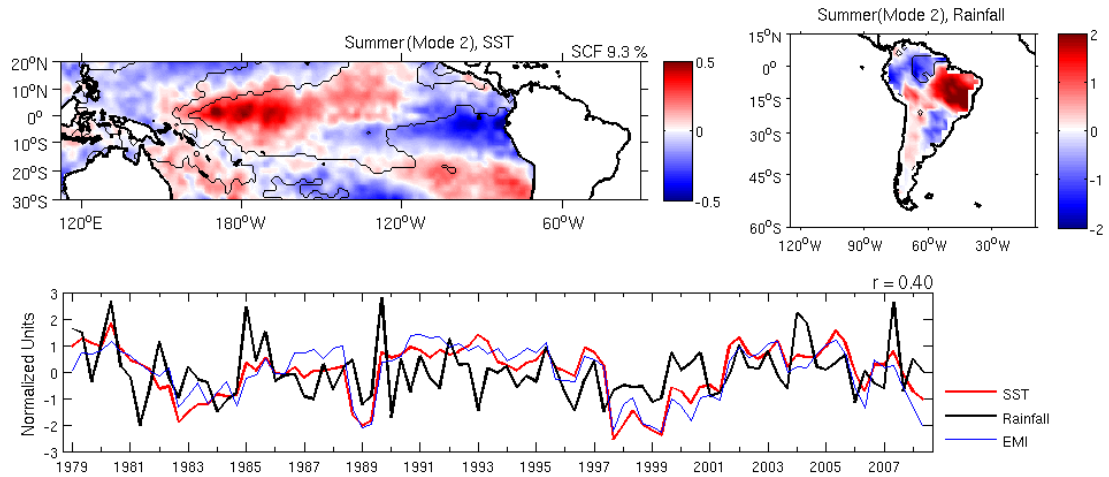


Figure 4.6: The second mode of an SVD analysis between the SST (left) and rainfall anomalies (right) during the austral summer period. It accounts for $9.3 \pm (2.4)$ % of the square covariance fraction (SCF). Black contours indicate statistical significant regions at the 90% confidence level according to a two-tailed Student t-test. Time series of the SVD expansion coefficient (below). Red (black) line is associated with the SST (rainfall) mode. The coupling strength (r) between these fields is 0.4. The thin blue line represents the EMI index. The correlation coefficient between the SST mode (red) and EMI index (blue) is 0.89. The correlations are statistically significant at the 95% confidence level.

The first and second modes are well separated from the second and third coupled modes of variability respectively as their associated standard errors are much smaller than the distance between their corresponding eigenvalues (North et al., 1982).

The low observed coupling strength suggests that another source of variability may also play a complementary role in the observed variability between the SST and rainfall anomalies during El Niño Modoki. In order to explore this, we extend the SST anomaly field in the SVD analysis including the tropical Atlantic Ocean (Fig. 4.7). It is observed that the amount of explained co-variability only increases from 9.3% to 10.5%. Furthermore, the coupling strength between these fields enhances and the corresponding correlation coefficient is now 0.51. With the inclusion of the Atlantic Ocean in the SVD analysis, the correlation between the SST time series and EMI index decreases to 0.69. However, both correlations are significant at the 95% confidence level. This coupling enhancement with the Atlantic Ocean suggests that the interannual rainfall anomalies during El Niño Modoki are likely to be forced by both remote and local forcings. The spatial mode linked to the SST anomalies over the Atlantic Ocean features of positive loading over the Northern Hemisphere especially near the western coast of Africa, and opposite loading over western South Atlantic. The occurrence of a negative loading off southeastern Brazilian coast suggests an influence of atmospheric forcing over the ocean. As this region spans over the oceanic portion of the SACZ, its associated cloud cover prevents the incoming shortwave radiation reach the ocean

surface and thus cools the underlying SST (Chavez and Nobre, 2004). The anomalous rainfall band associated with the SACZ protruding into the Atlantic Ocean can be seen in Figure 4.4b.

Previous studies have also reported similar features in regard to the second mode associated with rainfall presented here. It is described as either the first mode of interannual rainfall variability for the period of 1961-2000 by Grimm and Zilli (2009) and Grimm (2010), or as the fourth mode by Paegle and Mo (2002) for the period of 1950-1999, explaining approximately 22%, 27% and 7% of the total rainfall variance respectively.

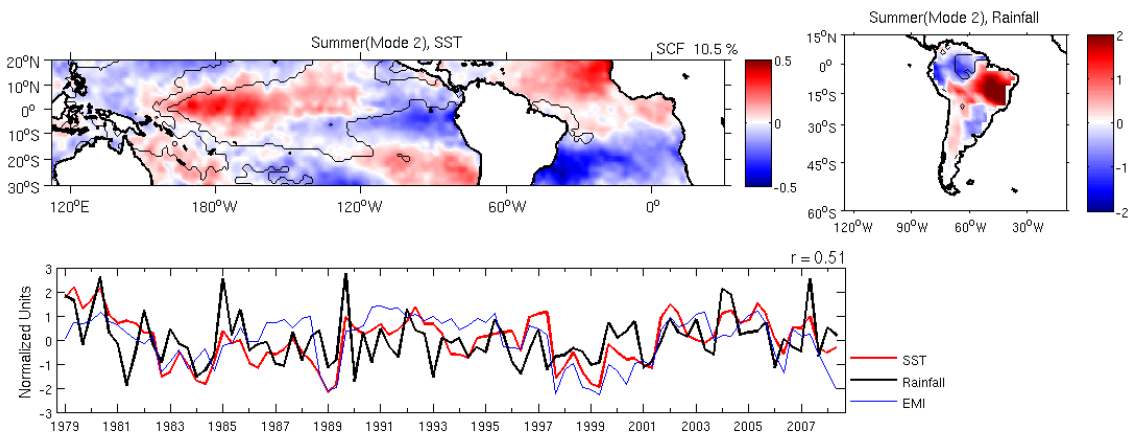


Figure 4.7: The second mode of an SVD analysis between the SST (left) and rainfall anomalies (right) conditions during the austral summer period including the tropical Atlantic SST anomalies. It accounts for $10.5 \pm (2.5)$ % of the square covariance fraction (SCF). Black contours indicate statistical significant regions at the 90% confidence level according to a two-tailed Student t-test. Time series of the SVD expansion coefficient (below). Red (black) line is associated with the SST (rainfall) mode. The coupling strength (r) between these fields is 0.51. The thin blue line represents the EMI index, the correlation coefficient between the SST mode (red) and EMI index (blue) is 0.69. The correlations are statistically significant at the 95% confidence level.

Consequently, the SVD analysis of El Niño including the tropical Atlantic Ocean was also performed. The main features over the tropical Pacific Ocean remain unchanged excepting the tropical Atlantic Ocean which shows a weak signal over the tropical basin. The amount of explained square covariance decreases from 33% to 28.5% with the inclusion of the tropical Atlantic Ocean (Fig 4.8). As in the case of the other two previous coupled modes, according to the EOF separation rule suggested by North et al. (1982), the first and second modes are well separated from the second and third coupled modes of variability respectively. The third explains 5% of the coupled variability and it is not regarded in this thesis.

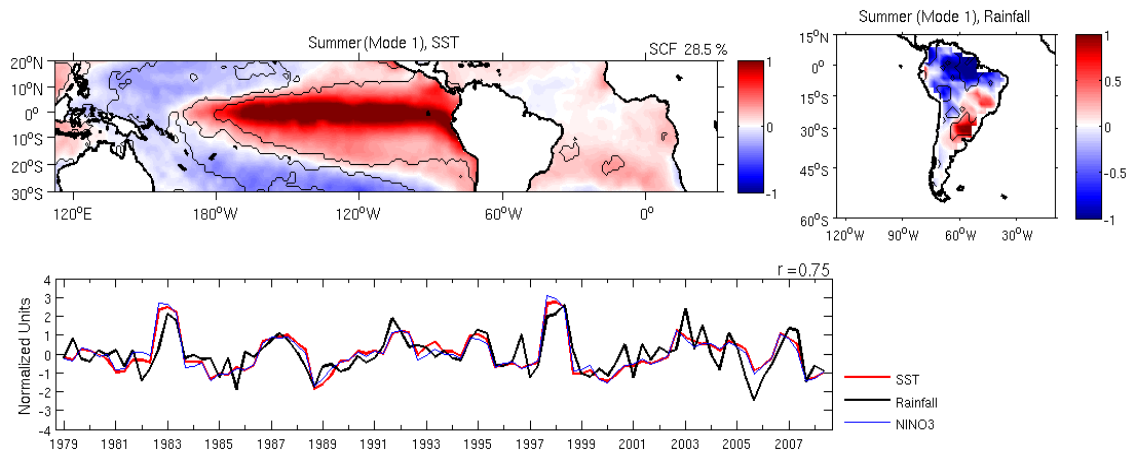


Figure 4.8: The first mode of an SVD analysis between the SST (left) and rainfall anomalies (right) during the austral summer period including the tropical Atlantic SST anomalies. It accounts for $28.5 \pm (7.0)$ % of the square covariance fraction (SCF). Black contours indicate statistical significant regions at the 90% confidence level according to a two-tailed Student t-test. Time series of the SVD expansion coefficient (below). Red (black) line is associated with the SST (rainfall) mode. The coupling strength (r) between these fields is 0.75. The thin blue line represents the NINO3 index, the correlation coefficient between the SST mode (red) and NINO3 index (blue) is 0.98. The correlations are statistically significant at the 95% confidence level.

A complete summary of the main statistics of the SVD analyses are given in the Table 4.1 below.

SVD analysis	Pacific		Pacific and Atlantic	
	Mode 1	Mode 2	Mode 1	Mode 2
Square covariance fraction	33%	9.3%	28.5%	10.5%
Coupling strength	0.75	0.40	0.75	0.51

Table 4.1: Square covariance fraction of El Niño (Mode 1) and El Niño Modoki (Mode 2) for the tropical Pacific Ocean only and for both the tropical Pacific and Atlantic oceans SVD analyses. The coupling strength is estimated by the correlation coefficient of the SVD time series between the SST and rainfall mode. The correlation coefficients are statistically significant at the 95% confidence level.

It is interesting to note that while the SCF of the first mode decreases from 33% to 28.5% with the inclusion of the Atlantic Ocean, the opposite occurs for the second mode. This suggests that the tropical Atlantic Ocean plays a role in modulating the South American rainfall conditions during El Niño Modoki years.

In particular the second rainfall mode provides evidence that this rainfall pattern can be linked to a remote forcing of El Niño Modoki in contrast with previous studies (Grimm and Zilli, 2009; Grimm, 2010). By using correlation analysis between the expansion coefficient time series and South American rainfall anomalies, Grimm and Zilli (2009)

and Grimm (2010) report little or no precipitation effect to the remote forcing from El Niño Modoki instead.

In the following sections, the SST time series of the expansion coefficient corresponding to the first and second SVD modes of Pacific and Atlantic oceans, namely SST PC1/PC2 respectively, are used to examine (unless otherwise specified) the observed atmospheric circulation associated with El Niño and El Niño Modoki events. In addition, the observed circulation fields are compared with the simulated response to the Pacific and Atlantic SST forcings.

4.4 Low-level circulation

4.4.1 Observed conditions during El Niño and El Niño Modoki

Figure 4.9 shows the observed and modelled 850-hPa horizontal winds and SLP anomalies. The most remarkable feature in regard to the anomalous low level circulation during El Niño events is the occurrence of equatorial westerlies from the anomalous high pressure region over the western Pacific to the anomalous low pressure region over the eastern Pacific (Fig. 4.9a). These anomalous westerlies represent the low-level component of the typical anomalous Walker circulation cell during El Niño events. Another feature to highlight is the weakening of the subtropical high pressure system over the eastern Pacific as a consequence of the anomalous negative SLP and cyclonic circulation that predominates over the western coast off South America. Significant anomalous southwesterly winds from the equatorial eastern Pacific into the North equatorial Atlantic Ocean are also evident during the summer period. This implies a weakening of the climatological northeast trade winds in the Atlantic high pressure system. In contrast, positive anomalous SLP is detected over the South Atlantic favouring an enhancement of the subtropical Atlantic high pressure system. Over the extratropical latitudes anomalous cyclones located over the southeast of New Zealand and the South Atlantic Ocean are also evident as well as the weakening of the climatological westerlies over the Southern Ocean. All these features are well known in the literature and they represent the typical conditions of El Niño events (Philander, 1990; Clarke, 2008; Latif and Keenlyside, 2009).

Over the South American continent, the most predominant and well recognized pattern is a northwesterly-to-southward meridional flow in response to an anomalous pressure gradient between the continent and the tropical Atlantic Ocean (Fig. 4.10a). Once the anomalous equatorial easterlies winds reach the western South American border, they

diverge into two branches in response to the predominant topography, i.e. the Andes Mountains. One branch converges with the anomalous southwesterlies from the equatorial Pacific into the Caribbean Sea, and the second branch is driven southward by the eastern flank of the Andes Mountains into the SESA region. The latter enhances the climatological South American Low Level Jet, leading to an increased moisture advection between the equatorial and subtropical regions over the continent (Zhou and Lau, 2001; Silva and Ambrizzi, 2006; Vera et al., 2006; Silva et al., 2009; Silva and Ambrizzi, 2010).

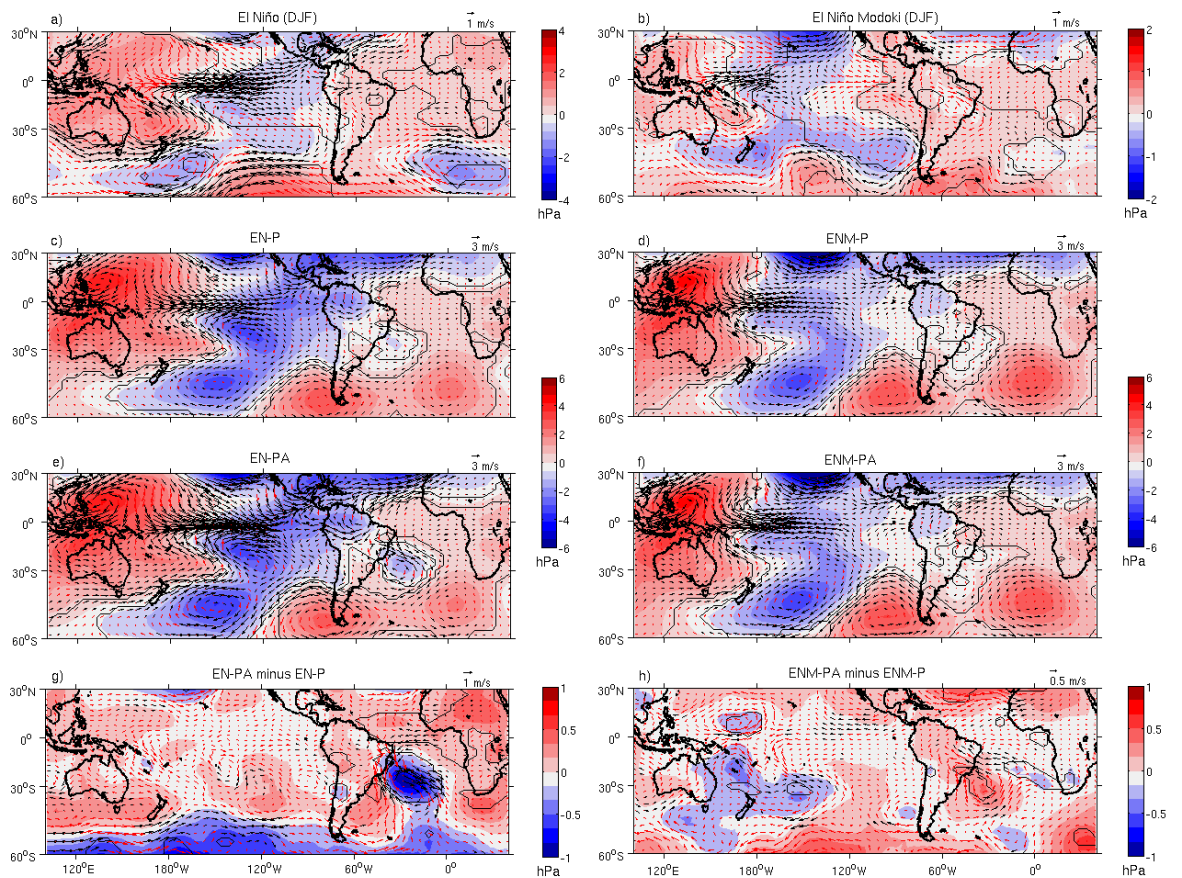


Figure 4.9: Regression of the observed DJF 850-hPa wind (vector) and SLP (shading) anomalies onto (a) SST PC1 (El Niño-related) and (b) PC2 (El Niño Modoki-related). Simulated 850-hPa wind and SLP anomalies for (c) EN-P, (d) ENM-P, (e) EN-PA, and (f) ENM-PA experiments. Difference between (g) EN-PA minus EN-P, and (h) ENM-PA minus ENM-P. Black contours (vectors) represent statistically significant regions (pixels) at the 90% confidence level according to a two-tailed Student t-test.

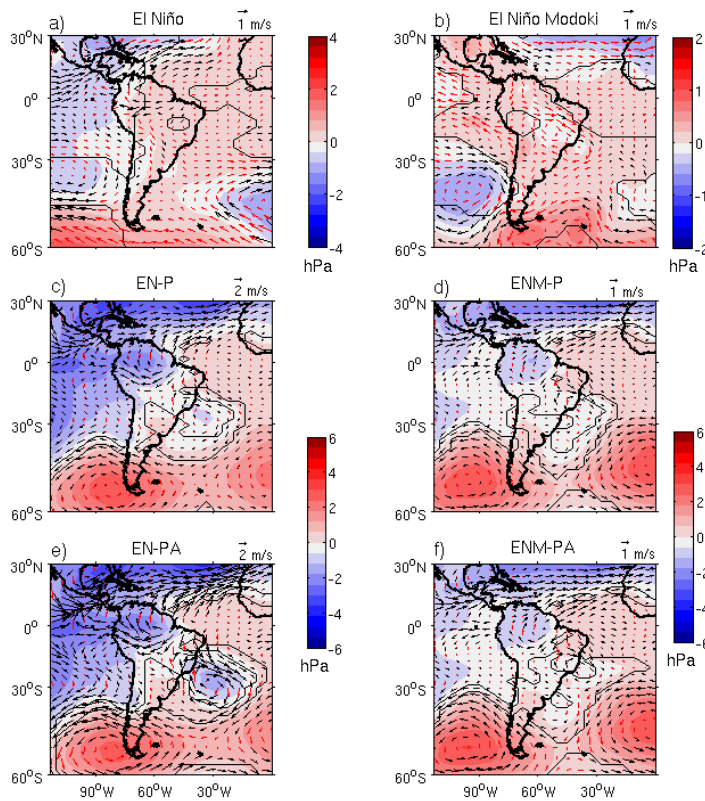


Figure 4.10: As in Fig. 4.9 but focused on South America. Difference between perturbation experiments not included. Black contours (vectors) encompass statistically significant regions (pixels) at the 90% confidence level according to a two-tailed Student t-test.

Contrasting differences are obtained during El Niño Modoki conditions (Fig. 4.9b). Overall the observed anomalous circulation is weaker than that during El Niño conditions. The most remarkable feature is the displacement of the anomalous low level wind convergence zone eastward of the international dateline. This configuration is a dynamic adjustment to the anomalous SLP tripole along the equator, where negative (positive) SLP anomalies roughly overlay the anomalous warming (cooling) distribution at the central (western and eastern) Pacific (Figs 4.1b, 4.9b). This wind anomaly convergence leads to an anomalous ascending motion over the central Pacific, thus establishing an anomalous double Walker circulation cell along the equatorial Pacific (Ashok et al., 2007; Weng et al., 2007; Ashok et al., 2009b). The easterly anomalies over the tropical Southeastern Pacific found during El Niño Modoki years are a direct consequence of the strengthened subtropical high pressure system and represents a contrasting feature compared to the canonical El Niño events. This strengthening is represented by the enhanced southeasterly trade winds and positive SLP anomalies over the northern flank of this high pressure system (Fig. 4.9b). Alternating anomalous high and low pressure centres over the extratropics from northeast New Zealand to South America are also a contrasting feature compared to El

Niño conditions. A large scale cyclonic circulation links Southern Australia and New Zealand, whereas during El Niño this pattern seems to be shifted south of New Zealand (Fig. 4.9). Weng et al. (2009) reported anomalous cyclonic circulation over the southeastern and southwestern Pacific and Atlantic Ocean. Only the cyclonic circulation over the southeastern Pacific is observed in our results suggesting that the anomalous cyclonic pattern in the Atlantic is not a robust feature. To obtain the circulation patterns Weng et al. (2009) used partial regressions onto the EMI and NINO3 indices. Therefore the different methodologies between both studies may explain this disagreement.

The anomalous circulation over the South American continent presents contrasting differences compared to that associated with El Niño such as, a well organized cyclonic vortex centered at 15°S over the central eastern Brazil. This vortex is linked to the continental and oceanic portions of the SACZ (Fig. 4.10b). This cyclonic circulation produces a weakening of the South American Low Level Jet east of Andes and consequently redirects the associated moisture transport coastward to the central eastern Brazil region instead. This pattern is associated with the positive loading of anomalous rainfall observed in SVD analysis and the negative loading over the SESA area (Fig. 4.7). An interhemispheric flow from the Caribbean Sea into the northern South America occurs during Modoki events (Fig. 4.10b). This anomalous circulation does not occur during El Niño, as the anomalous flow and moisture transport typically comes from the equatorial Atlantic Ocean instead (Zhou and Lau, 2001; McGuffie and Henderson, 2005). Furthermore, one of the responsible mechanism for the occurrence of the SALLJ is the deflection of the trade wind that crosses equatorial South America (Fig. 4.10a), however, the propagation of low level wind burst from the Northern Atlantic is also another proposed mechanism (Vera et al., 2006). The last resembles with the observed anomalous winds during El Niño Modoki conditions.

4.4.2 AGCM perturbation experiments

Low level circulation in the EN-P perturbation experiment displays the main features typical of El Niño conditions (Fig 4.9c). Strong low level westerlies wind prevails over the central and eastern Pacific. Around the South American western coast the anomalous wind diverge into two branches, as they do for observed wind, one branch deflects northeastward into the Caribbean Sea, and the second branch weakens the climatological high pressure system over the Southeastern Pacific. In addition, the anomalous winds over tropical South America are coherent with observations (Figs.

4.9a,c). A weakening of the climatological westerlies over the Southern Ocean is also supported by the EN-P experiment. No clear strong low level jet along the meridional axis of the continent is detected during EN-P (Fig. 4.10c). This suggests a weak SALLJ in the model and may indicate a source of deficiency in the modelled rainfall over the SESA region, supporting the negative rainfall bias previously reported in section 2.5.1. Besides the consequences of the low resolution, a successful representation of SALLJ represents an ongoing challenge for most climate models (Vera et al., 2006).

The perturbation experiment including the Atlantic Ocean (Fig. 4.9e), i.e. EN-PA, displays similar circulation response to EN-P except for the stronger wind anomalies. The coast off Eastern Brazil shows an anomalous cyclonic circulation largely in geostrophic balance with the local anomalous SLP in response to the anomalous meridional SST gradient over that area (Fig. 4.2a). In agreement with the modelling study of Barreiro et al. (2002) this anomalous cyclonic anomaly enhances the northward moisture transport to the oceanic portion of the SACZ and then increases the modelled rainfall in the EN-PA experiment (Figs. 4.4e,g ,4.9e).

The difference between EN-PA and EN-P perturbations experiments (Fig. 4.9g) highlights the strength of modelled cyclonic circulation in the off coast of Eastern Brazil. This indicates the role of the South Atlantic Ocean in weakening the subtropical High during El Niño events. In addition, Figure 4.9g also reveals significant anomalous easterlies along the equatorial Atlantic diverging into the Northern Hemisphere and also into the reported cyclonic anomalous pattern in the South Atlantic. The latter may decrease the associated moisture advection from the equatorial Atlantic to the continent and consequently weaken the moisture availability over the SESA region.

Barreiro and Tippmann (2008) suggest that when negative SST anomalies or normal conditions prevail over the equatorial Atlantic Ocean during El Niño events, stronger easterlies over the equatorial Atlantic are observed and consequently along the eastern flank of the Andes Mountains increasing the moisture advection toward the SESA region. Moreover, strong easterlies winds are registered over the continent in the EN-PA experiment (Fig.4.10e). The anomalous SST over the equatorial Pacific and Atlantic oceans generate an anomalous inter-basin SLP gradient that forces anomalous easterlies over the continent from the equatorial Atlantic Ocean (Wang et al., 2009). However the EN-PA experiment does not show an increase in anomalous rainfall over the SESA region (Fig. 4.4g), contrasting with the findings of Barreiro and Tippmann (2008). This fact suggests that part of this associated moisture is being advected toward the oceanic portion of the SACZ instead where the increase in simulated rainfall

is evident over this region (Figs. 4.4e,g and 4.10e). Consequently, SESA does not experience increased moisture transport and thus rainfall, which explains the rainfall difference between the EN-P and EN-PA experiments.

The simulated low level wind anomalies in ENM-P (Fig. 4.9d) successfully reveal the observed SLP tripole, however, the positive SLP anomalies at eastern Pacific are weaker than in observations. Consequently the equatorial westerlies anomalies extend farther east compared to observations (Figs. 4.9b,d). The ENM-P perturbation experiment still simulates the observed westward shift of low level wind convergence compared to EN-P. In the ENM-P experiment (observations) the low level convergence area is found east (west) of 120°W. Additionally, the EN-P experiment shows a weakening of climatological westerlies over the Southern Ocean and a more wave-train pattern than that for observations. The ENM-PA experiment fully represents the most important large scale features, except for an overall strengthening in the general circulation.

Over the northern portion of the continent, the modelled anomalous winds for ENM-P do not show the observed anomalous northerly wind from the Caribbean Sea. In fact the ENM-P and ENM-PA responses resemble those of El Niño simulations, although the latter exhibit a larger magnitude. In the El Niño Modoki experiments, the northeastward wind anomalies from the northern South America into the tropical North Atlantic flow are weak compared to El Niño experiments.

Negative SST anomalies are observed in the equatorial Atlantic Ocean during El Niño Modoki events (Fig. 4.2b). The difference between the ENM-P and ENM-PA experiments reveals easterly wind anomalies over the equatorial and North Atlantic Ocean (Fig. 4.9h). Additionally, stronger westerly wind anomalies occur over the tropical Northeastern Pacific and Western Pacific Ocean in the ENM-PA experiment. It suggests that cold waters in the equatorial Atlantic found during El Niño Modoki summers tend to reinforce the anomalous low level convergence region over the central Pacific, potentially strengthening the ascending branch of the anomalous Walker circulation. The findings of Barreiro and Tippmann (2008) are consistent with the previous result. The authors found that the negative SST anomalies over the equatorial Atlantic reinforce an anomalous SLP gradient between the western Atlantic and eastern Pacific. This in turn accelerates the low level winds from the equatorial Atlantic region toward the eastern Pacific and subsequently reinforces the low level convergence zone in the central Pacific region.

Stronger anomalous circulation in the ENM-PA compared to ENM-P experiment is also observed over the extratropics and indicates a weakening of the extratropical westerlies over the Pacific sector (Fig. 4.9h). The anticyclonic circulation, spanning over both the central eastern Brazil and the subtropical Atlantic Ocean (Fig. 4.9h) is a forced response to the observed tropical warming and subtropical cooling (Fig. 4.2b). Compared to Figure 4.4h, it means that the Atlantic Ocean would produce less dry conditions over the Amazon basin.

4.5 Upper level circulation

4.5.1 Observed conditions during El Niño and El Niño Modoki

Figures 4.11a and 4.12a show the upper level circulation during El Niño conditions, it reveals the typical response to a symmetric heating located along the equator (Gill, 1980). Namely a pair of anomalous anticyclones straddling the equator with strong equatorial easterly winds over the Pacific Ocean and westerlies winds over the subtropics in both hemispheres (Mo, 2000; Alexander et al., 2002; Paegle and Mo, 2002; Grimm and Zilli, 2009). In addition, strong equatorial westerlies are also evident over the Atlantic basin associated with the anomalous cyclonic circulation straddling the equatorial Atlantic Ocean (Figs. 4.11a, 4.12a). The anomalous easterlies over the Pacific Ocean are associated with the observed anomalous upper level divergent mass source spanning the central and eastern Pacific in response to the strong anomalous upward motion located over that region (Figs. 4.12a, 4.13a) (Wang, 2002a; Ashok et al., 2007; Weng et al., 2009). The anomalous upper level wind field also exhibits a zonal large scale cyclonic pattern over both the subtropical-to-extratropical Pacific and Atlantic oceans respectively (Fig. 4.11a), this is also supported by the observed asymmetric streamfunction anomalies (Fig. 4.12a). The northern flank of this pattern tends to strengthen the Subtropical Jet over South America, however this pattern is more intense and better defined during the austral spring when the Jet is climatologically stronger (Cazes Boezio et al., 2003). Figure 4.12a also supports a teleconnection pattern from the tropical central Pacific toward South America via extratropics. The teleconnection is weak, however, as the mean state during the summer period is not favourable for Rossby wave propagations (Cazes Boezio et al., 2003; Grimm, 2003a). Nevertheless wave train propagations are still detected, they extend from the Northwestern Australia and central Pacific toward the Southern Ocean (120°W) and then toward the Atlantic coast of subtropical South America (Fig. 4.12a). Furthermore in the continent, specifically over the Bolivian Altiplano (16°S), a

significant cyclonic anomaly is found. It dampens and shifts northward the climatological upper level anticyclone, known as the Bolivian High (Lenters and Cook, 1997; Cook, 2009). Negative (positive) rainfall anomalies over this region had been associated with a northward (southward) migration of this upper level anticyclone during the negative (positive) phase of the Southern Oscillation (Vuille, 1999; Garreaud and Aceituno, 2001).

Over the Atlantic coast of subtropical South America (approximately 30°S) an anomalous weak anticyclone is observed (Figs 4.11a, 4.12a). Additionally, the anomalous low level circulation does not show a similar anomaly in order to suggest a barotropic circulation regime over the same area (Fig. 4.10a).

The irrotational component of the anomalous upper level circulation is described by the velocity potential field and its associated divergent winds in Figure 4.13. During El Niño years (Fig. 4.13a), the central-to-eastern Pacific features a strong anomalous upper level mass source (divergent centre) associated with an anomalous upward motion. It spans from the subtropical Pacific Ocean over the Southern Hemisphere toward Central-North America including the subtropical North Atlantic. Three mass sinks (convergence centres) are found: over the western Pacific linking both hemispheres, the Atlantic coast of equatorial South America, and finally over northern Africa and the Mediterranean Sea. These centres are associated with anomalous downward motion over these regions (Wang, 2002a; Weng et al., 2009).

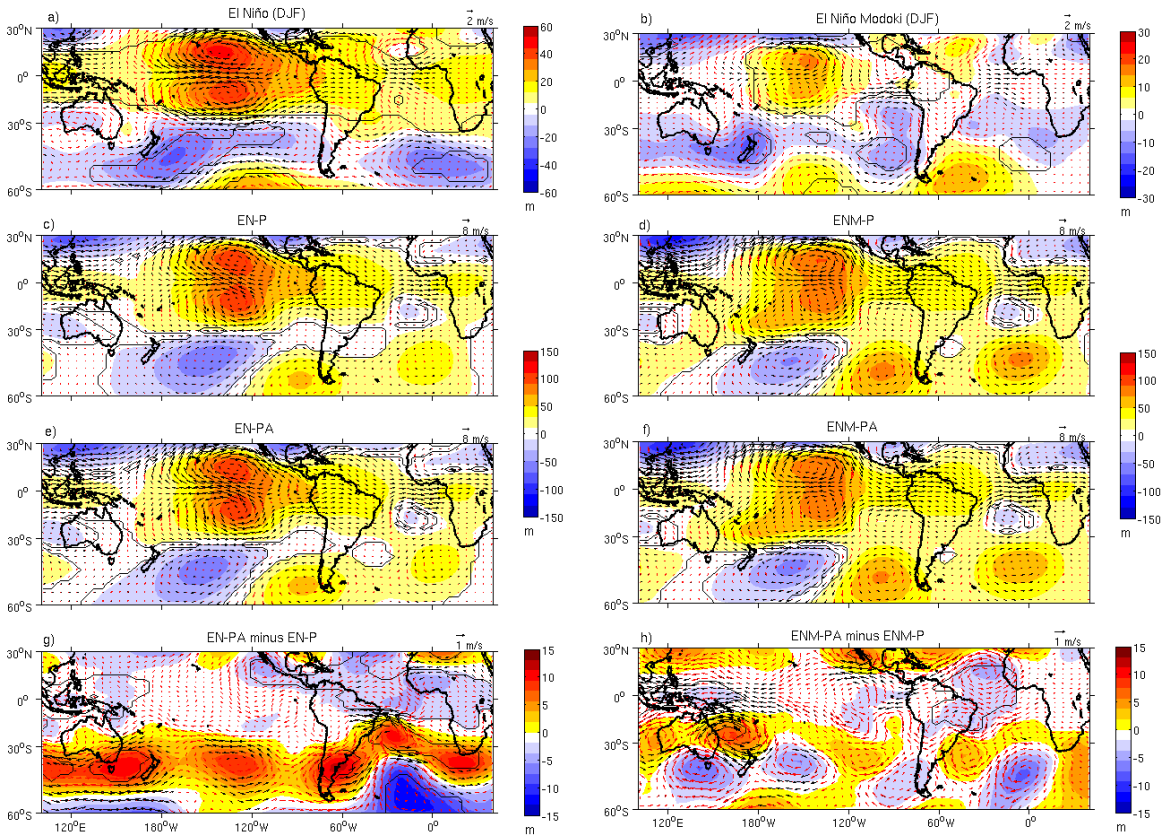


Figure 4.11: Regression of the observed DJF 200-hPa wind (vector) and geopotential height anomalies (shading) anomalies onto (a) SST PC1 (El Niño-related) and (b) PC2 (El Niño Modoki-related). Simulated 200-hPa wind and geopotential height anomalies for (c) EN-P, (d) ENM-P, (e) EN-PA, and (f) ENM-PA experiments. Difference between (g) EN-PA minus EN-P, and (h) ENM-PA minus ENM-P. Black contours (vectors) represent statistically significant regions (pixels) at the 90% confidence level according to a two-tailed Student t-test.

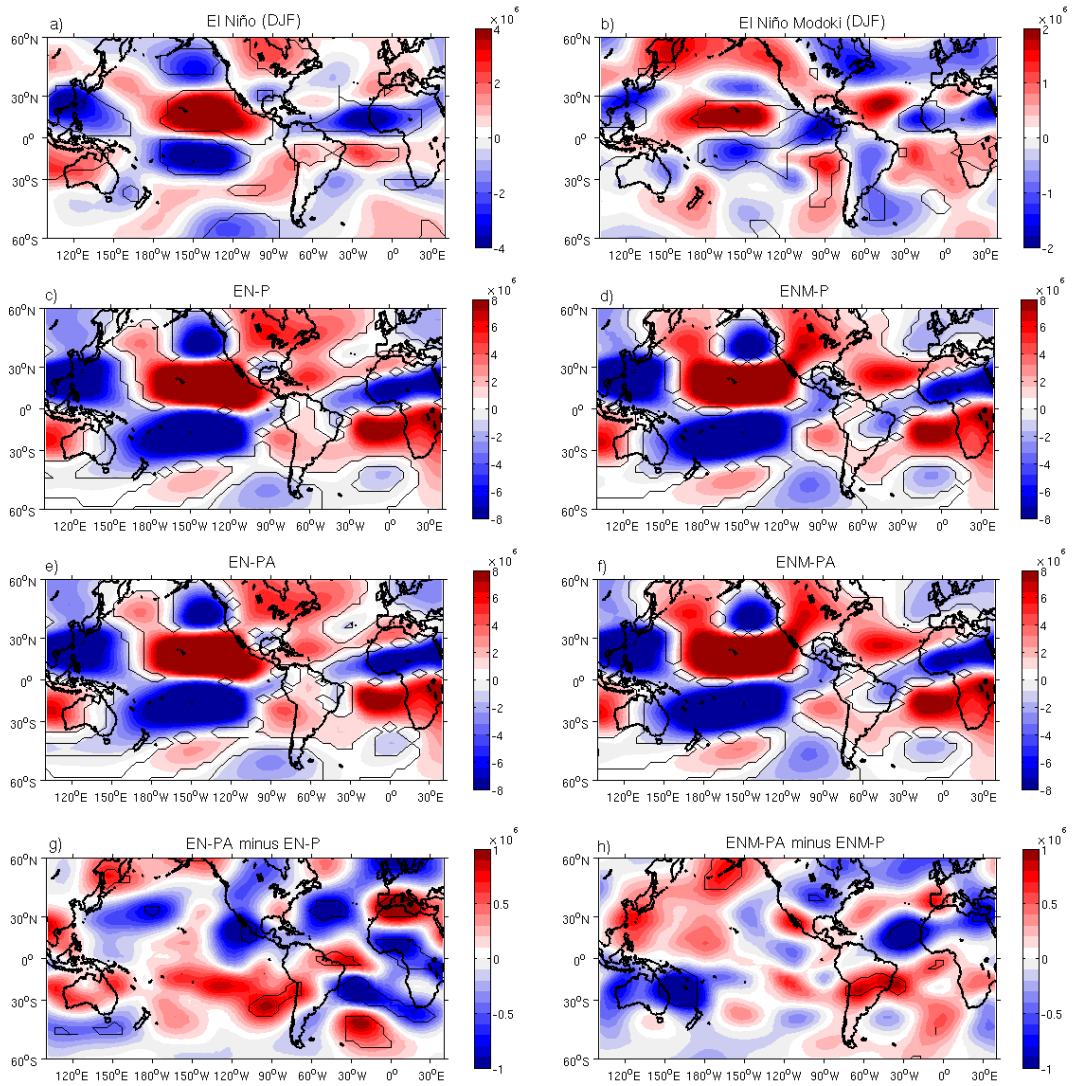


Figure 4.12: Regression of the observed DJF 200-hPa asymmetric streamfunction anomalies onto (a) SST PC1 (El Niño-related) and (b) PC2 (El Niño Modoki-related). Simulated anomalous 200-hPa asymmetric streamfunction for (c) EN-P, (d) ENM-P, (e) EN-PA, and (f) ENM-PA experiments. Difference between (g) EN-PA minus EN-P and (h) ENM-PA minus ENM-P, units are m^2/s . Black contours represent statistically significant regions at the 90% confidence level according to a two-tailed Student t-test.

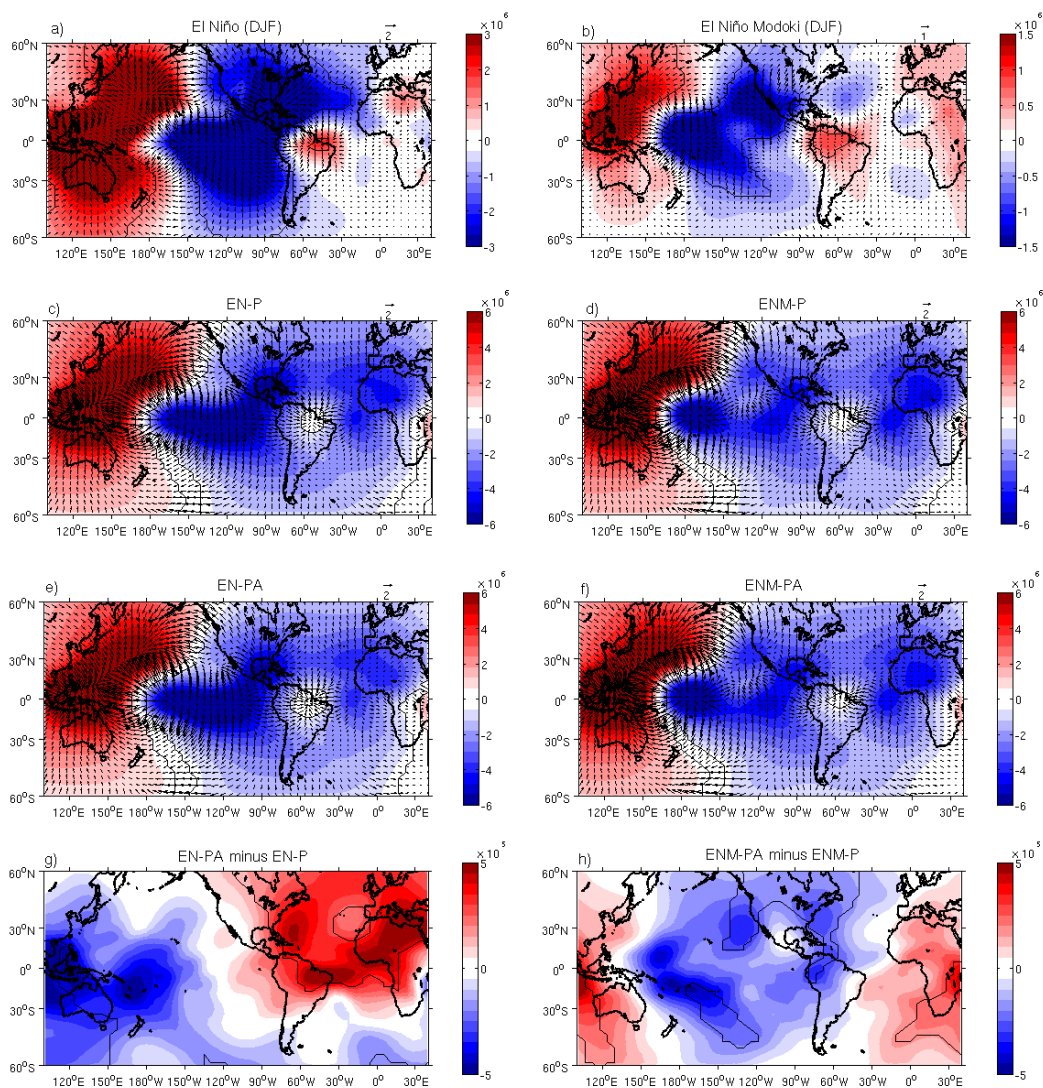


Figure 4.13: Composites of the observed anomalous 200-hPa divergent winds (vectors) and velocity potential (shading) during the summer period of (a) El Niño, and (b) El Niño Modoki (See Table 3.1). The blue (red) shading regions indicate anomalous upper level divergence (convergence) centres. Composites of simulated anomalous 200-hPa divergent winds and velocity potential for (c) EN-P, (d) ENM-P, (e) EN-PA, and (f) ENM-PA perturbation experiments, and the velocity potential anomaly difference between (g) EN-PA minus EN-P and (h) ENM-PA minus ENM-P. The units of divergent wind (velocity potential) are m/s (m^2/s). Black contours represent statistically significant regions at the 90% confidence level according to a two-tailed Student t-test.

The most remarkable feature in the anomalous upper level circulation during El Niño Modoki conditions is the displacement of the pair of anticyclones to the central-to-western Pacific in agreement with the observed anomalous warming (Figs. 4.1b, 4.11b). In addition, the streamfunction anomaly field shows anomalous divergent winds over the equatorial Pacific around 120°W , which is part of an anomalous quadrupole pattern straddling the equator (Figs. 4.11b, 4.12b). In fact, this is the upper level manifestation of the typical anomalous double Walker circulation cell during El Niño Modoki events (Ashok et al., 2007; Weng et al., 2007; Ashok et al., 2009b; Weng et al.,

2009). Because of the occurrence of this anomalous quadrupole during El Niño Modoki, the anomalous subtropical jet presents a meandering structure rather than a well defined enhanced jet as occurs during El Niño. In fact, the anomalous upper level cyclone located over the tropical Eastern South America introduces strong meridional wind anomalies into the zonal flow (Figs. 4.11a, b, 4.12a, b).

Although the summer season is not favourable for wave-train-like propagations, the anomalous 200-hPa geopotential height and asymmetric streamfunction fields (Figs. 4.11b, 4.12b) still provide some evidence of subtropical-to-extratropical teleconnections from the central-western Pacific toward South America, in a PSA-like patterns (Mo, 2000). Moreover, we will show in Chapter 6 that an important wave-like propagation occurs in the extratropics by the early summer period. In particular the extratropical propagation seems to be originated from Northeastern Australia during El Niño Modoki, thus representing a displacement of the source centre location compared to El Niño (Figs. 4.12a,b). This propagation reaches the Southern Atlantic Ocean and it is mostly centered at 46°S. The tropical propagation emanates from the area associated with the SPCZ in the tropical Pacific and it seems to be linked with the SACZ region over the South American continent. Another example occurs in the Northern Hemisphere, where PNA propagations are also evident. A wave-train propagates northeastward from the central equatorial Pacific toward northwest coast of Canada and then turning southeastward from northeastern Canada toward the tropical North Atlantic (Fig 4.12b) (Horel and Wallace, 1981; Nobre and Shukla, 1996; Alexander and Liu, 2007). Weng et al. (2009) provide a detailed description between the differences in the PNA teleconnection pattern between El Niño and El Niño Modoki conditions during this season.

In particular there are some differences in the position of the stationary waves over the SESA region during different El Niño conditions (Drumond and Ambrizzi, 2003; Silva and Ambrizzi, 2006). During El Niño events an anomalous anticyclone is found over the Atlantic coast of South America around 30°S, whereas during El Niño Modoki this anomaly is shifted southward over the extratropics (45°S) (Figs 4.12a,b). Over Brazil a similar anticyclonic anomaly is registered during El Niño Modoki. As its low level counterpart reveals a cyclonic pattern (Fig. 4.10b), it resembles a baroclinic circulation regime prevailing over central eastern Brazil. This baroclinic circulation anomaly is associated with the second mode of rainfall variability (Fig. 4.7) and is consistent with the findings of Grimm and Zilli (2009).

Other contrasting differences between El Niño and El Niño Modoki are also supported by the 200-hPa anomalous velocity potential and its associated divergent winds (Figs. 4.13a,b). During El Niño Modoki the overall magnitude of the velocity potential field is weaker than El Niño. The anomalous upper level mass source over the equatorial Pacific is shifted westward, centered around 180°W compared to El Niño events. The upper level mass sink located over the western Pacific is mostly focused over the Northern Hemisphere. Likewise the South American mass sink source is found over the northwestern South American coast instead compared to El Niño conditions. Weng et al. (2009) report this upper level convergence region mostly located over the eastern Pacific Ocean. This difference is likely to be a consequence of the slightly different month selection used in the regression analysis. In particular, they consider the January-February-March period as the equivalent to our summer season. El Niño Modoki shows a progression from weak to strong downward motion onto the eastern Pacific from the austral summer to autumn periods as it will be shown in the next chapter, thus explaining this difference. Nonetheless, their reported results are still essentially the same compared to those in Figure 4.13.

4.5.2 AGCM perturbation experiments

The perturbation experiments undertaken for El Niño and El Niño Modoki conditions capture the main observed characteristics of the upper level circulation (Figs. 4.11, 4.12), such as the pair of anomalous anticyclones symmetric about the equatorial Pacific, PSA-like propagation emanating from the heating source over the equatorial Pacific toward the extratropics, although the correct position of the stationary waves is not well simulated compared to observations.

In the EN-P and EN-PA experiments, the equatorial easterlies (westerlies) in the Pacific (Atlantic) Ocean are slightly stronger in EN-P than EN-PA. This fact is better represented by the asymmetric streamfunction anomaly difference (Fig. 4.12g), the positive and negative anomaly differences located over the eastern Pacific indicate a strengthened anomalous anticyclone straddling the equator in the EN-P compared to EN-PA experiment. The same is true for the anomalous cyclonic pattern straddling the equator over the equatorial Atlantic Ocean (Fig. 4.12g). In other words, there are stronger upper level equatorial westerlies over the Atlantic Ocean in the EN-P compared to EN-PA experiment. Furthermore, the observed anomalous cyclone located over the equatorial north Atlantic during El Niño seems to be shifted eastward

over Africa in the EN-P and EN-PA experiments compared to observations (Figs. 4.12a, c, e). As a consequence the simulated upper level winds over that area are weaker than in observations.

Figures 4.11g and 4.12g also reveal remarkable differences over the subtropics and extratropics. In particular, the EN-PA experiment suggests that the anomalous Atlantic SST conditions may strengthen the upper level wave-like propagation over the extratropics. In addition, a local response highlights over the Atlantic coast of tropical South America. This anomaly difference represents a baroclinic response, as its low level counterpart is an anomalous cyclonic circulation regime (Figs. 4.9e,g, 4.12g). This upper level circulation response is weaker in the EN-PA than EN-P experiment due to the response to the observed local warming over this area (Fig. 4.2a).

The anomalous velocity potential fields of the perturbation experiments simulate the major characteristics regarding its corresponding observed fields during El Niño conditions (Figs. 4.13a, c, e). A strong upper level mass source associated with upward motion is found along the equatorial Pacific, and also slightly covering the western Pacific compared to observations. An upper level convergence centre is found over the western Pacific and the Atlantic coast of equatorial South America in agreement with observation. The observed upper level convergence centre located over northern Africa is not represented in the perturbation experiments. The difference between EN-P and EN-PA is displayed by Figure 4.13g. The major differences in the upper level divergence and convergence centres occur from the tropical South Atlantic to the North Atlantic Ocean, and over the tropical western Pacific Ocean. The upper level divergence over the Atlantic Ocean is weaker in the EN-PA than EN-P experiment. The simulated downward motion over equatorial South America, however, is stronger in the EN-PA experiment. Over the western Pacific region, the simulated anomalous upper level convergence is weaker in the EN-PA compared to the EN-P experiment.

The perturbation experiments performed for El Niño Modoki conditions also represent the main observed features of the anomalous upper level circulation. In particular, The observed upper level easterlies and westerlies diverging from the central equatorial Pacific are well represented in the ENM-P and ENM-PA perturbation experiments, likewise the observed upper level westerlies over the equatorial Atlantic Ocean (Figs. 4.11b,d,f). In addition, the simulated asymmetric streamfunction anomalies support the performance of the model, with a well simulated quadrupole straddling the equator in the Pacific Ocean (Figs. 4.12b,d,f). Another noteworthy feature is the anomalous anticyclone located over Northeast Brazil which is shifted compared to observations

(Figs. 4.12b,d,f). However, this anticyclone is not simulated under during El Niño conditions (Figs. 4.12c,d,e,f). Furthermore, the experiments capture an enhanced subtropical-to-extratropical upper level circulation in the El Niño Modoki compared to the El Niño experiments, which suggests the importance of the extratropical circulation during El Niño Modoki conditions (Figs. 4.11c,d, 4.12c,d).

Teleconnection patterns from the equatorial Pacific towards South America via the extratropics are also detected in both the ENM-PA and ENM-P experiments. The midlatitude wavetrain pattern is similar to the EN teleconnection, however the modelled response in ENM case is slightly stronger as previously noted (Figs. 4.11c,d,e,f).

The difference between both perturbation experiments (Figs. 4.11h, 4.12h) suggests a weaker upper level circulation over the tropical Atlantic and Pacific oceans and stronger over the subtropical to extratropical regions in the ENM-PA experiment. Over the tropics this is also supported by the negative difference of velocity potential over the central Pacific (Fig. 4.13h). In particular this negative difference indicates a strong upward motion in the ENM-PA experiment. It is especially strong and significant around the SPCZ and also over the northeastern Pacific (40°N) regions. Over the equatorial South America a stronger mass sink in the ENM-P compared to ENM-PA experiment is found. This represents a contrasting result compared with the EN experiments in which this mass sink is stronger in the EN-PA experiment instead.

4.6 Vertical circulation

4.6.1 Observed conditions during El Niño and El Niño Modoki

The observed vertical velocity associated with the Walker circulation cell across the equatorial Pacific Ocean shows the well known vertical structure during the mature phase of El Niño (Wang, 2002b). An anomalous ascending branch predominates over the central to eastern equatorial Pacific (Fig. 4.14a, blue shading), in conjunction with two strong descending branches (red shading) located over the western equatorial Pacific and central-to-eastern equatorial South America. The ascending branch is associated with strong convection activity and positive rainfall anomalies spanning over the anomalously warm waters (Figs. 4.3a, 4.14a). The descending branches weaken the convection activity, inhibiting the formation of clouds and thus leading to dry conditions over Indonesia and northern South America.

In response to the El Niño Modoki-related shift of the anomalous warming location, the anomalous ascending branch is mostly focused over the equatorial central-to-western Pacific, more specifically around the International Date Line (Fig. 4.14b). The descending branches are located over the western Pacific and the eastern Pacific including the equatorial coast of South America. These branches are associated with negative rainfall anomalies over their corresponding regions. It is worth mentioning that the descending branch located over the eastern Pacific is weak in austral summer, however it represents an early transition into a fully developed and stronger descending branch during the autumn period as it will be shown in the next chapter.

The weak vertical circulation pattern during El Niño Modoki is consistent with the observed anomalous large scale rainfall distribution during El Niño Modoki events (Fig.4.3b). It shows the displacement of the convection activity centres compared to the canonical El Niño events as shown by previous studies (Ashok et al., 2007; Ashok et al., 2009b; Weng et al., 2009).

To quantify these relationships with the NINO3 and EMI indices respectively, we defined a Walker Index for South America by performing the difference between the 500-hPa vertical velocity anomalies over the eastern Pacific and eastern equatorial South America as shown in Figure 4.15. Maximum negative cross correlation (-0.77) between the Walker and NINO3 indices is found at zero lag (Fig. 4.16, upper panel). A similar relationship is reported by Wang (2002b), but using the associated descending branch located over the western Pacific (5°S-5°N, 120°E-160°E) instead. As expected

the cross correlation between the Walker and EMI indices is weak and positive (0.28), with the EMI index leading by 6 months. A second Walker Index (Fig. 4.15, solid line), i.e. the Modoki-Walker Index is then defined, according to the observed changes in the Walker circulation cell and the features in the composite of the 500-hPa vertical velocity anomalies for El Niño Modoki. This index better describes the relationship, a maximum negative cross correlation (-0.51) between the Modoki-Walker and EMI indices is observed at zero lag (Fig. 4.16, lower panel), which means a strong upward motion over the central Pacific during the peak of El Niño Modoki.

4.6.2. AGCM perturbation experiments

The perturbation experiments undertaken for El Niño conditions (e.g. EN-P in Fig. 4.14c) fully support the main observed features of the vertical circulation associated with the Walker circulation cell. The position of the corresponding ascending and descending branches are well simulated compared to observations (Figs. 4.14a,c,e). Furthermore, this is in agreement with its associated anomalous large scale rainfall pattern (Fig. 4.3c). The tropical Atlantic role in the vertical circulation is shown in Figures 4.14e,g. The AGCM experiments difference (Fig. 4.14g), EN-PA minus EN-P, suggests that the descending (ascending) branch over the equatorial South America (tropical Atlantic) is reinforced (weakened) when the Atlantic SST anomalies are taken into account in the simulations. The stronger downward motion over the continent in the EN-PA experiment is in agreement with the stronger negative rainfall anomalies over this region (Figs. 4.4e,g, 4.14g).

The AGCM experiments carried out for El Niño Modoki conditions, namely the ENM-P and EMM-PA experiments, reveal the corresponding shift of the ascending motion toward the international dateline (Figs.4.14b,d,f). Additionally, the correct position of the anomalous descending branch over the eastern equatorial Pacific (90°W) is well simulated, likewise the corresponding descending branch over the western equatorial Pacific is in agreement with previous AGCM studies (Ashok et al., 2009b). However in the El Niño Modoki experiments the double convective-cell in the equatorial Pacific is well simulated, the shift of the descending branch over South America does not show any significant change compared to the El Niño experiments except for its lower magnitude. This branch is mainly focused between the 60°W-30°W meridional band. A hint of this has been already revealed by the simulated velocity potential, there are virtually no changes in the upper level convergence centres between the different experiments (Figs. 4.13e,f). The role of the tropical Atlantic SST anomalies during El

Niño Modoki is shown in Figure 4.14h and it is the opposite compared to El Niño conditions. Contrasting effects in response to the tropical Atlantic influence are noted, a weaker (stronger) descending (ascending) branch over the continent (tropical Atlantic) is detected in the ENM-PA experiment, contrasting with the stronger descending branch in the EN-PA experiment. The weak descending branch over the continent in the ENM-PA experiment supports the weak negative rainfall anomalies over the equatorial portion of the continent in the ENM-PA experiment as shown in Figure 4.4h.

Therefore, the tropical Atlantic conditions seem to modulate the magnitude of the downward motion over the continent associated with the Walker circulation cell and consequently the magnitude of the simulated rainfall. In particular, the AGCM experiments undertaken for El Niño (El Niño Modoki) conditions suggest that when the tNA and tSA regions are cool and warm respectively (cool to normal) strong (weak) subsidence is simulated over the tropical South America. The next section is aimed at providing further details about the tropical Atlantic conditions during El Niño and El Niño Modoki.

It is also worth mentioning that the vertical velocity is not a standard output in the model. So, we just used an approximation to the vertical velocity using the Kinematic Method (Wallace and Hobbs, 2006). The method aims at integrating the continuity equation in the vertical, and one of the consequences is that the vertical velocity is not zero at upper levels. It could explain some baroclinic patterns at upper levels in the experiments. However, below the 200 hPa level the estimated vertical velocity is a good approximation compared to observed fields.

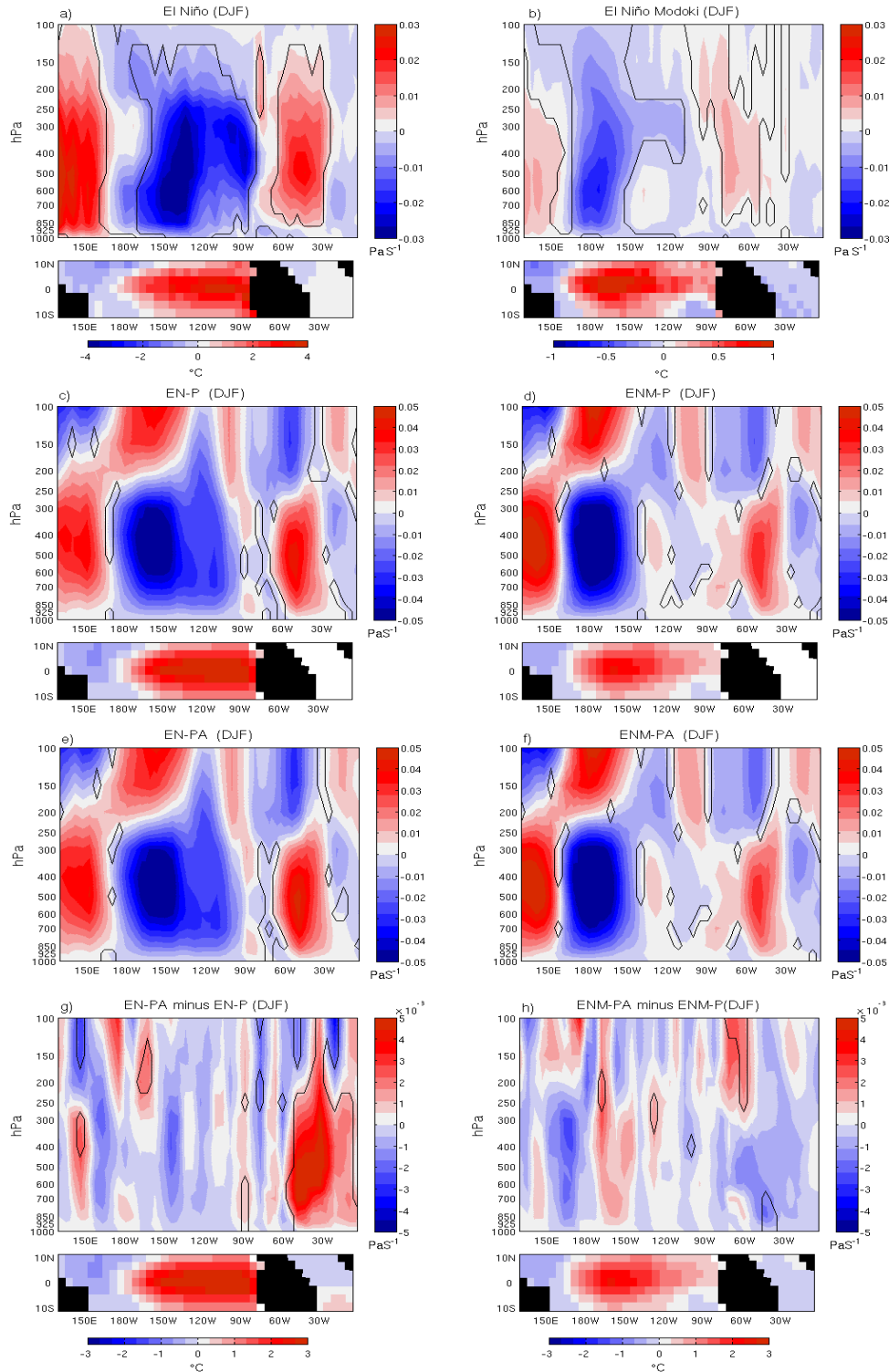


Figure 4.14: Composites of the observed vertical velocity anomalies during (a) El Niño and (b) El Niño Modoki events (See Table 3.1). The simulated vertical velocity anomaly for (c) EN-P, (d) ENM-P, (e) EN-PA, (f) ENM-PA, and the vertical velocity anomaly difference between (g) EN-PA minus EN-P, and (h) ENM-PA minus ENM-P perturbation experiments. The vertical velocity was averaged over the 10°N-10°S latitudinal band. Blue (red) shading is associated with upward (downward) motion. The associated SST anomalies (°C) are shown below. Black contours represent statistically significant regions at the 90% confidence level according to a two-tailed Student t-test.

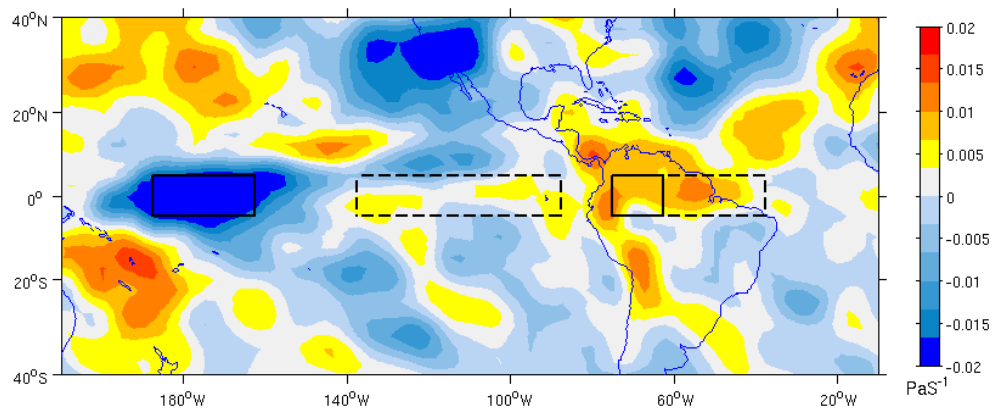


Figure 4.15: Composite of the observed anomalous 500-hPa vertical velocity during the summer period of El Niño Modoki conditions (See Table 3.1). Negative (positive) values indicate ascending (descending) motion. Dashed black boxes indicate the regions, i.e. eastern equatorial Pacific (5°N-5°S, 138°W-88°W) and eastern equatorial South America (5°N-5°S, 63°W-38°W), used to estimate the Walker Index during El Niño conditions. Solid Black boxes indicate the regions, i.e. central equatorial Pacific (5°N-5°S, 188°W-163°W) and western equatorial South America (5°N-5°S, 75°W-63°W), used to estimate a suitable Walker Index during El Niño Modoki conditions, i.e. the Modoki-Walker Index.

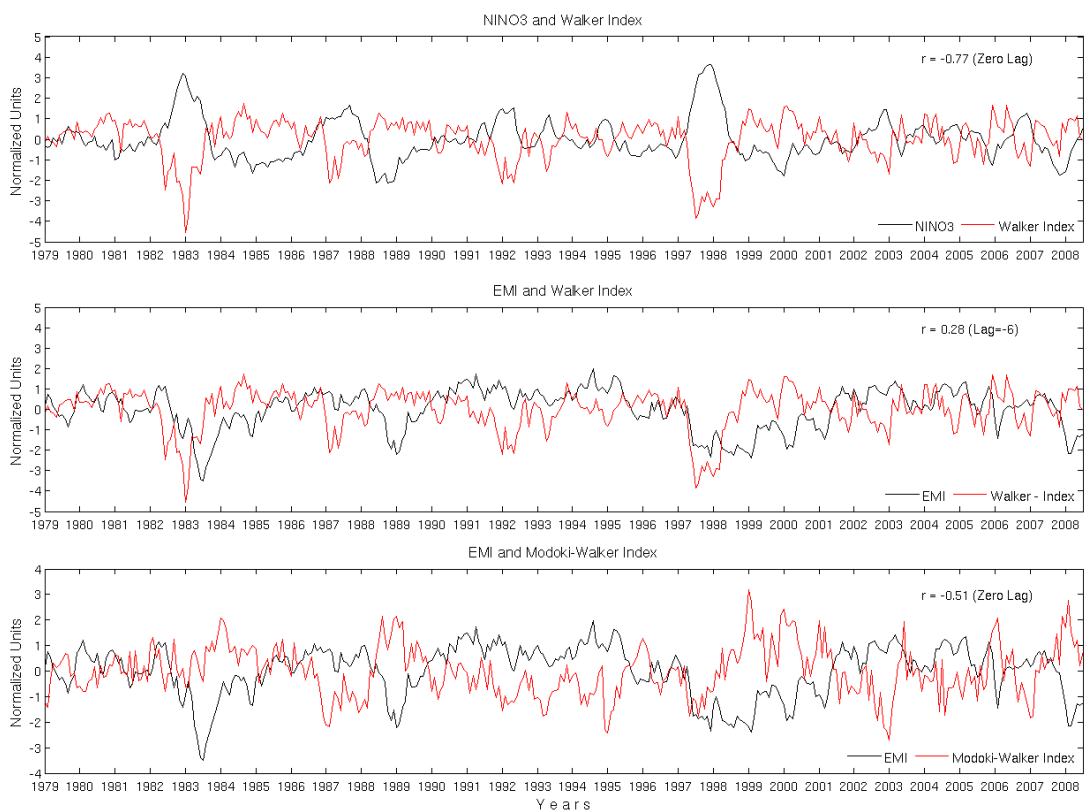


Figure 4.16: (upper) The NINO3 and Walker indices and its corresponding correlation coefficient in the upper right corner (-0.77 at zero lag). (Middle) The EMI and Walker indices and its corresponding correlation coefficient in the upper right corner (0.28, when the EMI leads the Walker Index by 6 months). (Lower) The EMI and the Modoki-Walker indices and its corresponding correlation coefficient in the upper right corner (-0.51 at zero lag). The correlations are statistically significant at the 95% confidence level.

4.7 Tropical Atlantic conditions and its relationship with El Niño and El Niño Modoki

One of the most outstanding features of the Atlantic Ocean variability is the occurrence of a meridional SST gradient straddling the equator that has a strong impact in the southward migration of the Atlantic ITZC that in turn modulates rainfall variability over northern South America. In this section we investigate the relationship between the anomalous SST conditions in the tropical Atlantic Ocean with El Niño and El Niño Modoki conditions. To explore this relationship, we use the components of the Atlantic gradient Index independently as defined by Giannini et al. (2004). This Index represents the difference of the area-averaged of SST anomalies over the tNA, i.e. tropical North Atlantic (5°N-25°N, 60°W-30°W) and tSA, i.e. tropical South Atlantic (25°S-5°S, 30°W-0°E) (See the green boxes in the upper left panel in Fig. 4.19).

We initially focus on the SST anomalies over the tNA region as its correlation with ENSO is known to be significantly influenced by the equatorial Pacific remote forcing during El Niño events (Wang, 2002c; Huang et al., 2005). Furthermore, previous studies have found that the maximum cross correlation between the tNA and the NINO3 indices is approximately 0.47, when the tNA SST anomalies lag the NINO3 SST anomalies by 4 to 5 months (Curtis and Hasternrath, 1995; Enfiled and Mayer, 1997; Saravanan and Chang, 2000; Wang, 2002c; Giannini et al., 2004; Huang et al., 2005).

Figure 4.17 depicts the times series of the NINO3 and EMI versus the tNA and tSA indices respectively. The maximum positive correlation between the NINO3 and tNA indices is 0.43, significant at the 95% level, and occurs when the tNA SST anomalies lag the NINO3 SST anomalies by 5 months in agreement with the already mentioned studies (Fig. 4.17a). It means that after the peak of El Niño, i.e. during the austral summer, an anomalous warming generally follows over the tNA region by the next autumn. The relationship between the NINO3 and tSA indices is negative instead, the correlation coefficient is -0.43 with tSA leading NINO3 SST anomalies (Fig. 4.17b). The relationship between the tNA and the EMI indices is rather weak and not significant. The tNA leads the EMI index by 4 months with a correlation of -0.20 (Fig. 4.17c), whereas the lagged cross correlation with the tSA Index is also weak (-0.22) with the tSA lagging the EMI index by 3 months (Fig. 4.17d).

Figure 4.18 shows a second lagged correlation analysis performed during El Niño and El Niño Modoki years only. We find that during El Niño Modoki years the correlation between the EMI and tNA indices is negative (-0.63) at zero lag (Fig. 4.18a). Further

the correlation between the NINO3 and tNA indices is positive (0.76) with the tNA lagging the NINO3 index by 1 month (Fig. 4.18a). It suggests an opposite relationship compared to the EMI index. A similar situation is found over the tSA region, during El Niño Modoki years a negative cross correlation (-0.63) between the EMI and tSA indices occurs when the tSA lags the EMI index by 5 months (Fig. 4.18b). Note that this correlation remains especially strong throughout the winter period. In contrast this relationship is mainly positive during El Niño conditions, a positive cross correlation (0.76) between the tSA and NINO3 indices is found at zero lag. Therefore, during El Niño and El Niño Modoki years distinct anomalous SST conditions predominate over the tropical Atlantic. Anomalous warm (cool to normal) conditions tend to occur during El Niño (El Niño Modoki) events over the tropical Atlantic Ocean. To further illustrate this, the monthly evolution of the Atlantic SST anomalies during El Niño and El Niño Modoki events is shown in Figure 4.19.

It is worth mentioning that the occurrence of the anomalous warming over the tNA region during the austral autumn period is evident (Figure 4.19, left panels), as described by the maximum positive cross correlation between the NINO3 and tNA indices. One proposed mechanism to explain this anomalous warming over the tNA region is known as the atmospheric bridge (Alexander et al., 2002; Wang, 2005). The descending branch of the anomalous Walker circulation during El Niño weakens the climatological ascending motion over South America and the tropical Atlantic Ocean, thus weakening the Atlantic Hadley circulation. Consequently, this decreases the climatological descending motion over the area associated with the subtropical high in the tropical North Atlantic. As a consequence, this reduces the northeast trade winds and the evaporative cooling over the tNA region, leading to warm SST anomalies over the tNA region.

The observed anomalous cooling over most of the tropical and subtropical Atlantic during El Niño Modoki is also evident, contrasting with their corresponding evolution during El Niño events (Fig. 4.19, right panels). This fact a priori suggests that the atmospheric bridge mechanism is not effective in producing an anomalous warming over the tNA region during El Niño Modoki conditions. This fact can be verified by undertaking coupled general circulation experiments, however, these kinds of experiments are beyond the current scope of this thesis. Chapter 5 offers a mechanism which attempts to explain the anomalous cooling over the tNA region in response to a distinct anomalous Walker circulation cell during El Niño Modoki conditions. This would

suppress the weakening of the trade winds over the equatorial Atlantic as typically tend to occur during El Niño conditions.

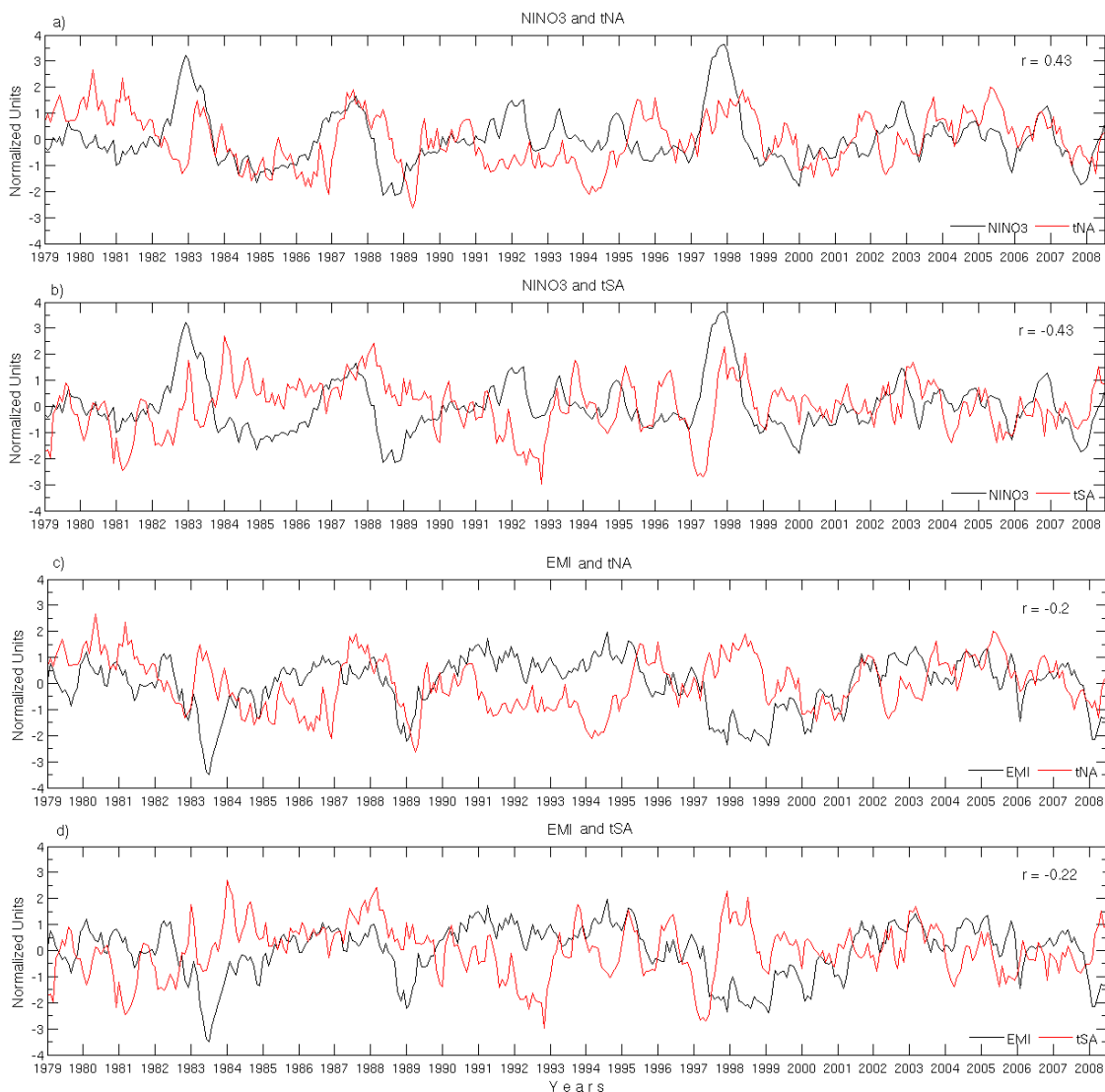


Figure 4.17: Time series of (a) the NINO3 and tNA, (b) NINO3 and tSA, (c) EMI and tNA, and (d) EMI and tSA indices. The NINO3 and EMI (tNA and tSA) indices are represented in black (red) lines. The maximum correlation coefficient (r) of the corresponding lagged cross correlations is indicated in the upper right corner of each panel. In: (a) the tNA lags the NINO3 index by 5 months, (b) the tSA leads the NINO3 index by 8 months, (c) the tNA leads the EMI index by 4 months, (d) the tSA lags the EMI index by 3 months. Only the correlations undertaken for the NINO3 index are statistically significant at the 95% confidence level.

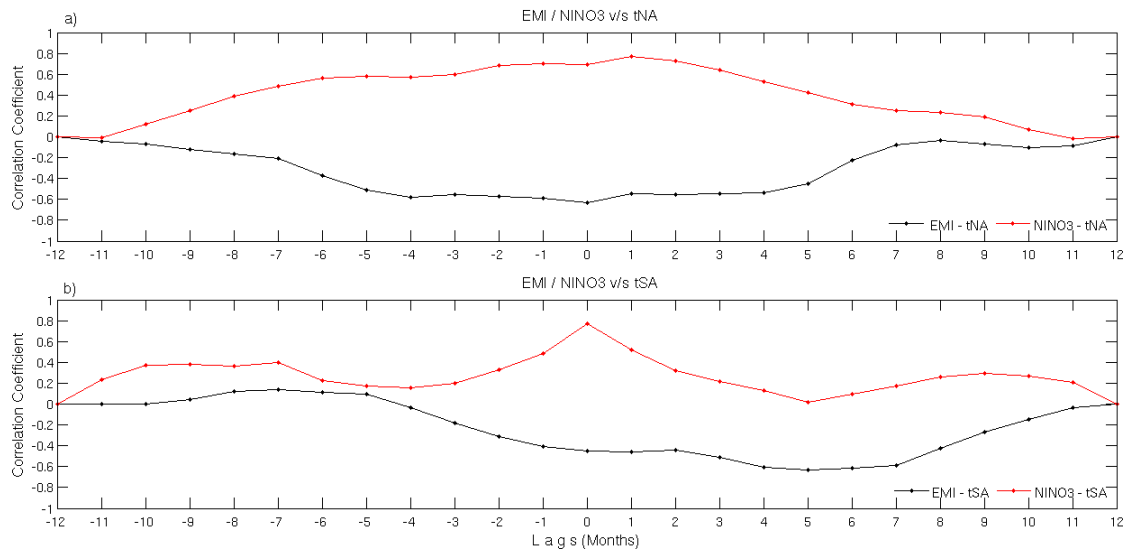


Figure 4.18: (a) Cross correlation between the EMI and tNA (black) and the NINO3 and tNA indices (red). (b) Cross correlation between the EMI and tSA (black) and the NINO3 and tSA indices (red). The analysis is undertaken during El Niño and El Niño Modoki years only according to the Table 3.1.

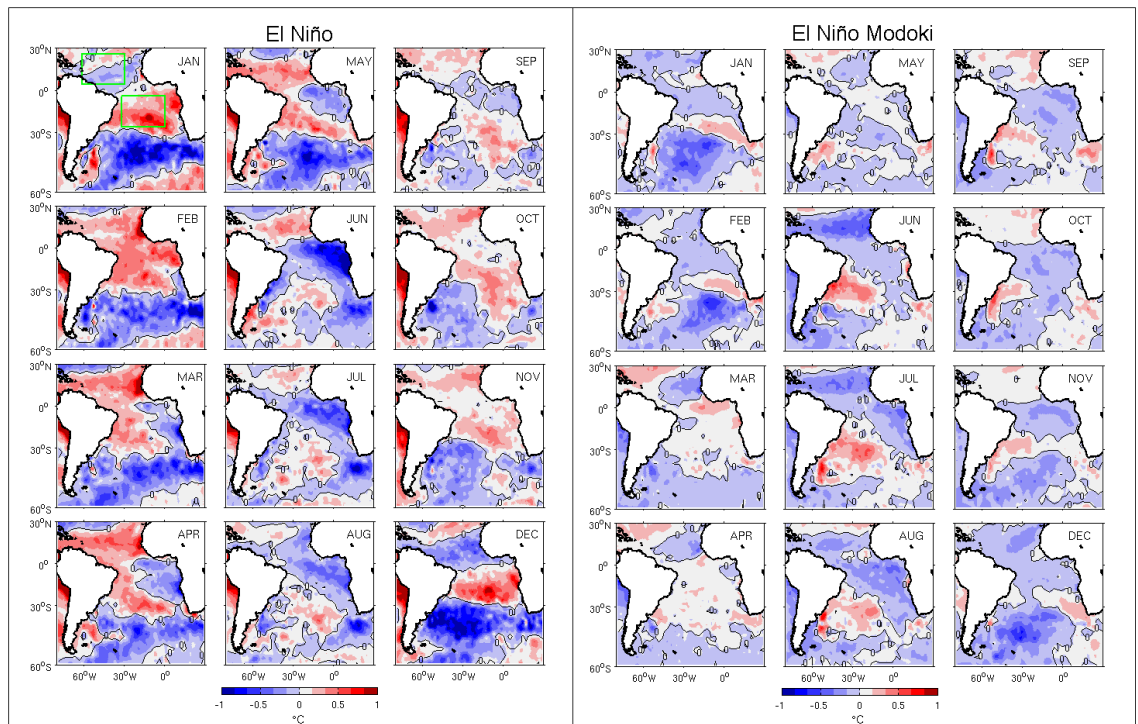


Figure 4.19: Composite of the monthly evolution of the Atlantic SST anomalies during (left) El Niño and (right) El Niño Modoki. Months are indicated in the upper right corner of each box. The monthly evolution is determined according to the Table 3.1. Solid green rectangles (left panel of January) indicate the tNA (5°N-25°N, 60°W-30°W) and tSA (25°S-5°S, 30°W-0°E) regions respectively as described by Giannini et al. (2004). Black line represents zero contour SST anomalies.

4.8 South American rainfall variability and its remote connections with SST anomalies

Figure 4.20 shows a correlation coefficient map associated with the rainfall PC1 (upper panel), PC2 (lower panel) time series and monthly SST anomalies during the summer period. The correlations between the rainfall PC1 time series with the SST anomalies during the summer period show the expected connection of the South American rainfall with the canonical El Niño events, in agreement with previous studies (Zhou and Lau, 2001; Grimm and Zilli, 2009; Grimm, 2010). In the extratropical South Pacific Ocean, positive correlations are also highlighted with a similar magnitude compared to those over the equatorial Pacific. Other positives correlated regions include the Indian Ocean and a zonal band over the Atlantic Ocean linking the tropical South America with the south-western side of the African continent, whereas over the subtropical Pacific and Atlantic oceans the correlations are negative.

The time series associated with the second coupled mode of rainfall variability is weakly correlated with an El Niño Modoki-like anomalous SST pattern (Fig. 4.20, lower panel). Grimm and Zilli (2009) have reported a weak or no connection between this rainfall mode and the equatorial Pacific remote forcing. Further, the weak signal in the equatorial Pacific Ocean and our second coupled mode of rainfall and SST variability (Fig. 4.7) suggest that this rainfall mode may be a result of different forcings. Namely a weak remote forcing from the central Pacific and the extratropical region combined with local forcing from the tropical Atlantic Ocean. Additionally, there is evidence of an alternating signal of negative and positive correlations spanning from the Eastern Australia to Southern South America via the extratropics. These anomalies are in agreement with our reported features of lower and upper level circulation anomalies. Furthermore, the second rainfall mode is positively (negatively) correlated with the SST anomalies located over the tNA (tSA) region. The negative correlation located off tropical Brazil may represent a negative feedback between the atmosphere and the local SST anomalies over this region as a consequence of strong convection activity of the SACZ. The negative correlated area associated with the SPCZ region, namely 33°S-120°W, further supports the teleconnection link between the SACZ and the SPCZ region. The latter features strong anomalous convection activity and thus positive rainfall anomalies during El Niño Modoki conditions (Ashok et al., 2007; Weng et al., 2009). Moreover, Figures 4.3b,d clearly depict significant observed and modelled positive rainfall anomalies associated with enhanced convection activity in the SPCZ region during El Niño Modoki events. Teleconnection links between the SPCZ and the

SACZ have been previously reported (Lau and Chan, 1983; Kalnay et al., 1986; Grimm and Silva Diaz, 1995; Paegle and Mo, 1997). Even though the PC2 time series is weakly correlated with an El Niño Modoki like pattern over the equatorial Pacific, it seems to be more correlated with the extratropical dynamics associated with El Niño Modoki conditions, namely the SPCZ and upper level wave train-like propagations.

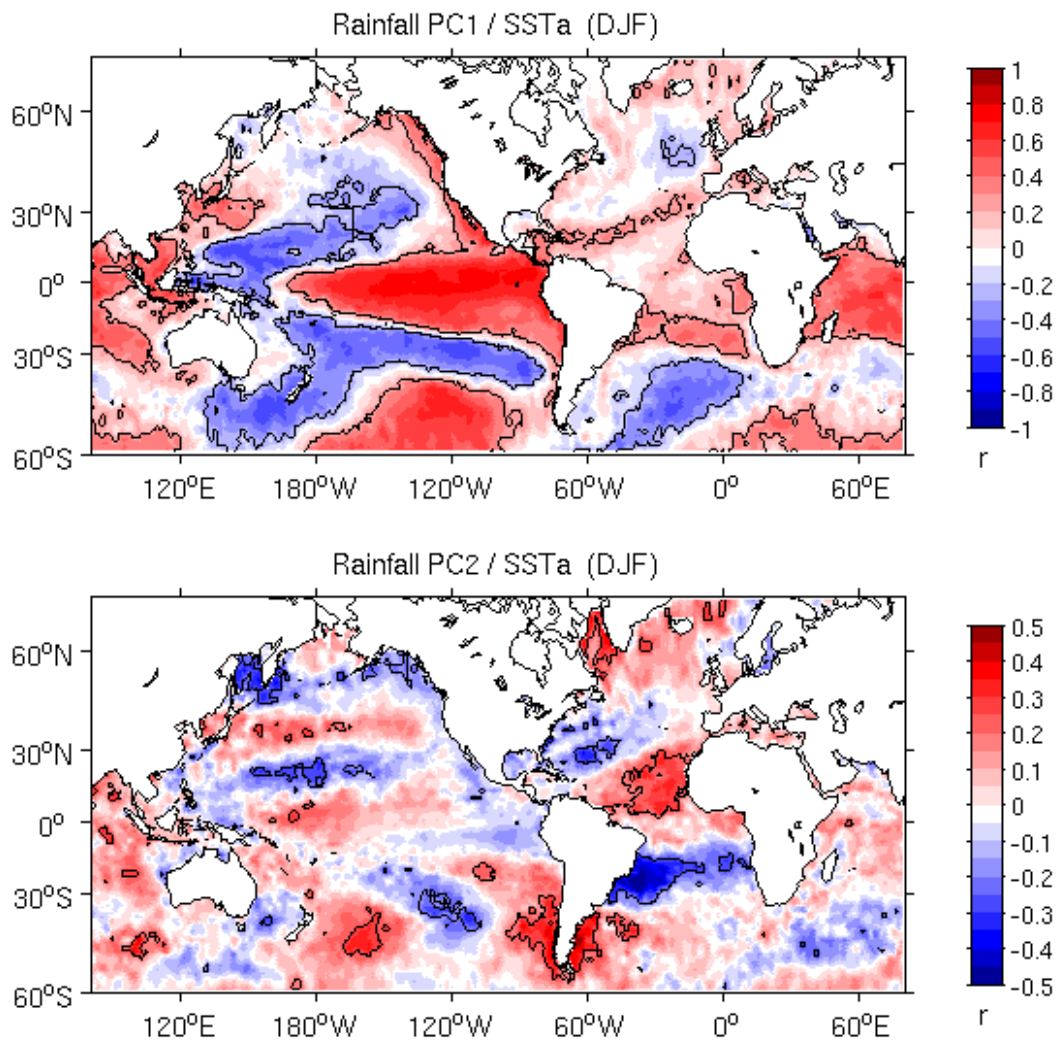


Figure 4.20: Correlation between the expansion coefficient time series of the first (upper panel) and second (lower panel) rainfall modes of variability, PC1 and PC2 respectively, with the monthly SST anomalies during the austral summer period. The black contours encompass areas where the correlations are statistically significant at the 90% confidence level.

4.9 Summary and discussion

In this chapter we compared the impacts of El Niño and El Niño Modoki in the South American rainfall variability during the austral summer period. In order to identify inter-El Niño variations, we used the NINO3 and the EMI indices to select the corresponding events from observations according to a 0.7 standard deviation threshold as a selection criterion. In addition, we identified statistical modes of co-variability between the tropical Pacific and Atlantic SST and South American rainfall anomalies. By using composite and regression analyses we compared their associated atmospheric fields with composites of AGCM perturbation experiments. To undertake these experiments, we prescribed monthly SST conditions during El Niño and El Niño Modoki over the equatorial Pacific and the tropical-to-extratropical Atlantic Ocean, whereas climatological SST was applied elsewhere. This study is based on the period 1979 to 2008, which spans a warm Pacific Decadal Oscillation (PDO) phase.

The main findings are summarized as follows:

During the summer period, the impacts on interannual rainfall variability of El Niño (El Niño Modoki) conditions are described by the first (second) mode of coupled variability between tropical Pacific SST and South American rainfall anomalies. In particular, the first (second) mode depicts negative (positive) loading over the tropics, whereas positive (negative) anomalies predominate over the subtropics. The SVD analysis undertaken with the Pacific and Atlantic SST anomalies provides statistical evidence that the second coupled mode may also represent an interaction between local (Atlantic Ocean) and remote (Pacific Ocean) forcings with the South American rainfall variability. The remote connection is also associated with convection activity in the SPCZ region in agreement with previous studies.

The observed changes in rainfall anomalies over equatorial South America between both interannual events are fully explained by contrasting changes in the vertical circulation associated with the descending branch of the Walker circulation cell over the continent. In the tropics during El Niño events, there is an anomalously strong SALLJ which is associated with an enhanced (a weakened) moisture advection toward the SESA (SACZ) region, setting favourable (unfavourable) conditions for anomalous precipitation there. However during El Niño Modoki events, the SALLJ seems to be shifted toward central eastern Brazil, where an anomalous low pressure area exists (associated with the SACZ), producing a cyclonic vortex that redirects the associated moisture advection toward the SACZ region leading to negative anomalies over SESA.

Contrasting differences are also noted in the anomalous upper level circulation pattern between both interannual events. During El Niño (El Niño Modoki) conditions the pair of anomalous anticyclones (anticyclones and cyclones) straddling the equator fully represents the anomalous single (double) convective cell associated to the Walker circulation. Over the continent an anomalous cyclonic pattern is observed and associated with a weakened and shifted northward Bolivian High during El Niño events, whereas a large scale anticyclonic anomaly linked to the SACZ is evident during El Niño Modoki conditions. This represents the upper level manifestation of intense local convection activity over this area.

Extratropical-to-subtropical teleconnection patterns associated with the South American rainfall seem to be quite different between both interannual events. During El Niño conditions the upper level anticyclone over the subtropics does not reinforce the SALLJ, whereas during El Niño Modoki events this anomaly is shifted southward as part of a basin-wide wave-like propagation from the eastern Australian region. The AGCM perturbation experiments further support the importance of the extratropical circulation during El Niño Modoki compared to Niño conditions during the summer period as suggested by observations.

The AGCM experiments capture the correct sign of anomalous precipitation over the equatorial South American and SESA regions according to either El Niño or El Niño Modoki anomalous forcings. However the area associated with the SACZ region, just shows an increased anomalous rainfall in the perturbation experiment associated with El Niño Modoki compared to El Niño experiment, suggesting some degree of sensitivity to a shift in the remote forcing location.

During El Niño conditions, the strength of the anomalous rainfall over the SESA region can be modulated by the anomalous SST conditions of the oceanic portion of the SACZ in tropical South Atlantic Ocean. Additionally, the AGCM experiment for El Niño conditions suggests that most of the associated moisture is advected onshore leading to a decrease (increase) of the positive rainfall anomalies over the SESA (SACZ) region. Further, the Atlantic SST conditions seem to also modify the strength of the negative rainfall anomalies over the equatorial portion of the continent by changes in the strength of the anomalous descending branch associated with the anomalous Walker circulation cell. In particular, the AGCM perturbation experiments undertaken for El Niño Modoki (El Niño) conditions suggest a weakening (strengthening) in the anomalous rainfall magnitude over the northern portion of the continent as a consequence of the Atlantic SST anomalies.

One of the key differences in the interannual rainfall variability between El Niño and El Niño Modoki events during the austral summer period is found over the region associated with the SACZ. As already stated, our second mode associated with the South American rainfall variability has been linked to weak or no remote forcing by Grimm and Zilli (2009). However via an SVD analysis we suggest that El Niño Modoki represents a coupled oscillatory mode with South American rainfall, and that the tropical Atlantic SST anomalies can even make a contribution to the coupling strength between these fields. Furthermore, the perturbation experiments show an increase in the anomalous rainfall over the SACZ during El Niño Modoki compared to El Niño conditions, therefore suggesting some degree of sensitivity of the SACZ to a remote anomalous warming location. This fact has also been shown in idealized sensitivity experiment by Hill et al. (2011). In particular, they show an increased monsoon activity and therefore positive rainfall anomalies over the region associated with the SACZ when an idealized forcing is applied over either the western or central-to-western Pacific Ocean. In our results, the observed weak and westward-shifted descending branch associated with the anomalous Walker circulation over equatorial South America during El Niño Modoki may lead to locally favourable conditions for anomalous precipitation over the SACZ region. A supporting example of local processes can be the soil moisture anomalies. They are able to alter the surface temperature and hence modify the surface pressure, circulation and rainfall anomalies over the SACZ during the summer season (Grimm, 2003b; Grimm and Zilli, 2009). In particular, Grimm et al. (2007) provide evidence of a surface-atmosphere feedback, in which the precipitation anomalies associated with the previous season, i.e. spring, may set up either favorable or unfavorable environmental conditions leading to a positive or negative rainfall anomalies peaking during the next season, i.e. summer. They state that high (low) spring precipitation leads to high (low) soil moisture anomalies inducing low (high) late spring surface temperature and consequently the high (low) surface pressure that is associated with low level moisture divergence (convergence) via an anticyclonic (cyclonic) circulation pattern that redirects moisture toward the SESA (central eastern Brazil) region. In our observational results, this cyclonic anomaly is in agreement with the anomalous pattern over this area during El Niño Modoki conditions (See Fig. 4.10b). This land-atmosphere feedback is hypothesized to be induced by the local topography and to be also valid during non-ENSO years (Grimm et al., 2007).

In regard to the teleconnection patterns, during El Niño Modoki the upper level circulation provides evidence of a distinct remote forcing compared to canonical El Niño events. In particular an anomalous quadrupole pattern straddling the equator,

represented by the upper level asymmetric streamfunction anomalies, is evident during El Niño Modoki conditions, which is also well represented by their corresponding AGCM perturbation experiments. Additionally, a wave-train-like propagation linking the Eastern Australia and the southern tip of South America via the extratropics is also evident in observations during El Niño Modoki, and of particular importance the teleconnection link established under this condition between the SPCZ and the SACZ regions. Vera et al. (2004) reported an enhanced wave-flux activity associated with a strong anomalous convection in the SPCZ region during some El Niño years, this region was found to act as a secondary Rossby wave source reinforcing the extratropical circulation in upper levels and then affecting the subtropical regions of the continent. The effect of the observed anomalous low level wind convergence over the central equatorial Pacific seems to favour the enhanced convection activity in the SPCZ during the austral summer period of El Niño Modoki years as reported by Weng (2009), whereas its upper level manifestation occurs as an anticyclonic anomaly and enhanced upper level divergence as seen in the observations and the corresponding perturbation experiments respectively. These upper level features are then associated with our second mode of rainfall, however, only the extratropical teleconnection is reported by Grimm and Zilli (2009) but also recognizing a weak or null ENSO link. One of the likely reasons may lie in the different period of analysis. Their (our) study span the period of 1961-2000 (1979-2008), which covers a cold-to-warm (warm) phase of the PDO (Mantua et al., 1997). According to Kayano and Andreoli (2007), the PDO may provide the background conditions to enhance (weaken) the ENSO teleconnection-related effects and therefore rainfall anomalies over South America when both phenomena are in the same (opposite) phases. Moreover, Andreoli and Kayano (2005) suggest that the El Niño signal in South American rainfall variability is more (less) evident during warm (cold) PDO regime. Thus, the fact of covering two difference phases of the long frequency PDO variability in the study of Grimm and Zilli (2009) may had led them to underestimate the teleconnection effects associated with El Niño Modoki. This represents one of the advantages of this study, as our approach considers the same PDO phase leading us to avoid unnecessary complexity in order to evaluate the different impacts between El Niño and El Niño Modoki.

The observed changes in interannual rainfall variability over the SESA region are supported by the observed changes in low level circulation between both interannual events (Silvestri, 2004). During El Niño events it was found that a strong meridional flow enhances the moisture transport toward the SESA region, this moisture supply represents a limiting factor for precipitation in this area (Doyle and Barros, 2002).

However during El Niño Modoki, the occurrence of a strong cyclonic circulation pattern over central eastern Brazil acts to redirect the SALLJ northeastward therefore shifting the moisture advection toward the SACZ region and consequently reducing the moisture availability over the SESA region. In particular, the study case of Silva and Ambrizzi (2006) also provides supporting evidence of contrasting circulation regimes between El Niño events of 1997-1998 and 2002-2003. The observed shift in the SALLJ during El Niño event of 2002-2003, i.e. an El Niño Modoki event, toward Southeast Brazil (climatological position of the SACZ) contrasts with the typically strong SALLJ toward the SESA region observed during El Niño event of 1997-1998. This fact was also confirmed by AGCM perturbation experiments by Hill et al. (2009), they reported a SALLJ shift during El Niño of 2002-2003 (1997-1998) leading to a moisture convergence and positive rainfall anomalies over the southeast Brazil (SESA) region. Furthermore, Drumond and Ambrizzi (2003) studied the events of 1982-1983, 1986-1987, 1991-1992, and 1997-1998 further supporting the large inter-event variability in the rainfall signal over the SESA and southeastern Brazil areas. Interannual rainfall variability over the SESA region also has been associated with an upper level forcing. During El Niño events, an upper level cyclonic center is located over the tropics (i.e. the weakened Bolivian High system) accompanied with an anticyclonic vortex around the SESA area. The overall effect is known to reinforce the SALLJ and its associated moisture transport toward the SESA (Mendes da Silva and Ambrizzi, 2009). In addition, Silvestri (2004) states that only the strong El Niño events present upper level wave train propagation toward the southern latitudes strengthening the upper level Subtropical Jet. However, in our analyses this anomaly is weak and does not seem to enhance the SALLJ as no barotropic circulation was found over this area. This suggests that positive rainfall anomalies over the SESA region are due to the anomalously strong SALLJ, and that the proposed upper level reinforcing mechanism is not present during El Niño conditions according to our inter El Niño classification. Slightly different analyzed period (Silvestri, 2004) and the different approach to classifying the interannual events (Silva et al., 2009) may account for the observed differences compared to our results. During El Niño Modoki events, the upper level anticyclone located over this region during El Niño events is shifted toward the extratropics instead, and consequently is not favourable for an enhanced SALLJ. Thus our results tend to partially differ from the literature when using a strict inter El Niño classification criterion within the same PDO phase. In the last Chapter of this thesis we focus on the upper level circulation during the spring period, it will be shown that the occurrence of an anticyclonic anomaly over the SESA region is a feature of El Niño

Modoki instead which tends to peak by the early summer period. This fact in conjunction with a different classification criterion may have led previous studies to provide a different description of the anomalous upper level circulation over this region during El Niño conditions. Namely, to report an upper level reinforcement of the anomalous SALLJ via an anticyclonic anomaly located over the SESA region. Furthermore, in the sensitivity experiments undertaken by Hill et al. (2011) no anomalous upper level anticyclone is modelled over the subtropics when an idealized forcing is applied over the equatorial eastern Pacific. However, according to this study the interaction between the anomalous circulation in the upper and lower levels over the subtropics just occurs when an anomalous warming is superimposed over the central-to-eastern equatorial Pacific, partially resembling in Modoki-like anomalous forcing.

Barreiro and Tippmann (2008), tested a likely Atlantic modulation of the rainfall variability over the SESA region during the summertime of El Niño conditions. They suggest that when the anomalous SST conditions over equatorial Atlantic are cool or normal (warm) during El Niño events, there are equatorial easterlies (westerlies) winds over the Atlantic Ocean leading to strong (weak) southward moisture transport over the continent and consequently strong (weak) positive rainfall anomalies over the SESA region. However, our AGCM experiment results suggest that the anomalous SST conditions in the SACZ region may also modulate the amount of rainfall over SESA during El Niño conditions. In particular, we show weak (strong) anomalous rainfall over the SESA (oceanic portion of the SACZ) region in the EN-PA perturbation experiment. This means that an important part of the moisture is being redirected to the SACZ region instead and thus reducing the associated moisture availability over the SESA region when prescribing anomalous SST over the Atlantic in El Niño experiments. Furthermore, Barreiro and Tippmann (2008) classified El Niño years according to the sign of the ZI Index (i.e. a mean of the zonal 850 mb winds over the 60°W-20°W, 5°S-5°N region). When $ZI > 0$ ($Z < 0$), there are anomalous westerlies (easterlies) over the western equatorial Atlantic Ocean. As a consequence they presented a mixed classification of El Niño events and in fact their composites of SST anomalies do not show evidence of an anomalous warming around the oceanic SACZ region. This contrasting finding suggests the importance of both the SST anomalies over the equatorial Atlantic Ocean and the off region of the SACZ in the modulation of the interannual rainfall over the SESA region during El Niño events. Finally it is worth mentioning that our observation suggests that the ZI Index should only be used during canonical El Niño events as a proxy of moisture supply and associated rainfall

anomalies over the SESA region. The supporting reason is the occurrence of a cyclonic anomaly located over the central eastern Brazil during the summer period of El Niño Modoki acting to redirect the SALLJ and weakening the associated moisture advection that usually reaches to the SESA region during canonical events. As the ZI index just describes the zonal wind over the western equatorial Atlantic sector, it may give a false sense of strong moisture advection toward the SESA region even during El Niño Modoki conditions.

Chapter 5

Changes in the Walker circulation cell between El Niño and El Niño Modoki events and implications for South American rainfall during autumn

In this chapter we explore the contrasting features of the Walker circulation cell during the austral autumn period, and its potential implications for the seasonal migration of the Atlantic ITCZ. It is important to mention that although the austral autumn period represents one of the rainy seasons in tropical South America, there are virtually no studies about inter El Niño variations and their impacts over the continent for this season. Thus results presented here may represent an important contribution in this regard.

5.1 Anomalous SST conditions

Figure 5.1 depicts a composite of anomalous SST during El Niño and El Niño Modoki conditions. In particular, during El Niño conditions the overall spatial distribution of the anomalous SST field over the Pacific Ocean remains essentially the same compared to the austral summer period except for the location of the maximum SST anomalies. They are mostly focused in the equatorial coast of South America compared with the corresponding summer period (Figs. 4.1a,5.1a), whereas over the central equatorial Pacific region they do not exceed the 2°C (Philander, 1990; Elliot et al., 2001). A weaker, but also contrasting, anomalous SST field is observed during El Niño Modoki conditions (Fig. 5.1b). The warm SST anomalies are mostly centered over the central-to-western Pacific region, spanning the subtropics of both hemispheres. This warm anomaly is flanked by negative SST anomalies at both western and especially eastern Pacific regions. It will be shown that the autumn season is the period which mostly contributes to the anomalous SST gradient along the equator during El Niño Modoki events.

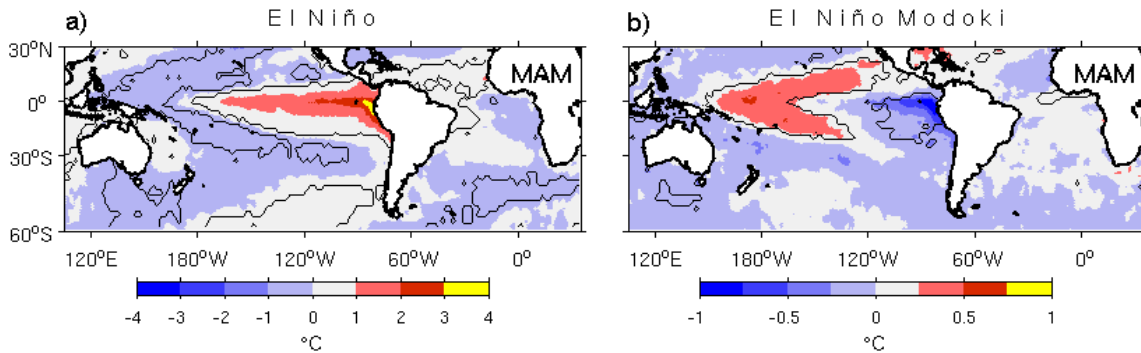


Figure 5.1: Composite of the SST anomalies during the austral autumn for (a) El Niño and (b) El Niño Modoki conditions (See Table 3.1). The SST data is from the HadISST1 dataset as described by Rayner et al. (2003). The SST anomalies are a departure of the monthly climatology based on the period from January 1979 through July 2008. Black contours represent statistically significant regions at the 90% confidence level according to a two-tailed Student t-test.

As already stated in Chapter 4 (section 4.7), the most outstanding difference in the anomalous SST field over the Atlantic Ocean between El Niño and El Niño Modoki events seems to occur over the tNA region, namely tropical North Atlantic (Fig. 5.2). The tNA is anomalously warm (cold) during El Niño (El Niño Modoki). This anomalous warming occurring during El Niño conditions is well known (Curtis and Hasternrath, 1995; Enfiled and Mayer, 1997; Giannini et al., 2004) as well as the suggested mechanism by which it develops, i.e. the atmospheric bridge (Alexander et al., 2002). This comprises of changes in the Walker circulation cell over the equatorial Pacific, whose net effect is to weaken the northeast trade wind in the tropical North Atlantic region by reducing the climatological downward motion over the subtropical high pressure system in the tropical North Atlantic region. As a consequence the corresponding reduction in the wind velocity and therefore in the associated evaporation rates lead to an anomalous warming over this area. This feature contrasts with the cool-to-normal conditions over the tNA region during El Niño Modoki, a priori suggesting that the atmospheric bridge mechanism is not operating.

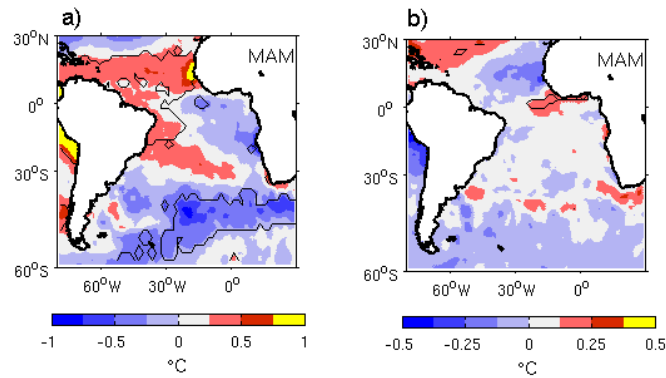


Figure 5.2: As in Fig. 5.1, but for the Atlantic Ocean only. (a) El Niño, and (b) El Niño Modoki conditions. Black contours represent statistically significant regions at the 90% confidence level according to a two-tailed Student t-test.

The following sections examine the observed atmospheric conditions during El Niño and El Niño Modoki events and the simulated response to the Pacific and Atlantic SST anomalies during these episodes.

5.2 Rainfall composites

5.2.1 Large scale features

Figure 5.3 shows the observed and simulated anomalous rainfall composites during El Niño and El Niño Modoki conditions. In response to the contrasting anomalous SST distribution between both interannual events, the observed large scale anomalous rainfall features show the expected anomalous distribution. During El Niño an anomalous positive rainfall band dominates over the equatorial Pacific, whereas negative rainfall anomalies are found over the subtropical latitudes of the Northern and Southern Hemispheres (Fig. 5.3a). Negative rainfall anomalies are also seen over the tropical Atlantic Ocean, representing the anomalously weak convection activity in the Atlantic ITCZ during austral autumn season (Ropelewski and Halpert, 1987; 1989; Philander, 1990; Chang et al., 2000; Chiang et al., 2002; Giannini et al., 2004). The negative rainfall anomalies over the northern portion of the South American continent are associated with the combined impacts of the descending branch of the Walker circulation cell over this region (Wang, 2002b) and the shifted Atlantic ITCZ. Observations also reveal an anomalously weakened SPCZ and positive rainfall anomalies over the SESA region. The experiment undertaken for El Niño conditions with prescribed SST anomalies over the Pacific Ocean only (Fig. 5.3c), namely EN-P, clearly simulates the observed large scale features. However some noteworthy differences are detected. For example the positive anomalous rainfall band over the

equatorial Pacific seems to be segmented in two regions, one in the eastern and one in the central Pacific. In particular, the positive rainfall anomalies over the eastern Pacific are clearly overestimated compared with observations. The negative anomalies associated to the SPCZ are more zonally orientated compared to observation.

A distinct response is observed during El Niño Modoki years. Over the equatorial Pacific there are negative rainfall anomalies prevailing from the central to the eastern Pacific, representing an anomalously weak ITCZ contrasting with canonical El Niño events (Figs. 5.3a,b). The positive rainfall anomalies over the central-to-western Pacific indicate a shift of the ITCZ, whereas over the subtropics in the Southern Hemisphere they are associated with anomalous convection activity in the SPCZ region. Although the anomaly magnitude is weak, it suggests an anomalously strong (weak) SPCZ during El Niño Modoki (El Niño) events. The corresponding perturbation experiment of El Niño Modoki conditions (Fig. 5.3d), i.e. ENM-P, displays the major anomalous rainfall features over the equatorial Pacific, although the overall anomalous rainfall pattern is especially overestimated over western Pacific and Indonesian regions. In particular the simulated anomalous SPCZ tends to clearly persists from the tropics toward the extratropical coast of South America in El Niño Modoki experiment, whereas it is anomalously weak in El Niño experiment in agreement with the observed conditions. El Niño Modoki experiment also reveals a southward shift of the Atlantic ITCZ, which is not clear from observation (Figs. 5.3b,d). A detailed description of the anomalous rainfall conditions over the continent and tropical Atlantic regions is provided in the next section.

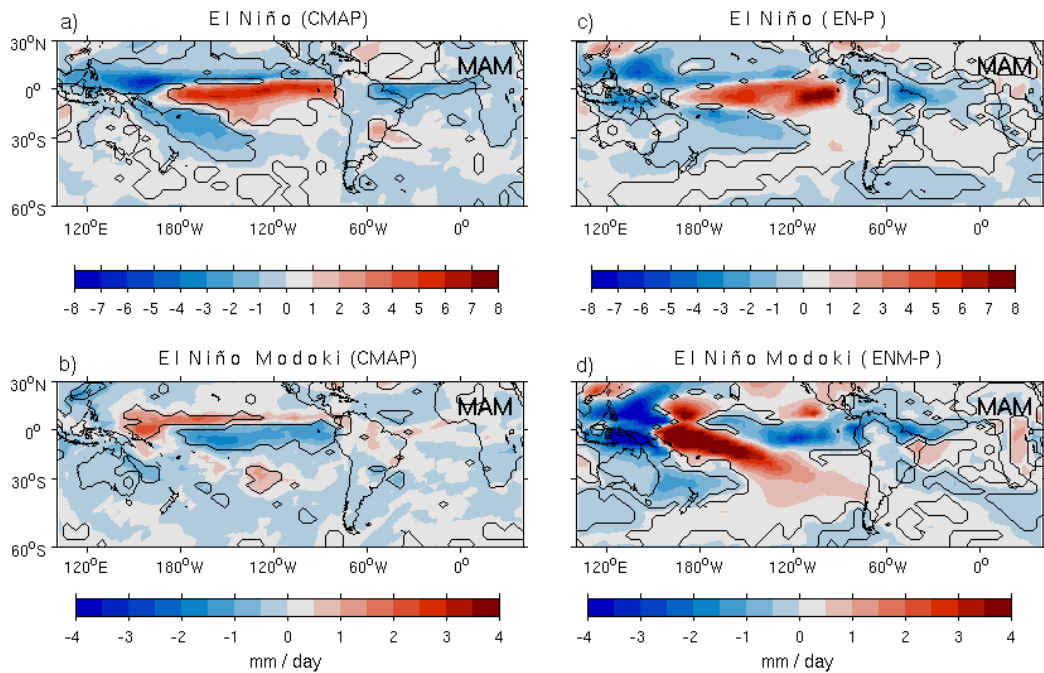


Figure 5.3: Composites of the observed rainfall anomalies (CMAP) during (a) El Niño, and (b) El Niño Modoki conditions (See Table 3.1), (c) modelled rainfall anomalies for El Niño (EN-P), and (d) El Niño Modoki (ENM-P) perturbation experiments. The forcing was applied over the Pacific Ocean only. Black contours represent statistically significant regions at the 90% confidence level according to a two-tailed Student t-test.

5.2.2 South American rainfall anomalies

A clearer view of the different impacts between El Niño and El Niño Modoki events over the continent is given by the anomalous rainfall composites in the Figure 5.4. During the autumn period of El Niño events, the anomalous rainfall signal over the continent features of a dipole-like pattern, thus resembling to the corresponding anomalous rainfall pattern of the summer period (Figs. 4.4a,5.4a). In particular, this dipole consists of positive rainfall anomalies over the SESA region and negative rainfall anomalies over the northern portion of the continent. In addition, positive rainfall anomalies are also seen over the equatorial Pacific coast of the continent (Fig. 5.4a) in response to the proximity of an anomalous coastal warming which is directly associated with a strong convection activity over this region. The occurrence of negative rainfall anomalies over the northern region is known to be a consequence of a weakened Atlantic ITCZ in response to the descending branch of the anomalous Walker circulation cell, which is driven by strong anomalous convection activity at the eastern Pacific during El Niño events (Wang, 2002c). The corresponding experiments, i.e. EN-P and EN-PA, show negative and positive rainfall anomalies over the northeastern and subtropical portion of the continent respectively. The large scale convective rainfall

band at the equatorial Pacific is shifted westward compared to observations (Figs. 5.4a,c,e). If we retain the anomalous Atlantic effects by removing the remote forcing associated with El Niño, i.e. EN-PA minus EN-P, we can detect an anomalous negative rainfall band over the equatorial Atlantic flanked by two anomalous positive rainfall bands located over its northern and southern boundary. This negative band is a consequence of stronger subsidence over the Atlantic ITCZ in the EN-PA experiment, i.e. when the Atlantic SST anomalies are considered in the simulation. The positive rainfall difference indicates more positive rainfall anomalies over the tNA region, and the oceanic portion associated with the SACZ region respectively. In particular, the latter anomaly is also associated with the anomalous rainfall dipole found during the summer period (Fig. 4.4g), indicating some degree of seasonal persistence. The rainfall anomalies over the SESA are weaker in the EN-PA experiment. Thus the observed and prescribed Atlantic SST conditions during the austral autumn period seem to reinforce (weaken) subsidence over the Atlantic ITCZ (the rainfall anomalies over the SESA region).

The anomalous rainfall signal associated with El Niño Modoki conditions (Fig. 5.4b) depicts negative anomalies over the equatorial Pacific coast and the SESA regions, whereas positive anomalies are found over the tropical portion of the continent and also over the tropical Atlantic Ocean. The positive rainfall anomalies over northern South America and the equatorial Atlantic seem to be associated with the southward migration of the ITCZ, contrasting with the observed anomalous conditions during El Niño events. The corresponding perturbation experiments (Figs. 5.4d,f), i.e. ENM-P and ENM-PA, show weak negative anomalies slightly northward from the SESA region, and also over most of the northern coast of the continent compared to the perturbation experiments undertaken for El Niño conditions. Therefore the ENM-P and ENM-PA experiments do not reproduce the positive rainfall anomalies over the continent associated with the Atlantic ITCZ as seen in observations (Figs. 5.4b,d,f).

The effects of the Atlantic SST anomalies during El Niño Modoki conditions are shown in Figure 5.4h. This figure further highlights the positive rainfall anomalies over the inner part of the continent, i.e. central eastern Brazil and part of northern South America, and over the tropical Atlantic associated with the ITCZ. These regions are mostly negative in the experiments representing El Niño conditions (Figs. 5.4c,e). It is worth mentioning that the difference between ENM-PA and ENM-P (Fig. 5.4h) displays a ITCZ shifted southward compared to observations (Fig. 5.4b), in agreement with the reported bias about the Atlantic ITCZ location (See section 2.5.1). In the ENM-PA

experiment, the negative anomalies associated with the SESA region tend to be northward shifted compared to observations (Figs. 5.4f,b).

The Figures 5.4i,j show the difference between El Niño Modoki and El Niño experiments, i.e. ENM-P minus EN-P and ENM-PA minus EN-PA, respectively. The regions of major differences are seen over the eastern equatorial Pacific (negative rainfall anomalies in the ENM-P experiment), the SESA region (stronger positive rainfall anomalies in the EN-P experiment), and the region associated with the Atlantic ITCZ influence (stronger negative rainfall anomalies in the EN-P experiment). In particular, the positive difference associated with the Atlantic ITCZ region clearly indicates less anomalous rainfall in the ENM-P compared to the EN-P experiment as a response of the shift in the remote anomalous warming location. This suggests a different behaviour of the Atlantic ITCZ between El Niño and El Niño Modoki conditions. The corresponding relationships of the experiments forced with Atlantic SST anomalies remain essentially the same except for some slight local difference in the magnitude and the negative band over the tNA.

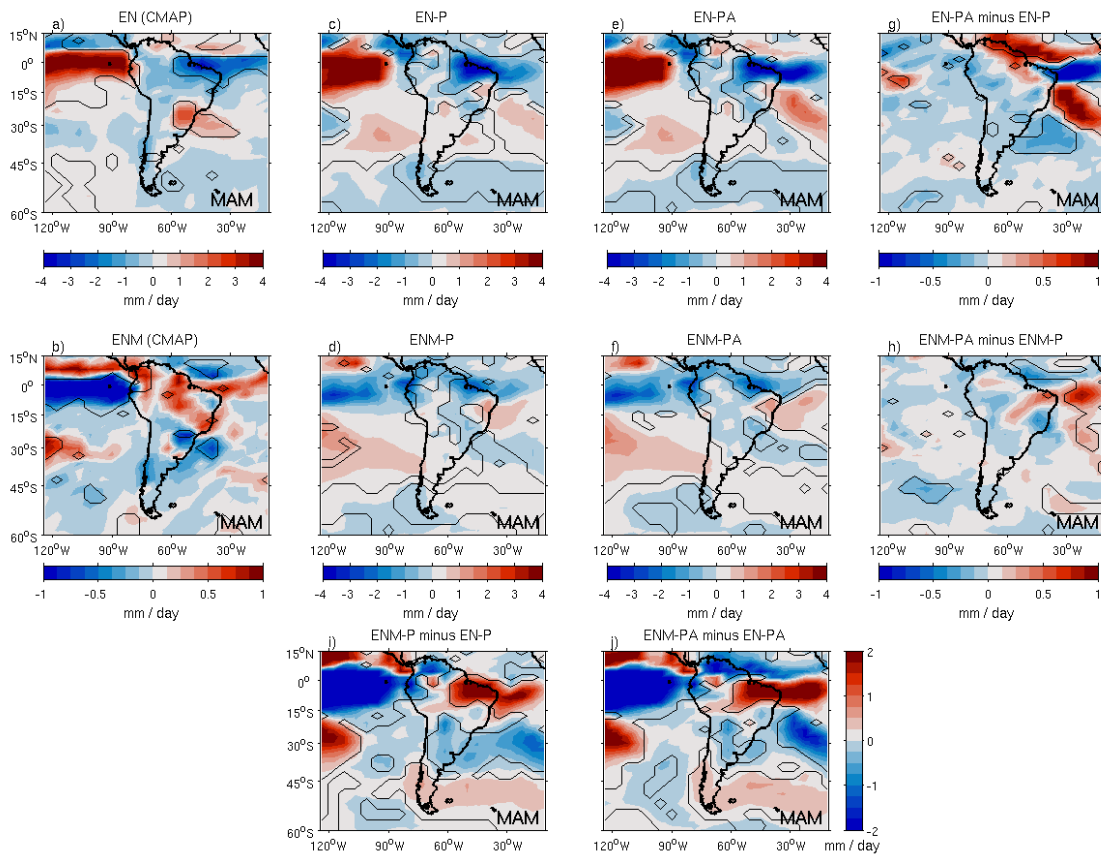


Figure 5.4: Observed rainfall anomalies for (a) El Niño, (b) El Niño Modoki. Modelled rainfall anomalies for (c) El Niño (EN-P), (d) El Niño Modoki (ENM-P), and including the perturbation experiments forced with SST anomalies over the Atlantic Oceans according to (e) EN-PA, (f) ENM-PA, and including the difference between (g) EN-PA minus EN-P, (h) ENM-PA minus ENM-P, (i) ENM-P minus EN-P and (j) ENM-PA minus EN-PA perturbation experiments. Black contours represent statistically significant regions at the 90% confidence level according to a two-tailed Student t-test.

5.3 Assessing coupled modes of SST and rainfall variability

As in the previous Chapter, we obtain the statistical modes of co-variability between the anomalous SST and South American rainfall. The reported impacts of El Niño conditions in the rainfall variability are represented by the leading coupled mode (Fig. 5.5), particularly the positive and negative loading over the SESA and Central Eastern South America respectively. As in the composites, the SST mode also supports the strong anomalous warming over the equatorial coast of the continent. This coupled oscillatory mode is responsible for the 31% of the squared covariance fraction. It shows a strong coupling between its associated fields with a correlation coefficient between the SST and rainfall expansion coefficient time series of 0.7. The correlation between the SST expansion coefficient time series and the NINO3 index is 0.98. The rainfall

mode agrees with the results of Grimm (2010), who performed an EOF analysis of the South American rainfall anomalies for the period of 1961-2000. Additionally, the corresponding correlation analysis between the rainfall expansion coefficient time series and anomalous SST resembles our spatial SST mode essentially showing the same anomalous features. In that case the first mode explains approximately 29% of the total rainfall variance.

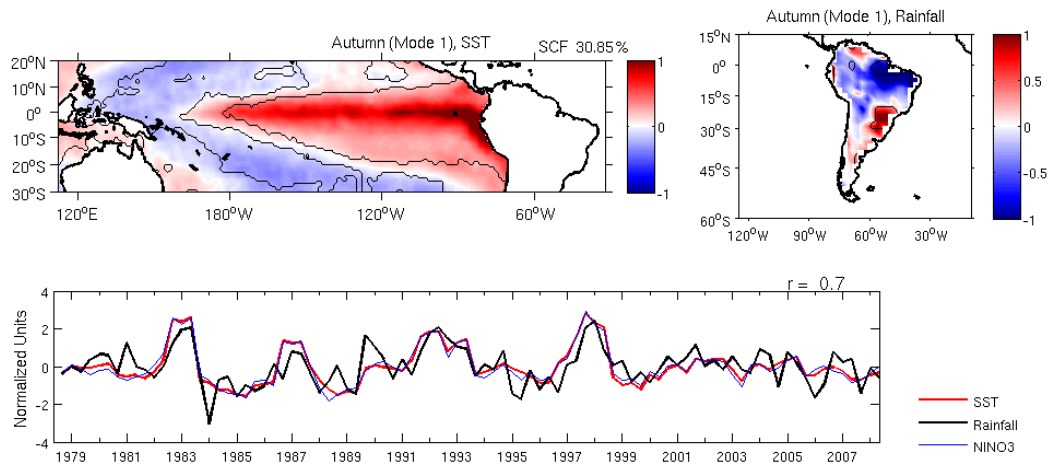


Figure 5.5: The first mode of an SVD analysis between the SST (left) and rainfall anomalies (right) during the austral autumn period. It accounts for $31 \pm (8)$ % of the square covariance fraction (SCF). Black contours indicate statistical significant regions at the 90% confidence level according to a two-tailed Student t-test. Time series of the SVD expansion coefficient (below). Red (black) line is associated with the SST (rainfall) mode. The coupling strength (r) between these fields is 0.7. The thin blue line represents the NINO3 index. The correlation coefficient between the SST mode (red) and the NINO3 index (blue) is 0.98. The correlations are statistically significant at the 95% confidence level.

Figure 5.6 shows the second mode of the SVD analysis between Pacific SST and South American rainfall anomalies. This mode accounts for 9.73% of the squared covariance fraction. The SST spatial mode represents the observed anomalous SST field associated with El Niño Modoki (See Fig. 5.1). The correlation between the SST mode and the EMI index is 0.95. Similarly the rainfall mode features a positive loading over the inner part of northern South America, resembling the corresponding rainfall composite (Fig. 5.4b). The correlation coefficient between the SST and rainfall time series is 0.6, suggesting a possible coupling between these fields. The SST pattern of the second SVD mode for the austral autumn shown here is in agreement with the study of Taschetto and England (2009). The authors undertake a similar analysis between tropical Pacific SST and Australian rainfall anomalies during the 1978-2004 period of the autumn season. In particular their second coupled account for 25% of the square covariance fraction, and their SST mode, which is associated with El Niño Modoki, is in agreement with our SST mode reported here. Comparison of the

anomalous rainfall pattern described here with previous studies is more difficult. There are no available studies with similar analyses for the South American rainfall during the austral autumn.

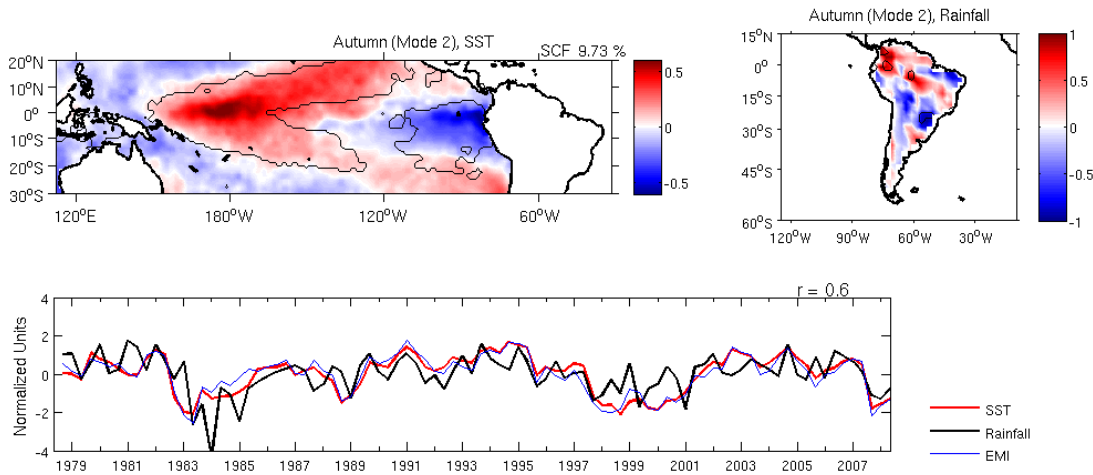


Figure 5.6: The second mode of an SVD analysis between the SST (left) and rainfall anomalies (right) associated with El Niño Modoki conditions during the austral autumn period. It accounts for $9.7 \pm (2.6)$ % of the square covariance fraction (SCF). Black contours indicate statistical significant regions at the 90% confidence level according to a two-tailed Student t-test. Time series of the SVD expansion coefficient (below). Red (black) line is associated with the SST (rainfall) mode. The coupling strength (r) between these fields is 0.6. The thin blue line represents the EMI index. The correlation coefficient between the SST mode (red) and the EMI index (blue) is 0.95. The correlations are statistically significant at the 95% confidence level.

Finally, the first mode is well separated from the second mode of variability according to the separation rule suggested by North et al. (1982). Notwithstanding the standard error of the second mode is comparable to distance between the eigenvalues of second and third modes, as the latter accounts for 6.8% of the square covariance fraction. However we have presented supporting statistical analyses, which suggest that the second mode is a physically coupled oscillation between the SST anomalies associated with El Niño Modoki and the South American rainfall anomalies.

In order to provide additional evidence of the statistical links between these fields, Figure 5.7 shows the correlation coefficient maps between the rainfall time series of the first and second SVD analyses (PC1 and PC2 respectively) and the anomalous SST field during austral autumn period. This further suggests the link of the South American rainfall variability with a remote forcing from the equatorial Pacific associated with El Niño and El Niño Modoki events respectively. In particular, the correlation of PC1 is positively (negatively) correlated with the SST anomalies over the tNA (tSA) region. Positive correlations are also observed over the Indian Ocean basin. The correlation

patterns over the subtropical and extratropical Pacific Ocean resemble those of the corresponding patterns of the summer season (See Fig. 4.20).

Correlations with PC2 suggest a remote connection between the South American rainfall and the Modoki-like pattern in the equatorial Pacific Ocean. The positive correlations are mostly focused over the central-to-western Pacific Ocean encompassed by negative correlations at western and eastern boundaries respectively. Furthermore, negative correlations over the eastern Indian Ocean off Western Australia are apparent. Negative correlations dominate over the tSA region, particularly in the Atlantic coast off Brazil. Another contrasting feature compared to the PC1 correlation with the SST anomalies are the alternating positive and negative correlations as nearly-zonal bands spanning the equatorial Pacific toward the Northern and Southern Hemisphere respectively. A similar feature is also observed over the Atlantic Ocean.

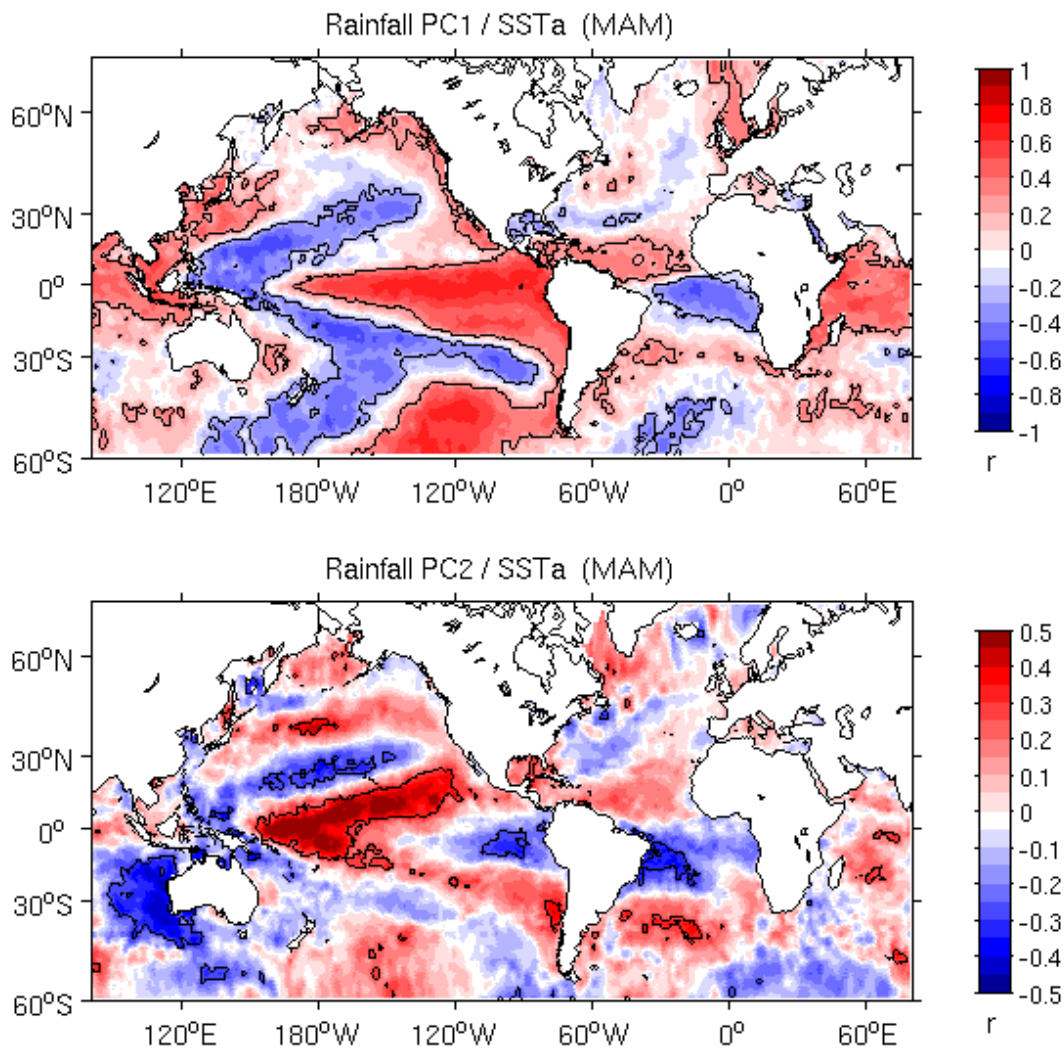


Figure 5.7: Correlation coefficient map between the expansion coefficient time series of the first (upper panel) and second (lower panel) rainfall modes of variability, PC1 and PC2 respectively, with the monthly SST anomalies during the austral autumn period. The black contours encompass areas where the correlations are statistically significant at the 90% confidence level.

5.4 Low-level circulation

5.4.1 Observed conditions during El Niño and El Niño Modoki

Figure 5.8 depicts the observed and simulated anomalous SLP and 850-hPa horizontal wind anomalies during the autumn periods of El Niño and El Niño Modoki conditions. In particular, the main features of the large scale low level circulation of El Niño conditions are similar to those during the summer period (Figs. 4.9a, 5.8a). There are particularly strong westerly wind anomalies in response to the anomalous SLP gradient along the equatorial Pacific. Over the equatorial Atlantic Ocean, strong easterly wind anomalies

predominate converging with the anomalous westerlies from the equatorial Pacific over the eastern coast of South America. Additionally, a cyclonic circulation regime is observed in the subtropical eastern Pacific associated with an anomalous weak high pressure system. An anomalous positive SLP is observed in the South Atlantic region enhancing the subtropical high pressure system during El Niño years. Over the extratropical South Atlantic Ocean, an anomalous anticyclonic and cyclonic circulation patterns are detected. Furthermore, the climatological westerlies are weak over the extratropical Pacific. These findings are in agreement with previous studies (Philander, 1990; Latif and Keenlyside, 2009; Sarachik and Cane, 2010).

During El Niño Modoki the large scale circulation is evidently weaker compared to canonical events. The most noteworthy atmospheric response is the wind convergence zone over the central equatorial Pacific (Fig. 5.8b). As during the summer period, this represents a distinct feature compared to the canonical El Niño events. This low level convergence zone is located closer to the international dateline (about 170°W) than during the summer period (about 150°W) (Figs. 4.9b, 5.8b). Furthermore, there are significant winds along the SPCZ region that enhances the anomalous moisture advection intensifying the convection activity. This is in agreement with weak and positive rainfall anomalies observed there (Fig. 5.3). This anomalous feature contrasts with El Niño conditions, as the SPCZ tends to shift northwards.

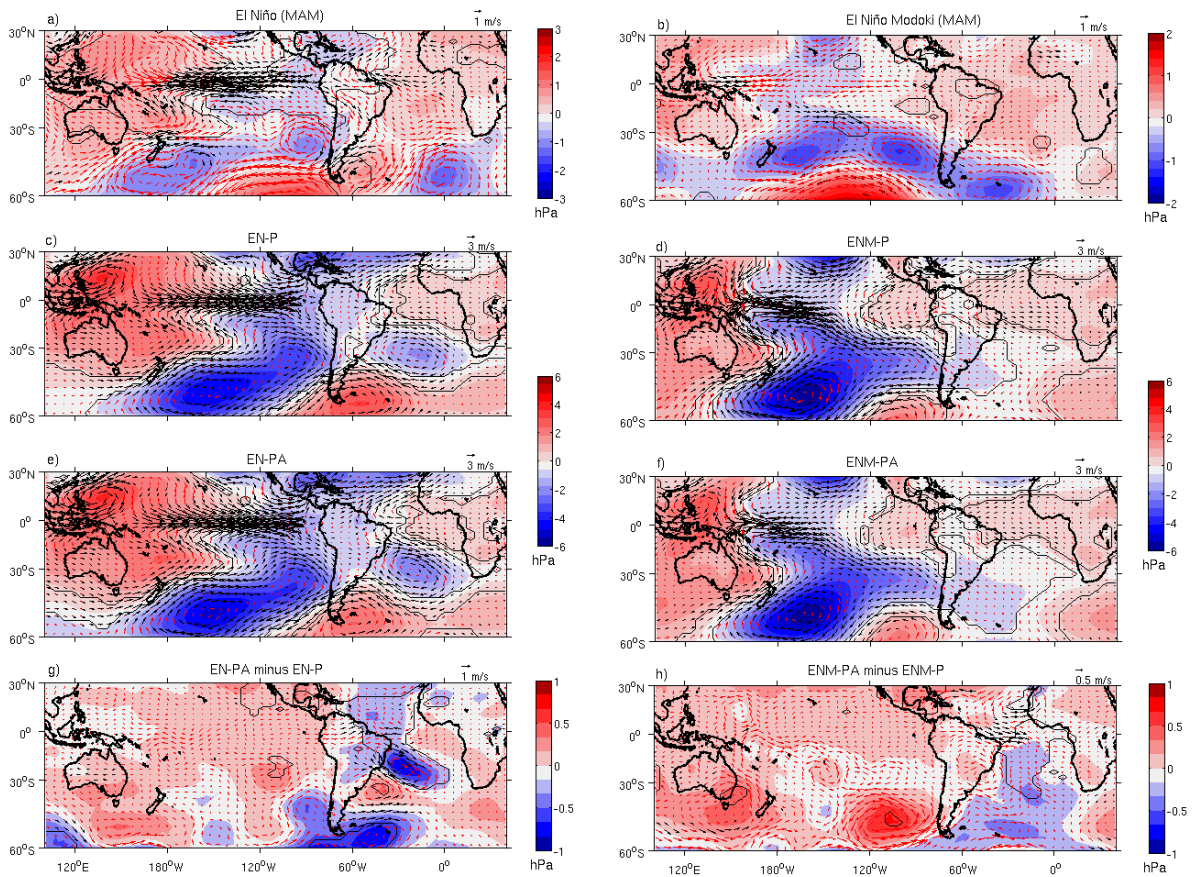


Figure 5.8: Regression of the observed MAM 850-hPa wind (vector) and SLP (shading) anomalies onto (a) SST PC1 (El Niño-related) and (b) PC2 (El Niño Modoki-related). Simulated 850-hPa wind and SLP anomalies for (c) EN-P, (d) ENM-P, (e) EN-PA, and (f) ENM-PA experiments. Difference between (g) EN-PA minus EN-P, and (h) ENM-PA minus ENM-P. Black contours (vectors) represent statistically significant regions (pixels) at the 90% confidence level according to a two-tailed Student t-test.

Like the previous figure, Figure 5.9 focuses over the South American continent only. Similarly to the summer period, the observed El Niño signal in low level anomalous circulation over the South American continent features of a well defined SALLJ meridional flow (Fig. 5.9a). The Atlantic trade winds are enhanced by the northern portion of the stronger than average South Atlantic subtropical high. This reinforces the zonal winds over the continent that in turn deflects southward forming a well defined low level jet toward the SESA region. This circulation pattern leads to an enhanced moisture transport from the Amazon basin to the subtropical region of South America favouring precipitation over the SESA region. This anomalous flow is highly coherent with the observed positive rainfall anomalies in both the composite (Fig. 5.4a) and the SVD analyses (Fig. 5.5).

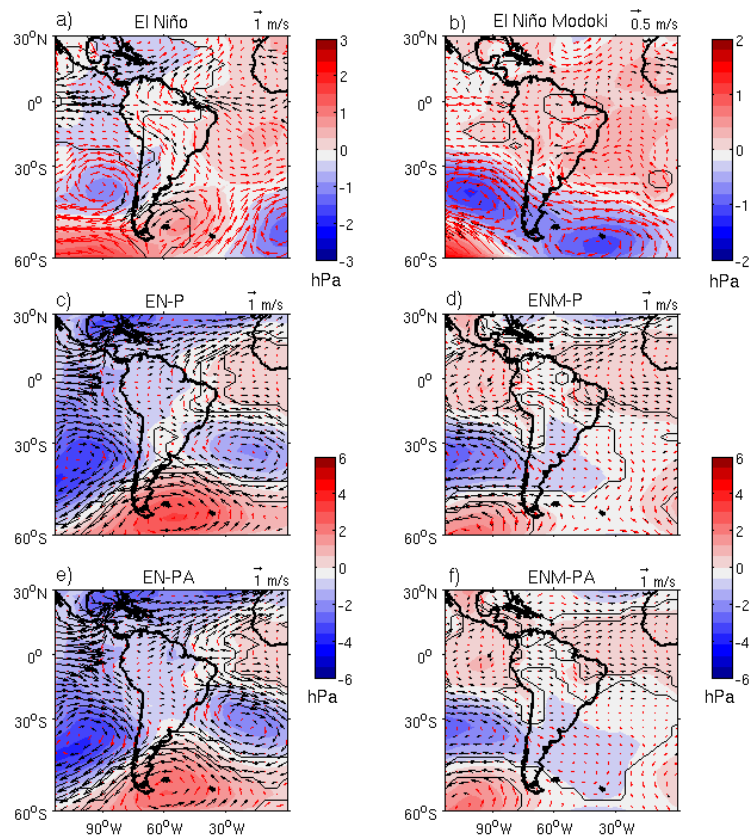


Figure 5.9: As in Fig. 5.8 but focused on South America. Difference between perturbation experiments not included. Black contours (vectors) encompass statistically significant regions (pixels) at the 90% confidence level according to a two-tailed Student t-test.

The anomalous regional scale circulation pattern over the continent during El Niño Modoki conditions features a cyclonic circulation anomaly over the central eastern Brazil. It is likely to represent the final stage of the fully developed anomalous cyclone spanning over both the continent and the tropical Atlantic Ocean as observed during the previous summer period (Figs. 4.10b, 5.9b). As in the summer period, this anomalous cyclone acts to weaken and redirect the climatological SALLJ during El Niño Modoki conditions. The southern flank of this anomalous cyclone seems to interact with an anomalous anticyclone pattern centered at 30°S - 30°W over the South Atlantic Ocean. This suggested interaction can be thought of in terms of a reinforcement of the anomalous cyclone over the continent combined with an anomalous moisture divergence in the continent, specifically over the SESA region. Consequently, this leads to negative rainfall anomalies over this region as detected in the SVD and composites analyses (Figs. 5.4b, 5.6). This associated moisture advection is driven by an anomalously strong subtropical high. Besides the associated moisture advection from the tropical latitudes into the continent and consequently over the SESA

region, the existence of a moisture path onto SESA located further south over the South Atlantic Ocean is well known in the literature (Vera et al., 2006).

5.4.2 AGCM perturbation experiments

The perturbation experiments undertaken for El Niño conditions (Figs. 5.8c,e), namely the EN-P and EN-PA experiments, simulate the main features of the large scale anomalous circulation such as the strong anomalous westerly winds along the equatorial Pacific in response to the anomalous SLP gradient (Figs. 5.8a,c). Similarly, the anomalous large scale cyclonic circulation over the subtropical-to-extratropical Pacific Ocean seems to be fairly well simulated compared to observations. The major differences between observations and simulations are seen over the Atlantic Ocean. In particular the subtropical high system over the South Atlantic is weak in the simulations, whereas observations show an opposite anomalous pattern (Figs. 5.8a,c,e). This contrasting feature may be a consequence of the reported biases in the section 2.5.5. The experiments show a weak inflow from the equatorial Atlantic onto northeastern South America (Figs. 5.9a,c,e) and a weak anomalous flow toward the SESA region similar to observations. The difference between both perturbation experiments (Fig. 5.8g), EN-PA minus EN-P, reveals that the anomalous Atlantic SST conditions can increase the magnitude of the easterly winds over the equatorial Atlantic. In contrast, their magnitude decreases over the equatorial portion of the continent. Furthermore, over the oceanic portion of the SACZ there is a cyclonic circulation pattern in geostrophic balance with the local SLP anomaly associated with the local warming of the previous summer season. This represents a season-to-season persistence of the anomalous warming pattern affecting the anomalous local circulation.

The perturbation experiments representing El Niño Modoki conditions (Figs. 5.8d,f) overestimate the anomalous circulation in the Pacific. In addition, the modelled low level convergence zone (around 120°W) is clearly shifted eastward compared to observations (around 170°W). As the anomalous cooling over the eastern Pacific tends to increase during autumn compared to the summer period (compare Figs. 4.1b and 5.1b), the anomalous SLP gradient is then stronger and consequently are the anomalous equatorial easterly winds. Even though the experiments simulate a strong anomalous SLP along the equatorial Pacific, the easterly wind anomalies are not well simulated in the ENM-P and ENM-PA experiments. The large scale cyclonic circulation pattern covering the subtropical to extratropical Pacific regions is not well simulated

(Figs. 5.8b,d,f), however, the position of the anomalous northwesterly wind over the subtropical South America coming from the anomalous convection centre in the central equatorial Pacific resembles observations. It is important to note that this large scale cyclonic circulation pattern barely spans the South Atlantic Ocean in the observations (Figs. 5.8b,f). The difference between the ENM-PA and ENM-P perturbation experiments (Fig. 5.8h) reveals a strong low level circulation in the ENM-P experiment. For instance the anomalous flow emanating from the central Pacific toward the subtropical latitudes of South America is much stronger in the ENM-P experiment (Figs. 5.8d,f).

The experiments forced with prescribed anomalous SST over the Pacific basin reveal distinct anomalous circulation over the Atlantic basin (Figs. 5.9c,d). It suggests a high degree of sensitivity to a remote anomalous warming location. In particular, in the EN-P experiment there is a large scale cyclonic anomaly acting to weaken the climatological subtropical high in the Atlantic, it however differs from observations (Fig. 5.9a). In the ENM-P experiment, an organized large-scale is not evident, suggesting that the subtropical high is not strongly affected during El Niño Modoki conditions.

5.5 Upper level circulation

5.5.1 Observed conditions during El Niño and El Niño Modoki

The upper level circulation represented by the asymmetric streamfunction anomalies during El Niño conditions (Fig. 5.10a) shows similar conditions to the austral summer period (Fig. 4.12a), such as the typical pair of anticyclones straddling the equator that represents a perturbed Walker circulation cell in response to a symmetric anomalous convection centre over the eastern equatorial Pacific (Gill, 1980). Another feature is the occurrence of two anomalous cyclones straddling the equator over the tropical Atlantic. The pair of anticyclones (cyclones) straddling the equator over the Pacific (Atlantic) Ocean represents strong upper level anomalous easterlies (westerlies) along the equator. Some differences also arise compared to the summer period, such as the absence of an anticyclonic anomaly in the proximity of the SESA region. In fact this anomaly is quite weak and shifted eastward to the oceanic region, i.e. it is centered over 33°S, 30°W. This fact suggests that the anomalous upper level circulation does not reinforce the anomalous SALLJ in lower levels, which is more significant during the austral spring season (Cazes Boezio et al., 2003). Furthermore, no extratropical teleconnection patterns between the tropical Pacific and the South American continent via the extratropics are evident.

The anomalous irrotational component of the upper level circulation (Fig. 5.11a) depicts a high degree of resemblance to that from austral summer (Fig. 4.13a). A strong upper level divergence source, associated with anomalous vertical upward motion spans most of the eastern Pacific and North Atlantic oceans. The main upper level convergence mass centre, associated with anomalous vertical downward motion is located from the subtropical western Pacific in the Southern Hemisphere toward the Northwestern Pacific in the northern latitudes.

The upper level circulation during El Niño Modoki conditions (Fig. 5.10b) shows a contrasting anomalous circulation regime compared to El Niño events. The most outstanding feature during autumn is the presence of an anomalous quadruple straddling the equator over the Pacific Ocean. It represents the perturbations of an anomalous double convective cell over the equatorial Pacific, which is a typical feature of El Niño Modoki events (Ashok et al., 2007; Ashok et al., 2009b). Like in El Niño case, over the Atlantic Ocean a pair of anomalous cyclone straddling the equator is also present, however, they are weak and less defined compared to El Niño conditions (Figs. 5.10a,b). During this season, remote teleconnections from the equatorial Pacific via the extratropics are more evident compared to the canonical El Niño conditions (Figs. 5.10a,b). There are wave-like propagations emanating from the tropics toward both hemispheres and then arching northeastward (southeastward) from the extratropics toward the subtropics in the Southern (Northern) Hemisphere. In particular an anticyclonic anomaly is observed over the subtropical South Atlantic spanning across the continent over the SESA region contrasting with El Niño conditions. If we compare the low level circulation over the continent (Fig. 5.9b), it is observed a similar anomaly located at 30°S associated with SESA and the oceanic regions, indicating an anomalous barotropic circulation regime during this period and hence suggesting an upper level influence in the local circulation over the continent. In other words, the upper level anticyclonic anomaly seems to interact with southern the flank of the observed anomalous cyclonic pattern located over the central eastern Brazil (Figs. 5.9b, 5.10b). This feature is not present during El Niño conditions.

Besides the weaker magnitude of the anomalous velocity potential field in El Niño Modoki compared to El Niño, it further supports the contrasting features across the equatorial domain compared to the canonical El Niño events (Figs. 5.11a,b). An upper level mass source is seen over both western Pacific and equatorial Atlantic oceans, whereas an upper level mass convergence centre is located over the central-to-eastern equatorial Pacific region. Additionally there are two weak secondary upper level

convergence centres, one is located over the SESA region and the other is diagonally arching from equatorial South America toward the northern latitudes of the tropical Atlantic Ocean. The opposite anomalous conditions are observed over the equatorial Pacific and Atlantic domain during the canonical El Niño conditions (Figs. 5.11a,b). The observed differences suggest an opposite anomalous vertical circulation associated with both a distinct perturbation in the Walker circulation cell over the Pacific Ocean and to a different anomalous SST conditions in the tropical Atlantic Ocean.

It is important to mention the observed contrast between the downward and upward motions over the equatorial Atlantic Ocean between El Niño and El Niño Modoki respectively. It suggests a different response in the Atlantic ITCZ seasonal migration and thus potentially affecting the South American anomalous rainfall differently.

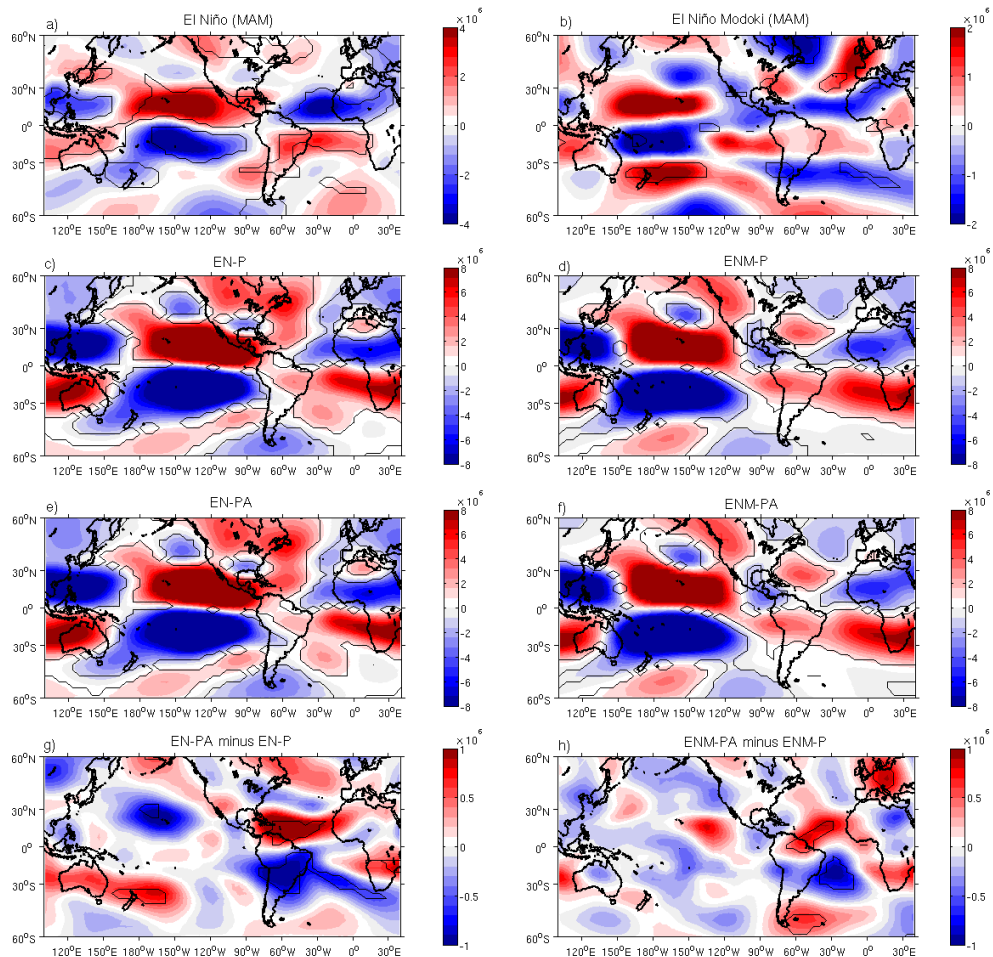


Figure 5.10: Regression of the observed MAM 200-hPa asymmetric streamfunction anomalies onto (a) SST PC1 (El Niño-related) and (b) PC2 (El Niño Modoki-related). Simulated anomalous 200-hPa asymmetric streamfunction for (c) EN-P, (d) ENM-P, (e) EN-PA, and (f) ENM-PA experiments. Difference between (g) EN-PA minus EN-P and (h) ENM-PA minus ENM-P, units are m^2/s . Black contours represent statistically significant regions at the 90% confidence level according to a two-tailed Student t-test.

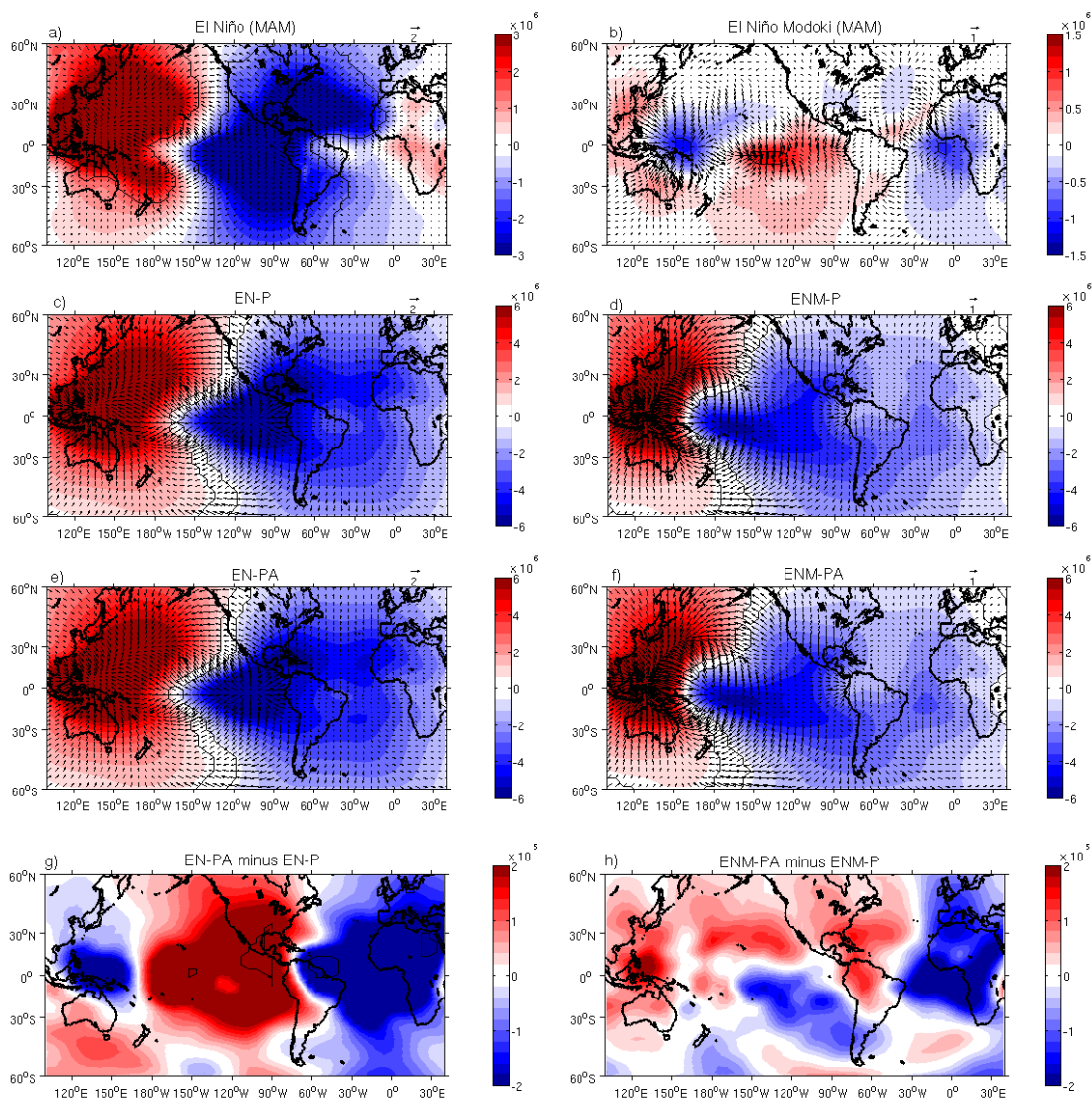


Figure 5.11: Composites of the observed anomalous 200-hPa divergent winds (vectors) and velocity potential (shading) during the autumn period of (a) El Niño, and (b) El Niño Modoki conditions (See Table 3.1). The blue (red) shading regions indicate anomalous upper level divergence (convergence) centres. Composites of simulated anomalous 200-hPa divergent winds and velocity potential for (c) EN-P, (d) ENM-P, (e) EN-PA, and (f) ENM-PA perturbation experiments, and the velocity potential anomaly difference between (g) EN-PA minus EN-P and (h) ENM-PA minus ENM-P. The units of divergent wind (velocity potential) are m/s (m^2/s). Black contours represent statistically significant regions at the 90% confidence level according to a two-tailed Student t-test.

5.5.2 AGCM perturbation experiments

The perturbation experiments undertaken according to El Niño conditions (Figs. 5.10 c,e), namely EN-P and EN-PA, represent the main features of the upper level tropical circulation in response to a symmetric heating located over the equator (Gill, 1980). The pair of anomalous anticyclones and cyclones straddling the equator over the Pacific and Atlantic oceans respectively are in agreement with the observed conditions (Fig. 5.10a), despite larger magnitudes. Over the subtropics the upper level response tends to resemble a PSA-like pattern (Mo, 2000), although the correct position of the stationary wave is not well simulated compared to observations which is not surprising for climate models. The difference between both perturbation experiments (Fig. 5.10g), EN-PA minus EN-P, suggests a weaker anomalous circulation over South America and Atlantic Ocean when latter is taken into account in the simulations. Over the Pacific Ocean other significant changes include a weakening in the western side of the anomalous anticyclones straddling the equator over both hemispheres in the EN-PA experiment.

The simulated velocity potential fields for El Niño conditions shows that the approximate locations of the anomalous upper level divergence centres are in agreement with observations (Figs. 5.11a,c,e). Likewise, the locations of the upper level convergence centres over the western Pacific are fairly realistic compared to observations. Over the eastern Pacific and the western sections of equatorial South America the anomalous divergent winds are also similar compared to observations (Figs. 5.11a,c,e). They are in agreement with the associated and well known descending motion over this region during canonical El Niño events, as it will be shown by the corresponding vertical circulation anomalies in the next section. The difference between both perturbation experiments (Fig. 5.11g), EN-PA minus EN-P, shows a stronger divergence (convergence) centre over the central-to-eastern (western) Pacific in the EN-P perturbation experiment, whereas strong anomalous upper level divergence over both the tropical north and south Atlantic regions occur in the EN-PA experiment instead (Figs. 5.11c,e,g).

The corresponding perturbation experiments for El Niño Modoki conditions (Figs. 5.10d,f) feature an anomalous upper level anticyclonic and cyclonic circulation pattern straddling the equator over the western and eastern Pacific respectively and a pair of anomalous cyclones over the Atlantic ocean. This simulated response is in agreement with the observed upper level anomalies over the tropical Pacific during El Niño Modoki

events. The position of the stationary waves over the Southern Ocean is slightly shifted westward compared to the EN-PA and EN-P experiments (Figs. 5.10c,d,e,f) as a response to the westward location of the equatorial heating source. However the observed remote teleconnection from the tropics via extratropics toward the SESA region is not simulated in the ENM-P and ENM-PA experiments (Figs. 5.10b,d,f). The difference between both perturbation experiments (Fig. 5.10h), i.e. ENM-PA minus ENM-P, reveals a weakening of the anomalous cyclonic upper level circulation over the tSA and tNA regions respectively.

The simulated anomalous velocity potential fields in the ENM-P and ENM-PA experiments reveal different features compared to observations (Figs. 5.11b,d,f), especially in regard to the location of the anomalous convergence and divergence centres. The observed upper level mass source over the western Pacific is located around 150°E (Fig. 5.11b), whereas in the perturbation experiments this centre is shifted to the east of the international dateline, i.e. between 180°W and 150°W, along the equatorial Pacific. Similarly the upper level mass sink is more localized over the eastern equatorial coast of the continent, whereas in observations this centre predominates along the central to eastern Pacific instead (Figs. 5.11b,d,f). As in observations the equatorial Atlantic and part of the tSA regions feature of an anomalous upper level mass source, representing contrasting features compared to El Niño experiments (Figs. 5.11b,e,f).

The anomaly difference in the simulated velocity potential fields of El Niño Modoki experiments (Fig. 5.11h), i.e. ENM-PA minus ENM-P, shows a stronger upper level mass source over the tropical Atlantic in the ENM-PA compared to the ENM-P experiment. Similarly the upper level mass source (sink) over the central equatorial to subtropical (western) Pacific is found to be stronger when SST anomalies in the Atlantic Ocean are taken into account in the simulations.

Finally, although the experiments undertaken for El Niño Modoki conditions differ from the observed conditions, they partially capture the shift of the anomalous divergent mass centre location between both interannual events over the equatorial Pacific (e.g. Figs. 5.11 c d).

5.6 Vertical circulation

5.6.1 Observed changes in the Walker circulation between El Niño and El Niño Modoki events

Figure 5.12 depicts composites of observed and simulated anomalies of vertical velocity averaged between 10°S and 10°N. During El Niño events, the vertical velocity anomaly shows strong ascending motion over central and especially in the eastern equatorial Pacific, whereas anomalous descending motion occurs elsewhere (Fig. 5.12a). In particular the corresponding magnitude of the subsidence over the western Pacific is stronger than over the tropical South America and Atlantic Ocean. Both ascending and descending branches of the anomalous Walker cell are associated with positive and negative rainfall anomalies respectively, as shown in the composites (Figs. 5.3a, 5.4a) and SVD analyses for the autumn period (Figs. 5.5,5.6).

Although the overall vertical velocity magnitude is weak during El Niño Modoki conditions, contrasting features are observed (Fig. 5.12b). In particular, the central to western Pacific features of anomalous upward motion, whereas downward motion is found over the equatorial eastern Pacific. This anomalous configuration during El Niño Modoki events is the opposite to that of El Niño episodes due to the different anomalous warming location over the equatorial Pacific (Figs. 5.12a,b). This also implies that the classical double convective cell of El Niño Modoki (Ashok et al., 2007) evolves into a single convective cell pattern over the equatorial Pacific Ocean during the autumn season. Over the South American longitudes, there is an anomalous uplift that provides favourable conditions for anomalous precipitation over the Amazon basin, contrasting with El Niño conditions (Figs. 5.12a,b). Over the Atlantic coast of the continent anomalous subsidence is observed, whereas over the oceanic region anomalous uplift dominates (between 0 and 30°W). The latter is also another noteworthy difference compared to the tropical Atlantic conditions during El Niño events, where it is dominated by an anomalous downward motion instead (Figs. 5.12a,b). These results corroborate the findings of Ambrizzi et al. (2005), who documented the anomalous vertical circulation and the associated rainfall anomalies over South America during two types of El Niño.

5.6.2 AGCM perturbation experiments

The perturbation experiments undertaken for El Niño conditions, namely EN-P and EN-PA respectively, represent the main features compared to the corresponding observed conditions during the autumn period (Figs. 5.12a,c,e). The observed strong upward motion close to the equatorial coast of the continent is particularly well simulated in both perturbation experiments, as a direct consequence of the strong underlying warm SST anomalies over this region. Similar to the strong downward motion over the western Pacific, the anomalous downward motion over the continent and tropical Atlantic Ocean are well simulated in both experiments. If we isolate the response due to the anomalous Atlantic SST conditions under an assumption of linearity, i.e. EN-PA minus EN-P, we have access to the potential Atlantic role in the vertical circulation over the continent and thus in the impacts of rainfall variability. The difference between both perturbation experiments (Fig. 5.12g) reveals stronger (weaker) downward motion over the tropical Atlantic (tropical coast) region in the EN-PA experiment. In particular the downward motion over the continent is in agreement with the observed negative rainfall anomalies in both the composite (Fig. 5.4a) and the SVD analyses (Fig. 5.5). Furthermore, the stronger subsidence over the tropical Atlantic in the EN-PA experiment is coherent with the simulated stronger negative rainfall anomalies (Fig. 5.4g) suggesting unfavourable conditions for convection activity associated with the Atlantic ITCZ during the autumn period.

The response of El Niño Modoki in the experiments, i.e. ENM-P and ENM-PA, resembles the main observed features of the vertical circulation cell associated with a perturbed Walker circulation over the equatorial Pacific Ocean (Figs. 5.12b,d,f). The modelled anomalous uplift over the western Pacific is slightly shifted eastward compared to observations, due to a displacement of the warm SST in observation. Its counterpart over the eastern Pacific, the corresponding descending branch is consistent with the observed and simulated large scale anomalous rainfall patterns during the autumn period (Figs. 5.3b,d,f). Over the South American continent the response is similar to that of El Niño experiments, however, its magnitude is weaker (e.g. Figs 5.12e,f). During El Niño Modoki events, the anomalous vertical circulation over the tropical Atlantic Ocean exhibits anomalous upward motion (Figs. 5.12b,d,f), representing a contrasting feature over this region compared to canonical El Niño events (Figs. 5.12a,c,e). Furthermore, it is important to note that the ENM-P is enough to represent an anomalous upward motion over the tropical Atlantic region in response to a different remote anomalous warming location. Thus this shift may favour

anomalous rainfall over the tropical Atlantic sector and consequently the prevailing anomalous SST conditions may modulate rainfall over the continent.

The most outstanding difference between both perturbation experiments, i.e. ENM-PA minus ENM-P, lies in the stronger upward motion over the tropical Atlantic region, further confirming the contrasting conditions in the vertical circulation over this region between both interannual events (Figs. 5.12g,h). Consequently, it may provide favourable conditions for the Atlantic ITCZ southward migration, contrasting with the simulated and observed conditions over the tropical Atlantic during El Niño events.

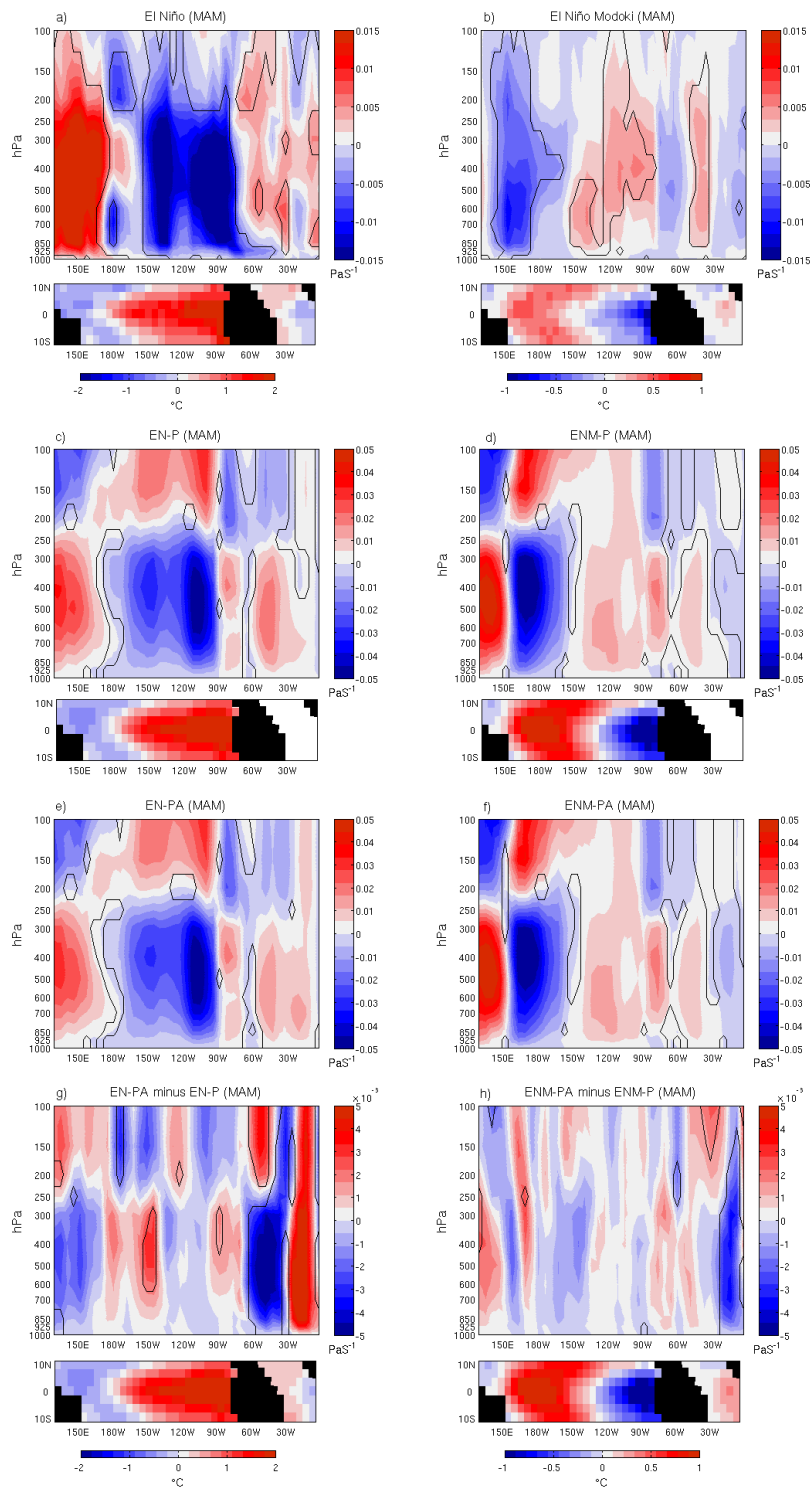


Figure 5.12: Composites of the observed vertical velocity anomalies during (a) El Niño and (b) El Niño Modoki events (See Table 3.1). The simulated vertical velocity anomaly for (c) EN-P, (d) ENM-P, (e) EN-PA, (f) ENM-PA, and the vertical velocity anomaly difference between (g) EN-PA minus EN-P, and (h) ENM-PA minus ENM-P perturbation experiments. The vertical velocity was averaged over the 10°N-10°S latitudinal band. Blue (red) shading is associated with upward (downward) motion. The associated SST anomalies (°C) are shown below. Black contours represent statistically significant regions at the 90% confidence level according to a two-tailed Student t-test.

5.7 A rainfall Index as a proxy of the seasonal migration of the Atlantic ITCZ

Figure 5.13 depicts the rainfall climatology of South America for the austral summer and autumn periods. In particular during the summer season (Fig. 5.13, left panel), the South American monsoon is mostly dominated by a rainfall band diagonally extending from an area of maximum precipitation over the central Amazon toward the southeastern region protruding into the Atlantic Ocean. As already stated in the section 2.5.1, this rainfall band is known as the SACZ. The peak of the SACZ occurs during the summer period, whereas the Atlantic ITCZ is completely confined over the Northern Hemisphere. During the autumn period (Fig. 5.13, right panel) the rainfall associated with the SACZ quickly retreats northward (Marengo et al., 2001). Then the Atlantic ITCZ moves southward reaching its southernmost position during March and thus influences the rainfall variability over the continent (Hastenrath and Heller, 1977; Moura and Shukla, 1981; Zhou and Lau, 2001; Chiang et al., 2002; Cook, 2009).

We can relate the rainfall variability associated with the seasonal Atlantic ITCZ southward migration and its relationship with El Niño and El Niño Modoki events via the Northeast Brazil rainfall anomaly Index (FQI). The FQI is created by the Join Institute for the study of the Atmosphere and Ocean (JISAO), and is currently available for the period 1849-2002 at <http://jisao.washington.edu/data/brazil/>. This index combines normalized rainfall time series measured at two locations, namely the coastal area of Fortaleza (3.7°S, 38.5°W) and 100 km inland in the Quixeramobim region (5.3°S, 39.3°W). The approximate locations of these stations are indicated by the white circle in the right panel of Figure 5.13. As this area is only affected by the Atlantic ITCZ variability, the geographical location of the Fortaleza and Quixeramobim regions implies that the FQI can provide useful information about only one source of rainfall variability, namely the Atlantic ITCZ seasonal migration and its associated convection activity during the autumn period, thus allowing us to relate it to remote forcing from the Pacific Ocean.

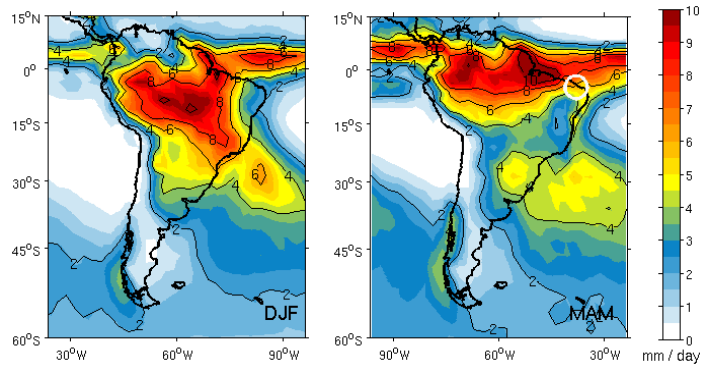


Figure 5.13: Composites of the rainfall climatology of (left panel) the austral summer and (right panel) autumn seasons. The white circle in the right panel displays the approximate locations of the Fortaleza (3.7°S, 38.5°W) and Quixeramobim (5.3°S, 39.3°W) rainfall stations used to estimate the Northeast Brazil rainfall Index (FQI). The rainfall climatology analysed period is from January 1979 through July 2008 based on CMAP dataset as described by Xie and Arkin (1996).

Figure 5.14 shows a correlation analysis of the FQI versus the EMI and NINO3 indices. In particular, during the autumn months of El Niño events the relationship between the FQI rainfall and NINO3 indices is negative, their correlation coefficient is -0.52 at zero lag and significant at the 90% confidence level. This relationship indicates that the Northeast Brazil experience below average rainfall during the autumn periods of El Niño. This is consistent with the composite and SVD analyses (Figs. 5.4a, 5.5), that show the occurrence of negative rainfall anomalies over the northern portion of the continent, especially over the central eastern Brazil including the Northeast region. Furthermore, the occurrence of negative rainfall anomalies spanning the tropical Atlantic region (Fig. 5.4a) further supports the inhibition of anomalous convection activity associated with the Atlantic ITCZ during El Niño conditions.

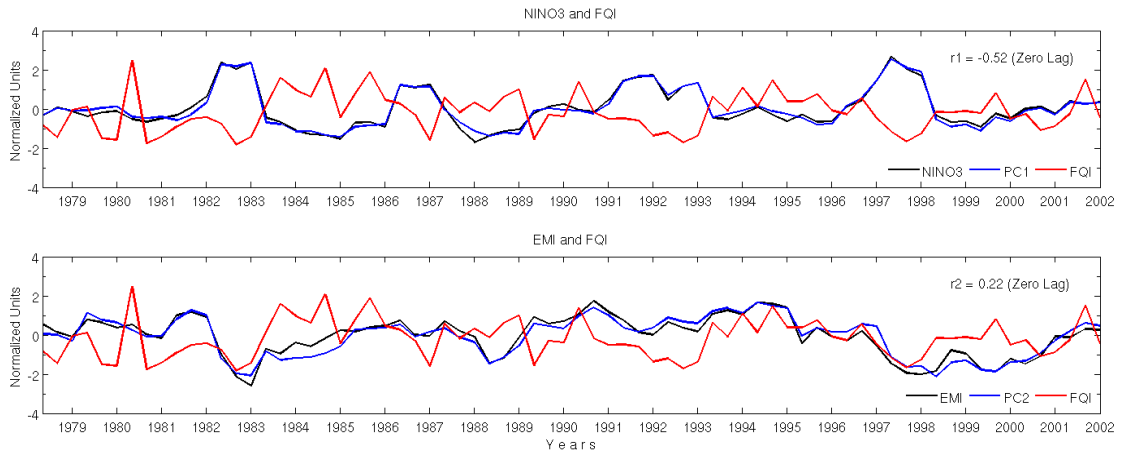


Figure 5.14: Time series of (upper panel) PC1 (blue) and the NINO3 (black), FQI (red) indices. The lagged cross correlation (r_1) between the NINO and FQI indices is -0.52 at zero lag. The time series of (lower panel) PC2 (blue) and the EMI (black), FQI (red) indices. The lagged cross correlation (r_2) between the EMI and FQI indices is 0.22 at zero lag. Just the correlation of the upper panel is statistically significant at the 90% confidence level.

Although the correlations undertaken with the time series associated with El Niño Modoki events (EMI and PC2) are not significant, they still suggest a hint of an opposite relationship compared to the El Niño events similar to what have been shown for the AGCM perturbation experiments. The positive relationship between the FQI and EMI indices ($r = 0.22$) supports the results shown by the composite (Fig. 5.4b) and the SVD analyses (Fig. 5.6). It suggests that El Niño Modoki is not as effective as El Niño events in inhibiting the southward migration of the Atlantic ITCZ and its associated convection activity.

5.8 Observed and modelled OLR conditions

In order to provide further support to the contrasting anomalous conditions between El Niño and El Niño Modoki events, we also use the regressed OLR anomalies onto the SST PC1 and PC2 time series, they are shown in Figure 5.15. In particular, the observed OLR anomalies during El Niño events (Fig. 5.15a) represent the main large scale convective regions. As expected and in agreement with the observed anomalous rainfall composite (Fig. 5.3a) the major region of strong anomalous convection is located along the central-to-eastern equatorial Pacific, whereas the opposite anomalous conditions prevails over the western Pacific, equatorial South America and Atlantic Ocean. These regions are associated with below average convective activity and consequently with negative rainfall anomalies. The corresponding AGCM perturbation experiments (Figs. 5.15c,e), i.e. EN-P and EN-PA, simulate the main observed anomalous features and particularly the inhibition of convective precipitation over equatorial South America associated with the Atlantic ITCZ. It is worth mentioning

that the simulated OLR anomalies over the equatorial Pacific represents a broader convective area than in observations (e.g. Figs. 5.15a,c). The difference between both perturbation experiments (Fig. 5.15g), i.e. EN-PA minus EN-P, reveals an increased convective activity over the SESA region when the Atlantic SST are considered in the simulation (Fig. 5.4g). The positive OLR difference over the equatorial Atlantic Ocean suggests that the anomalous Atlantic SST conditions can reinforce the inhibition of the southward migration of the Atlantic ITCZ, which is associated with positive and negative OLR rainfall anomalies in the tropics of South America.

In agreement with the displaced warming location, the anomalous convective centre is seen over the central-to-western equatorial Pacific during El Niño Modoki, contrasting the observed conditions during canonical El Niño events (Figs. 5.15a,b). The tropical portion of South America features negative OLR anomalies, implying more favourable conditions for local convection compared to El Niño events (Figs. 5.15a,b). Over the tropical Atlantic the observed OLR anomalies are much weaker than in El Niño conditions and also shifted to north in agreement with a southward migration of the Atlantic ITCZ (Figs. 5.15a,b). In the corresponding perturbation experiments (Figs. 5.15d,f) the overall anomalous pattern is not well simulated compared to El Niño experiments. There are negative OLR anomalies over the central-to-western equatorial Pacific and positive anomalies over the eastern equatorial Pacific. Over the Atlantic equatorial portion of the continent there are northward shifted positive OLR anomalies linked to the Atlantic ITCZ dynamics, however, their magnitudes are weak compared to El Niño experiments (Figs. 5.15c,d,e,f) suggesting some degree of sensitivity to a remote anomalous warming location. In the equatorial Atlantic the anomaly difference between the corresponding AGCM experiments (Figs. 5.15g,h), namely EN-PA minus EN-P and ENM-PA minus ENM-P, shows more supporting evidence about the different anomalous behaviour of the Atlantic ITCZ between both interannual events. During El Niño (El Niño Modoki) experiments the OLR anomaly difference is positive (negative) along the equatorial Atlantic, supporting a stronger inhibition (occurrence) of anomalous convective activity associated to the Atlantic ITCZ when the Atlantic SST anomalies are considered in the simulations.

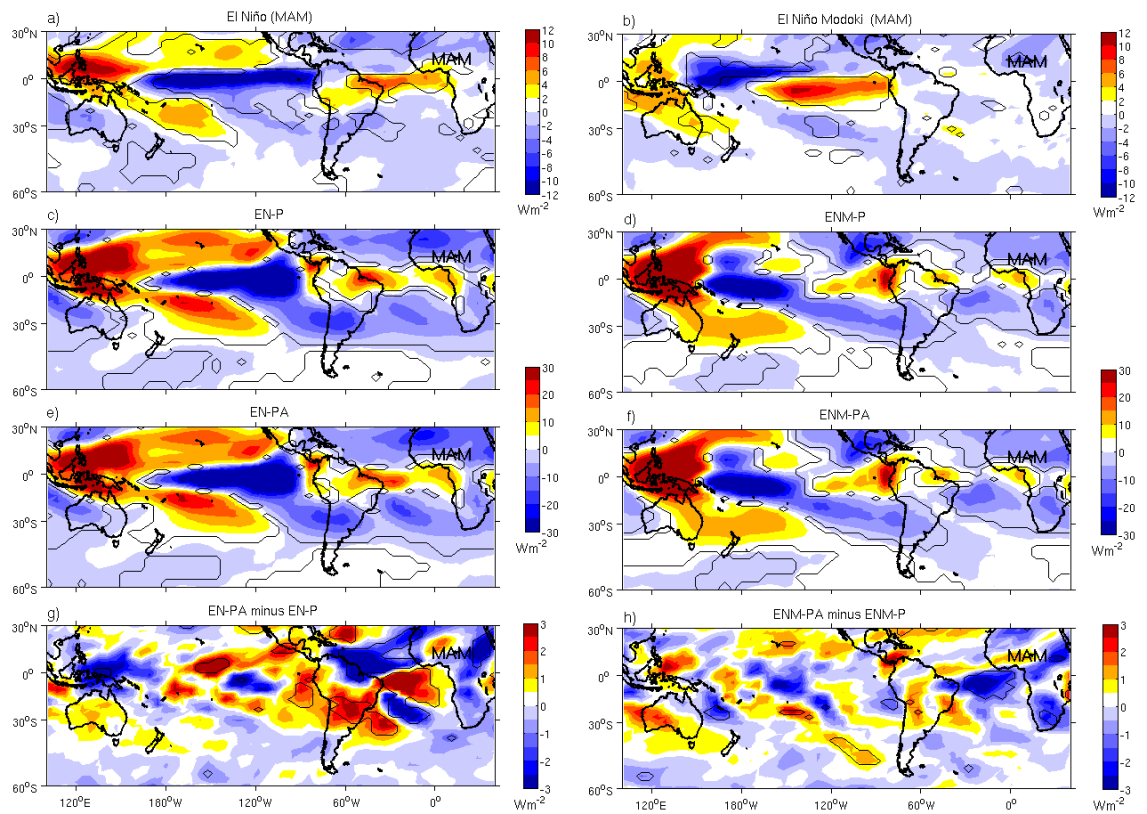


Figure 5.15: Regression of the observed MAM OLR (Wm^{-2}) anomalies onto (a) SST PC1 (El Niño-related) and (b) PC2 (El Niño Modoki-related). Simulated anomalous OLR for (c) EN-P, (d) ENM-P, (e) EN-PA, and (f) ENM-PA experiments. Difference between (g) EN-PA minus EN-P and (h) ENM-PA minus ENM-P. Black contours represent statistically significant regions at the 90% confidence level according to a two-tailed Student t-test.

5.9 Summary and discussion

In this chapter we have examined the influence of the Pacific SST anomalies on South America rainfall and circulation for the austral autumn period using composite, regression and SVD techniques. In order to identify the different responsible mechanisms of the observed variability between both interannual events, we support the observational results with AGCM perturbation experiments forced with the monthly evolution of El Niño and El Niño Modoki. Notwithstanding the austral autumn season is also one of the climatological rainy periods of South America, there is a lack of recent studies estimating inter El Niño variations and their related impacts on interannual rainfall variability. In fact, the overwhelming majority tend to focus on the South American monsoon period instead. Therefore, the results presented here can provide an important contribution in this regard.

We summarize the main finding as follows,

The statistical coupled modes of variability successfully isolate the main physical modes associated with El Niño and El Niño Modoki interannual events. They represent the main features of the anomalous warming location over the equatorial Pacific Ocean, explaining 30.85% and 9.73% of the square covariance fraction between the anomalous Pacific SST and South American rainfall for the first and second SVD modes respectively.

The first SST mode represents El Niño and is coupled with negative (positive) loading over the northern portion of the continent (SESA region). The second SST mode of variability is associated with El Niño Modoki and oscillates with positive (negative) loading over the tropical South America (subtropics).

Over the tropics the responsible mechanism of the observed variability is associated with perturbations in the Walker circulation. During El Niño there is a strong descending branch spanning the equatorial South America and the Atlantic Ocean, which is well represented in the AGCM experiments. This anomalous descending branch is associated with negative rainfall anomalies over these regions by inhibiting the local convection that usually occurs by the autumn season. During El Niño Modoki events, the observed anomalous warming shift toward the central-to-western Pacific in conjunction with the cold conditions over the eastern Pacific produces an opposite anomalous single convective cell with an anomalous descending branch over the eastern Pacific Ocean instead. These conditions in conjunction with the warm SST

anomalies over the tropical Atlantic region, i.e. a negative Atlantic gradient, may favour the southward incursion and the consequent increase of anomalous convection of the Atlantic ITCZ during this period supporting the positive rainfall anomalies over the tropics. The AGCM experiments reproduce most of the corresponding changes of El Niño Modoki conditions, especially the anomalous shift of the Walker circulation over the equatorial Pacific Ocean and also the anomalous upward motion over the tropical Atlantic. Over the South American continent just a weakening in the local subsidence is simulated.

Over the subtropics, the positive rainfall anomalies occurring over the SESA region are mostly associated with the SALLJ during El Niño events as clearly seen in observations. However, during El Niño Modoki events the occurrence of a low level cyclonic anomaly over central eastern Brazil acts to weaken and redirect the associated moisture transport of the SALLJ. This keeps the moisture availability for local convection over the tropics. The anomalous low level cyclone interacts with a barotropic anticyclone positioned southward offshore of SESA. In particular it was found that the southern flank of the cyclonic anomaly is modulated by the northern part of the barotropic anticyclone. The associated low level flow coming from the Atlantic Ocean toward the continent tends to diverge over the SESA region in agreement with the negative rainfall anomalies there. The northern branch of this anomalous flow seems to reinforce the anomalous cyclonic vortex over central eastern Brazil. This barotropic anticyclone seems to be a consequence of wave-like propagations emanating from the anomalous convective centre over the central-to-western equatorial Pacific region during El Niño Modoki conditions. However, during canonical events no clear propagations linking the equatorial Pacific with the South American continent via the extratropics are detected for the autumn season.

Thus, during El Niño conditions, the interannual rainfall variability over the South American subtropics is modulated by the anomalous SALLJ, whereas during El Niño Modoki the upper level circulation seems to play an important role in generating the anomalous circulation regime that influences the interannual rainfall anomalies over the region.

Finally, Figure 5.16 summarizes the impacts and its responsible mechanisms for explaining the observed rainfall variability over tropical and subtropical South America in response to inter-El Niño variations.

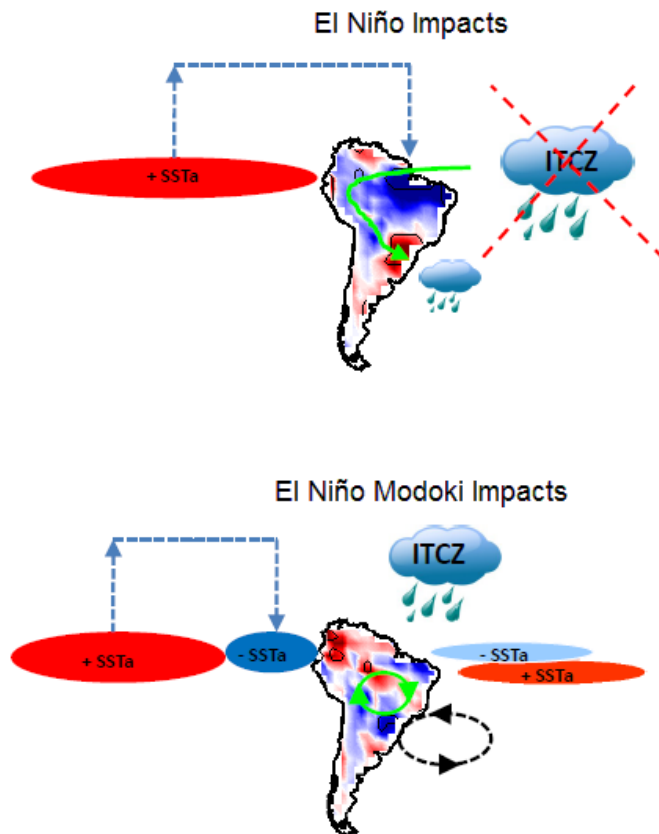


Figure 5.16: Schematic of the impacts of (upper) El Niño and (lower) El Niño Modoki on South American rainfall during autumn and its associated mechanisms. During El Niño the anomalous ascending branch of the Walker circulation over the eastern equatorial Pacific is compensated with anomalous subsidence over the tropical regions of the continent inhibiting the associated convection activity of the Atlantic ITCZ, leading to negative rainfall anomalies over the tropics. Additionally an anomalously strong SALLJ (green) brings moisture toward SESA favouring anomalous rainfall. The shift in the anomalous warming location during El Niño Modoki leads to anomalous subsidence over the eastern Pacific. Consequently, this favours the normal seasonal migration of the Atlantic ITCZ allowing the Atlantic SST to reinforce the associated convection favouring positive rainfall anomalies. An anomalous offshore barotropic anticyclone (black) is triggered over the subtropics as a consequence of wave-like propagation emanating from the central Pacific. It interacts with the anomalous low level cyclonic pattern (green) leading to anomalous divergence and negative rainfall anomalies over SESA and also to a weakening of the climatological SALLJ further increasing the positive rainfall anomalies over the tropics. Over the continent red (blue) shading indicates positive (negative) rainfall anomalies.

During El Niño Modoki events, the anomalous low level easterlies along the equatorial Pacific, which comprise the northern flank of an anomalously strong subtropical high pressure system, contribute to the advection of cold water along the eastern equatorial Pacific. The strong anomalous easterly winds over the equatorial Pacific start during austral summer, becoming progressively weak but still favourable for advection of cold water by the autumn season. Consequently, it leads to an anomalously strong SST gradient along the equatorial Pacific with particularly strong negative SST anomalies of approximately -1°C at the eastern side compared to the corresponding SST pattern of the summer season. This anomalous SST gradient, in turn, generates equatorial anomalies of SLP leading to an anomalous low level wind convergence over the central-to-western Pacific. By continuity, an anomalous single Walker cell is formed over the equatorial Pacific Ocean with an ascending (descending) branch overlying the warm (cold) SST anomalies in the central-to-western (eastern) region. The shift of the anomalous convection centre during El Niño Modoki seems to impact the equatorial South America and Atlantic Ocean regions by favouring conditions for convection and the seasonal migration of the Atlantic ITCZ during autumn, which does not occur during El Niño conditions. In addition, the AGCM experiments show that the combined effects of El Niño Modoki SST anomalies with a negative inter-hemispheric SST gradient in the tropical Atlantic, i.e. cold (warm) SST conditions in the tNA (tSA) region, enhance the associated convection of the ITCZ. The role of the anomalous SST conditions in the tropical Atlantic region in modulating the Atlantic ITCZ and the consequences for anomalous rainfall over the South America have been shown in previous studies (Chang et al., 2000; Pezzi and Cavalcanti, 2001; Giannini et al., 2004; Munnich and Neelin, 2005). Negative Atlantic gradient conditions had been studied in conjunction with anomalous La Niña conditions (Pezzi and Cavalcanti, 2001). However, here we show evidence that similar anomalous conditions can also occur during El Niño Modoki events. Based on the results for the composites of the Atlantic SST (Fig. 4.19 in the Chapter 4, or Fig. 5.2), and vertical velocity anomalies (Fig. 5.12) we speculate a suppression of the atmospheric bridge mechanism (Alexander et al., 2002) during El Niño Modoki conditions. Consequently, no warm SST anomalies develop over the tNA region (Figs. 5.2a,b) as typically tend to occur during canonical events (Saravanan and Chang, 2000). We recall to the reader that from the previous analysis in Chapter 4 we found a positive correlation of 0.43 between the SST anomalies in the NINO3 and tNA regions similar to previous studies, whereas the correlation between the EMI and the tNA indices was found to be negative (-0.2). Therefore, if the suppression of the atmospheric bridge as a consequence of a shift in the anomalous warming location

over the equatorial Pacific is correct, it may allow suitable environmental conditions for the formation of cool to normal SST anomalies over the tNA region which leads to a weak negative Atlantic gradient and therefore favouring the southward incursion of the Atlantic ITCZ during autumn. Although the magnitude of the Atlantic gradient is weak, Chiang et al. (2002) support that the ITCZ position can be very sensitive to small variations of tropical SST conditions. Furthermore, Chiang et al. (2000) found that when the influence of El-Niño-related Walker circulation is weak during the autumn period, the rainfall variability over Northeast Brazil can be controlled by the Atlantic SST which in turn modulates the ITCZ position. However, when the Walker circulation influence is strong, i.e. strong El Niño event, there is a suppression of the ITCZ precipitation over the equator and the 2°S to 10°S latitudinal Atlantic band. This is in agreement with our results, they support the reinforcement of the anomalous convection associated to ITCZ in response the Atlantic gradient during El Niño Modoki. Additionally, the modelling study of Saravanan and Chang (2000) found that the most significant influence of ENSO over the tropical Atlantic occurs during the autumn period and is associated with the anomalous Walker circulation. They conclude that rainfall variability over the tropical Atlantic and the northeast Brazil is a result of both local and remote contributions, namely Atlantic SST and ENSO forcing respectively, with the latter having a more important contribution.

More recently Rodriguez et al. (2011) have identified that the weak (strong) and short (long)-lived El Niño events with anomalous warming over the central (eastern) Pacific can be associated with a negative (positive) Atlantic gradient by the autumn period leading to positive (negative) rainfall anomalies over Northeast Brazil. The responsible mechanism for the occurrence of the positive SST anomalies in tropical South Atlantic is due to wave-like propagations emanating from the central Pacific during summer. It leads to a weakening of the South Atlantic subtropical high system, which in turn favours the occurrence of the positive SST by autumn and thus establishing a negative Atlantic gradient. Consequently it enhances the anomalous rainfall associated to ITCZ. Although our results do not show the same position of the stationary waves in order to suggest a weakening of the subtropical high system in the South Atlantic, the occurrence of the Atlantic ITCZ migration during El Niño Modoki (or weak El Niño) seems to be a robust result compared to that study. Moreover, we remark that the El Niño Modoki experiment forced with SST anomalies in the Pacific only, i.e. ENM-P, is enough to support this fact. It suggests that the Atlantic ITCZ response is due to a shift in the anomalous warming location.

Over the subtropics, i.e. the SESA region, there is influence of the anomalous upper level circulation during El Niño Modoki conditions which leads to negative rainfall anomalies there. However during El Niño events, the anomalous positive rainfall signal over the SESA region is mainly due to the anomalous low level circulation. The influence occurs via the SALLJ acting to enhance the associated moisture transport toward this region, this anomalous flow has virtually no upper level modulation. The anomalously strong SALLJ is a consequence of strong inter-basin SLP gradient between the eastern equatorial Pacific and the western equatorial Atlantic. Over the continent the anomalous equatorial easterly winds are deflected southward due to their interaction with the local topography, which produces the anomalously strong SALLJ during El Niño events (Vera et al., 2006). However, according to observations during El Niño Modoki conditions the inter-basin SLP gradient does not occur between the equatorial Pacific and Atlantic oceans. The eastern equatorial Pacific features of anomalous cold SST conditions leading to positive SLP anomalies over the equator and thus no anomalous inter-basin SLP gradient is established. Although our perturbation experiments successfully reproduce the anomalous equatorial SLP pattern of El Niño and El Niño Modoki conditions, the characteristics of the anomalous low level circulation over the continent tend to differ from observations.

Another important feature to mention is the observed anomalous upper level convergence (divergence) centre, as described by the anomalous velocity potential and divergent winds, over the SESA region during El Niño Modoki (El Niño) conditions. In particular, the convergence (divergence) centre is associated with an anomalous downward (upward) motion which is unfavourable (favourable) for local convection and rainfall over this area during El Niño Modoki (El Niño) conditions. Further, during El Niño Modoki, the anomalous divergent wind suggests an anomalous upward motion in the subtropical Atlantic in conjunction with compensatory subsidence over the SESA region, whereas during El Niño conditions the weakened local Hadley cell over the continent provides favourable conditions for anomalous upward (downward) motion and positive (negative) rainfall anomalies over the SESA (tropical) region. We also examined the local Hadley circulation over the continent during El Niño Modoki conditions (Figure not shown) and just a weak and not well organised meridional cell was observed, this issue may require further analysis.

Finally, it is worth mentioning that the lack of ocean-atmosphere feedback in the simulations may account for some of the large scale differences, especially in the associated fields of El Niño Modoki.

Chapter 6

Anomalous conditions of El Niño and El Niño Modoki events and their impacts during the winter and spring seasons

As the strongest rainfall signal over the continent is found during the austral summer and autumn, this chapter provides a limited revision of the more relevant features associated with El Niño and El Niño Modoki conditions. The analysis focuses on the major differences between the interannual events, i.e. the vertical circulation during the austral winter and on the upper level circulation during spring. The winter and spring periods are the prior seasons to the mature stage of El Niño and El Niño Modoki in summer.

6.1 The winter season

6.1.1 Assessing coupled modes of SST and rainfall variability

Figure 6.1 displays the first mode of covariability between the anomalous SST and South American rainfall during the winter period. This mode accounts for 29% of the total square covariance fraction, and it is a strongly coupled oscillation as the correlation between the expansion coefficient time series (black and red lines) is 0.63. The spatial SST mode shows a typical El Niño pattern with strong positive loading over the eastern equatorial Pacific region. The spatial mode associated with anomalous rainfall depicts positive loading over the subtropical area including the SESA region, whereas the occurrence of negative loading prevails over the northern portion of the continent and mostly confined over the Northern Hemisphere. The positive loading over the subtropics bear some degree of resemblance with the corresponding patterns of the summer and autumn periods, however they seem to be slightly shifted northward (Figs. 4.5, 5.5, 6.1). Similar spatial features in both the anomalous SST and rainfall fields are shown by Grimm (2010). The EOF analysis undertaken for the rainfall anomalies accounts for 25.33% of the total variance of the winter season during the period 1961-2000.

This leading mode is well separated from the second coupled as there is a large distance between their corresponding eigenvalues taking into account the associated standard errors by North et al. (1982). The correlation coefficient between the NINO3 index and the expansion coefficient time series is 0.96, statistically significant at the 95% confidence level.

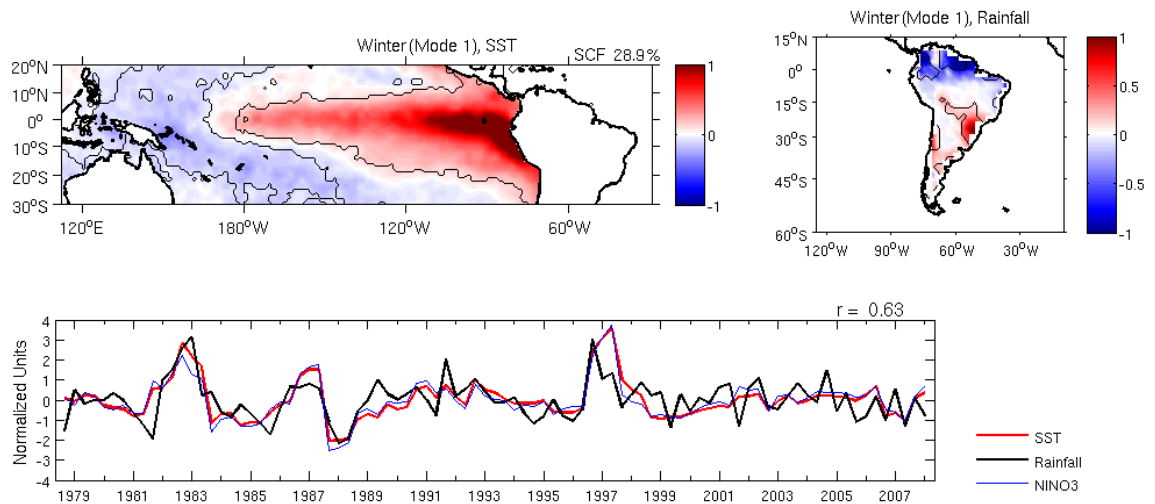


Figure 6.1: The first mode of an SVD analysis between the SST (left) and rainfall anomalies (right) during the austral winter period. It accounts for $29.0 \pm (7.5)$ % of the square covariance fraction (SCF). Black contours indicate statistical significant regions at the 90% confidence level according to a two-tailed Student t-test. Time series of the SVD expansion coefficient (below). Red (black) line is associated with the SST (rainfall) mode. The coupling strength (r) between these fields is 0.63. The thin blue line represents the NINO3 index. The correlation coefficient between the SST mode (red) and the NINO3 index (blue) is 0.96. The correlations are statistically significant at the 95% confidence level.

The second coupled mode of co-variability is shown by Figure 6.2. It explains approximately 10% of the total square covariance fraction. The anomalous SST and rainfall fields are strongly coupled as the correlation coefficient between both expansion coefficient time series is 0.58. Following North et al. (1982) we found that its associated standard error is comparable to the distance between the eigenvalues of second and third modes of co-variability, i.e. the latter accounts for 8.5% of the square covariance fraction, implying some degree of contamination. However, we regard this mode as a physical oscillation associated with the winter period of El Niño Modoki events. We support this with the high correlation between the EMI index and the associated expansion coefficient time series of the SST mode which is 0.82, significant at the 95% confidence level. Furthermore, the composite analysis also supports the main anomalous features of this rainfall mode as shown in the observed anomalous rainfall composited in Figure 6.4b (Section 6.1.3). The spatial SST mode displays the

typical anomalous gradient along the equator as described by Ashok et al. (2007) and Weng et al. (2007), whereas its associated time series (red line) seems to show some decadal variability especially after 1988. Weng et al. (2007) show evidence of decadal variability in the EMI index via wavelet analysis.

The spatial rainfall mode is better defined over the equatorial areas and also northward of the equator. It shows contrasting positive loading over the northern portion of the continent compared to the corresponding rainfall pattern associated with the first mode (Figs. 6.1, 6.2), whereas not well defined anomalous pattern is found over the subtropics. This rainfall pattern is in agreement with that shown by Weng et al. (2007), who found positive anomalous rainfall over the northeastern portion of South America straddling the equator. As we found significant and contrasting results over the equatorial portion of the continent between both interannual events, the remaining emphasis will be on the anomalous Walker circulation cell.

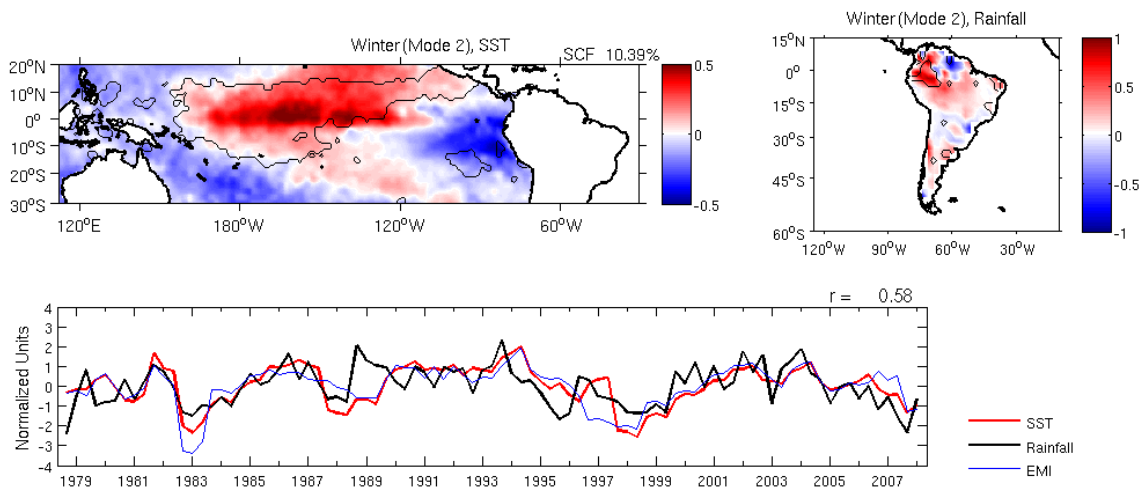


Figure 6.2: The second mode of an SVD analysis between the SST (left) and rainfall anomalies (right) during the austral winter period. It accounts for $10.4 \pm (2.6)$ % of the square covariance fraction (SCF). Black contours indicate statistical significant regions at the 90% confidence level according to a two-tailed Student t-test. Time series of the SVD expansion coefficient (below). Red (black) line is associated with the SST (rainfall) mode. The coupling strength (r) between these fields is 0.58. The thin blue line represents the EMI index. The correlation coefficient between the SST mode (red) and the EMI index (blue) is 0.82. The correlations are statistically significant at the 95% confidence level.

In order to provide additional evidence of the statistical links between these fields, Figure 6.3 shows the correlation map between the rainfall time series of the first and second mode SVD analyses (PC1 and PC2 respectively) and the SST anomalies during the winter period. The correlations associated with the leading mode reveal significant and positive coefficients in the eastern-to-central equatorial Pacific resembling to an El-Niño-like signal (upper panel), similarly positive correlations are found over the extratropical areas of the northern and southern Pacific respectively. Negative correlations are seen over the equatorial and subtropical western Pacific Ocean, as well as the equatorial Atlantic Ocean. Over the Indian Ocean basin, positive correlations are seen along the eastern coast of the African continent. A similar pattern of correlations between the South American rainfall anomalies and remote SST anomalies during El Niño events during this period has been reported by Grimm (2010).

The correlation map between the expansion coefficient time series associated with the second rainfall mode (PC2) and the SST anomalies displays a distinct connection compared to El Niño conditions (Fig. 6.3 lower panel). First, over the Pacific Ocean the equatorial pattern resembles to a Modoki-like structure. Over the extratropics positive anomalies are around the international dateline south of New Zealand, whereas north of New Zealand the correlations are mainly negative. Additionally, this anomalous South American rainfall mode is also negatively correlated with the SST anomalies located in the southern tip of the continent, contrasting with El Niño conditions. Second, significant negative correlations link South American rainfall with tNA and North Atlantic Ocean. Although these regions are not significant during El Niño conditions, they are mostly the opposite during El Niño Modoki (compare upper and lower panel). Along the coastal region of the subtropical North Atlantic Ocean positive correlations are registered. Finally, negative correlations are observed over the tropical Indian Ocean during El Niño Modoki conditions, whereas positive correlations occur for El Niño case instead.

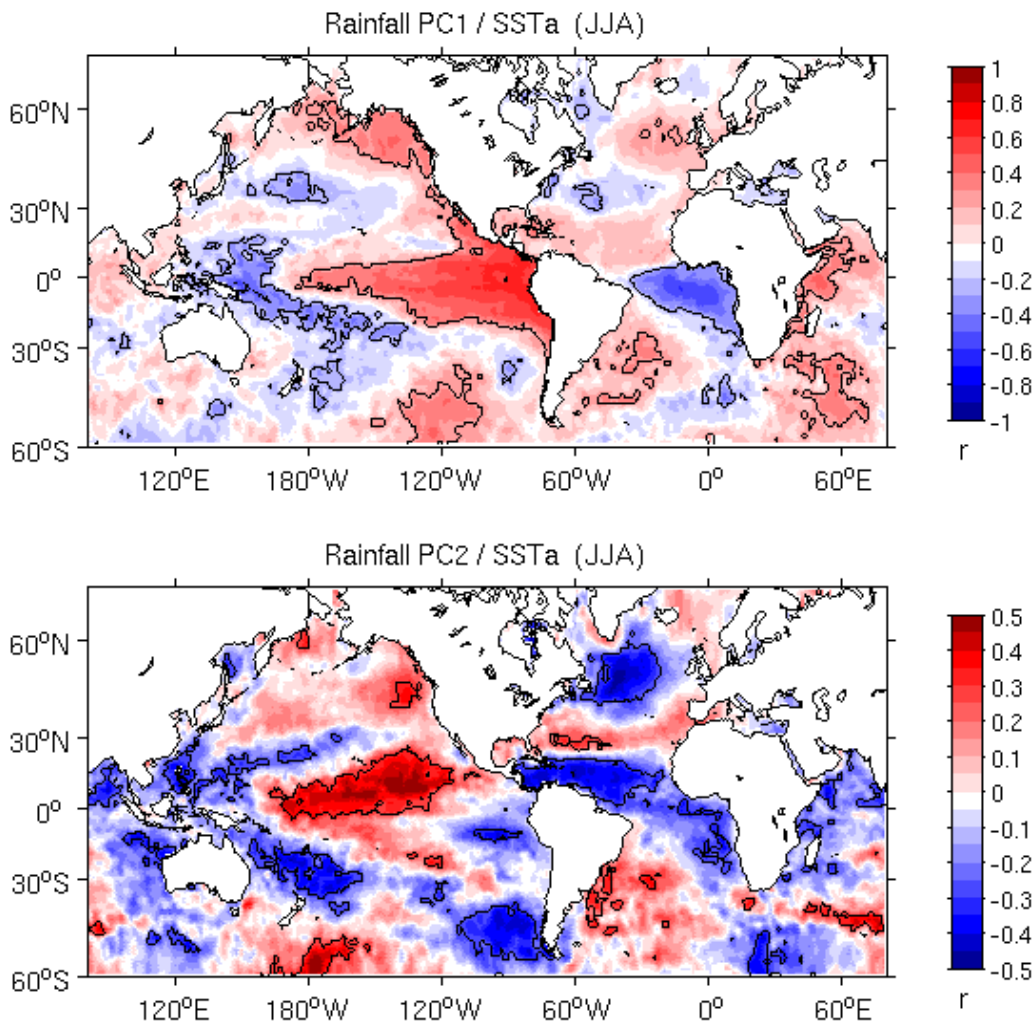


Figure 6.3: Correlation between the expansion coefficient time series of the first (upper panel) and second (lower panel) rainfall modes of variability, PC1 and PC2 respectively, with the monthly SST anomalies during the austral winter period. The black contours encompass areas where the correlations are statistically significant at the 90% confidence level.

6.1.2 AGCM perturbation experiments: Anomalous Rainfall

Figure 6.4 shows the composites of anomalous observed and modelled rainfall during El Niño and El Niño Modoki conditions. The perturbation experiments undertaken for El Niño conditions (Figs. 6.4c,e), i.e. EN-P and EN-PA, simulate the main observed characteristics reported in the SVD analysis (Fig. 6.1) and those observed in the anomalous rainfall composite (Fig. 6.4a). In particular the observed negative rainfall anomalies over the tropics are reasonably well simulated in both experiments, whereas the positive anomalies over the subtropics are underestimated. The impacts of the Atlantic SST anomalies are confined over the tropical region (Fig. 6.4g). In particular, the positive rainfall anomalies over the tNA region are associated with the

climatological position of the Atlantic ITCZ (Zhou and Lau, 2001; Cook, 2009) and to warm-to-normal SST conditions in this region (e.g. Figs. 3.7,6.3). This condition seems to enhance the magnitude of the negative rainfall anomalies over equatorial South America in the EN-PA experiment (Figs. 6.4e,g). Over the subtropical areas of the continent, the positive rainfall anomalies are less extensive and weakened in response to the Atlantic forcing (Figs. 6.4c,e,g).

The observed anomalous rainfall characteristics during El Niño Modoki conditions exhibits similar features to the precipitation pattern of the second SVD mode (Figs. 6.2, 6.4b), such as the positive rainfall anomalies over the northwest region.

The perturbation experiments ENM-PA and ENM-P do not capture well the observed rainfall pattern over South America (Fig. 6.4d,f). In particular, negative rainfall anomalies predominate over the northern portion of the continent instead. These anomalies are, however, weaker compared to El Niño experiments (Figs. 6.4c,d,e,f,i,j). This is more evident when SST anomalies are prescribed over the Atlantic Ocean as depicted by the positive anomaly difference between the ENM-PA and EN-PA experiments (Fig. 6.4j). Over the subtropics the simulated rainfall anomalies are mainly positive (Figs. 6.4d,f). However, their magnitude is also weaker compared to El Niño experiments, which is better represented by the negative anomaly difference between the corresponding experiments, namely ENM-P minus EN-P and ENM-PA minus EN-PA (Figs. 6.4i,j). The precipitation response to El Niño Modoki and Atlantic SST (Figs. 6.4f,h) shows less rainfall over the ITCZ and more rainfall over the subtropical South Atlantic in the ENM-PA compared to the ENM-P experiment. It is worth noting that the correlation coefficient map between the second mode of rainfall and anomalous SST (Fig. 6.3) displays positive (negative) values over the subtropical (tropical) South Atlantic region, which a priori supports the simulated rainfall response over the Ocean. However, the observed rainfall composite (Fig. 6.4b) depicts an opposite signal across 30°S over the Atlantic Ocean. While the simulations respond to the ocean conditions, it is possible that in reality the observed negative rainfall is a response to atmosphere conditions instead. The lack of ocean-atmosphere in the experiments would thus explain the difference in rainfall pattern between observed and simulated fields during El Niño Modoki conditions.

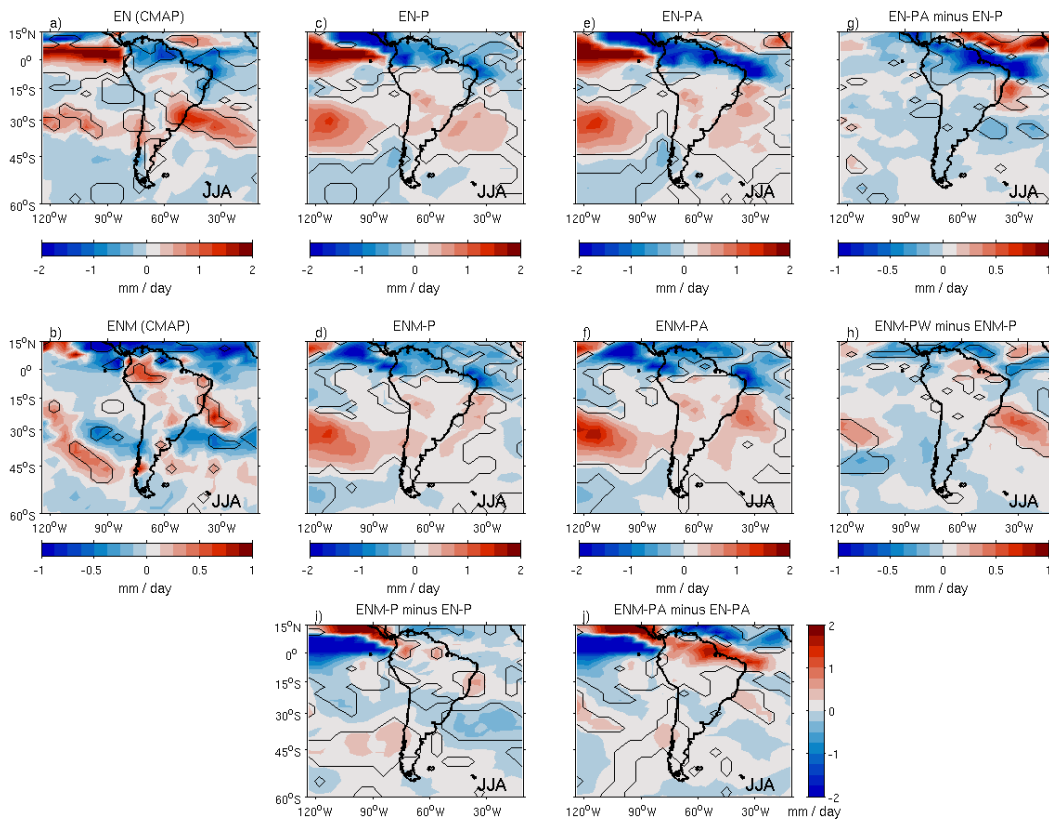


Figure 6.4: Observed rainfall anomalies for (a) El Niño, (b) El Niño Modoki. Modelled rainfall anomalies for (c) El Niño (EN-P), (d) El Niño Modoki (ENM-P), and including the perturbation experiments forced with SST anomalies over the Atlantic Oceans according to (e) EN-PA, (f) ENM-PA, and including the difference between (g) EN-PA minus EN-P, (h) ENM-PA minus ENM-P, (i) ENM-P minus EN-P and (j) ENM-PA minus EN-PA perturbation experiments. Black contours represent statistically significant regions at the 90% confidence level according to a two-tailed Student t-test.

6.1.3 Vertical circulation

The observed anomalous vertical circulation during El Niño conditions (Fig. 6.5a) features anomalous uplift over the central-to-western equatorial Pacific in conjunction with anomalous downward motion elsewhere. They represent a shift in the Walker circulation cell respectively. In particular, the overall pattern share the same large scale characteristic compared to the previous seasons (Figs. 4.14, 5.12) except for a weaker anomalous downward motion over the eastern equatorial Pacific. It is worth mentioning that the occurrence of the local baroclinicity in the anomalous vertical velocity over the eastern equatorial region of the continent during El Niño conditions is likely to be a partial contribution of the vertical velocities averaged over the Southern Hemisphere that is part of the 10°N-10°S zonal band used to represent the associated Walker circulation.

In response to the warm SST during El Niño Modoki events, an anomalous upward motion is mostly found over the central-to-western equatorial Pacific (Fig. 6.5b), whereas the eastern side of the basin features weak anomalous downward motion contrasting with the anomalous vertical circulation found during El Niño conditions (Figs. 6.5a,b). Weak anomalous ascending branches occur over the eastern and western coasts of South America, providing favourable conditions for anomalous precipitation (Figs. 6.2,6.4b,6.5b). This feature is not seen over the continent during El Niño events, as the entire tropical area is mostly covered by anomalous subsidence instead and consequently with the opposite effects in anomalous precipitation (Figs. 6.4a,6.5a,b). Finally, the equatorial Atlantic Ocean shows weaker anomalous downward conditions compared to El Niño.

The perturbation experiments undertaken for El Niño conditions, i.e. the EN-P and EN-PA, represent the main observed conditions associated with the observed anomalous Walker circulation (Figs. 6.5a,c,e), namely strong (weak) anomalous upward motion over the central (eastern) equatorial Pacific and anomalous downward motion elsewhere. The anomalous cool SST conditions in the equatorial Atlantic increase the local anomalous downward motion over the ocean and the continent, as depicted by the difference between the EN-PA minus EN-P experiments (Fig. 6.5g). This is in agreement with the stronger negative rainfall anomalies over the equatorial regions in the EN-PA experiment (Figs. 6.4e,g).

The El Niño Modoki experiments simulate ascending motion over western Pacific and a strong compensatory subsidence anomaly over Indonesian longitudes (Figs. 6.5d,f). This anomalous downward motion contrasts with observations (Figs. 6.5b,d,f). During El Niño Modoki, the anomalous SST conditions over the equatorial Atlantic are similar compared to El Niño events (Figs. 6.3, 6.5a), consequently the response in the anomalous vertical circulation due to the Atlantic influence (Fig. 6.5h) also corresponds to an anomalous local subsidence over equator. Over South America, however, this anomalous branch is weakened in the ENM-PA experiment, contrasting with the response during the EN experiment.

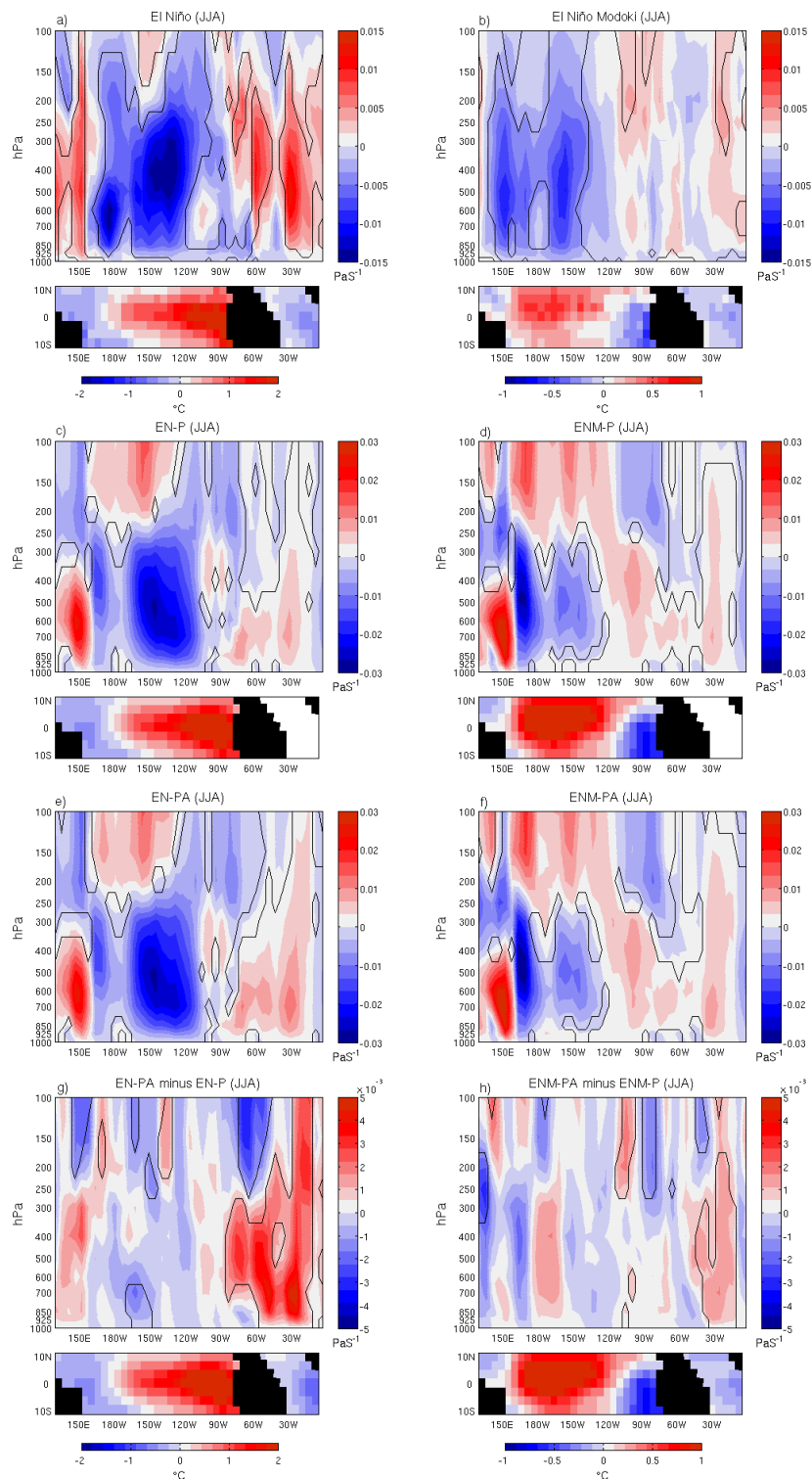


Figure 6.5: Composites of the observed vertical velocity anomalies during (a) El Niño and (b) El Niño Modoki events (See Table 3.1). The simulated vertical velocity anomaly for (c) EN-P, (d) ENM-P, (e) EN-PA, (f) ENM-PA, and the vertical velocity anomaly difference between (g) EN-PA minus EN-P, and (h) ENM-PA minus ENM-P perturbation experiments. The vertical velocity was averaged over the 10°N-10°S latitudinal band. Blue (red) shading is associated with upward (downward) motion. The associated SST anomalies (°C) are shown below. Black contours represent statistically significant regions at the 90% confidence level according to a two-tailed Student t-test.

6.2 The spring season

6.2.1 Assessing coupled modes of SST and rainfall variability

The first mode of co-variability between the anomalous SST and South American rainfall during the austral spring period is shown in Figure 6.6. The SST spatial mode features strong positive loading spanning the central-to-eastern equatorial Pacific and negative loading over the western Pacific, representing the typical anomalous conditions during El Niño events (Philander, 1990; Trenberth and Caron, 2000; Latif and Keenlyside, 2009). This field co-oscillates in conjunction with positive (negative) loading over the subtropical (tropical) South America. These fields together explain approximately 32% of the square covariance fraction. The coupling strength is high, as the correlation coefficient between both times series is 0.61, significant at the 95% confidence level.

Grimm and Zilli (2009) reported, via an EOF analysis, a similar anomalous distribution compared to our first rainfall mode. In this mode, however, the positive loading over the subtropics tend to spread southward. That feature is part of the first EOF mode that accounts for 18.5% of total rainfall variance for the period 1961-2000. Grimm (2010) also presented a similar anomalous rainfall structure for the same period using principal component analysis. Their leading mode accounts for 30.16% of the rainfall total variance. In both studies the rainfall mode is connected with ENSO.

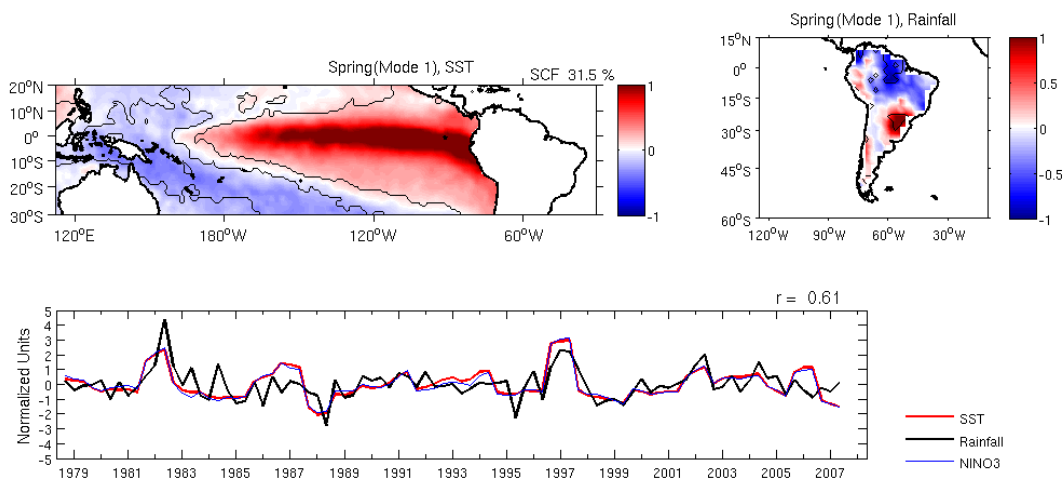


Figure 6.6: The first mode of an SVD analysis between the SST (left) and rainfall anomalies (right) during the austral spring period. It accounts for $31.5 \pm (8.4)$ % of the square covariance fraction (SCF). Black contours indicate statistical significant regions at the 90% confidence level according to a two-tailed Student t-test. Time series of the SVD expansion coefficient (below). Red (black) line represents the SST (rainfall) mode. The coupling strength (r) between these fields is 0.61. The thin blue line represents the NINO3 index. The correlation coefficient between the SST mode (red) and the NINO3 index (blue) is 0.99. The correlations are statistically significant at the 95% confidence level.

The second mode of covariability between the anomalous SST and South American rainfall explains approximately 10% of the square covariance fraction and is shown in Figure 6.7. The SST spatial mode features an anomalous gradient along the equator with positive loading over the central Pacific encompassed by negative loading at the eastern and western equatorial sides of the basin. This SST mode oscillates with positive loading over the western equatorial and subtropical South America, whereas weak and negative loading are found over the eastern equatorial and tropical regions. The positive anomalous signal is shifted to south compared to El Niño-related impacts (Figs. 6.6,6.7). The coupling strength between these fields is also strong, the correlation coefficient is 0.59. Furthermore, the correlation coefficient between the SST expansion coefficient time series and the EMI index is 0.95, therefore the second mode represents El Niño Modoki events and their associated impacts during the spring season.

It is worth mentioning that the positive loading in the rainfall field of the second mode located over the subtropics is shifted southward compared with its counterpart of the first mode (Figs. 6.6, 6.7). Additionally, our first and second modes are well separated from the second and third modes of covariability respectively according the suggested criterion of North et al. (1982). The third coupled mode of anomalous SST and rainfall variability accounts for 4.8% of the square covariance fraction and is not regarded in this thesis.

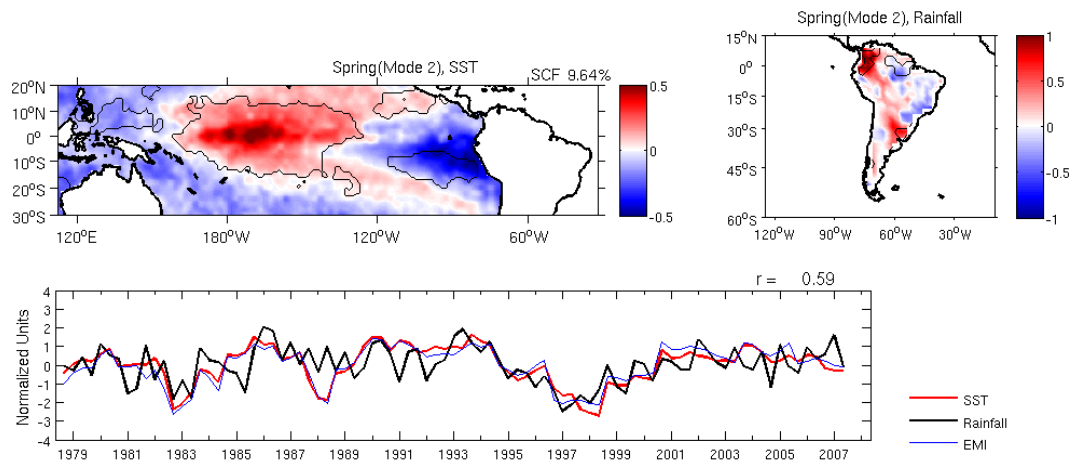


Figure 6.7: The second mode of an SVD analysis between the SST (left) and rainfall anomalies (right) during the austral spring period. It accounts for $9.6 \pm (2.5)$ % of the square covariance fraction (SCF). Black contours indicate statistical significant regions at the 90% confidence level according to a two-tailed Student t-test. Time series of the SVD expansion coefficient (below). Red (black) line is associated with the SST (rainfall) mode. The coupling strength (r) between these fields is 0.59. The thin blue line represents the EMI index. The correlation coefficient between the SST mode (red) and the EMI index (blue) is 0.95. The correlations are statistically significant at the 95% confidence level.

As for the austral autumn in the previous chapter, the impacts of Inter El Niño variations onto South American climate during spring have received less attention than during summer. The only possible comparison with previous studies is the EOF analysis of the South American rainfall anomalies during the spring period undertaken by Grimm and Zilli (2009). In particular, they presented a second mode of rainfall variability that explains 16.7% of the total rainfall variance for the period 1961-2000, and is also well correlated with an ENSO-like signal over the eastern equatorial Pacific, clearly contrasting with our SST mode. Furthermore, their second rainfall mode does not share the same features compared to our second mode. Grimm and Zilli (2009) show a well defined dipole-like oscillation with positive anomalies over part of southeastern South America and south of Central Brazil, whereas negative anomalies predominate over equatorial South America. This is a distinct signal compared to our second rainfall mode which shows a small dipole-like pattern over equatorial South America in conjunction with positive rainfall anomalies over subtropical latitudes.

Figure 6.8 shows the correlations between the SST anomalies and the rainfall expansion coefficient time series of the two leading SVD modes. The connections between the leading mode of the South American rainfall and SST anomalies during the spring period tend to be more correlated over the Southern Hemisphere (Fig. 6.8, upper panel). In particular, the analysis shows an El Niño-like pattern with positive correlations over the central and eastern tropical Pacific. Similar correlations are also

found over the extratropical South Pacific and along the eastern African coast over the Indian Ocean. Negative correlations dominate over the western Pacific protruding into the subtropical latitudes of both hemispheres, whereas some weak and negative (positive) correlations are also detected along the equatorial (subtropical South) Atlantic Ocean.

The second mode of rainfall associated with El Niño Modoki conditions shows broader remote connections compared to El Niño conditions (Fig. 6.8, lower panel). In particular the equatorial Pacific features a Modoki-like signal with positive (negative) correlation over the central (eastern and western) equatorial Pacific, whereas the subtropical regions of both hemispheres tend to be negatively correlated. Positive correlations are also found over the northeastern Pacific Ocean. The second mode of rainfall is negatively correlated with the surrounding regions of the Drake Passage in the Southern Ocean, likewise over most of the North Atlantic Ocean excepting the western area, where the correlations are the opposite. The eastern Indian Ocean is also significant and negatively correlated with the second mode of South American rainfall.

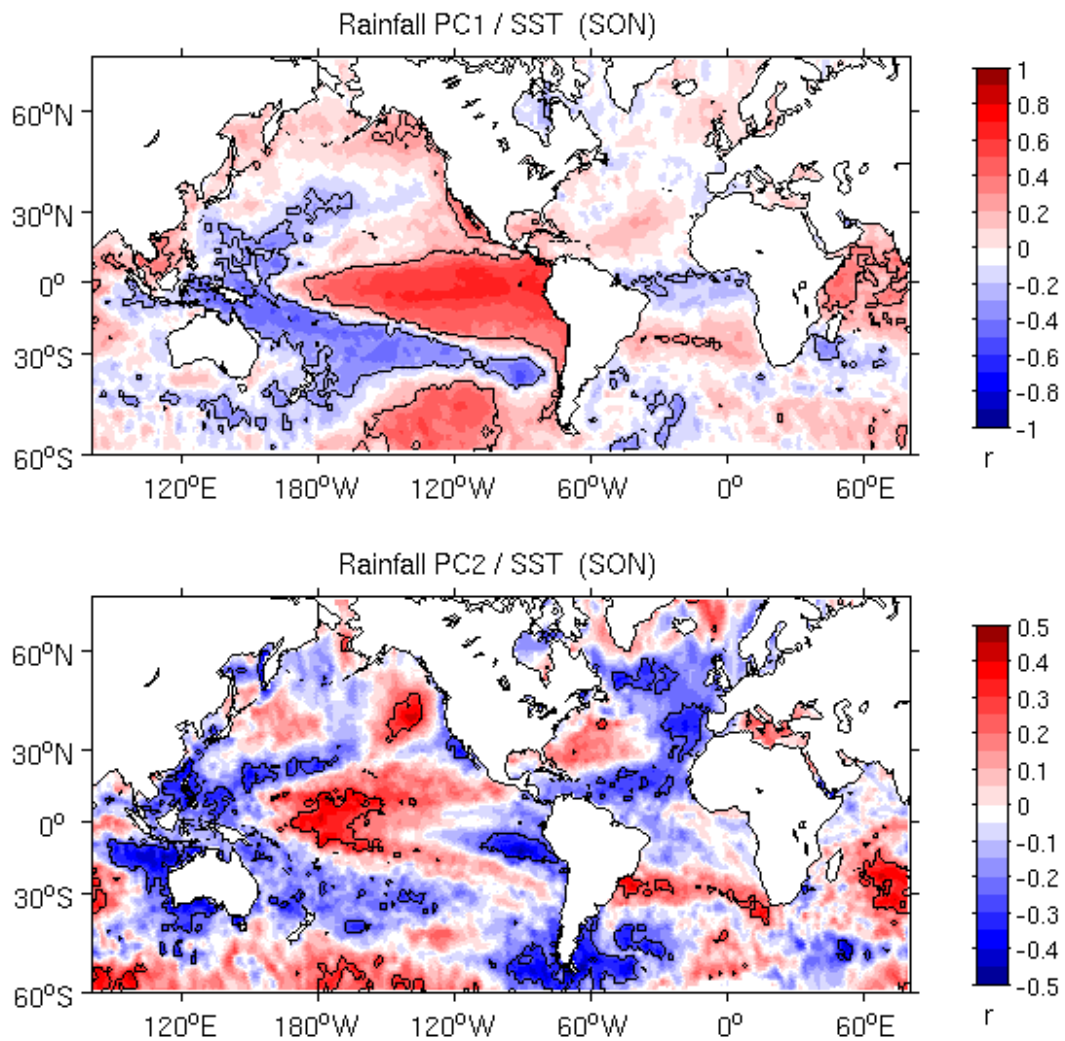


Figure 6.8: Correlation between the expansion coefficient time series of the first (upper panel) and second (lower panel) rainfall modes of variability, PC1 and PC2 respectively, with the monthly SST anomalies during the austral spring period. The black contours encompass areas where the correlations are statistically significant at the 90% confidence level.

6.2.2 AGCM perturbation experiments: Anomalous Rainfall

Figure 6.9 shows the composites of anomalous observed and modelled rainfall during El Niño and El Niño Modoki conditions. The positive (negative) loading over the SESA (tropics) during El Niño conditions captured in the SVD analysis are also well represented in the observed composite of anomalous rainfall (Figs. 6.6,6.9a). The AGCM perturbation experiments representing El Niño conditions (Figs. 6.9c,e), namely EN-P and EN-PA, simulate some of the main observed anomalous features except for the positive anomalous rainfall over the eastern equatorial coast of the continent. The positive anomalies over the subtropics, i.e. associated with the SESA region, are clearly weak in the model compared with observations, whereas the predominance of

negative anomalies over the tropics seems to be well simulated. The response of the anomalous rainfall to the Atlantic influence (Figs. 6.9e,g) depicts positive rainfall anomalies over Northeast Brazil and the surrounding regions. Over the continent, the negative and positive anomalies over the tropics and subtropics respectively tend to be stronger in the EN-PA compared to the EN-P experiment.

The main observed features in the composite of anomalous rainfall during El Niño Modoki conditions are also in agreement with the results shown by the second mode of anomalous rainfall (Figs. 6.9b, 6.7). The AGCM perturbation experiments (Figs. 6.9d,f), namely ENM-P and ENM-PA, show that the negative rainfall anomalies over the South American tropics are in agreement with the observed conditions (Figs. 6.9b,d,f). However, the anomalous positive rainfall over SESA and subtropical South Atlantic is not captured in the experiments. The observed positive rainfall anomalies over the eastern equatorial coast of South America are weakly captured in the ENM-P and ENM-PA experiments (Figs. 6.9b,d,f), however, in the simulations they tend to be located over the Southern Hemisphere compared to observations.

The Atlantic influence in the simulated rainfall anomalies is depicted in the Figure 6.9h. It reveals stronger negative (positive) rainfall anomalies over the tropics (subtropics) in the ENM-PA compared to the ENM-P experiment. Increased rainfall anomalies are also seen over the subtropical southern Atlantic in the ENM-PA experiment. Thus anomalous Atlantic SST conditions tend to reinforce the anomalous precipitation over the continent during the spring season of El Niño Modoki conditions.

Based on AGCM experiments, SVD and composite analyses, there are few slight changes in the anomalous rainfall pattern between El Niño and El Niño Modoki. For instance, over the subtropical regions observations show positive rainfall anomalies during El Niño conditions to the north of SESA region while during El Niño Modoki the positive rainfall occurs over SESA (Figs. 6.6,6.7,6.9a,b). Despite weaker magnitudes, this shift is represented in the perturbation experiments. In particular in the EN-P there are positive anomalies just north of 30°S throughout the continent, whereas in the ENM-P the eastern coast is mostly negative and positive anomalies tend to predominate south of the SESA region as in observations (Figs. 6.9c,d).

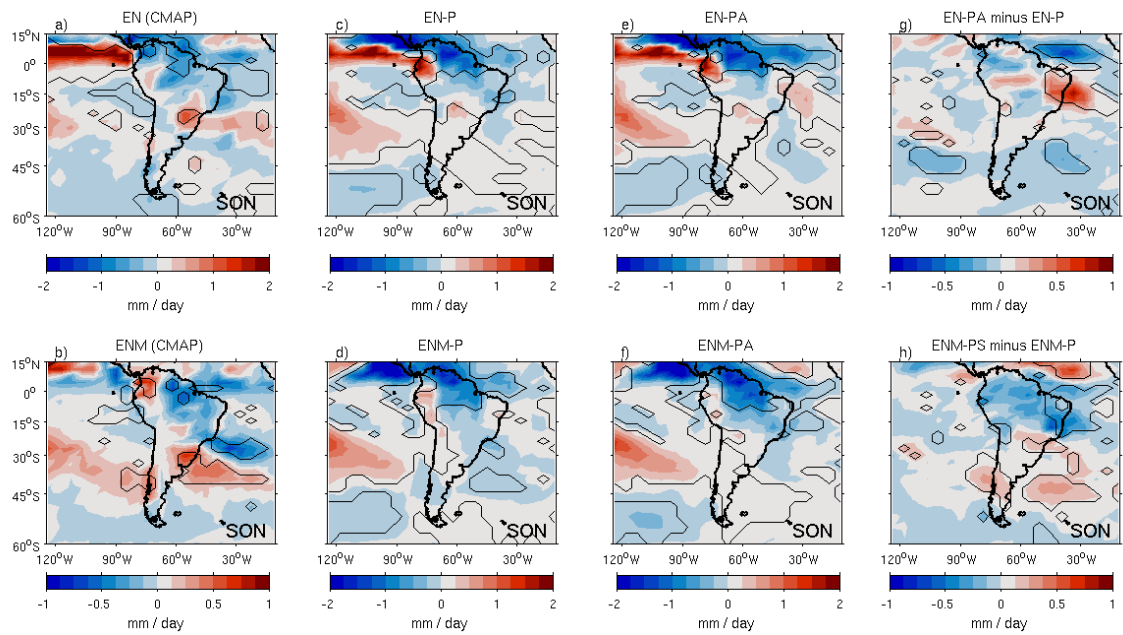


Figure 6.9: Observed rainfall anomalies for (a) El Niño, (b) El Niño Modoki. Modelled rainfall anomalies for (c) El Niño (EN-P), (d) El Niño Modoki (ENM-P), and including the perturbation experiments forced with SST anomalies over the Atlantic Oceans according to (e) EN-PA, (f) ENM-PA, and including the difference between (g) EN-PA minus EN-P, (h) ENM-PA minus ENM-P. Black contours represent statistically significant regions at the 90% confidence level according to a two-tailed Student t-test.

6.2.3 Lower level circulation

Figure 6.10 displays the regressed fields of the observed SLP and 850-hPa horizontal winds anomalies onto the NINO3 and EMI indices and the composites of the corresponding perturbation experiments during the austral spring period. During El Niño conditions there is an anomalously strong meridional flow represented by the SALLJ (Fig. 6.10a). The SALLJ tends to converge in the coastal region of northern SESA with the western flank of a large scale cyclonic anomaly at the South Atlantic Ocean. This convergence zone is in agreement with positive rainfall anomalies reported in the SVD and composites analyses (Figs. 6.6, 6.9a).

The observed anomalous circulation during El Niño Modoki conditions shows an anomalous low level convergence zone over the southern SESA region, whereas an anomalous cyclonic pattern found northward over the continent seems to weaken the climatological SALLJ that typically brings moisture toward the SESA region (Vera et al., 2006). The occurrence of an oceanic anomalous anticyclone approximately centered at 30°S - 30°W seems to play an important role in the associated moisture transports toward the southern SESA region but also in the reinforcement of the anomalous

cyclone located over the continent. The occurrence of a positive signal over southern SESA is in agreement with the two major pathways of moisture supply, which are located over the tropics and the subtropics as shown by Vera et al. (2006). We suggest that the occurrence of this oceanic anticyclonic anomaly is a consequence of wave-like propagations emanating from the central equatorial Pacific toward the subtropics via the extratropical regions and consequently affecting the subtropical circulation and the anomalous rainfall there. The next section will show more evidence to confirm this.

The perturbation experiments undertaken for El Niño and El Niño Modoki conditions (Figs. 6.10c,d,e,f), namely EN-P, ENM-P, EN-PA and ENM-PA, show a strong easterly flow over the equatorial portion of the continent, which is not supported by the observations. However, the experiments undertaken for El Niño conditions show a weak anticyclonic circulation resembling the observed weakened subtropical Atlantic high (Figs. 6.10a,c,e). This feature is not simulated in the ENM-P and ENM-PA perturbation experiments (Figs. 6.10c,d,e,f).

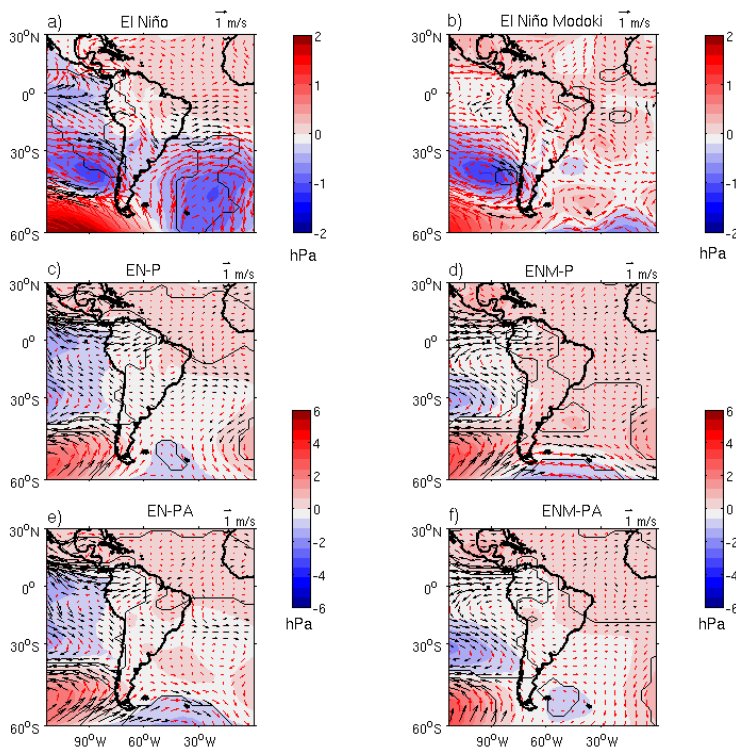


Figure 6.10: Regression of the observed anomalous 850-hPa winds (vectors) and SLP (shading) for the spring period during (a) El Niño, and (b) El Niño Modoki onto the SST PC1, PC2 time series respectively. The simulated anomalous 850-hPa winds and SLP composites of (c) EN-P, (d) ENM-P, (e) EN-PA, and (f) ENM-PA perturbation experiments. Black contours (vectors) represent statistically significant regions (pixels) at the 90% confidence level according to a two-tailed Student t-test.

6.2.4 Upper level circulation

Figure 6.11 shows the evolution of the anomalous 200-hPa geopotential height and horizontal wind anomalies from the austral spring (SON) through the summer (DJF) period during El Niño and El Niño Modoki conditions via lagged composites. The lagged regressed patterns onto the NINO3 and EMI indices also display essentially the same features (not shown). In particular, the left panel reveals the progressive strengthening of the anomalous anticyclones straddling the equator from the spring (SON) through the summer (DJF) when the upper level easterlies are fully developed. Furthermore, a significant enhancement of the Subtropical Jet is observed over the SESA region from the spring (SON) through the mid-summer (NDJ), peaking by the mid-spring period (OND) during El Niño conditions. This Subtropical Jet has been associated with a strengthening of the SALLJ favouring anomalous precipitation over this region during El Niño conditions (Silva and Ambrizzi, 2006; Grimm and Zilli, 2009; Silva et al., 2009). The peak of this anomalous upper level jet agrees with the findings reported by Cazes Boezio et al., (2003) and Grimm and Zilli (2009).

The evolution of the anomalous upper level circulation during El Niño Modoki conditions also tends to peak by the OND period (right panel in Fig. 6.11). However, the overall pattern is rather distinct compared to El Niño events. The upper level wave-like propagations during El Niño Modoki are more evident and clearer during the OND period, suggesting the importance of the extratropical circulation during El Niño Modoki conditions. Consequently, the observations suggest a different mechanism to be associated with the positive rainfall anomalies over the SESA region, namely wave-like propagations emanating from the central equatorial Pacific toward the subtropics via the extratropics. In particular the anticyclonic anomaly over the SESA region seems to reinforce the low level circulation leading to positive rainfall anomalies over this area and thus implying a barotropic anomalous circulation regime (Figs. 6.7, 6.9b, 6.10b, 6.11), whereas during El Niño conditions the enhanced Subtropical Jet acts to favour the positive rainfall anomalies northward of the SESA region via the anomalously strong SALLJ (Figs. 6.6, 6.9a, 6.10a, 6.11). Silva et al. (2009) associated the strengthening of the SALLJ due to an anomalous upper level anticyclone around the SESA region during El Niño years. The occurrence of the most distinct anomalous upper level feature during El Niño Modoki, namely wave-like propagations, confirms that the atmospheric basic state during the spring period seems to be favourable for upper level wave-like propagations from the tropical central Pacific toward South America via the extratropics as previously noted in other studies (Cazes Boezio et al.,

2003; Grimm, 2003a). Furthermore, Grimm and Zilli (2009) provide observational evidence that these favourable conditions allow such propagations by November.

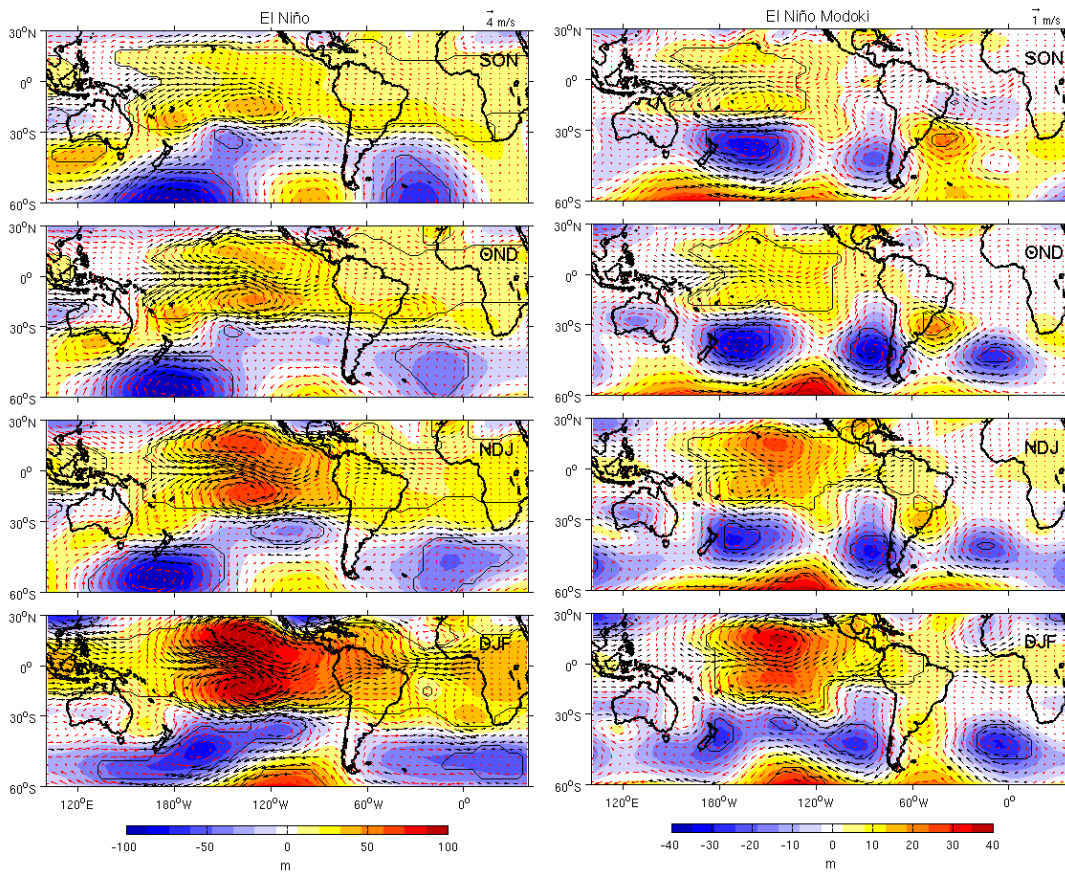


Figure 6.11: (Left panels) Lagged composites of the observed 200-hPa geopotential height and horizontal winds anomalies from the spring throughout the summer season (from top to bottom) during El Niño conditions. (Right panels) As in the left panel but for El Niño Modoki conditions. For the composite years see Table 3.1. Black contours (vectors) represent statistically significant regions at the 90% confidence level according to a two-tailed Student t-test. The composited period is indicated in the upper right corner of each plot.

Figure 6.12 shows the composites of the observed and modelled 200-hPa geopotential height and horizontal wind anomalies during the spring (SON) period. During El Niño conditions the observed anomalous upper level circulation features of the well known pair of anomalous anticyclones straddling the equator over the eastern Pacific (as in the other seasons), which is represented by the AGCM perturbation experiments (Figs. 6.12a,c,e). However, the simulated anticyclones are not well simulated as during the summer period. As in observation, the experiments also reflect the typical perturbations of the anomalous Walker circulation over the equatorial Pacific as reported in the previous chapters.

During El Niño Modoki, the observed anomalous anticyclones straddling the equator are shifted westward compared to El Niño, i.e. west of 120°W, accompanied by two

anomalous cyclones over the eastern equatorial Pacific. The anomalous upper level divergence centre is approximately located at 120°W (Figs. 6.12b). As previously reported, over subtropical South America an anomalous anticyclone predominates contrasting with El Niño conditions (Figs. 6.12a,b).

The AGCM perturbation experiments capture the general characteristics of the anomalous observed upper level circulation. However, there are some slight differences like the location of the anomalous upper level divergence centre. This is located west of 120°W compared to observations (Figs. 6.12b,d,f). Although the experiments do not reproduce the correct position of the observed stationary waves, the experiments undertaken for El Niño Modoki conditions clearly depict the importance of the anomalous upper level circulation as suggested by observations. In particular, the upper level anticyclonic anomaly over the subtropical South America associated with the SESA region, approximately centered at 33°S - 35°W, is reasonably well simulated (Figs. 6.12b,d). This feature contrasts with El Niño experiments, where virtually no rotational anomaly is modelled in the subtropics associated with the SESA region. It is also worth mentioning that the extratropical circulation shows slightly distinct magnitudes during El Niño Modoki experiments compared to El Niño conditions as the increase of the simulated magnitude of geopotential height anomalies over the extratropics (e.g. Figs. 6.12c,d). This fact also suggests that the extratropics may play a role in the propagation of teleconnection patterns as suggested by the observations during El Niño Modoki compared with El Niño events.

The Atlantic influence during El Niño conditions (Figs. 6.12e,g) can also influence the anomalous upper level circulation. The difference between both perturbation experiments, namely EN-P minus EN-PA, reveals a weaker Subtropical Jet in the EN-PA compared to the EN-P experiment (Fig. 6.12g). A similar effect seems to occur during El Niño Modoki conditions, the large scale extratropical circulation is stronger in the ENM-PA than in the ENM-P experiment (Figs. 6.12d,f,h). However over the SESA region, the anomalous anticyclone is weakened instead and slightly shifted northward (Figs. 6.12d,f).

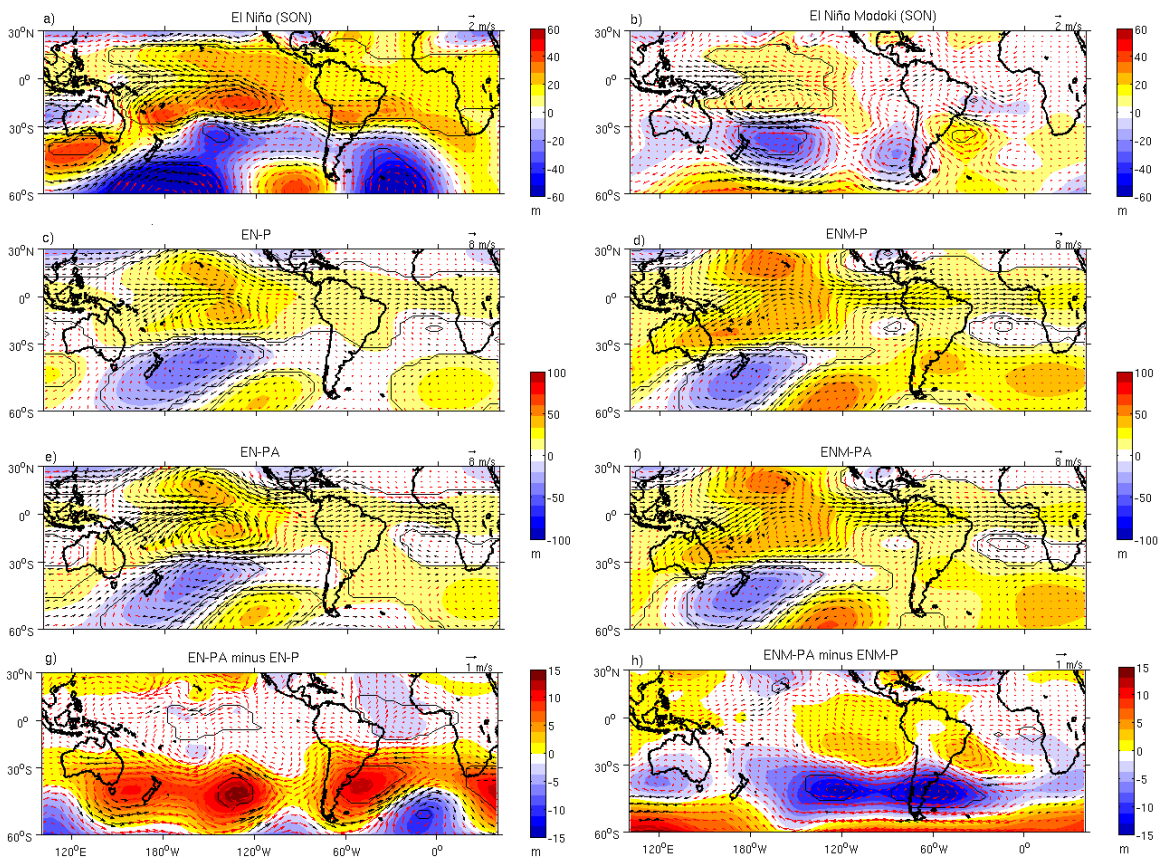


Figure 6.12: Composites of the observed SON 200-hPa wind (vector) and geopotential height anomalies (shading) anomalies during (a) El Niño and (b) El Niño Modoki conditions (See Table 3.1). Simulated 200-hPa wind and geopotential height anomalies for (c) EN-P, (d) ENM-P, (e) EN-PA, and (f) ENM-PA experiments. Difference between (g) EN-PA minus EN-P, and (h) ENM-PA minus ENM-P. Black contours (vectors) represent statistically significant regions at the 90% confidence level according to a two-tailed Student t-test.

6.3 Summary and discussion

During the austral winter period the most significant contrast in anomalous rainfall between El Niño and El Niño Modoki conditions over South America is found over the tropics. In particular, northern South America experiences below (above) average rainfall during El Niño (El Niño Modoki) conditions. During austral spring, negative (positive) rainfall anomalies predominated over the tropics (subtropics), representing El Niño impacts over the continent. However, El Niño Modoki presents only slight deviations compared to the impacts over the subtropics associated with El Niño conditions.

The main findings can be summarized as follows,

El Niño impacts over the continent are represented by negative (positive) rainfall anomalies over the tropics (subtropics) during both the winter and spring seasons. This pattern appears as the first mode in a SVD analysis for austral winter and spring. Besides the connections of the first rainfall mode and SST anomalies over the equatorial Pacific, other remote regions seem to be connected with South American rainfall including the extratropical regions of the Pacific basin, the equatorial Atlantic Ocean and the western Indian Ocean.

The negative rainfall anomalies over the tropics are associated with the anomalous descending branch of the Walker circulation due to anomalous convection activity over the central-to-eastern Pacific. This feature is well represented in the AGCM perturbation experiments during the winter period. Furthermore, the anomalous cool conditions over the equatorial Atlantic act to reinforce the anomalous subsidence over both the ocean and tropical South America and consequently increasing the magnitude of the negative rainfall anomalies. During the spring period, the observed positive anomalies found northward of the SESA region are likely to be also driven by the upper level circulation, specifically by the position of the enhanced Subtropical Jet, which is also supported by the AGCM experiments.

El Niño Modoki impacts during the austral winter and spring periods are represented by the second mode of covariability between the anomalous SST and rainfall. During the winter period, the tropical regions contrast with El Niño conditions, as positive rainfall anomalies predominate there. During spring, the subtropical region features positive rainfall anomalies tending to resemble to El Niño impacts over this area. However, the position of the positive anomalous rainfall signal was found to be located north (south)

of the SESA region during El Niño (El Niño Modoki) conditions. This anomalous signal during El Niño Modoki is likely to be influenced by remote teleconnection from the central Pacific linking South America via a wave-train-like pattern, whereas the anomalous signal during El Niño conditions can be associated with an enhanced SALLJ instead. However, it is worth mentioning that Silva et al. (2011) and references therein suggest that the teleconnection during El Niño events leads to a modification of the waveguide that favours the cyclones passage over the SESA region, thus contributing to enhanced rainfall variability over there. The increase in the cyclone frequency over SESA has not been examined in this study as a higher resolution is needed to assess this source of variability. In our study some distinct remote connections with the SST anomalies also arise when comparing with El Niño conditions, such as over the southern tip of the continent, the tNA region, North Atlantic Ocean and the eastern Indian Ocean basin, they all have some degree of resemblance between the corresponding winter and spring seasons. Finally, the AGCM perturbation experiments clearly support the importance of the anomalous upper level circulation at the extratropics during El Niño Modoki conditions compared with El Niño events.

The most significant and contrasting impacts between El Niño and El Niño Modoki events are found over the tropics during the winter period. The observed positive rainfall anomalies over the northern regions during El Niño Modoki are in agreement with the findings of Weng et al. (2007). They are, however, represented by weaker simulated negative rainfall anomalies compared to El Niño experiments, which is also associated with a corresponding weakening in the anomalous descending branch over the continent. The biases found in the model over this region during the winter period (see section 2.5.1) may account for these anomalies as well as the lack of land-atmosphere coupling. Moreover, during the winter period of El Niño Modoki events the tropical South America is encompassed by cool SST anomalies at both the eastern tropical Pacific and Atlantic oceans respectively. This leads to anomalous descending branches over these oceanic and coastal regions. The lack of anomalous downward motion over the continent compared to El Niño conditions provides favourable conditions for local convection activity over the eastern and western coast of equatorial South America and consequently positive rainfall anomalies tend to predominate there. However during El Niño events, the proximity of a strong anomalous warming and the associated convection activity toward the equatorial coast of the continent leads to an anomalous descending motion throughout the tropical zonal band including the South American continent and the Atlantic Ocean regions. This leads to a stable atmospheric column inhibiting convection activity and consequently negative rainfall anomalies are

observed over these regions. Additionally, the AGCM perturbation experiments suggest that the observed anomalous downward motion over the continent is enhanced if the Atlantic SST conditions are cooler than normal, whereas a similar effect tends to occur over the equatorial Atlantic Ocean during El Niño Modoki except over the continent.

During the spring season contrasting differences are seen in the anomalous upper level circulation between both interannual events. Our observations and experiments of El Niño Modoki conditions indicate the occurrence of an anomalous upper level anticyclone over the SESA region as a consequence of a wave-like propagation emanating from the anomalous convection centre in the central equatorial Pacific, whereas an anomalously strong Subtropical Jet is a feature associated with the canonical El Niño events instead. Sensitivity perturbation experiments undertaken by Hill et al. (2011) show an anomalous anticyclone over the region associated with SESA, when a perturbation is prescribed over the central Pacific. In particular, they remark a Modoki-like anomalous upper level circulation under this forcing. Although the latter study was focused in the summer season, we show the lagged evolution of this anomaly peaking by the mid-spring to early summer (OND) period as also previously reported by other studies (Cazes Boezio et al., 2003; Grimm and Zilli, 2009), and also clearly contrasting with the lagged evolution of the enhanced Subtropical Jet typical of the canonical events. The overall effect of the anomalous upper level anticyclone is to reinforce the low level circulation affecting both the southern SESA and northern South America regions favouring the occurrence of positive rainfall anomalies. However, during canonical El Niño events the positive anomalous rainfall signal is found instead over the northern SESA region as a consequence of an enhanced Subtropical Jet.

We provide relevant evidence about the importance of assessing both interannual events independently to properly evaluate their associated impacts. Many studies report the occurrence of the anomalous anticyclone over the SESA region during El Niño conditions, but this can also be explained by a consequence of contamination from a mixed classification of the interannual events. As mentioned in the introduction (see section 1.1.2), Silva et al. (2009) used the NINO3.4 Index and consequently they classified the interannual events of 1993-1994, 2003-2004 as a neutral years, when they all arguably represent El Niño Modoki conditions in agreement with the suggested classification of Ashok et al. (2007). It worth mentioning that Although Silva et al. (2009) did not look for Inter El Niño variations and their associated impacts, they show an anomalous anticyclone in the region associated with SESA acting to enhance the SALLJ, and therefore favouring the anomalous precipitation over this area. Moreover,

their anomalous upper level anticyclone straddling the equator is accompanied by an anomalous cyclone at the eastern equatorial Pacific resembling our Modoki-type anomalous circulation, further suggesting contamination between canonical El Niño and El Niño Modoki events. In fact, the study case of Silva and Ambrizzi (2006) that focused on the 1997-1998 (El Niño) and 2002-2003 (El Niño Modoki) periods clearly show the most significant anomalous SST and anomalous upper level features in agreement with our results.

Vera et al. (2004) reported a strong (weak) PSA1 mode emanating from the east of the international dateline and linking the extratropics with the subtropical South America during the spring season of El Niño years, when cool (warm) conditions are found in the Subtropical South Central Pacific region in conjunction with strong (weak) convection activity in the SPCZ region, which they called “the WC (WW)” cases. In the WC case, the impact over the SESA region manifests as an upper level cyclonic anomaly at the southern tip of the continent accompanied by an anomalous anticyclone over the subtropics acting to reinforce the SALLJ and thus leading to positive rainfall anomalies over the SESA region as suggested by Grimm et al. (2000). Although we do not explore any potential role of the anomalous SST condition of the subtropical south central Pacific in our results, these previous findings are also likely to be a consequence of a contribution of anomalies from two different El Niño events leading to a mixed characterization of the anomalous circulation and associated fields. Further, in the study of Vera et al. (2004) there are two anomalous characteristics that can be associated with El Niño Modoki events as follows.

Firstly, the occurrence of strong convection activity associated with the SPCZ region during El Niño conditions. This feature has been also associated with El Niño Modoki conditions in response to the anomalous low level wind convergence zone over the central equatorial Pacific (Weng et al., 2007; Weng et al., 2009), which is also supported throughout this thesis. The occurrence of strong convection activity associated with the SPCZ region can induce a secondary Rossby wave source leading to a reinforcement of the extratropical circulation as shown by an increase in the wave flux activity during the conditions shown by Vera et al. (2004).

Secondly, the occurrence of an anomalous upper level anticyclone over the SESA region accompanied by an anomalous cyclone over the southern tip of the continent as previously mentioned. Our observations support the occurrence of an upper level wave-like propagation toward the SESA region via the extratropics, contrasting with the canonical El Niño events. Also, our perturbation experiments further confirm the

important role of the extratropics in the anomalous upper level circulation during El Niño Modoki conditions. Moreover, when prescribing the anomalous SST conditions during the spring period of El Niño Modoki events over the tropical Pacific, namely the ENM-P experiment, an anomalous upper level anticyclone associated with the SESA region is successfully simulated in agreement with observations, whereas in the corresponding El Niño experiment, namely the EN-P experiment, this anomaly is not simulated.

Although the lagged anomalous upper level circulation peaking by the OND period during El Niño Modoki conditions shares a high degree of resemblance to the strong PSA1 mode reported by Vera et al. (2004) during the WC cases, there is a shift in the correct position of the stationary waves around the South American continent. In particular the reported anomalous cyclone over the southern tip of the continent in the study of Vera et al. (2004) is located westward in our study, specifically along the extratropical coast of the eastern South America (Fig. 6.10, during the OND period). It is worth mentioning that, one of the reasons for such difference could be either the anomalous SST conditions over the subtropical south central Pacific region or the NINO3.4 Index used to classify El Niño events and consequently to associate them to a different atmospheric response over the Southern Hemisphere. On the basis that a likely contamination tends to occur when using the NINO3.4 Index, this probably leads them to distinguish two mixed anomalous responses. The “WC” case is the one which tends to partially resemble our Modoki-like classification, which their anomalous SST field tends to show strong SST anomalies toward the central Pacific like in the Modoki-type anomalous SST distribution. However, their WW field shows stronger SST anomalies toward the eastern equatorial coast of South America instead as in the canonical El Niño events. In the same study, another supporting example is also given by the anomalous OLR fields. During the WC (WW) case a strong (weak) convection activity is associated with the SPCZ region as observed during El Niño Modoki (El Niño) events.

Chapter 7

Concluding remarks

From the results presented in this thesis, we can conclude the following:

The El Niño Modoki signal can explain an important portion of the South American rainfall variability throughout the seasons. It shows many contrasting impacts on the anomalous rainfall variability compared with the El Niño events over the tropical and subtropical regions. The mechanisms involved in such variability rely on the shift in the anomalous Walker circulation cell, the strength and position of SALLJ, the strength of the Atlantic ITCZ and finally upper tropospheric wave-like propagations linking the equatorial Pacific with the subtropics. They combined with the anomalous Atlantic SST influence the anomalous rainfall signal. In particular, our results suggest that the upper level wave-like propagation affecting the subtropical regions is a characteristic of El Niño Modoki, whereas the impacts of canonical El Niño events over the subtropics are mostly associated with the anomalously strong SALLJ instead.

During the austral summer period, the second mode of interannual rainfall can be associated with El Niño Modoki conditions, which is represented by both remote and local variability, namely by tropical Pacific and Atlantic SST influences respectively. The combined effects of both a weak magnitude and a westward-shift of the anomalous descending branch over the continent favour convection activity over the SACZ and northern regions. The AGCM experiments during El Niño Modoki conditions suggest that the cold-to-normal SST anomalies over the tropical Atlantic may weaken the magnitude of the anomalous downward motion over the continent. The well known El Niño impact over the tropics is the opposite compared with El Niño Modoki as the occurrence of a strong anomalous descending branch over the tropics associated with the anomalous Walker circulation prevents anomalous convection activity there. Furthermore, the positive rainfall anomalies associated with the SACZ are remotely connected to enhanced anomalous convection activity in the SPCZ region as simulated in the El Niño Modoki perturbation experiments. Over SESA, El Niño Modoki impacts feature negative rainfall anomalies as most of the associated moisture transport is instead advected toward the tropical regions. However, the positive rainfall anomalies occurring over the SESA region associated with El Niño events seem to be only due to an anomalously strong moisture advection of the SALLJ without an evident reinforcing

upper level mechanism as typically reported in the literature. Furthermore, we show a distinct evolution of the anomalous upper level circulation between both interannual events. The typical anomalous anticyclone reported over the SESA region reported during El Niño years is clearly reproduced in this study for El Niño Modoki events and is a consequence of wave-like propagations emanating from the central Pacific during El Niño Modoki peaking by the early summer period. Even though the model does not reproduce the correct position of the stationary waves, the associated perturbation experiments do confirm the importance of the anomalous extratropical circulation during El Niño Modoki compared to El Niño conditions.

During austral autumn, we identify both a direct and indirect mechanism of El Niño Modoki influence on South American rainfall. The direct mechanism relies on the combination of the anomalous warming in the central Pacific combined with the occurrence of positive (negative) SST anomalies over the tSA (tNA) region. It leads to a reinforcement of the convection activity associated with the seasonal southward migration of the Atlantic ITCZ as suggested by the AGCM experiments. This mechanism leads to positive rainfall anomalies over the tropical South America. The resulting anomalous rainfall pattern contrasts with the negative rainfall anomalies typically produced by strong downward motion during canonical El Niño events. This relationship is also supported by the existence of a positive (negative) correlation between the EMI (NINO3) with the rainfall index of northeast Brazil, which can be used as a proxy of the Atlantic ITCZ variability. The indirect mechanism affects both the subtropical and tropical regions. In particular, the low level circulation in the subtropics is influenced by upper tropospheric wave-like propagations during El Niño Modoki conditions. The overall effect is to induce an anomalous anticyclone leading to a divergent flow over SESA and the consequent negative rainfall anomalies, but also to a reinforcement of the anomalous low level cyclone over the continent acting to redirect and weaken the SALLJ, further enhancing rainfall over the tropics. This finding also contrasts with El Niño events, as the significant and positive anomalous rainfall signal over the SESA region is associated with an anomalously strong SALLJ that brings moisture from the tropics toward the subtropics instead.

During the winter period, the most contrasting anomalous signal between both interannual events is found over the tropics. The main responsible mechanism is the shift in the anomalous convective cell between both interannual events, favouring negative (positive) rainfall anomalies during El Niño (El Niño Modoki) events. Over the

subtropics no clear anomalous signal is found during El Niño Modoki, whereas well defined positive rainfall anomalies occur over the subtropics during El Niño conditions.

The spring season is the only period when positive rainfall anomalies are found over the subtropics during El Niño Modoki conditions, whereas positive rainfall anomalies tend to occur over this region throughout the seasons during El Niño events. This anomalous signal is mostly focused south of the SESA region during El Niño Modoki compared to El Niño events and is forced by a barotropic anticyclone as part of upper level wave-like propagations emanating from the central equatorial Pacific. It enhances the associated low level moisture transport toward the subtropical region and its occurrence is confirmed by the AGCM perturbation experiments contrasting with El Niño events. In addition, the low level cyclonic anomaly over the north of the continent redirecting and weakening the climatological SALLJ seems to also be reinforced by the anomalous barotropic anticyclone as in the autumn case. The shift in the position of this barotropic anomaly compared to the autumn period seems to favour the occurrence of positive rainfall anomalies over southern of SESA during El Niño Modoki conditions. During the spring season, the AGCM experiments also resolve the importance of the upper level extratropical circulation during El Niño Modoki compared to El Niño conditions.

Finally it is important to point out that these results may be limited by the coarse resolution of the model employed in this study as stated very early on. Furthermore, the approach adopted here just considers the atmospheric response to an anomalous warming over the ocean, with no inclusion of ocean-atmosphere feedbacks. Therefore, the potential roles of ocean-atmosphere, of importance in the tropical Atlantic, and of coupled land-atmosphere processes have been ignored in this study. Further, we note that our study only covers a single phase of the background low-frequency PDO mode (i.e. warm phase). Despite these limitations, this work has shed new light on the teleconnection between different El Niño events and South American rainfall variability over seasonal to interannual time-scale.

References

- Aceituno, P., 1988: On the functioning of the Southern Oscillation in the South American sector. Part I: Surface climate. *Monthly Weather Review*, **116**, 505-524.
- Alexander, M., and Z. Liu, 2007: Atmospheric bridge, oceanic tunnel and global climatic teleconnections. *Review of Geophysics*, **45**(RG2005), 34.
- Alexander, M., I. Bladé, and M. Newman, 2002: The atmospheric bridge: the influence of ENSO teleconnections on air-sea interactions over the global oceans. *J. Climate*, **15**, 2205-2231.
- Ambrizzi, T., E. B. de Souza, and R. S. Pulwarty, 2005, The Hadley and Walker regional circulations and associated ENSO impacts on South American seasonal rainfall, in *Hadley Circulation: Present, Past and Future*, edited by H. F. Diaz and R. S. Bradley, pp. 203-235.
- Andreoli, R., and M. Kayano, 2005: ENSO-related rainfall anomalies in South America and associated circulation features during warm and cold Pacific decadal oscillation regimes. *International Journal of Climatology*, **25**, 2071-2030.
- Ashok, K., C. Y. Tam, and W. J. Lee, 2009a: ENSO Modoki impact on the Southern Hemisphere storm track activity during extended austral winter. *Geophysical Research Letters*, **36**.
- Ashok, K., S. K. Behera, S. A. Rao, H. Y. Weng, and T. Yamagata, 2007: El Niño Modoki and its possible teleconnection. *J. Geophys. Res.*, **112**, C11007, doi:10.1029/2006JC003798.
- Ashok, K., S. Iizuka, S. A. Rao, N. H. Saji, and W. J. Lee, 2009b: Processes and boreal summer impacts of the 2004 El Niño Modoki: An AGCM study. *Geophysical Research Letters*, **36**.
- Barreiro, M., and A. Tippmann, 2008: Atlantic Modulation of El Niño on summertime rainfall over southeastern South America. *Geophys. Res. Lett.*, **35**(L16704), doi:10.1029/2008GL035019.
- Barreiro, M., A. Giannini, P. Chang, and R. Saravanan, 2004, On the role of the south Atlantic atmospheric circulation in tropical Atlantic variability, in *Earth's Climate: The Ocean-Atmosphere Interaction*, edited by C. Wang, S. P. Xie and J. A. Carton, pp. 143-156.
- Barriero, M., P. Chang, and R. Saravanan, 2002: Variability of the South Atlantic Convergence Zone simulated by an Atmospheric General Circulation Model. *Journal of Climate*, **15**, 745-763.
- Beck, C., J. Grieser, and B. Rudolf, 2005, A New Monthly Precipitation Climatology for the Global Land Areas for the Period 1951 to 2000. DWD, Klimastatusbericht KSB 2004, ISSN 1437-7691, ISSN 1616-5063 (Internet), ISBN 3-88148-402-7, 181-190.
- Biasutti, M., H. Sobel, and Y. Kushnir, 2006: AGCM Precipitation Biases in the Tropical Atlantic. *J. Climate*, **19**(6), 935-958.

Björnsson, H., and S. Venegas, 1997: A Manual for EOF and SVD analyses of climate data., Department of Atmospheric and Oceanic Sciences and Centre for Climate and Global Change Research, McGill University, Montreal, Canada. 52 pp.

Cazes Boezio, G., A. Robertson, and C. Mechoso, 2003: Seasonal dependence of ENSO teleconnections over South America and relationships with precipitation in Uruguay. *Journal of Climate*, **16**, 1159-1176.

Cess, R. D., and G. L. Potter, 1987: Exploratory studies of cloud radiative forcing with a general circulation model. *Tellus*, **39**(A), 460-473.

Clarke, A., 2008, *An Introduction to the Dynamics of El Niño and the Southern Oscillation*, 308 pp., Elsevier, San Diego.

Cook, 2009, South American Climate Variability and Change: Remote and Regional Forcing Processes in *Past Climate Variability in South America and Surrounding Regions*, edited by F. Vimeux, F. Sylvestre and M. Khodri, pp. 193-212, Springer Science.

Curtis, S., and S. Hasternrath, 1995: Forcing of the anomalous sea surface temperature evolution in the tropical Atlantic during Pacific warm events. *Geophysical Research Letters*, **100**, 15835-15847.

Chang, P., R. Saravanan, L. Jin, and G. Hegerl, 2000: The effect of Local Sea Surface Temperatures on Atmospheric Circulation over the Tropical Atlantic Sector. *Journal of Climate*, **13**, 2195-2216.

Chavez, R., and P. Nobre, 2004: Interactions between sea surface temperature over the South Atlantic Ocean and the South Atlantic Convergence Zone. *Geophysical Research Letters*, **31**, L003204, doi:003210.001029/002003GL018647.

Chiang, J., Y. Kushnir, and S. Zebiak, 2000: Interdecadal changes in eastern Pacific ITCZ variability and its influence on the Atlantic ITCZ. *Geophysical Research Letters*, **27**, 3687-3690.

Chiang, J., Y. Kushnir, and A. Giannini, 2002: Deconstructing Atlantic Intertropical Convergence Zone variability: Influence of the local cross-equatorial sea surface temperature gradient and remote forcing from the eastern equatorial Pacific. *Journal of Geophysical Research*, **107**(D1), 1-19.

Chouinard, C. M., M. Beland, and N. McFarlane, 1986: A simple gravity wave drag parameterization for use in medium-range weather forecast models. *Atmosphere-Ocean*, **24**(2), 91-110.

Christensen, J. H., B. Hewitson, A. Busuioc, A. Chen, X. Gao, I. Held, R. Jones, R. K. Kolli, W.-T. Kwon, R. Laprise, V. M. Rueda, L. Mearns, C. G. Menéndez, J. Räisänen, A. Rinke, A. Sarr, and P. Whetton, 2007, Regional Climate Projections, in *Climate Change 2007: The Physical Science Basis. Contribution of Working Group I to the Fourth Assessment Report of the Intergovernmental Panel on Climate Change*, edited by S. Solomon, D. Qin, M. Manning, Z. Chen, M. Marquis, K.B. Averyt, M. Tignor and H.L. Miller, pp. 847-940, Cambridge University Press, Cambridge, United Kingdom and New York, NY, USA.

Doyle, M., and V. Barros, 2002: Midsummer low-level circulation and precipitation in subtropical South America and related sea surface temperature anomalies in the South Atlantic. *Journal of Climate*, **15**, 3394-3410.

Drumond, A., 2001, Simulações Numéricas de Períodos Extremos da Oscilação Sul e seu Impacto sobre o Clima das Américas. Dissertação de Mestrado thesis, Universidade de São Paulo, São Paulo.116 pp.

Drumond, A., and T. Ambrizzi, 2003: Estudo observacional e numérico da variação da circulação atmosférica nas Américas em episódios extremos da Oscilação Sul. *Revista Brasileira de Meteorologia*, **18**(1), 1-12.

Drumond, A. R. M., and T. Ambrizzi, 2006: Inter ENSO variability and its influence over the South American monsoon system. *Advances in Geosciences*(6), 167-171.

Elliot, J., S. Jewson, and R. Sutton, 2001: The Impact of the 1997/98 El Niño Event on the Atlantic Ocean. *Journal of Climate*, **14**(6), 1069-1077.

Enfield, D., and D. Mayer, 1997: Tropical Atlantic sea surface temperature variability and its relationship to El Niño-Southern Oscillation. *Journal of Geophysical Research*, **102**, 929-945.

Fels, S. B., and M. D. Schwarzkopf, 1975: Simplified exchange approximation - New method for radiative-transfer calculations. *J. Atmos. Sci.*, **32**(7), 1475-1488.

Fels, S. B., and M. D. Schwarzkopf, 1981: An efficient, accurate, algorithm for calculating CO₂ 15 μm band cooling rates. *Journal of Geophysical Research-Oceans and Atmospheres*, **86**(NC2), 1205-1232.

Florenchie, P., C. Reason, J. Lutjeharms, M. Rouault, C. Roy, and S. Masson, 2004: Evolution of interannual warm and cold events in the southeast Atlantic Ocean. *J. Climate*, **17**, 2318-2334.

Garreaud, R. D., and P. Aceituno, 2001: Interannual rainfall variability over the South American Altiplano. *J. Climate*, **14**(12), 2779-2789.

Gates, W. L., and A. B. Nelson, 1975: A new (revised) tabulation of the Scripps topography on a 1 degree global grid: Part I, Terrain heights., Technical Report R-1276-1-ARPA, The Rand Corporation, Santa Monica, CA.132 pp.

Giannini, A., R. Saravanan, and P. Chang, 2004: The preconditioning role of Tropical Atlantic Variability in the development of the ENSO teleconnection: implications for the prediction of Nordeste rainfall. *Climate Dyn.*, **22**(8), 839-855, doi:810.1007/s00382-00004-00420-00382.

Giannini, A., J. Chiang, M. Cane, Y. Kushnir, and R. Seager, 2001: The ENSO Teleconnection to the Tropical Atlantic Ocean: contributions of remote and local SSTs to rainfall variability in the Tropical Americas. *J. Climate*, **14**, 4530-4544.

Gill, A., 1980: Some simple solutions for heat-induced tropical circulation. *Quarterly Journal of the Royal Meteorological Society*, **106**, 447-462.

Gordon, H. B., and S. P. Ofarrell, 1997: Transient climate change in the CSIRO coupled model with dynamic sea ice. *Monthly Weather Review*, **125**(5), 875-907.

Gordon, H. B., L. D. Rotstayn, J. L. McGregor, M. R. Dix, E. A. Kowalczyk, S. P. O'Farrell, L. J. Waterman, A. C. Hirst, S. G. Wilson, M. A. Collier, I. G. Watterson, and T. I. Elliot, 2002: The CSIRO Mk3 climate system model, Technical Report CSIRO Atmospheric Research, Victoria, Australia. 60 pp.

Gregory, D., and P. R. Rowntree, 1990: A mass flux convection scheme with representation of cloud ensemble characteristics and stability-dependent closure. *Monthly Weather Review*, **118**, 1483-1506.

Grimm, A., 2003a: The El Niño Impact on the summer monsoon in Brazil: regional processes versus remote influences. *J. Climate*, **26**(2), 263-280.

Grimm, A., 2003b: How do La Niña events disturb the summer monsoon system in Brazil? *Climate Dynamics*, **22**, 123-138.

Grimm, A., 2010: Interannual climate variability in South America: impacts on seasonal precipitation, extreme events, and possible effects of climate change. *Stoch. Environ. Res. Risk Assess.*, 1-18, doi:10.1007/s00477-00010-00420-00471.

Grimm, A., and P. Silva Diaz, 1995: Analysis of tropical-extratropical interactions with influence functions of a barotropic model. *Journal of Atmospheric Science*, **52**, 3538-3555.

Grimm, A., and T. Ambrizzi, 2009, Teleconnections into South America from the Tropics and Extratropics on Interannual and Intraseasonal Timescales, in *Past Climate Variability in South America and Surrounding Regions*, edited by F. Vimeux, F. Sylvestre and M. Khodri, pp. 159-191, Springer.

Grimm, A., and T. Tedeschi, 2009: ENSO and Extreme Rainfall Events in South America. *J. Climate*, **22**(7), 1589-1609.

Grimm, A., and M. Zilli, 2009: Interannual Variability and Seasonal Evolution of Summer Monsoon Rainfall in South America. *J. Climate*, **22**(9), 2257-2275.

Grimm, A., V. Barros, and M. Doyle, 2000: Climate variability in southern South America associated with El Niño and La Niña events. *J. Climate*, **13**, 35-58.

Grimm, A., J. Pal, and F. Giorgi, 2007: Connection between spring conditions and peak summer monsoon rainfall in South America: Role of Soil moisture anomalies, surface temperature, and topography in eastern Brazil. *Journal of Climate*, **20**, 5929-5945.

Hasternrath, S., and L. Heller, 1977: Dynamics of climatic hazards in Northeast Brazil. *Quarterly Journal of the Royal Meteorological Society*, **103**(435), 77-92.

Hill, K., A. Taschetto, and M. England, 2009: South American rainfall impacts associated with inter-El Niño variations. *Geophys. Res. Lett.*, **36**, L19702, doi:10.1029/2009gl040164.

Hill, K., A. Taschetto, and M. England, 2011: Sensitivity of South American summer rainfall to tropical Pacific Ocean SST anomalies. *Geophysical Research Letters*, **38**(L01701), doi:10.1029/2010GL045571.

Horel, J. D., and J. M. Wallace, 1981: Planetary-scale atmospheric phenomena associated with the southern Oscillation. *Monthly Weather Review*, **109**, 813-829.

Huang, H. P., A. W. Robertson, and Y. Kushnir, 2005: Atlantic SST gradient and the influence of ENSO. *Geophys. Res. Lett.*, **32**(20), L20706, doi:20710.21029/22005gl023944.

Jin, F.-F., 1997a: An Equatorial Ocean Recharge Paradigm for ENSO. Part II: A Stripped-Down Coupled Model. *J. Atmos. Sci.*, **54**(7), 830-847.

Jin, F.-F., 1997b: An Equatorial Ocean Recharge Paradigm for ENSO. Part I: Conceptual Model. *J. Atmos. Sci.*, **54**(7), 811-829.

Kalnay, E., K. Mo, and J. Paegle, 1986: Large-amplitude, short-scale stationary Rossby waves in the Southern Hemisphere: Observations and mechanistic experiments to determine their origin. *Journal of Atmospheric Science*, **43**, 252-275.

Kalnay, E., M. Kanamitsu, R. Kistler, W. Collins, D. Deaven, L. Gandin, M. Iredell, S. Saha, G. White, J. Woollen, Y. Zhu, M. Chelliah, W. Ebisuzaki, W. Higgins, J. Janowiak, K. C. Mo, C. Ropelewski, J. Wang, A. Leetmaa, R. Reynolds, R. Jenne, and D. Joseph, 1996: The NCEP/NCAR 40-year reanalysis project. *Bull. Am. Meteor. Soc.*, **77**(3), 437-471.

Kao, H. Y., and J. Y. Yu, 2009: Contrasting Eastern-Pacific and Central-Pacific Types of ENSO. *J. Climate*, **22**(3), 615-632.

Kayano, M., and R. Andreoli, 2007: Relations of South American summer rainfall interannual variations with the Pacific Decadal Oscillation. *International Journal of Climatology*, **27**, 531-540.

Kayano, M., V. Rao, and A. Moura, 1988: Tropical circulations and the associated rainfall anomalies during two contrasting years. *Journal of Climatology*, **8**, 477-488.

Kiladis, G., and H. Diaz, 1989: Global climatic anomalies associated with extremes in the Southern Oscillation. *J. Climate*, **2**, 1069-1090.

Kousky, V., and C. Ropelesky, 1989: Extremes in the Southern Oscillation and their relationship to precipitation anomalies with emphasis on the South American region. *Rev. Bras. Meteo.*, **4**, 351-363.

Kowalczyk, E. A., J. R. Garrat, and P. B. Krummel, 1994: Implementation of a soil-canopy scheme into the CSIRO GCM - regional aspects of the model response, Technical Report (32) CSIRO Division of Atmospheric Research, Victoria, Australia. 59 pp.

Kug, J. S., F. F. Jin, and S. I. An, 2009: Two Types of El Niño Events: Cold Tongue El Niño and Warm Pool El Niño. *J. Climate*, **22**(6), 1499-1515.

Kug, J. S., J. Choi, S. I. An, F. F. Jin, and A. T. Wittenberg, 2010: Warm Pool and Cold Tongue El Niño Events as Simulated by the GFDL 2.1 Coupled GCM. *J. Climate*, **23**(5), 1226-1239.

Lacis, A. A., and J. E. Hansen, 1974: Parameterization for absorption of solar-radiation in earths atmosphere. *J. Atmos. Sci.*, **31**(1), 118-133.

Larkin, N. K., and D. E. Harrison, 2005a: On the definition of El Niño and associated seasonal average US weather anomalies. *Geophys. Res. Lett.*, **32**(13), L13705, doi:13710.11029/12005gl022738.

Larkin, N. K., and D. E. Harrison, 2005b: Global seasonal temperature and precipitation anomalies during El Niño autumn and winter. *Geophys. Res. Lett.*, **32**(16).

Latif, M., and N. S. Keenlyside, 2009: El Niño/Southern Oscillation response to global warming. *Proc. Natl. Acad. Sci.*, **106**(49), 20578-20583.

Lau, K., and P. Chan, 1983: Short-term climate variability and atmospheric teleconnection from satellite-observed outgoing longwave radiation. Part I: Simultaneous relationship. *Journal of Atmospheric Science*, **40**, 2735-2750.

Lenters, J., and H. Cook, 1997: On the origin of the Bolivian High and related circulation features of the South American climate. *J. Climate*, **54**, 656-677.

Liebmann, B., and C. A. Smith, 1996: Description of a Complete (Interpolated) Outgoing Longwave Radiation Dataset. *Bulletin of the American Meteorological Society*, **77**, 1275-1277.

Mantua, N., S. Hare, Y. Zhang, J. Wallace, and R. Francis, 1997: A Pacific interdecadal climate oscillation with impacts on salmon production. *Bulletin of the American Meteorological Society*, **78**, 1069-1079.

Marengo, J., B. Liebmann, and V. Kousky, 2001: Onset and end of the rainy season in the Brazilian Amazon Basin. *Journal of Climate*, **14**, 833-852.

McGregor, J. L., 1993: Economical determination of departure points for semi-lagrangian models. *Monthly Weather Review*, **121**(1), 221-230.

McGuffie, K., and A. Henderson, 2005, *A Climate Modelling primer*, 280 pp., John Wiley & Sons Ltd, Sussex.

Mendes da Silva, G., and T. Ambrizzi, 2009: Summertime moisture transport over Southeastern South America and extratropical cyclones behaviour during inter El-Niño events. *Theor. Appl. Climatol.*, **101**(3-4), 303-310.

Mo, K., 2000: Relationships between low-frequency variability in the Southern Hemisphere and sea surface temperature anomalies. *J. Climate*, **13**(20), 3599-3620.

Moura, A., and J. Shukla, 1981: On the dynamics of droughts in northeast Brazil: Observations, theory and numerical experiments with a general circulation model. *Journal of Atmospheric Science*, **38**(7), 2653-2675.

Munnich, M., and J. D. Neelin, 2005: Seasonal influence of ENSO on the Atlantic ITCZ and equatorial South America. *Geophys. Res. Lett.*, **32**(21), L21709, doi:21710.21029/22005gl023900.

National Geophysical Data Center, 2-minute Gridded Global Relief Data (ETOPO2V2), 2006, <http://www.ngdc.noaa.gov/mgg/fliers/06mgg01.html>, Accessed 23 August 2011.

Navarra, A., and V. Somoncin, 2010, *A Guide to Empirical Orthogonal Functions for Climate Data Analysis*, 151 pp., Springer, Netherlands.

Nobre, P., and J. Shukla, 1996: Variations of sea surface temperature, wind stress and rainfall over tropical Atlantic and South America. *J. Climate*, **10**(4), 2664-2479.

- North, G. R., T. L. Bell, and R. F. Cahalan, 1982: Sampling errors in the estimation of empirical orthogonal functions. *Monthly Weather Review*, **110**, 699-706.
- O'Farrell, S. P., 1998: Investigation of the dynamic sea ice component of a coupled atmosphere-sea ice general circulation model. *J. Geophys. Res.*, **103**(C8), 15751-15782.
- Paegle, J., and K. Mo, 1997: Alternating wet and dry conditions over South America during summer. *Monthly Weather Review*, **125**, 279-291.
- Paegle, J., and K. Mo, 2002: Linkages between summer rainfall variability over South America and sea surface temperature anomalies. *J. Climate*, **15**(12), 1389-1407.
- Pezzi, L. P., and I. F. A. Cavalcanti, 2001: The relative importance of ENSO and tropical Atlantic sea surface temperature anomalies for seasonal precipitation over South America: a numerical study. *Climate Dyn.*, **17**(2-3), 205-212.
- Philander, S., 1990, *El Niño, La Niña and the Southern Oscillation*, 293 pp., Academic Press, San Diego.
- Phipps, S. J., 2006a, On the Long-Term Climate Studies Using a Coupled General Circulation Model. Phd thesis, University of Tasmania, Hobart.314 pp.
- Phipps, S. J., 2006b: The CSIRO Mk3L climate system model, Technical Report 3, Antarctic Climate & Ecosystem Cooperative Research Centre, Hobart, Tasmania, Australia.237 pp.
- Phipps, S. J., 2010: The CSIRO Mk3L climate system model v1.2 The Antarctic Climate & Ecosystems Cooperative Research Centre, Hobart, Tasmania, Australia.121 pp.
- Pulwarty, R. S., 1994, Annual and interannual variability of convection over tropical South America. Ph.D. thesis, University of Colorado, Boulder.220 pp.
- Randall, D. A., R. A. Wood, S. Bony, R. Colman, T. Fichefet, J. Fyfe, V. Kattsov, A. Pitman, J. Shukla, J. Srinivasan, R. J. Stouffer, A. Sumi, and K.E. Taylor, 2007, Climate Models and Their Evaluation, in *Climate Change 2007: The Physical Science Basis. Contribution of Working Group I to the Fourth Assessment Report of the Intergovernmental Panel on Climate Change*, edited by S. [Solomon, D. Qin, M. Manning, Z. Chen, M. Marquis, K.B. Averyt, M. Tignor and H.L. Miller], pp. 589-662, Cambridge University Press, Cambridge.
- Rao, V., and K. Hada, 1990: Characteristic of rainfall over Brazil: annual and variations and connections with the Southern Oscillation. *Theor. Appl. Climatol.*, **42**, 81-91.
- Rayner, N. A., D. E. Parker, E. B. Horton, C. K. Folland, L. V. Alexander, D. P. Rowell, E. C. Kent, and A. Kaplan, 2003: Global analyses of sea surface temperature, sea ice, and night marine air temperature since the late nineteenth century. *J. Geophys. Res.*, **108**(D14), 4407, doi:4410.1029/2002jd002670.
- Reynolds, R., N. Rayner, T. Smith, D. Stokes, and W. Wang, 2002: An improved in situ and satellite SST analysis for climate. *Journal of Climate*, **15**, 1609-1625.

Rodrigues, R., R. Haarsma, E. Campos, and T. Ambrizzi, 2011: The Impacts of Inter-El Niño Variability on the Tropical Atlantic and Northeast Brazil Climate. *J. Climate*, **24**(13), 3402-3422.

Ropelewski, and Halpert, 1987: Global and Regional Scale Precipitation Patterns Associated with the El Niño/Southern Oscillation. *Monthly Weather Review*, **115**, 1606-1626.

Ropelewski, and Halpert, 1989: Precipitation patterns associated with the high index phase of the Southern Oscillation. *J. Climate*, **2**(3), 268-284.

Rotstayn, L. D., 1997: A physically based scheme for the treatment of stratiform clouds and precipitation in large-scale models .1. Description and evaluation of the microphysical processes. *Quart. J. Roy. Meteor. Soc.*, **123**(541), 1227-1282.

Rotstayn, L. D., 1998: A physically based scheme for the treatment of stratiform clouds and precipitation in large-scale models. II: Comparison of modelled and observed climatological fields. *Quart. J. Roy. Meteor. Soc.*, **124**(546), 389-415.

Rotstayn, L. D., 2000: On the "tuning" of autoconversion parameterizations in climate models. *Journal of Geophysical Research-Atmospheres*, **105**(D12), 15495-15507.

Rudolf, B., and B. U. Schneider, 2005: Calculation of Gridded Precipitation Data for the Global Land-Surface using in-situ Gauge Observations, Proceedings of the 2nd Workshop of the International Precipitation Working Group IPWG, Monterey October 2004, EUMETSAT, ISBN 92-9110-070-6, ISSN 1727-432X, 231-247.

Santoso, A., W. Cai, M. England, and S. Phipps, 2011: The Role of the Indonesian Throughflow on ENSO Dynamics in a Coupled Climate Model. *J. Climate*, **24**, 585-601.

Sarachik, E., and M. Cane, 2010, *The El Niño- Southern Oscillation Phenomenon*, 369 pp., Cambridge University Press, New York.

Saravanan, R., and P. Chang, 2000: Interaction between Tropical Atlantic Variability and El Niño-Southern Oscillation. *Journal of Climate*, **13**(13), 2177-2194.

Sciremammano, F., 1979: A Suggestion for the Presentation of Correlations and Their Significance Levels. *Journal of Physical Oceanography*, **9**(6), 1273-1276.

Schwarzkopf, M. D., and S. B. Fels, 1985: Improvements to the algorithm for computing CO₂ transmissivities and cooling rates. *Journal of Geophysical Research-Atmospheres*, **90**(ND6), 10541-10550.

Schwarzkopf, M. D., and S. B. Fels, 1991: The simplified exchange method revisited - An accurate, rapid method for computation of infrared cooling rates and fluxes. *Journal of Geophysical Research-Atmospheres*, **96**(D5), 9075-9096.

Servain, J., 1991: Simple climate indices for the tropical Atlantic Ocean and some applications. *J. Geophys. Res.*, **96**(C8), 15137-15146.

Silva, G., and T. Ambrizzi, 2006: Inter-El Niño variability and its impact on the South American low-level jet east of the Andes during austral summer -two case studies. *Adv. Geosci.*, **6**, 283-287, doi:210.5194/adgeo-5196-5283-2006.

Silva, G., and T. Ambrizzi, 2010: Summertime moisture transport over Southeastern South America and extratropical cyclones behavior during inter-El Niño events. *Theor. Appl. Climatol.*, **101**(3), 303-310.

Silva, G., T. Ambrizzi, and J. Marengo, 2009: Observational evidences on the modulation of the South American Low Level Jet east of the Andes according the ENSO variability. *Ann. Geophys.*, **27**(2), 645-657.

Silva, G., A. Drumond, and T. Ambrizzi, 2011: The impact of El Niño on Sout American summer climate during different phases of the Pacific Decadal Oscillation. *Theor. Appl. Climatol.*, **106**(3-4), 307-319.

Silvestri, G., 2004: El Niño signal variability in the precipitation over southeastern South America during austral summer. *Geophysical Research Letters*, **31**(L18206), doi:10.1029/2004GL020590.

Souza, E. B., and P. Nobre, 1998: Uma revisão sobre o Padrão de Dipolo no Oceano Atlântico tropical. *Rev. Bras. Meteo.*, **13**(1), 31-44.

Souza, E. B., M. T. Kayano, J. Tota, L. Pezzi, G. Fisch, and C. Nobre, 2000: On the influences of the El Niño, La Niña and Atlantic dipole pattern on the Amazonian rainfall during 1960-1998. *Acta Amazonica*, **30**(2), 305-318.

Taschetto, A. S., and M. H. England, 2009: El Niño Modoki Impacts on Australian Rainfall. *J. Climate*, **22**(11), 3167-3174.

Taschetto, A. S., C. C. Ummenhofer, A. Sen Gupta, and M. H. England, 2009: Effect of anomalous warming in the central Pacific on the Australian monsoon. *Geophys. Res. Lett.*, **36**.

Taschetto, A. S., R. J. Haarsma, A. Sen Gupta, C. C. Ummenhofer, K. J. Hill, and M. H. England, 2010: Australian Monsoon Variability Driven by a Gill-Matsuno-Type Response to Central West Pacific Warming. *J. Climate*, **23**(18), 4717-4736.

Trauth, M., 2010, *Matlab Recipes for Earth Sciences*, 3rd ed., 237 pp., Springer, Netherland.

Trenberth, K. E., and J. M. Caron, 2000: The Southern Oscillation Revisited: Sea level pressures, surface temperatures and precipitation. *J. Climate*, **13**, 4358-4365.

Trenberth, K. E., and D. P. Stephaniak, 2001: Indices of El Niño evolution. *J. Climate*, **14**, 1697-1701.

Trenberth, K. E., and L. Smith, 2009: Variations in the Three-Dimensional Structure of the Atmospheric Circulation with Different Flavors of El Niño. *J. Climate*, **22**(11), 2978-2991.

Venegas, S., L. Mysak, and N. Straub, 1997: Atmosphere-ocean coupled variability on the South Atlantic. *Journal of Climate*, **10**, 2904-2920.

Vera, C., G. Silvestri, V. Barros, and A. Carril, 2004: Differences in El Niño response over the Southern Hemisphere. *J. Climate*, **17**(9), 1741-1753.

Vera, C., J. Baez, M. Douglas, C. Emmanuel, J. Marengo, J. Meitin, M. Nicolini, J. Nogues-Paegle, J. Paegle, O. Penalba, P. Salio, C. Saulo, M. Silva Dias, P. Silva Dias,

and E. Zipser, 2006: The South American Low-Level Jet Experiment. *Bull. Am. Meteor. Soc.*, 63-77.

Vincent, E., M. Lengaigne, C. Menkes, N. Jourdain, P. Marchesiello, and G. Madec, 2009: Interannual variability of the South Pacific Convergence Zone and implications for tropical cyclone genesis. *Climate Dyn.*, 1-16.

von Storch, H., and F. Zwiers, 2003, *Statistical Analysis in Climate Research*, 484 pp., Cambridge University Press, Cambridge.

Vuille, M., 1999: Atmospheric Circulation over the Bolivian Altiplano during dry and wet periods and extremes phases of the southern oscillation. *International Journal of Climatology*, **19**, 1579-1600.

Wallace, J., and P. Hobbs, 2006, *Atmospheric Science* Second ed., 483 pp., Academic Press, Amsterdam.

Wallace, J. M., and D. S. Gutzler, 1981: Teleconnections in the geopotential height field during the Northern Hemisphere winter. *Monthly Weather Review*, **109**, 784-812.

Wang, 2005, ENSO, Atlantic Climate Variability, and The Walker and Hadley circulations, in *The Hadley Circulation: Present, Past and Future*, edited by H. F. Diaz and R. S. Bradley, pp. 173-202.

Wang, and Hendon, 2007: Sensitivity of Australian rainfall to inter-El Niño variations. *J. Climate*, **20**(16), 4211-4226.

Wang, C., 2002a: Atmospheric Circulation Cells Associated with El Niño-Southern Oscillation. *J. Climate*, **15**, 399-419.

Wang, C., 2002b: Atmospheric Circulation Cells Associated with the El Niño-Southern Oscillation. *Journal of Climate*, **15**, 399-419.

Wang, C., 2002c: Atlantic Climate Variability and Its Associated Atmospheric Circulation Cells. *Journal of Climate*, **15**, 1516-1536.

Wang, C., F. Kucharski, R. Barimalala, and A. Bracco, 2009: Teleconnections of the tropical Atlantic to the tropical Indian and Pacific Oceans: A review of recent findings. *Meteorologische Zeitschrift*, **18**(4), 445-454.

Wang, W. C., X. Z. Liang, M. P. Dudek, D. Pollard, and S. L. Thompson, 1995: Atmospheric ozone as a climate gas. *Atmospheric Research*, **37**(1-3), 247-256.

Weng, H. Y., S. K. Behera, and T. Yamagata, 2009: Anomalous winter climate conditions in the Pacific rim during recent El Niño Modoki and El Niño events. *Climate Dyn.*, **32**(5), 663-674.

Weng, H. Y., K. Ashok, S. K. Behera, S. A. Rao, and T. Yamagata, 2007: Impacts of recent El Niño Modoki on dry/wet conditions in the Pacific rim during boreal summer. *Climate Dyn.*, **29**(2-3), 113-129.

Wilks, D., 2006, *Statistical Methods in the Atmospheric Sciences*, second ed., 627 pp., Elsevier Inc, San Diego, California.

Xie, P. P., and P. A. Arkin, 1996: Analyses of global monthly precipitation using gauge observations, satellite estimates, and numerical model predictions. *J. Climate*, **9**(4), 840-858.

Yeh, S. W., J. S. Kug, B. Dewitte, M. H. Kwon, B. P. Kirtman, and F. F. Jin, 2009: El Niño in a changing climate. *Nature*, **461**(7263), 511-U570.

Yu, J. Y., and S. T. Kim, 2010: Three evolution patterns of Central-Pacific El Niño. *Geophys. Res. Lett.*, **37**.

Zhou, J., and W. K. Lau, 2001: Principal modes of interannual and decadal variability of summer rainfall over South America. *Int. J. Climatol.*, **21**, 1623-1644.